Molecular Dynamics Simulation and Crystal-Field Theory : Predicting the optical spectra and structure of rare-earth doped inorganic glasses

Guy Cormier

A Thesis
in
The Department
of
Chemistry and Biochemistry

Presented in Partial Fulfilment of the Requirements
for the Degree of Doctor of Philosophy at
Concordia University
Montréal, Québec, Canada

April 1993

ISBN 0-315-84679-8

Canada

ABSTRACT

Molecular Dynamics Simulation and Crystal-Field Theory :
Predicting the optical spectra and structure
of rare-earth doped inorganic glasses

Guy Cormier, Ph.D.
Concordia University, 1993

An investigation of the local environment of rare-earth ions doped in inorganic glasses is presented. By the technique of Molecular Dynamics, we have simulated structural models of two rare-earth doped inorganic glasses, $Na_2O{\cdot}2SiO_2{:}Eu^{3+}$ and $SiO_2{:}Eu^{3+}$. The simulated structure of the base glasses and the local environment of the doped trivalent europium ions were investigated with the help of radial distribution functions, cumulative distribution functions and bond angle distributions of the various atomic species found in both glasses.

A successful validation of the simulated structural model of the $Na_2O{\cdot}2SiO_2{:}Eu^{3+}$ glass was performed through a comparison between (i) room-temperature absorption and broadband emission spectra of the experimental glass and (ii) calculated $^5L_6$, $^5D_3$, $^5D_2$, $^5D_1$, $^5D_0 \leftarrow {}^7F_{0,1}$ absorption and $^5D_0 \rightarrow {}^7F_J$ (J= 0 to 6) emission spectra of the simulated glass. The simulated spectra were obtained using a point-charge crystal-field model, which allows the calculation of the energies and transition probabilities of the electronic manifolds belonging to the simulated Eu^{3+} ions.

This validation culminated in the creation of an indirect link between the simulated structural model and the experimental spectra of

the corresponding laboratory glass. This link permitted the investigation of various spectral properties of rare-earth doped glasses, amongst them, Fluorescence Line Narrowing measurements, spectral correlations of individual structural factors and the effects of J-mixing and overall covalency on transitional energies and inhomogeneous broadening.

This study lead us to conclude that the presence of a limited number of distorted "*sites*" for rare-earth ions doped in oxide glasses is fallacious and tends to disprove the various structural models previously proposed for local rare-earth environments. The rare-earth environments are rather composed of a continuous distribution of local-fields which satisfy energetic bonding requirements of the Eu^{3+} ions while disregarding structural bonding requirements normally attributed to complexes or crystalline compounds. It was found that none of the individual structural factors greatly influences the electronic spectra of doped ions in inorganic glasses. Rather, we present evidence that it is the overall electrostatic and covalent energy, with an emphasis on the preponderance of J-mixing, of the individual sites which holds the greatest influence.

Finally, we have theoretically investigated an experimental technique named Dilution Narrowed Laser Spectroscopy (DNLS) which could eventually lead to the observation of the optical spectrum of isolated rare-earth ions doped in glass fibers. We propose that the structural/spectral model created through Molecular Dynamics and point-charge crystal-field calculations is presently the most reliable means to interpret DNLS and single-ion spectra.

RÉSUMÉ

Simulation par Dynamique Moléculaire et Théorie du Champ-Cristallin : Prédiction de spectres optiques et de la structure de verres inorganiques dópés aux ions terres rares

Guy Cormier, Ph.D.
Université Concordia, 1993

Cette thèse présente une étude de l'environnement local d'ions terres rares dópés dans des verres inorganiques. La technique de Dynamique Moléculaire est utilisée afin de simuler des modèles structuraux de deux verres inorganiques dopés, i.e. $Na_2O{\cdot}2SiO_2{:}Eu^{3+}$ et $SiO_2{:}Eu^{3+}$. La structure simulée des verres de base, ainsi que l'environnement local des ions europium trivalent ont été étudies à l'aide des fonctions suivantes : les fonctions de distribution radiale, les fonctions de distribution cumulative ainsi que les distributions d'angles de liaisons. Ces fonctions se rapportant, bien-entendu, aux diverses espèces atomiques constituant ces verres.

La validité du modèle structural du verre de $Na_2O{\cdot}2SiO_2{:}Eu^{3+}$ a été vérifiée à l'aide d'une comparaison entre, premièrement, les spectres optique d'absorption et d'émission du verre expérimental et, deuxièmement, de spectres d' absorption ($^5L_6$, $^5D_3$, $^5D_2$, $^5D_1$, $^5D_0 \leftarrow {}^7F_{0,1}$) et d'émission ($^5D_0 \rightarrow {}^7F_J$ (J= 0 à 6)) calculés à partir du modèle simulé de ce verre. Les spectres simulés, ont été calculés à l'aide de la théorie du champ cristallin appliquée à des charges ponctuelles. Cette théorie nous permet d'obtenir l'énergie et les probabilités de transition des niveaux Stark électroniques appartenant aux ions Eu^{3+} simulés. Cette validation

nous a permis de créer un lien indirect entre le modèle structural simulé et les spectres optiques expérimentaux du verre réel correspondant. Ce lien permet donc, l'investigation de diverses propriétés spectrales de verres dopés aux terres rares. Nous avons étudié les propriétés suivantes, (i) la technique d'affinement de raies de fluorescence, (ii) les corrélations spectrales de facteurs structuraux individuels, et (iii) l'effet qu'ont la covalence globale et le "J-mixing" sur les énergies transitionnelles et l'élargissement inhomogène.

Cette étude nous conduit à conclure que la présence d'un nombre minime de "*sites*" déformés, qu'occupent les ions terres rares dopés dans des verres d'oxyde, est fausse. Ceci tend à réfuter les divers modèles structuraux proposés, ces trente dernières années, sur l'environnement local d'ions terres rares. Ces environnements sont plutôt composés d'une distribution continue de champs locaux qui satisfont les besoins énergétiques des ions Eu^{3+} tout en ne tenant aucun compte des besoins structuraux normalement associés aux complexes organo-métalliques ou aux composés cristallins. Il a été trouvé qu'aucun des facteurs structuraux individuels, tel le nombre de coordination ou la longueur de liaison moyenne des premiers ligands, n'influencent les spectres électroniques des ions terres rares dopés dans des matrices vitreuses inorganiques. Nous apportons certains faits qui semblent indiquer que l'énergie globale (électrostatique et covalente) des sites individuels, avec une prépondérance sur le phénomène de "J-mixing", soit uniquement responsable des divers caractéristiques spectrales observées.

Par ailleurs, nous présentons une investigation théorique d'une nouvelle méthode expérimentale, la spectroscopie laser d'affinement par dilution, qui permettra éventuellement d'observer le spectre électronique d'ions uniques dopés dans des fibres optiques. Nous proposons que le modèle spectral/structural présenté dans cette thèse est présentement la méthode la plus fiable qui existe afin d'interpréter les spectres obtenus par cette technique

ACKNOWLEDGEMENTS

First and foremost, I would like to thank my research supervisor, Dr. John A. Capobianco. Throughout the many years that I have known him, he has taught me countless things. Without the advice that he so freely and kindly gave, I sincerely think that this work would not have seen the light of day.

I would like to thank the members of my research committee, Drs. Peter H. Bird and Lawrence D. Colebrook for their contributions to this thesis. Dr. Colebrook was particularly helpful with my introduction to Unix and to the Personal Iris workstation.

Je désire remercier le Dr. André Monteil du Laboratoire de Physico-Chimie des Matériaux Luminescents. Son accueil à Lyon, ses judicieux conseils, sa participation au projet de Dynamique Moleculaire et son amitié m'ont aidé à mener à bien cette thèse.

Dr. Clyde A. Morrison was extremely kind and generous during my visit at the Harry Diamond Laboratories. Discussing with him the intricacies of the crystal-field theory was both very enlightening and extremely useful. I am also indebted to him for the crystal field calculation programmes which he made available to me.

Discussions, personally and through my research supervisor, with Drs Marvin J. Weber of Lawrence Livermore National Laboratories and Stephen H. Garofalini of Rutgers University were more than appreciated.

I am obliged to Dr. Thomas F. Soules of General Electric for the original Molecular Dynamics programme, Dr. Peter Taylor of AECL Research and Prof. Marco Bettinelli of the Università di Padova for kindly supplying the europium-doped sodium disilicate samples.

I wish to thank my colleagues and friends, Drs. Pierre-Paul Proulx and Nick Raspa. Their companionship was a part of everyday life which I am thankful and which I will miss much. Merci pour tout, les gars.

I would especially like to thank Andronique Ioannidis for her friendship. The wonderful time we spent together made thesis writing a thoroughly enjoyable process.

A travers mes années passées à l'université, il y a toujours eu l'amitié de Robert Brisebois, Diane Beauchemin et Julie Giasson. Durant les bons temps et les moments difficiles, ils ont toujours été là. Merci.

Finally, I appreciate the support brought by post-graduate scholarships from the Natural Science and Engineering Research Council of Canada (NSERC) and the Fonds pour la Formation de Chercheurs et l'Aide à la Recherche (FCAR).

A mes parents: pour leur encouragement, leur patience et leur amour.

Machines exist: let us then exploit them to create beauty - a modern beauty, while we are about it. For we live in the twentieth century.

Aldous Huxley

TABLE OF CONTENTS

LIST OF FIGURES

LIST OF TABLES

CHAPTER 1

1. INTRODUCTION

Throughout it's brief history, humanity has been fascinated with glass. It's ability to be transformed into utilitarian objects and works of art is unique in the world that surrounds us. From the early glasswork of the Phoenicians, who are credited with being the first to fabricate transparent glass, to the stained glass windows of Gothic cathedrals (beautifully exemplified at Chartres or Notre-Dame de Paris) and finally to the optical fibers and glass lasers of today's technology, glass has become an indispensable part of everyday life.

In 1932, in his seminal paper on glass structure, Zachariasen [1] wrote the following introductory statement :

> *"It must be frankly admitted that we know practically nothing about the atomic arrangement in glasses."*

Even today one could argue that this is still the case [2]. Although crystallographers are able to predict with a high degree of accuracy the positions of atoms in crystalline solids using techniques such as X-ray and neutron diffraction, glass researchers are still unable to ascertain the exact atomic ordering of glass structures.

Trying to resolve structural information from a glass with the techniques developed for crystallography using radiation scattering

reveals only the average structural characteristics of the glass [3]. The structure can be characterized solely by a statistical description through the distribution of interatomic distances. On the other hand, solid-state spectroscopic methods are frequently employed for the analysis of the atomic site symmetry about a given ion type which acts as a localized structural probe. In glasses, these methods suffer from the complications due to the lack of periodicity found in disordered solids [4]. Gathering information from dopant ions in glasses, where concentrations are usually very low (typically 10^{16}-10^{20} ions/cm^3), can also be a major problem. Usually the sensitivity of the experimental method is very low. Currently, one of the best experimental techniques for studying the localized atomic structure of glasses is Extended X-Ray Absorption Fine Structure (EXAFS) [5]. EXAFS provides information about the average site occupied by a selected trace element in a compositionally complex glass without interference from the major components. Structural data is given in the form of average short-range interatomic distances, coordination number and Debye-Waller factors for a given atomic specie. However, even in EXAFS, mathematical manipulations to extract the relevant information from the data can mask the finer details of the structure.

Since we are interested in knowing the exact positions of atoms in a glass, and no experimental technique is able to yield this information, we are forced to look elsewhere to solve this problem. One tool that we possess is the ability to create atomic-scale models by computer simulation. Application of computer simulation techniques, such as Molecular Dynamics (MD) [6] or the Monte-Carlo (MC) method [7],

enables the glass scientist to both (i) model structural representations at the atomic level and (ii) calculate average structural, thermodynamic and transport properties of a given glass. If these calculated average properties are identical to those found for the laboratory glass, it can be assumed that the modelled atomic structure must be representative of this laboratory glass.

In this thesis, we shall utilise such computer techniques to investigate the local structure and luminescent properties of doped ions (i.e. trivalent rare-earths as exemplified by the Eu^{3+} ion) in insulating glass matrices (alkali silicates) .

A more precise understanding of the microstructure of insulating glasses can only increase our power over the many varying properties of these glasses. Eventually, one could envision the tailor-making of glasses for such diverse uses as nuclear fuel waste immobilization [8], glass lasers [9], amplifiers for optical fibers [10], photo- and electrochromic materials [11,12] and optical storage devices [13].

Computerized tailor-making of laser glasses would be a much more reliable and practical way of investigating the plethora of compositions possible in the oxide and fluoride systems. Glass-making is still, today, very much an art-form. An analogy has actually been made between glass-making and soup-making [14]. No one really knows the atomic scale effects most additives might have when present in a glass. Therefore, a thorough investigation of such additives with respect to the variation of spectroscopic, optical and thermomechanical properties is

quintessential to the improvement of laser glasses. One can easily envision a glass-maker replacing the crucibles and furnaces of his research laboratory by a computerized expert-system, telling it exactly what laser properties he requires (e.g. tunability range, maximum lasing wavelength) and after a certain time getting the exact composition of that particular glass. Evidently, much effort is needed to bring us to this expert-system. The work presented here is but one of the first steps that will take us towards this goal.

1.1 THE STRUCTURE OF GLASSES

1.1.1 Definition of Glass

Let us follow the process of glass formation, starting at high temperatures, where a liquid (or melt) is present. It can be shown that when a liquid cools, it's volume decreases. Normally, crystallization occurs at the melting point T_m, where a drastic decrease in volume occurs. As the temperature continues to decrease the volume decreases further but with a lower temperature coefficient representative of the small expansion coefficient of the crystal. The thermodynamic equilibrium process of crystallization is shown by the solid curve in Figure 1.1.1.1 . When conditions are such that no crystallization occurs at T_m, then the volume continues to decrease along the dashed curve. The liquid present is in a supercooled state, which is a metastable thermodynamic equilibrium. With descending temperature, an increase

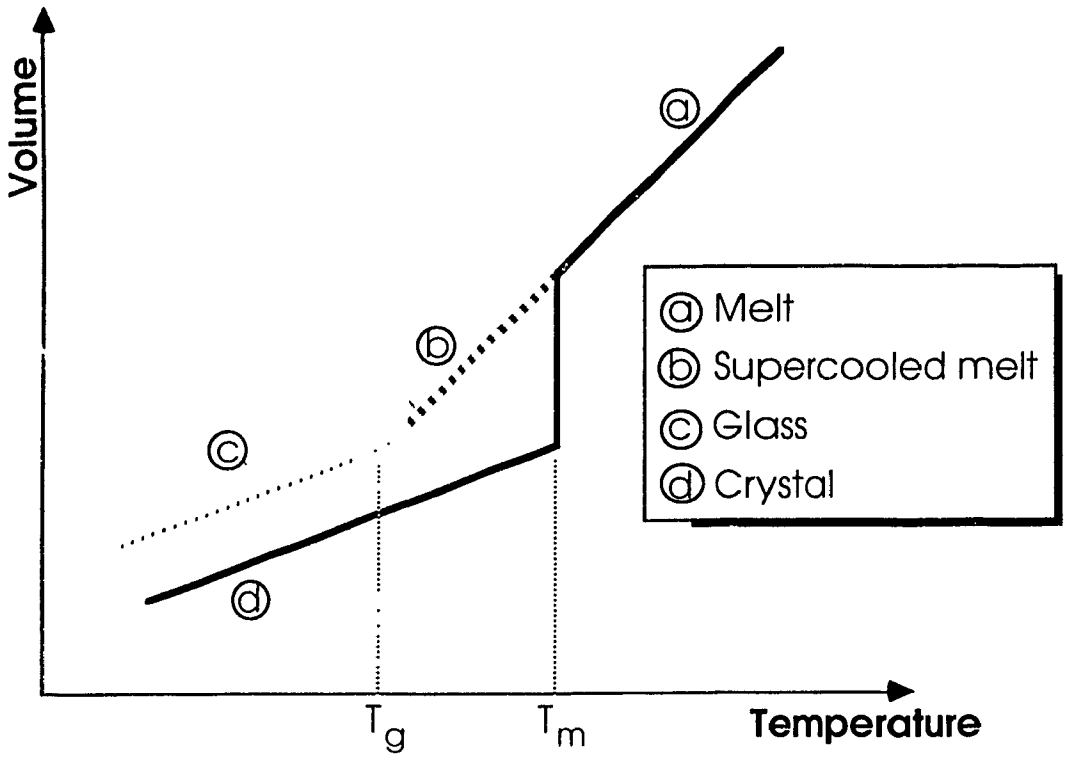

Figure 1.1.1.1 Schematic diagram of the temperature dependence of volume.

of the viscosity of the liquid is observed. At a certain temperature, called the glass transition temperature T_g, the viscosity is so high that the supercooled liquid cannot reach equilibrium. At this point the liquid becomes a solid. Kinetic considerations will determine which of the two processes, crystallization or vitrification, will occur. If the cooling is sufficiently fast to preclude crystal nucleation and growth, vitrification will proceed. On the other hand, the crystalline phase being thermodynamically more stable, crystal growth,if allowed to take place, will always dominate over the formation of the amorphous phase.

The definition of glass could then be stated as : In a physico-chemical sense, glasses are essentially non-crystalline solids obtained by freezing supercooled liquids.

Vitrification is a property found for many different types of substances. Table 1.1.1.1 lists the most important classes of materials which show vitrification.

TABLE 1.1.1.1

CLASSES OF VITRIFIABLE SUBSTANCES

VITRIFIABLE SUBSTANCES	EXAMPLES
Elements	phosphorous, sulfur and selenium
Oxides	SiO_2 , GeO_2 , B_2O_3
Chalcogenides	As-S, As-Se, P-Se, Ge-Se
Halides	BeF_2 and $ZnCl_2$
Organic compounds	methanol, glycerol, toluene
Organic polymers	polyethylene, polyvinyl chloride
Metal alloys	Ni-Nb, Cu-Zn

Covalently bonded glasses, of which the oxide glasses studied in this thesis are the primary example, have been extensively studied for the past 60 years due to their practical importance. In this period of time,

several hypothesis have been developed about the structure of such glasses. The hypothesis which has had the most impact[1] was proposed in the 1930's by Zachariasen [1] and modified by Warren [16] and is known as the Continuous Random Network model.

1.1.2 The Continuous Random Network Model

After systematic examination of the structures formed by different coordination polyhedra, Zachariasen showed that to be a glass-former, an oxide must satisfy the following group of rules :

1. The number of oxygens around a cation must be four or less.
2. None of the oxygens may be shared by more than two glass-forming cations.
3. The polyhedra must bond at corners and not on edges or faces.
4. At least three corners of each polyhedron must be shared with other polyhedra.

Zachariasen further suggested that the glass is formed by a non-periodic arrangement of glass-formers having slight variations in their bond lengths and bond angles while still retaining a defined geometry; this in effect will create a disordered network.

[1] This impact is still felt today, as the CRN model is being used to discuss the effects of modifier cations on short- and medium-range order [15].

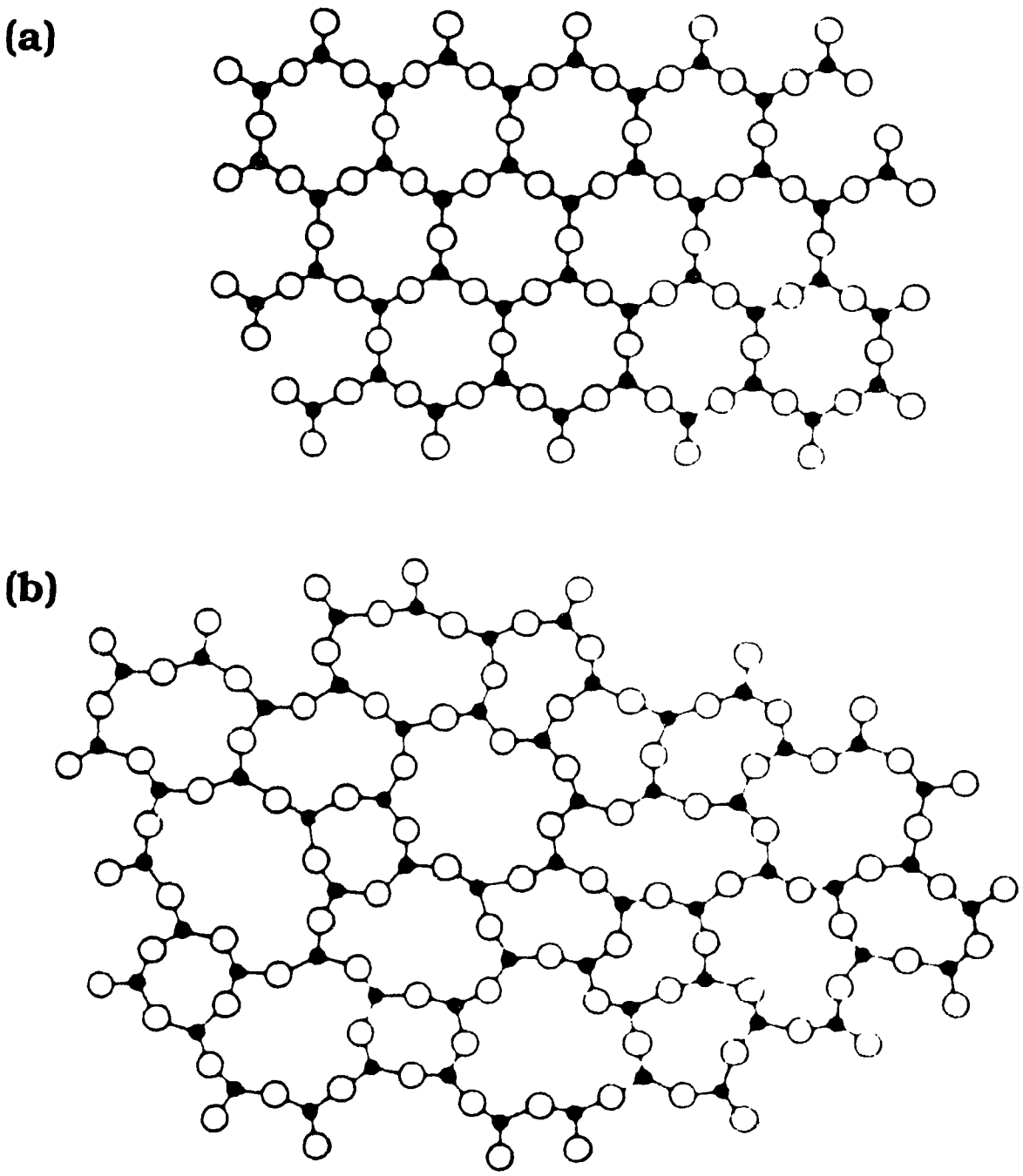

Figure 1.1.2.1 Two-dimensional representation of the structure of **(a)** a hypothetical crystalline compound A_2O_3, **(b)** the vitreous form of the same compound. After Ref. 1.

Figure 1.1.2.1 shows schematically a comparison between a hypothetical crystalline compound A_2O_3 and it's vitreous counterpart.

At the time the article was written, the only known glass-formers were oxides, of which only five formed glasses by themselves, (i.e. SiO_2, GeO_2, B_2O_3, P_2O_5, As_2O_5). Some glasses were also known to contain other cationic species (e.g. Na_2O, PbO, MgO). However, these oxides were not known to form glasses themselves. Zachariasen postulated that these cationic species were randomly distributed about the network and therefore must be an important disrupting factor. The term *network former* has been adopted for an oxide which forms the vitreous network, and *network modifier* for an oxide which does not participate directly in the network. In the case of the glasses reported in this thesis, SiO_2 is the network former, whereas Na_2O is a network modifier. This terminology is illustrated in Figure 1.1.2.2 where a two-dimensional schematic representation of a glass of the Na_2O-SiO_2 series is shown.

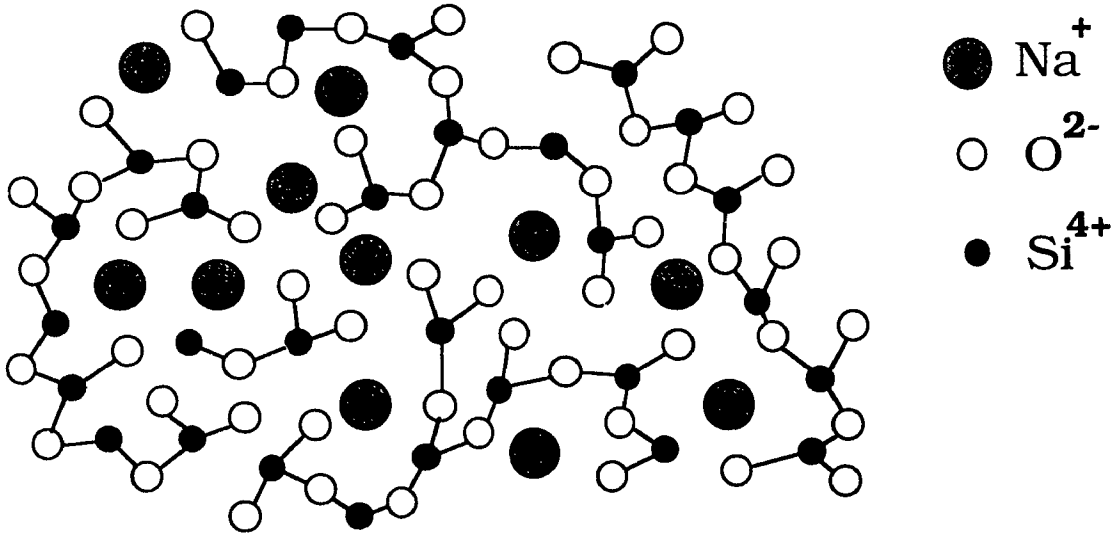

Figure 1.1.2.2 Two-dimensional schematic representation of a glass of the Na_2O-SiO_2 series.

In the single-component glass SiO_2, all O^{2} ions occur as bridging oxygens whereas in the alkali silicate glasses, nonbridging oxygens occur adjacent to the alkali ions. This is exemplified by the very simple reaction:

$$\equiv Si\text{-}O\text{-}Si\equiv + Na_2O \rightarrow \equiv Si\text{-}O\text{-}Na + Na\text{-}O\text{-}Si\equiv$$

where a breaking of the network occurs via the formation of non-bridging oxygens. This is schematically represented in Figure 1.1.2.3 . The formation of non-bridging oxygens represents the most important influence of the alkali oxides; the reason is that they cause a weakening of the glass structure since the strength in these glass systems increases with the number of Si-O-Si bridges. With increasing concentration of alkali oxide, the network is more and more disrupted till a point is reached where only isolated silicate tetrahedra are present. "Inverted" glasses are known [17] in which the network is essentially formed by the network-modifiers rather than the network-formers. These glasses were shown to have an inverse behaviour in certain properties, i.e. at high concentrations of network modifiers there is a reversal in the behaviour of intensive properties as a result of the formation of the network modifying lattice.

1.1.3 The structure of silicate glass

As seen in the previous section, silicate glasses are made up of a disordered three-dimensional silicate network which is randomly

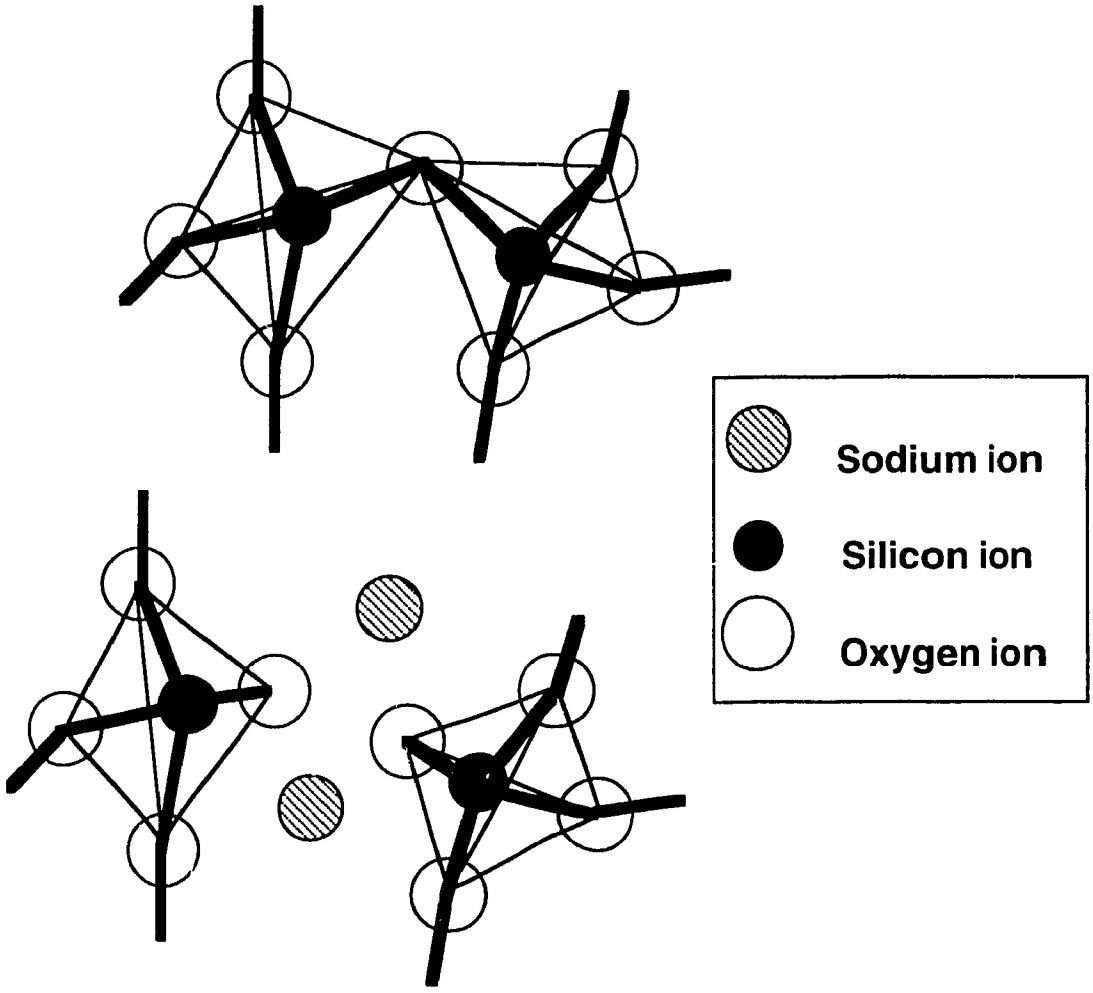

Figure 1.1.2.3 Rupture of a Si-O-Si bridge by the modifier oxide Na_2O. (top) a portion of the intact SiO_2 network, (bottom) formation of a pair of non-bridging oxygens.

modified by the presence of alkali or alkaline-earth oxides. The basic units that make up the silicate network are $[SiO_4]$ tetrahedra which are linked at corners. The average Si-O bond distance is 1.62Å and the average O-Si-O bond angle is found to be 110° [15,18]. This shows that the silicate tetrahedra are relatively undistorted. The Si-O Si bond angle varies from 120° to 180° with a maximum at about 144°. This wide variation in the Si-O-Si bond angle is the most important difference between the vitreous and the crystalline forms of SiO_2 and those of the silicates.

1.2 IONIC DOPING

Optical properties of insulating crystals and glasses can be drastically altered by the inclusion of small quantities of an ionic impurity. By such inclusion it is possible to render an ordinarily transparent or white material into a coloured material. The prime example of ionic doping is the precious gemstone, ruby. Rubies are essentially transparent corundum, α-Al_2O_3, containing a small quantity of the Cr^{3+} ion, which gives them their deep-red colouration and their extraordinary properties.

1.2.1 Rare-earth ions as dopants

The rare-earths are a group of fifteen elements (atomic numbers 57 through 71) found in group IIIB of the periodic table. This group is made up by the filling of the $4f$ shell. They usually occur as doubly or triply charged ions in ionic solids. In the triply charged ions, which is the

case of interest here, all $5d$ and $6s$ electrons are removed and the $4f$ shell is left partially occupied. The ground-state electronic configuration of the trivalent europium ion (atomic number 63) is :

$$1s^2 2s^2 2p^6 3s^2 3p^6 3d^{10} 4s^2 4p^6 4d^{10} 5s^2 5p^6 4f^6$$

or

$$[Xe]4f^6$$

The interest shown in the trivalent rare-earth ions by spectroscopists stems from the fact that the optically active $4f$ electrons are shielded by the outer, though less energetic, $5s$ and $5p$ shells of electrons. As a result, the $4f$ electrons are not strongly coupled to the neighbouring lattice and behave as inner electrons. Because of this, optical spectra (absorption and emission) of the trivalent rare-earths doped in solid-state materials will be comprised of a series of very sharp lines that closely resemble the corresponding free-ion spectra. There are three main interactions which control the properties of the f-electrons of a rare-earth ion doped in a solid : (i) the electrostatic interaction between electrons, which has the effect of coupling the individual angular momenta into orbital and spin angular momenta L and S; (ii) the spin-orbit interaction, which couples L and S to give J ; (iii) the crystal-field, which partly (or totally) raises the (2J+1)-fold degeneracy of a given J state. Thus the effect of the host material will be to split the free-ion electronic levels into a series of multiplets, as shown in Figure 1.2.1.1. The centre of gravity of each of these multiplets, is located within a few hundred wavenumbers of the free-ion levels. For the Eu^{3+} ion, the splitting of the free-ion levels is less than the separation between free-ion levels. What makes the

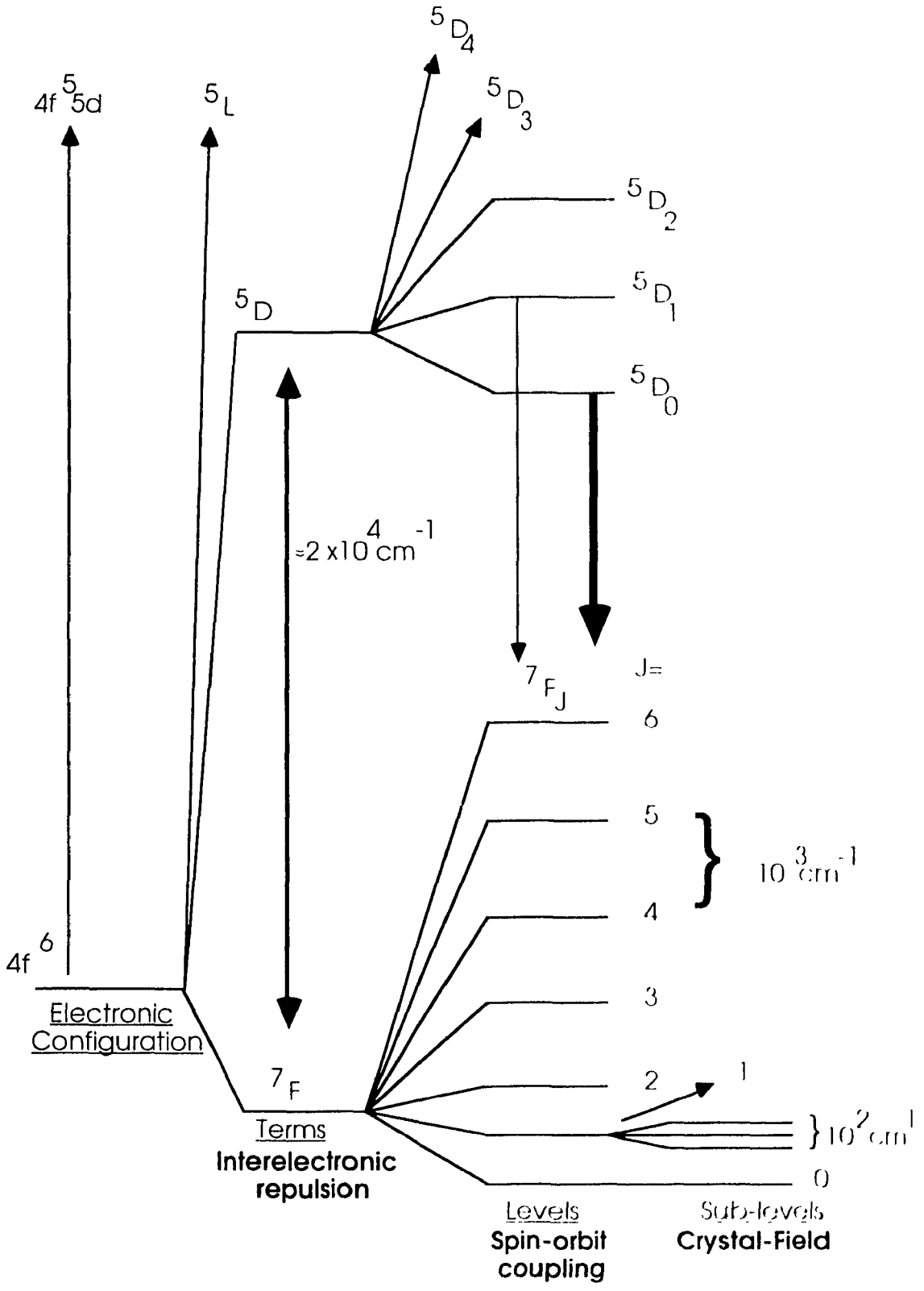

Figure 1.2.1.1 Splitting of the electronic levels of the Eu^{3+} ion.

trivalent rare-earth ions attractive to the optical spectroscopist is the fact that the crystal-field splitting will vary from host to host, reflecting the different symmetries and strengths of the different local environments.

In particular, the Eu^{3+} ion has a relatively simple energy level structure possessing a non-degenerate ground-state ($^7F_0$) and a non-degenerate emitting level ($^5D_0$) which makes it the ideal probe for crystal-field analysis for both crystalline and vitreous materials.

In Chapter 3 we will expound on the crystal-field theory, first introduced in 1929 by Bethe [19], a theoretical approach on the calculation of energy levels of rare-earth dopants in solids.

1.2.2 Ionic doping in glasses

Since the early 60's, several models have been proposed that discuss the local environments of rare-earth ions in oxide and fluoride glasses. These models were all based on spectroscopic studies. In the following section we will review the salient features of each of these models. They will not be presented in order of importance but rather chronologically.

Models developed in the 1960's

The first optical spectroscopic measurements of rare-earth doped oxide glasses were presented in the 1930's [20-22]. Some thirty years later, in 1963, Kurkjian *et al.* [23] presented an initial study on the

absorption and fluorescence spectroscopy of the Eu^{3+} ion in various alkali and alkaline-earth silicate glasses. Since at this time detailed theoretical crystal-field calculations for the rare-earth ions doped in glasses were non-existent, Kurkjian *et al.* only qualitatively described the behaviour of the optical properties of the Eu^{3+} ion as a function of glass composition and of europium concentration. Some assumptions were made based on ligand-field analysis of transition metal ions in glasses [24,25]. Studying glasses of the series x $Na_2O \cdot (1\text{-}x)SiO_2$:1 mol.% Eu_2O_3, (with x varying from 0.15 to 45) , they found that the position of the $^5D_0 \rightarrow {}^7F_0$ transition varies as much as 4 Å (or 12 cm $^{-1}$) with increasing sodium content. Basing themselves on Tomaschek [26], who noted that for transitions between two non-degenerate levels there is a red shift in energy with an increase of the rare-earth - ligand interaction, they qualitatively ascribed this behaviour to the following model. For a given glass composition, the Eu^{3+} ion is in a network-modifying position and is surrounded by seven oxygen ions (bridging and non-bridging). An increase in the concentration of the network-modifier, will show that more and more of the oxygen ions surrounding the Eu^{3+} are non bridging, thus increasing the crystal-field strength due to an increase in the ionicity of the Eu-O bond. As remarked before, this model was not based on crystal-field calculations and therefore, can only be considered as qualitative. One can also notice that they assumed the existence of a 7-fold coordination for the europium ion without any basis for such a statement.

In an attempt to investigate the Nd^{3+} environment in oxide glasses, Mockoveiak *et al.* [27] compared calculated oscillator strengths

from point-charge models with experimental values derived from absorption spectra of Nd^{3+}- doped silicate and borate glasses. The models they investigated were based on the crystalline sites of neodymium sesquioxide (6- and 7-coordinated) and neodymium ethylsulfate (9-coordinated). These models were chosen on the premise that the coordination of a given ion in glass is similar to the coordination of the same ion in a crystalline compound. Only oxygen first neighbours were considered in the point-charge calculations. Also, partial charges were used in order to place more emphasis on non-bridging oxygens. Comparing their calculated results of five Nd^{3+} transitions with that of experimental values, they found discrepancies of up to several orders of magnitude in most of the models. They attributed these discrepancies to the influence of covalent bonding, as discussed by Jörgensen *et al.* [28], however it was not taken into account in their calculations.

In 1967, Barber [29] presented results on the ytterbium ion (Yb^{3+}) as a microprobe in amorphous silica and in a sodium disilicate glass. The Yb^{3+} ion was chosen because of it's uncomplicated nature. Having only a single electron occupying its 4*f* level, it possesses a ground-state manifold, $^2F_{7/2}$, which splits into four sublevels and a unique excited-state manifold, $^2F_{5/2}$, which splits into three sublevels. Temperature-dependent absorption spectra were taken and used as a comparison to spectra constructed from a simple model. The model was based on an arrangement of eight oxygen atoms at the corners of a perfect cube, each having an Yb-O bond length of 2.30Å (average Yb-O distance in ytterbium gallium garnet) [30]. Since the absorption spectra were found to show the full splitting for each manifold, a highly symmetrical rhombohedral

deformation was applied to the cube to lower its point symmetry from O_h to D_3. The crystal-field splittings for both manifolds were calculated as a function of a distortion parameter, ρ. Assuming a Gaussian distribution on the parameter ρ, Barber proceeded to construct absorption and emission spectra from the calculated energy splittings. Despite the presence of problems with assigning relative intensities for each transition, the simulated spectra presented by Barber conveyed the principal features seen in the spectra of Yb^{3+} doped in the above mentioned glasses. Unfortunately, the primary results presented in Ref. 29 were not pursued further and no details of these calculations were published.

Starting with the crystallographic definition of a nonerystalline solid, Rice and DeShazer [31] and Mann and DeShazer [32] set about to correlate optical spectra of rare-earth ions in glasses with that of the corresponding rare-earth sesquioxide [33]. They studied, respectively, the Eu^{3+} ion doped in a borosilicate glass and the Nd^{3+} ion doped in a barium crown glass. They postulated that since a non-crystalline solid has short-range order without the long-range order of crystals, the short range environment of each rare-earth ion must approximate the corresponding crystalline environment. They observed a mirroring in the number of possible sites and in the splitting patterns, thus concluding the presence of a crystallike local environment of the rare-earth ion in the glass. Effectively, this model assumes that the rare-earth ions are *located* in *sites* which accommodate their exact bonding requirements, i.e. a particular coordination number with ligands at a proper distance. The high degree of inhomogeneous broadening of the optical spectra would be

taken care of by the site-to-site variation in the geometrical arrangement of the surrounding ligands while still retaining the crystallike environment for each of the *sites*.

Models developed in the 1970's

Robinson, Fournier and Bartram wrote a series of articles [34-39], on rare-earth sites in various oxide glass systems. They examined Yb^{3+} doped in phosphate, silicate and germanate glasses, Er^{3+} in alkali silicate glasses and Nd^{3+} doped in a barium rubidium silicate glass. They postulated from low-temperature absorption and emission spectra of the rare-earth ions that the principal rare-earth site in these glasses is sixfold coordinated with near-octahedral symmetry. An example of one of these sites is represented in Figure 1.2.2.1, where we see a Yb^{3+} ion surrounded by three phosphate tetrahedra, each supplying two non-bridging oxygens to the coordination shell of the rare-earth. A reduction in symmetry from a near-octahedral site (O_h) to a trigonally distorted site (D_3) is achieved by a displacement of the tetrahedra radially away from the rare-earth ion. They felt that this was necessary in order to provide space for the ion. To account for the widths and asymmetries of the electronic transitions in both absorption and emission spectra, they introduced a systematic distortion (simultaneous rotation of each of the tetrahedra about the three C_2 axes of the octahedral site) of the above-mentioned site. They proceeded to construct absorption and emission spectra based on the crystal-field splittings of the electronic energy levels.

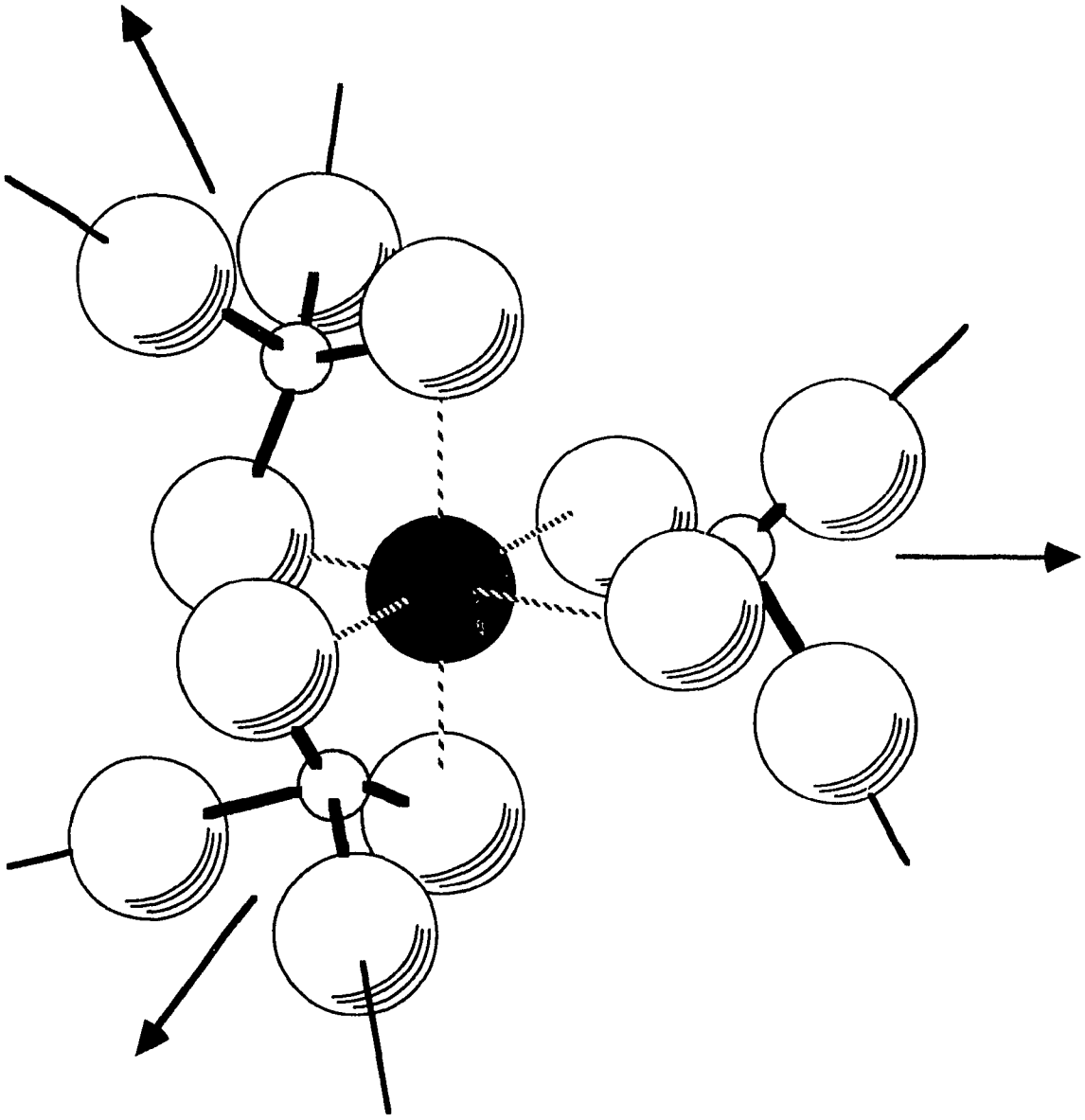

Figure 1.2.2.1 Representation of an octahedral rare-earth site in a phosphate glass. After Ref. 35.

The method employed is very much akin to that presented by Barber [29].

In order to confirm the near-octahedral symmetry of the sites, a fitting of the calculated energy of the rare-earth multiplets to the crystal-field calculations of Lea, Leask and Wolf [40] was performed. Basing themselves on the operator equivalent method [41], Lea, Leask and Wolf tabulated numerical solutions to the crystal-field Hamiltonian assuming cubic symmetry and no J-mixing. They presented their results as tables of eigenvectors and diagrams of eigenvalues expressed as a function of a mixing parameter (related to the ratio of the fourth and the sixth order crystal-field parameters). It was concluded that since the theoretical energy level scheme correlates with the ordering and positions of the energy levels observed for the Yb^{3+} and Er^{3+}ion in some oxide glasses, the site of rare-earth ions in oxide glasses must therefore be near-octahedral with a slight distortion to account for the observed splittings and widths of the electronic energy levels.

Following the same arguments as Rice and DeShazer [31] and Mann and DeShazer [32], Reisfeld and her collaborators [42-44] proposed that rare-earth ions in oxide glasses mimic the sites of the corresponding rare-earth sesquioxide. After examining some rare-earth ions (Eu^{3+}, Tm^{3+} and Er^{3+}) present in several oxide glasses, they postulated that the rare-earth ions are coordinated by four MO_4 undistorted tetrahedra (M = B,P or Si). Each of the coordinating tetrahedra contributes two non-bridging oxygens to the rare-earth ion, leading to an eightfold coordination. This eightfold coordination was justified by the fact that it is the most

common coordination of crystalline rare-earth oxides. The site symmetry is taken to be C_S, as for the Eu^{3+} ion in crystalline Eu_2O_3. The overall arrangement of the tetrahedra is such that the eight non-bridging oxygens are found at the corners of a distorted cube. The distortion results from the relative twisting of the tetrahedra. No crystal field calculations of the proposed model were presented. One intriguing point which they made, is that the number of sites in the glass could be obtained by comparing the half bandwidth of an inhomogeneously broadened transition arising from nondegenerate levels (e.g the $^5D_0 \rightarrow ^7F_0$ of Eu^{3+}) to that of the corresponding homogeneously broadened transition found in the rare-earth sesquioxide. As an example, they report [44] that for a Eu^{3+}-doped germanate glass, approximately 70 slightly different sites of C_S symmetry will be found.

Energy-selective spectroscopic techniques, such as laser induced fluorescence line narrowing (FLN) [45-49], have been used to overcome the difficulty presented by the inhomogeneous broadening of the fluorescence peaks. In this technique, energy subsets of the whole ensemble of doped ions are resonantly excited by a narrowband source such as a tunable dye laser. Fluorescence observed from the sample will specifically come from this subset. Using FLN measurements, Brecher and Riseberg attempted to create a geometric model of the Eu^{3+} ion in a highly modified silicate glass [50] and in a fluoroberyllate glass [51]. This was done by comparing the FLN spectra with energy levels derived from a simple point-charge model of ligands surrounding a Eu^{3+} ion in a distorted polyhedron. The structural model, shown in Figure 1.2.2.2, involves eight oxygen ligands arranged in a distorted Archimedian

antiprism, with C_{2v} symmetry, lying about the Eu^{3+} ion and a ninth oxygen introduced along the C_2 axis at a variable distance from the Eu^{3+}

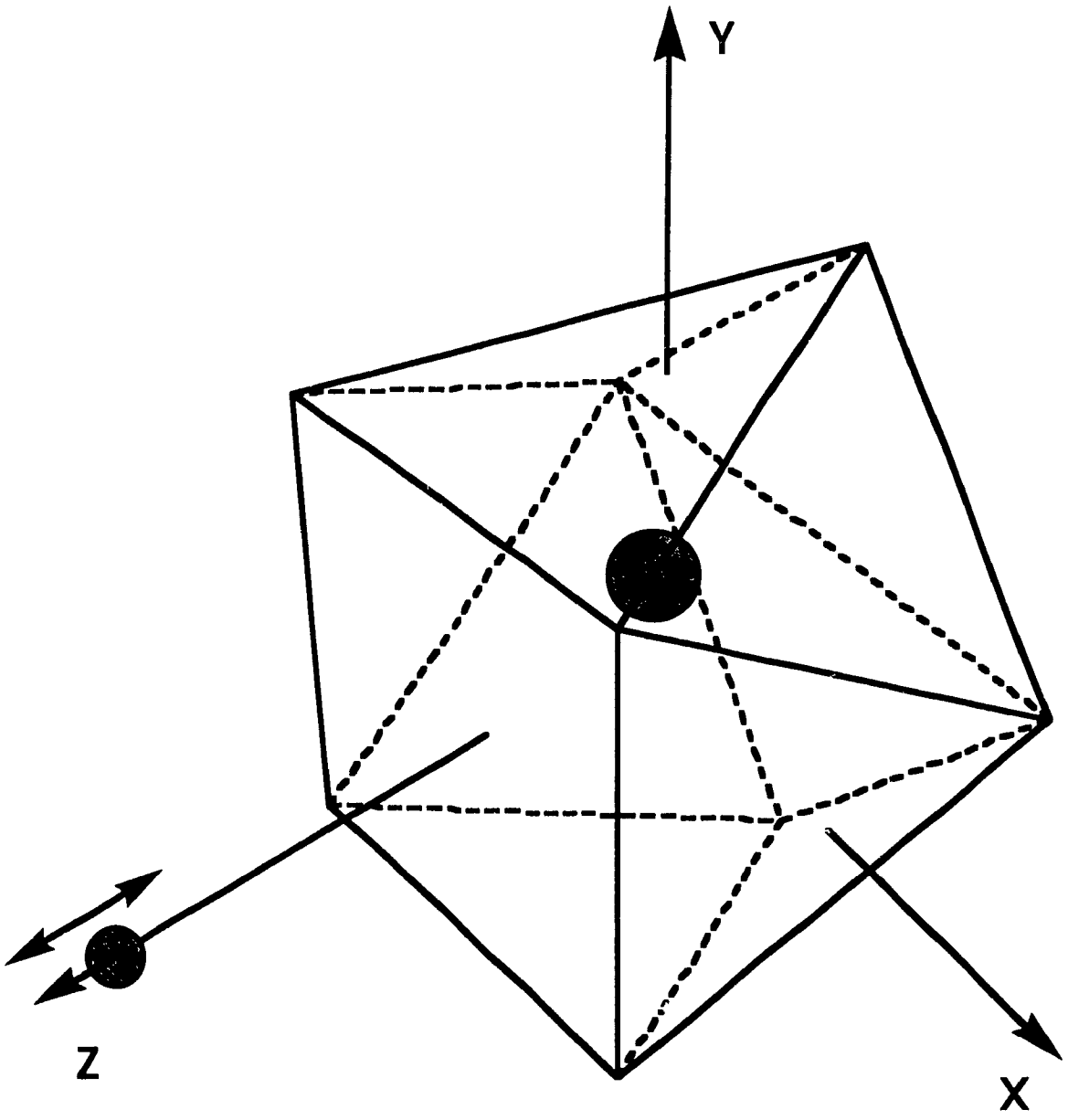

Figure 1.2.2.2 Structural model of the first coordination shell of the Eu^{3+} ion in a silicate glass. From Ref. 50.

ion. The introduction of the ninth ligand causes a rearrangement of the Archimedean antiprism. To take into account the continuous variation of the crystal-field as shown by the FLN experiment, a distortion parameter was introduced. This parameter spans the limits set by the model, i.e. at one end : eightfold coordination with equidistant ligands, at the other end : ninefold coordination with equidistant ligands. The crystal-field parameters using a point-charge model were calculated with respect to the distortion parameter. These were then compared to those derived from the measured splittings of the $^7F_1$ and $^7F_2$ manifolds obtained from the FLN experiment. A very good agreement was found for the behaviour of the sign and magnitudes of the crystal-field parameters.

1.3 MOLECULAR DYNAMICS

Since the advent of the modern computer, scientists have been interested in "experiments" on classical fluids and solids. The first reports of such calculations were presented in 1957 for the Monte-Carlo technique [52] and for the Molecular Dynamics method [53]. At that time, simple systems of hard spheres or of particles interacting with square-well potentials of attraction were commonly examined. In 1964 the first "realistic" simulation of liquid argon was presented by Rahman [54]. Since then, simulation techniques have been used to investigate such various materials as :

(i) atomic gases
(ii) amorphous silicon and germanium
(iii) molten ionic salts
(iv) oxide and fluoride glasses
(v) metallic glasses

Several review articles [55-57] and books [58,59] have appeared in the past years which summarise the advances achieved in the field of computer simulations using the Molecular Dynamics technique.

1.3.1 Molecular Dynamics simulations of glasses

The first application of a Molecular Dynamics simulation to glasses was made by Rahman, Fowler and Narten in 1972 [60]. The glass studied was BeF_2. The beryllium and fluorine atoms interacted through a Coulomb potential, an exponential repulsion term and some high-order spherically symmetric corrections. The structure of the simulated BeF_2 glass consisted of BeF_4 tetrahedra joined at the corners with fluctuating Be-F-Be angles. The overall structure closely resembled the continuous random network proposed for silica glass [1,16] and the "ball-and-stick" model of Bell and Dean [61].

Numerous simulations of oxide systems have since then appeared in the literature. The most important for the work presented in this thesis are those that deal with silica and silicate systems [62-78].

The first Molecular Dynamics study on silica was presented by Woodcock, Angell and Cheeseman [62]. With the use of a Born-Mayer-Huggins pair potential of the form given by Busing [79], they showed a structure which was four-coordinated. Thus, they demonstrated that the inclusion of covalency in the basically electrostatic potential was not

necessary for the simulation of a tetrahedral network structure. A comparison of the simulated radial distribution function with that deduced by Mozzi and Warren [18], showed a structure similar to the real glass but with some discrepancies (i.e. smaller O-O peak distance, larger Si-Si peak distance, O-Si-O bond angles being too broad and Si O-Si bond angle being too large). These discrepancies were mainly due to a lack in short range order and reflected the high concentration of bond defects. It is known [80] that partial covalency of the Si-O bonds introduces a bond directionality which is intimately related to the short range order in the silica (silicate) structure. Improvements in the potentials remedied this situation [65-67,74]. Feuston and Garofalini [75], with the introduction of a three-body interaction term similar to that developed by Stillinger and Weber [81], reported an increase in the short range order with a narrow O-Si-O angle distribution peaking at the accepted value (109°) and a much lower concentration of bond defects.

The simulation of silicate glasses went through much of the same process. The first reported simulation was from Soules [63]. A modified Born-Mayer-Huggins two-body potential was used in these early simulations. Again, a lack of short-range order prevented the simulation of a structure which agreed entirely with published structural data of real glasses. Improvements on the simulated structure were made by the use of various other potentials [69,77] and finally of a three body potential [76].

Specific results will be discussed in more detail in Chapter 5. Again, several review articles have dealt specifically with simulations of

structures of silicate melts and glasses [82-84]. The reader is referred to these for a more detailed discussion on the subject.

1.3.2 Application of the MD technique to the study of doped glasses

In 1980, Weber and Brawer published a series of articles on the structure simulation of rare-earth-doped fluoroberyllate glasses by the Monte-Carlo technique [85] and by Molecular Dynamics [86-90]. The glasses modelled were BeF_2 and alkali-modifed BeF_2 doped with the Eu^{3+} ion. Modifier ions were Na^+, Rb^+ and Ca^{2+}. The choice of fluoride systems was dictated by the use of an electrostatic pair potential of the Born-Mayer-Huggins type, since for fluorides the atomic interactions are essentially ionic in character.

Glasses of roughly 400 atoms were simulated in such a way that 100 different Eu^{3+} configurations, each at room temperature, were obtained. The most important results that were presented for the local environment of the rare-earth ions are summarised as follows : (i) the average coordination number for the Eu^{3+} ion is between six and seven in BeF_2 and between eight and nine in the modified glasses, (ii) each of the Eu^{3+} ions has a different local environment, (iii) F^- ions bonded to the Eu^{3+} are mostly non-bridging, (iv) no symmetry elements were found in any of the local environments.

A point-charge model of the crystal-field was used for the calculation of relative energy splittings. The point-charge crystal-field is given by [85]:

$$V = -A\sum_{L} \frac{q_L}{R_L^3} \sum_{q=-2}^{2} Y_q^2(\theta_L,\phi_L)U_q^{(2)} \qquad (1.3.2.1)$$

where ligand L of charge q_L is situated at a distance R_L from the rare earth ion, Y_q^2 is a second-order spherical harmonic , $U_q^{(2)}$ is the reduced tensor operator for the *f* electrons of Eu^{3+} and A is a positive parameter. Certain simplifications were introduced in the calculations : (i) only the $^7F_0$ and $^7F_1$ manifolds were treated, (ii) no J-mixing was assumed, (iii) only ligands within 2.75Å are considered in the calculation, (iv) only the second-order crystal-field parameters are included in the calculation, (v) only relative energy level splittings of the electronic manifolds can be inferred. Qualitative observations have been made which agree with experiment. Firstly, the range and distribution of crystal field energy levels agree with observations of both broadband and FLN spectra. Second, the high-energy asymmetry of the $^5D_0 \rightarrow ^7F_0$ emission profile together with the magnitude of the inhomogeneous broadening of the $^5D_0 \rightarrow ^7F_1$ band are both successfully predicted. Finally, the overall linewidths and average energy level splittings are predicted to be smaller in the modified glasses than in the BeF_2 glass.

In retrospect, Weber [91] felt that although a qualitative agreement was obtained by the simple electrostatic model, accurate calculations and simulations of both the local structure and electronic energy levels would be required to quantitatively predict and interpret optical spectra in glass.

Besides this series of papers from Weber and Brawer, only one other account of the simulation of doped glasses can be found in the literature [92]. In this paper, Hirao and Soga have made a cursory study of a series of four europium-doped sodium borate glasses. They have reported on a Molecular Dynamics simulation of approximately 120 atoms of the proper compositions, using a two-body potential of the Born-Mayer-Huggins type and a crystal-field analysis of the Eu^{3+} local environment using the method developed by Weber and Brawer. They did not make any attempts to modify or better the point-charge model. They report a large site-to-site variation in the europium local environment with an average coordination number found to be between 7.5 and 8.6 depending on the composition. They also found a large variation in the inhomogeneous linewidth with modifier content which they interpreted in terms of the variation of Eu-O and B-O bond lengths.

1.4 STATEMENT OF THE PROBLEM

The research presented in this thesis will hopefully permit us to shed some light on the following question : ***What is the local environment of rare-earth ions doped in an oxide glass matrix?***

We will attempt to solve this problem in five distinct steps :

(i) Simulate the doped glasses by using the method of Molecular Dynamics. Two glasses will be simulated, a silica glass, SiO_2, and a sodium disilicate glass, $Na_2O{\cdot}2SiO_2$, both glasses being doped with the trivalent europium ion (Eu^{3+}).

(ii) Calculate the crystal-field parameters, the electronic energy levels, the transition probabilities and branching ratios in order to generate electronic spectra of the rare-earth ions doped in the simulated oxide glasses.

(iii) Determine experimentally the absorption,emission and Fluorescence Line Narrowed spectra of the $Na_2O{\cdot}2SiO_2{:}Eu^{3+}$ glass. Derive from these spectra their crystal field parameters and other salient features.

(iv) Compare the simulated spectra and spectral features to those found for the laboratory glass.

(v) Develop a model for the local environment of the Eu^{3+} ions in SiO_2 and sodium silicate glasses.

Assuming the existence of a good agreement between the spectral features of the simulated and real glasses, we could then assume that the simulation yields a model which is an acceptable representation of the real structure. We would then be in possession of specific atomic structures of doped glasses which would permit us to "see" and quantify the multitude of local environments of doped ions. Therefore, we would be able to examine directly what type of environments are responsible for the spectral features found in absorption and emission spectra of lanthanide doped glasses.

CHAPTER 2

2. THE MOLECULAR DYNAMICS TECHNIQUE

2.1 FUNDAMENTALS OF THE MD TECHNIQUE

The molecular dynamics method used to perform the simulation of the atomic structure of the doped glasses is based on the numerical integration of the classical Newtonian equations of motion. In the case of an ensemble of N particles, we need to numerically solve 3N coupled (representing motion in three-dimensional space) second-order partial differential equations. These equations are solved in an iterative manner in order to simulate a time evolution of atomic positions. The N particules are simulated inside a box to which periodic boundary conditions are applied, thus making the box infinite and eliminating any surface or edge effects.

The force law used in the present calculation is derived from a pairwise (2-body) ionic spherical potential which includes the Pauling repulsive term. It is of the same form described by Mitra *et al.* [65,66,69] and is found to be

$$F(r_{ij}) = \frac{(q_i q_j)\, e^2}{4\pi\varepsilon_0} \frac{1}{r_{ij}^2} \left[1 + \text{sign}\,(q_i q_j) \cdot \left(\frac{\sigma_i + \sigma_j}{r_{ij}} \right)^n \right] \quad (2.1.1)$$

where q_i and q_j are the ionic charges, e is the electronic charge, ε_0 is the permittivity of vacuum, σ_i and σ_j are the ionic radii of the atoms i and j, n is a measure of the hardness of the repulsion and r_{ij} is the distance between atoms i and j. Charges, radii and n were reported by Mitra *et al.* [65,66,69] for silica and sodium silicate glasses. The *sign* function returns the value -1 or +1 depending on the sign of the operand $(q_i q_j)$. The associated potential is found to be

$$V(r_{ij}) = -\frac{(q_i q_j)\, e^2}{4\pi\varepsilon_0}\,\frac{1}{r_{ij}}\left| 1 + \text{sign}\,(q_i q_j)\cdot\frac{(\sigma_i+\sigma_j)^n}{n+1}\cdot\frac{1}{r_{ij}^{\,n}}\right| \qquad (2.1.2)$$

In Figure 2.1.1, we see a representation of this potential together with a decomposition of the potential into its attractive and repulsive parts. In Figure 2.1.2, we show a comparison between the potential used in this thesis and the Born-Mayer-Huggins potential [63]. The potentials showed in these two Figures are for the Si-O atomic pair and the various parameters and constants are taken from the literature [63,66]. The Born-Mayer-Huggins potential has been extensively used in the simulation of oxide and fluoride glasses. This potential is of the following form

$$V(r_{ij}) = A_{ij}\exp^{(-r_{ij}/\rho)} + \left|\frac{q_i q_j}{r_{ij}}\,\frac{e^2}{4\pi\varepsilon_0}\right| \qquad (2.1.3)$$

where the pre-exponential constant, A_{ij}, is defined as

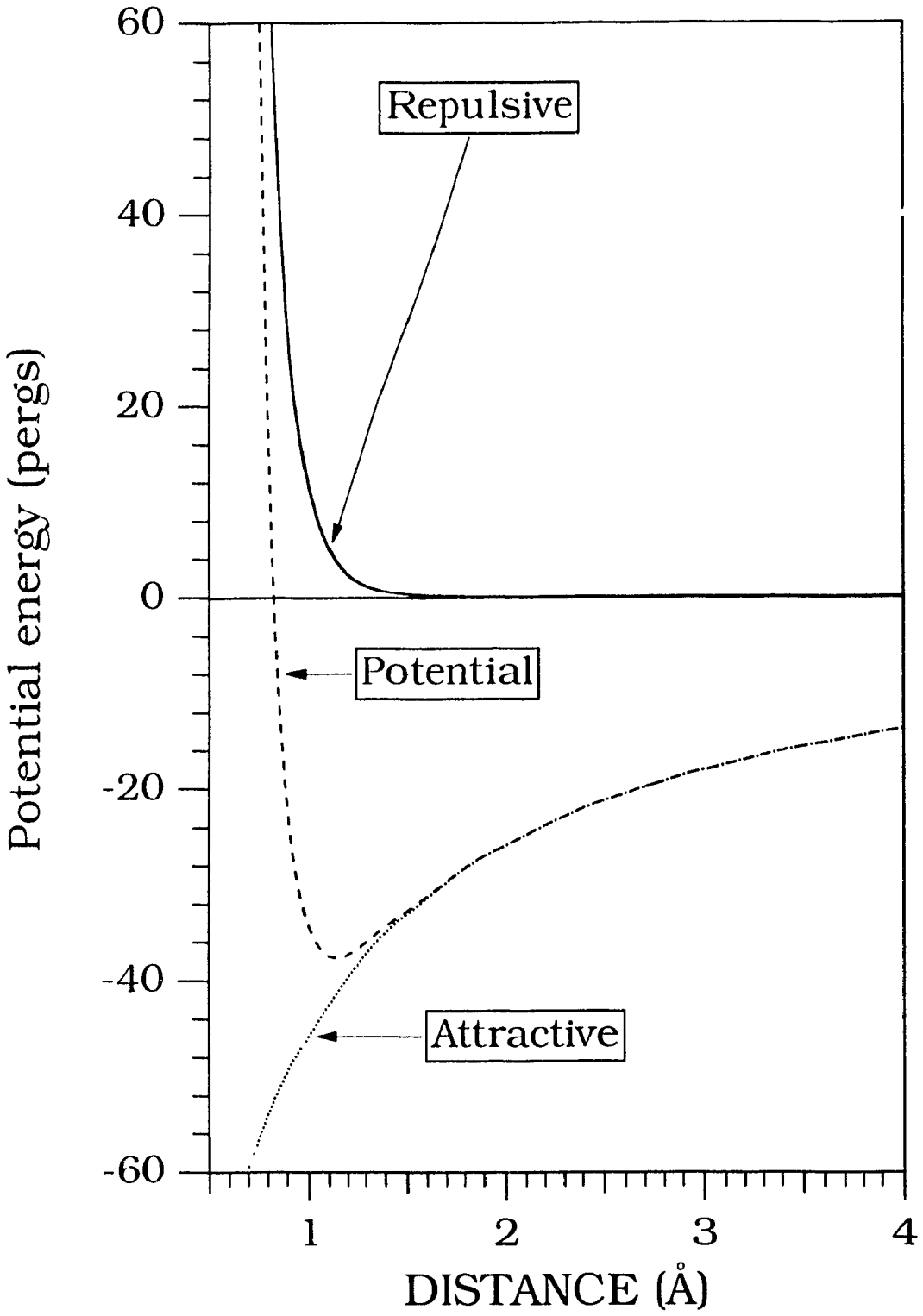

Figure 2.1.1 Representation of the Si-O interatomic potential used in this thesis.

$$A_{ij} = \left(1 + \frac{q_i}{n_i} + \frac{q_j}{n_j}\right) \cdot b \cdot \exp^{(r_i + r_j)/\rho} \qquad (2.1.4)$$

where q_i is the ionic charge, n_i is the number of valence electrons, and b and ρ are constants.

As we can see in Figure 2.1.2, the potential in the present simulations is much steeper and has a deeper potential well. This has been shown [65,66,69] to reduce the number of odd-coordinated defects in the glass.

The instantaneous force, for solving the Newtonian equations of motion, was determined for each ion over the set of atomic neighbours within 5.5Å. This length is large enough to include the neighbours of importance (approximately 100 ions) and small enough that an increase will not cause an effect on the structural characteristics of the glass. The force is decreased monotonically so that there is no discontinuity at a value of r_{max} = 5.5Å. This is done by multiplying the force by the following factor :

$$F'(r_{ij}) = F(r_{ij}) \cdot \left| 1 - \left(\frac{r_{ij}}{r_{max}}\right)^3 \right| \qquad (2.1.5)$$

Once the instantaneous force on each atom i is computed, at each time-step (Δt = 1.0fs), there is an update of the atomic coordinates and velocities. This is achieved using the Verlet algorithm [93] which introduces a simple finite-difference formula for the second order derivative

$$x_i(t+\Delta t) = 2x_i(t) - x_i(t-\Delta t) + \left(\frac{\Delta t^2}{m_i}\right)F_i(t) \qquad (2.1.6)$$

and then the first order derivative can be estimated from

$$v_i(t) \approx \frac{(x_i(t+\Delta t) - x_i(t-\Delta t))}{2\Delta t} \qquad (2.1.7)$$

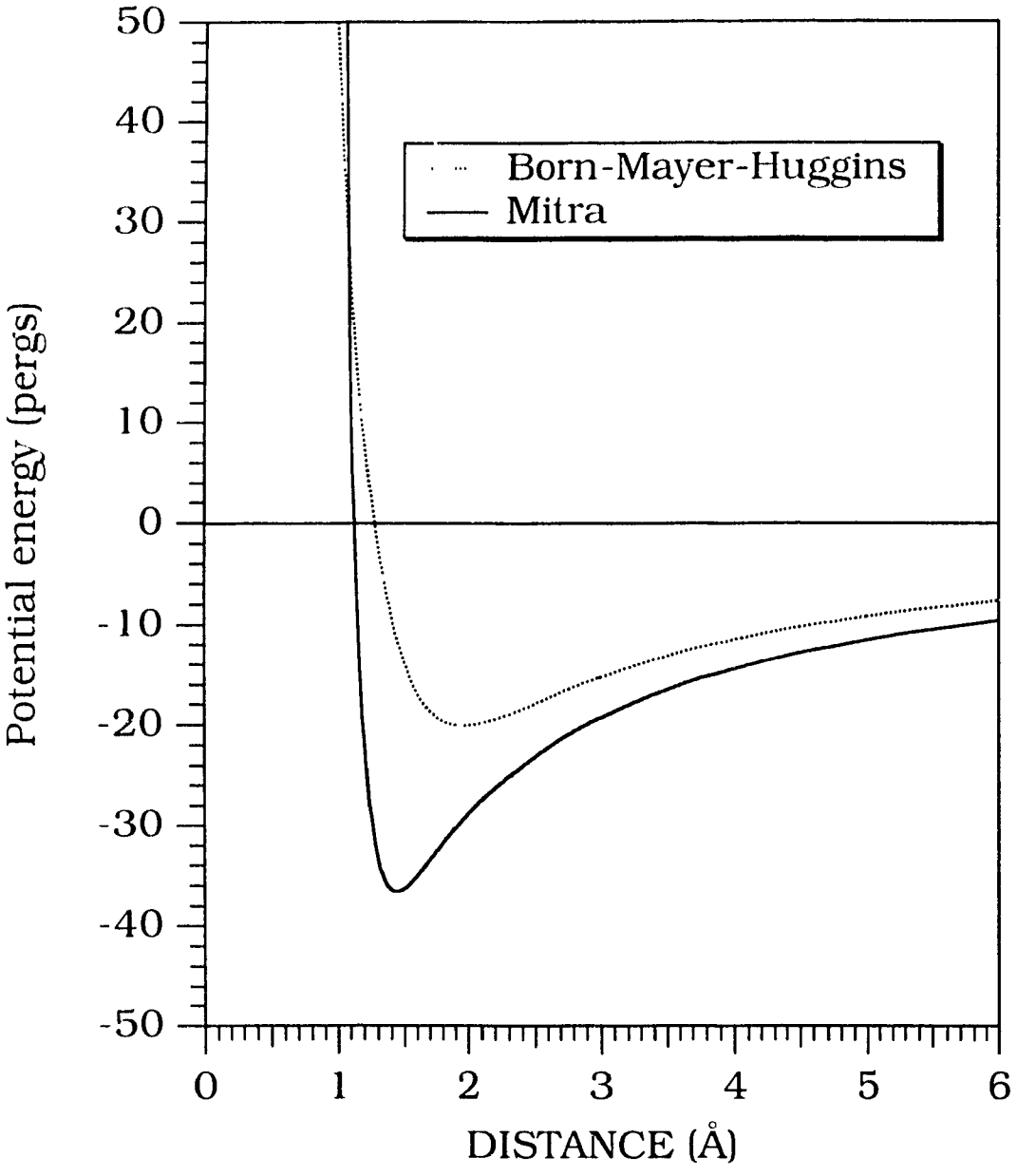

Figure 2.1.2 Comparison between the Born-Mayer-Huggins potential and the potential used in this thesis for the Si-O atomic pair.

2.2 DATA ANALYSIS OF MD RESULTS

The validity of the physical structure of the simulated glasses has been ascertained with several calculated properties. Some of these properties were used to monitor the simulation during the calculations to ensure that they were proceeding without faults.

2.2.1 Instantaneous energy and temperature

The instantaneous temperature of the atomic ensemble can be found from it's Maxwellian velocity distribution at a given moment. By calculating the average velocity of the atoms of a given atomic type L, $\mathbf{v}_L$, such as

$$\bar{\mathbf{v}}_L = \sum_{n_L} \left| (\mathbf{v}_x)_{n_L} + (\mathbf{v}_y)_{n_L} + (\mathbf{v}_z)_{n_L} \right| \qquad (2.2.1.1)$$

where n_L is the number of atoms of each atomic type and $\mathbf{v}_x$, $\mathbf{v}_y$ and $\mathbf{v}_z$ are the x,y, and z components of the velocity of each atom, we are able to calcuiate the total kinetic energy of the ensemble of atoms, E_k, expressed by

$$E_k = \frac{1}{2} \sum_L m_L \mathbf{v}_L^{\,2} \qquad (2.2.1.2)$$

where m_L is the mass of the atomic type L. The instantaneous temperature can then be approximated from the Maxwell-Boltzmann distribution as

$$T = \frac{2}{3}\frac{E_k}{kN} \qquad (2.2.1.3)$$

where k is the Boltzmann constant and N the number of atoms in the ensemble.

Once calculated, the instantaneous temperature was used to scale the atomic velocities such that the desired temperature be maintained.

The instantaneous energy of the ensemble of atoms can be found by the sum of the instantaneous total kinetic energy and the instantaneous total potential energy.

$$E = \left\langle \frac{1}{2}\sum_i m_i v_i^2 \right\rangle + \left\langle \sum_{i,j\neq i} V(r_{ij}) \right\rangle \qquad (2.2.1.4)$$

where $V(r_{ij})$ is the potential energy found by equation (2.1.2).

2.2.2 Pair and cumulative distribution functions

The pair and cumulative distribution functions (also identified by PDF and CDF, respectively) are derived from the time-averaged position

of the atoms throughout the simulated quench of the glass.

The formal expression for a pair distribution function of a certain pair ij of atom types is given by

$$g_{ij}(r) = \frac{1}{4\pi\rho_j r^2} \frac{d\langle N_{ij}(r)\rangle}{dr} \qquad (2.2.2.1)$$

where $N_{ij}(r)$ is the number of atoms of type j inside a sphere of radius (r) around a selected atom of type i, and ρ_j is the bulk density of the atoms of type j. Consequently, $d\langle N_{ij}(r)\rangle$ represents the number of atoms of type j found in thin spherical shells of radii of (r) and (r+dr) around an atom of type i. The calculation of $g_{ij}(r)$ is performed over hundreds of time steps to ensure an average value of g_{ij}.

From the pair distribution functions, one can also calculate the cumulative distribution functions. The CDFs can be defined as the average number of atoms of type j surrounding an atom of type i in a sphere of radius r. CDFs are obtained by integrating to distance r_0 the function $g_{ij}(r)$

$$C_{ij}(r) = 4\pi\rho_j \int_0^{r_0} g_{ij}(r) r^2 dr \qquad (2.2.2.2)$$

2.2.3 Distribution of bond angles

We can define an angle Θ between three adjacent atoms such that

$$\cos\Theta = \frac{\vec{r}_{ik} \cdot \vec{r}_{jk}}{|\vec{r}_{ik}||\vec{r}_{jk}|} \qquad (2.2.3.1)$$

where $\hat{r}_{ik}$ and $\hat{r}_{jk}$ are the directionality vectors between atom k and two of its neighbours i and j. This angle and the two vectors are represented in Figure 2.2.3.1.

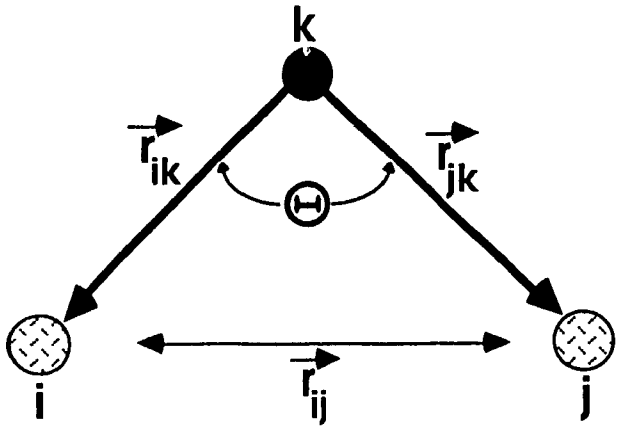

Figure 2.2.3.1 Schematic representation of the angle Θ and the directionality vectors $\hat{r}_{ik}$ and $\hat{r}_{jk}$ defined between 3 atoms i,j and k.

The distribution of bond angles can be defined as :

$$a_{ikj}(r_{ij},\Theta) = \frac{1}{n_0 2\pi^2 \sin\Theta} \frac{d\langle n(r_{ij},\Theta)\rangle}{dr_{ij}\, d\Theta} \qquad (2.2.3.2)$$

where $a_{ikj}(r_{ij},\Theta)$ represents the probability of finding a third ion k in a volume element $(2\pi^2 \sin\Theta\, dr_{ij}\, d\Theta)$, where Θ denotes the angle defined by equation 2.2.3.1 and r_{ij} is the distance between atom i and atom j.

2.2.4 Pictorial representation

Pictorial representations have been obtained from the final atomic positions for each glass by the use of the following method. Atoms present in a sphere of a given radius centered at a chosen position inside the simulated box have been extracted from the bulk of the configuration by calculating their distance from the target position. Periodic boundary conditions were taken into account in this calculation. The extracted atoms were then represented by a programme called PLUTO found in a molecular graphing package entitled PCDISPLAY (Serena Software, Bloomington, IN). This technique will allow the representation of a maximum of 125 atoms, corresponding to a sphere of approximately 7.5Å in radius. The display of given types of bonds or even specific bonds between atoms can be chosen at the convenience of the user. For example, this permits the display of only the silicate backbone or the oxygen first coordination shell surrounding a europium ion.

CHAPTER 3

3. THEORY

3.1 CRYSTAL-FIELD ANALYSIS

The crystal-field theory, first proposed by Bethe in 1929 [19], has been instrumental in the understanding of rare-earth ion spectroscopy. Many developments have later followed and one can find various texts on the subject [94,95]. With respect to the work which is described in this thesis, we will review the most important theoretical aspects which will lead to the simulation of electronic spectra from the glass configurations calculated with the Molecular Dynamics technique.

As introduced in section 1.2.1, the spectra of the Eu^{3+} ion doped in a crystalline or amorphous solid-state matrix shows (i) a series of bands which correspond to transitions between J states, and (ii) the removal of the degeneracy (or splitting) of these J multiplets due to the influence of the crystal-field.

3.1.1 The free ion

The Hamiltonian which describes the energies of the free-ion states is found to be a combination of various influences such that it may be described by a sum of individual Hamiltonians

$$\mathcal{H}_{fi} = \mathcal{H}_0 + \mathcal{H}_1 + \mathcal{H}_2 \qquad (3.1.1.1)$$

where each contribution is defined as follows. $\mathcal{H}_0$, the zeroth order Hamiltonian, represents the potential seen by an electron due to the presence of the nucleus and the complete inner electronic shells. This potential is treated as spherically symmetric and is usually termed "central-field approximation". In this approximation, the $4f$ electrons are completely independent of each other and contributions involving electrons in closed shells are neglected. The Hamiltonian, $\mathcal{H}_0$, is represented by the following equation [96]

$$\mathcal{H}_0 = \sum_{i=1}^{q} - \frac{\hbar^2}{2m} \nabla_i^2 + U(\mathbf{r}_i) \qquad (3.1.1.2)$$

where m is the mass of the electron, $\hbar\nabla_i$ is the momentum of the *ith* electron and $U(\mathbf{r}_i)$ represents an appropriate spherical average potential energy function of the *ith* electron in the field of the nucleus and all of the remaining electrons of the ion. The summation extends over all electrons in the $4f^6$ configuration of Eu^{3+}. In this approximation, the entire $4f^6$ configuration is degenerate.

The degeneracy is partially lifted by the interelectronic Coulomb interaction of the outer electrons, which is given by the second Hamiltonian in equation 3.1.1.1

$$\mathcal{H}_1 = \frac{e^2}{4\pi\varepsilon_0} \sum_{i>j=1}^{q} \frac{1}{|\mathbf{r}_i - \mathbf{r}_j|} \qquad (3.1.1.3)$$

where $|\vec{r}_i - \vec{r}_j|$ is the distance between the *ith* and *jth* electrons. This Coulomb interaction splits the energy level of the 4*f* electronic configuration into a number of LS terms.

The last Hamiltonian in equation 3.1.1.1 represents the spin-orbit coupling for multi-electron atoms, which is the case for the Eu^{3+} ion. This interaction leaves only J as a good quantum number since it mixes levels with different L and S. It is represented by [97,98]

$$\mathcal{H}_2 = \frac{\hbar^2}{2m^2c^2} \sum_{i=1}^{q} \frac{1}{r_i} \frac{dU(r_i)}{dr_i} \mathbf{s}_i \cdot \mathbf{l}_i \qquad (3.1.1.4)$$

where $\mathbf{s}_i$ and $\mathbf{l}_i$ are the spin and orbital angular-momentum operators.

This Hamiltonian may also be written as

$$\mathcal{H}_2 = \zeta \sum_{i=1}^{q} \mathbf{s}_i \cdot \mathbf{l}_i \qquad (3.1.1.5)$$

where the spin-orbit coupling parameter ζ can be expressed as a series of radial integrals [99]

$$\zeta = \frac{\hbar^2}{2m^2c^2} \int_0^\infty R_{4f}^2(r) \cdot \frac{1}{r} \frac{dU(r)}{dr} dr \qquad (3.1.1.6)$$

where $R_{4f}(r)$ is the radial wavefunction of the 4*f* electrons and U(r) is the above-mentionned central potential. The spin-orbit coupling parameter is

generally regarded as a parameter whose value is obtained from the energy separations of the J levels.

The three effects that we have just introduced have been shown in Figure 1.2.1.1, where $\mathcal{H}_0$ gives us the $4f^6$ electronic configuration, $\mathcal{H}_1$ gives us the terms which are due to interelectronic repulsion and $\mathcal{H}_2$ splits the terms into J levels due to the spin-orbit coupling.

One interesting feature about rare-earth spectra in solids, is that the positions of the electronic energy-level barycentres are relatively insensitive to the nature of the host material [100] and resemble quite closely the barycentres of the free-ion. Although the true energies of the free-ion are exceedingly difficult to obtain experimentally, solutions to the free-ion Hamiltonian of the Eu^{3+} ion have been given based on a theoretical analysis of the spectrum of Eu^{3+} in aqueous solutions. Table 3.1.1.1 presents values reported by Carnall, Fields and Rajnak [101] for the free-ion energy-level barycenters of Eu^{3+}, obtained through an analysis of $Eu(H_2O)_6$. These values will be used as initial free ion parameters for the crystal-field calculation which will be described theoretically in the following section of this Chapter. The free ion parameters which were used to generate this set of electronic energies are

(i) Coulomb : $E^0 = 0.000$, $E^1 = 5573.0$, $E^2 = 26.708$, $E^3 = 557.39$
(ii) Spin-Orbit : $\zeta_{4f} = 1326.0$
(iii) Configuration-interaction : $\alpha = 25.336$, $\beta = 580.25$, $\gamma = 1155.7$

TABLE 3.1.1.1

THE FREE-ION LEVELS FOR THE Eu^{3+} ION

Term	J-level	Level (cm^{-1})
^7F	0	0.0
	1	381.0
	2	1049.5
	3	1911.9
	4	2897.9
	5	3958.7
	6	5060.2
^5D	0	17316.6
	1	19057.3
	2	21529.8
	3	24420.7
^5L	6	25406.3

3.1.2 Crystal-field calculations for the Eu^{3+} ion

If we assume that the Eu^{3+} ion is located in free space, it will possess spherical symmetry which leads to totally degenerate J-levels. By placing the ion into a solid-state lattice, it will become influenced by the inhomogeneous electric fields arising from the presence of the atoms of the lattice (the so-called crystal-field). This will cause the lifting of the degeneracy of the J-levels. The Hamiltonian which is used to describe the rare-earth ion doped in a solid lattice, takes advantage of the fact that

optical transitions involve only changes in the electronic states of the f electrons. Since only the f electrons will be affected by the crystal field, we can safely assume that the crystal-field will act as a perturbation of the free-ion energy levels. The total Hamiltonian of a rare-earth ion doped in a solid can thus be described by

$$\mathcal{H} = \mathcal{H}_{fi} + \mathcal{H}_{CF} \qquad (3.1.2.1)$$

where $\mathcal{H}_{fi}$ is the free-ion Hamiltonian and $\mathcal{H}_{CF}$ is the crystal field Hamiltonian.

The simplest description of the crystal-field uses the point charge model, in which the atoms of the lattice surrounding the rare earth ion are described by point charges. This model neglects both the finite spatial extent of the ligand charge density and the wavefunction overlap of the optically active $4f$ electrons with the ligands [102].

The crystal-field Hamiltonian that describes the interaction of the Eu^{3+} ion with the host lattice can be written as

$$\mathcal{H}_{CF} = \sum_{nm}^{*} A_{nm} \sum_{i} r_i^n C_{nm}(r_i) \qquad (3.1.2.2)$$

where the first sum covers those values of n and m allowed by the symmetry of the site of the rare-earth. With n even, equation (3.1.2.2) is used to calculate the crystal-field splittings, for n odd it is used to calculate transition probabilities. The second sum is over $i = 6$ electrons

of the $4f^6$ configuration of the Eu^{3+} ion. The simplest description of the crystal-field uses the point-charge model, in which the atoms of the lattice surrounding the rare-earth ion are described by point charges. For point charges, eq_j located at $\vec{R}_j$, the crystal-field components, A_{nm} of equation (3.1.2.2) are given by

$$A_{nm} = -\frac{e^2}{4\pi\varepsilon_0}\sum_j q_j \frac{C_{nm}(\hat{R}_j)}{R_j^{n+1}} \qquad (3.1.2.3)$$

In equations (3.1.2.2) and (3.1.2.3) the irreducible spherical tensors, $C_{nm}(r)$, are related to the spherical harmonics $Y_{nm}(\theta,\phi)$ [103] by

$$C_{nm}(\hat{r}) = \sqrt{\left(\frac{4\pi}{2k+1}\right)} Y_{nm}(\theta,\phi) \qquad (3.1.2.4a)$$

and

$$C^*_{nm}(\hat{r}) = (-1)^m C_{n,-m}(\hat{r}) \qquad (3.1.2.4b)$$

where θ and ϕ are the polar coordinates of r.

Using the atomic positions given by the Molecular Dynamics simulation and by choosing appropriate ionic charges for each atom type, it is possible to calculate the crystal-field components, A_{nm}. Using the three-parameter theory of crystal-fields proposed by Leavitt et al. [104], the crystal-field parameters, B_{nm}, can be related to the crystal-field components by

$$B_{nm} = \rho_n A_{nm} \qquad (3.1.2.5)$$

The ρ_n are ion dependent, host independent quantities given by the expression

$$\rho_n = \langle r^n \rangle_{HF} \cdot (1-\sigma_n) \cdot \tau^n \qquad (3.1.2.6)$$

where the $\langle r^n \rangle_{HF}$ parameters are the Hartree-Fock radial expectation values for the Eu^{3+} ion [105] and the σ_n are linear shielding factors (Sternheimer shielding factors) [106]. The τ parameter is a scaling parameter introduced to account for the inadequacy of the bare Hartree Fock wavefunction and the expansion of the free-ion wavefunction [107]. The values of ρ_n reported for Eu^{3+} are found in Table 3.1.2.1.

TABLE 3.1.2.1

VALUES FOR THE PARAMETERS ρ_n FOR THE Eu^{3+} ION

	ρ_n ($\AA^n$)
ρ_2	0.1666
ρ_4	0.4836
ρ_6	1.2503

We must note that the B_{nm} parameters are complex numbers except for the B_{n0}. Obviously this also applies to the A_{nm} crystal field components discussed above.

The B_{nm} crystal-field parameters are directly related to the point symmetry of the local environment of the Eu^{3+} ion. In Table 3.1.2.2, we show the relation which exists between the point symmetry and the non

vanishing B_{nm} parameters for the 32 possible point groups. For reasons which are discussed in Section 5.2, we have chosen to analyse the simulated structure using a C_2 point-group symmetry. Because of this, 14 B_{nm} parameters need be considered.

From the B_{nm} crystal-field parameters, it is possible to calculate the crystal-field strength. A quantitative measure of the strength of the interaction between the rare-earth ion and the surrounding lattice is found using the following equation [108]

$$S_{CF} = \left\{ \frac{1}{3} \sum_{n} \frac{1}{(2n+1)} \left[B_{n0}^2 + 2 \sum_{m>0,n} \left(ReB_{nm}^2 + ImB_{nm}^2 \right) \right] \right\}^{1/2} \quad (3.1.2.7)$$

where the sum on n covers the values of 2,4,6.

The splitting of the J-manifolds, which is due to the crystal-field perturbation, is directly related to the crystal-field strength; in general, the larger the value of S_{CF}, the stronger the splitting will be.

3.1.3 Selection rules

As we have mentioned before, the electrons which participate in optical electronic transitions in a trivalent rare-earth ion are those situated on the $4f$ electronic shell. Generally speaking, two radiative processes are possible when these electrons interact with electro-

TABLE 3.1.2.2

INDEPENDENT NON' ANISHING B_{nm} FOR THE 32 POINT GROUPS

Point group	**Non-vanishing B_{nm} parameters**
C_1, C_i	all B_{nm} (B_{21} real)
C_2 C_s C_{2h}	B_{20}, ReB_{22}, B_{40}, B_{42}, B_{44}, B_{60}, B_{62}, B_{64}, B_{66}
D_2 C_{2v} D_{2h}	B_{20}, ReB_{22}, B_{40}, ReB_{42}, ReB_{44}, B_{60}, ReB_{62},ReB_{64}, ReB_{66}
C_4 S_4 C_{4h}	B_{20}, B_{40}, ReB_{44}, B_{60}, B_{64}
D_4,C_{4v} D_{2d},D_{4h}	B_{20}, B_{40}, ReB_{44}, B_{60}, ReB_{64}
C_3,S_6	B_{20}, B_{40}, ReB_{43}, B_{60}, B_{63}, B_{66}
D_3 C_{3v} D_{3d}	B_{20}, B_{40}, ReB_{43}, B_{60}, ReB_{63}, ReB_{66}
C_6,C_{3h} C_{6h},D_6 C_{6v},D_{3h} D_{6h}	B_{20}, B_{40}, B_{60}, ReB_{66}
T,T_d,T_h O,O_h	B_{40}, ReB_{44}, B_{60}, ReB_{64}

magnetic radiation, (i) absorption, when the ground-state electronic distribution is rearranged to a higher energy state, (ii) emission, when an ion being in a higher energy state emits a photon to return to a lower energy state. The presence of the electro-magnetic radiation field is necessary to produce a coupling between the different stationary states that can result in transitions from one state to another. The interaction of the electrons with the electro-magnetic field can be accomplished through the electric or magnetic dipole terms. Whether or not a radiative transition between states a and b is allowed and, if allowed, how strong the transition is will depend on the value of the following matrix element

$$\langle b | \dot{\mu} \cdot \hat{\varepsilon} | a \rangle \qquad (3.1.3.1)$$

where $\dot{\mu} \cdot \hat{\varepsilon}$ is the appropriate dipole operator.

For electric dipole interactions, the operator is

$$\dot{\mu}_e \cdot \hat{\varepsilon}_E \qquad (3.1.3.2a)$$

where

$$\dot{\mu}_e = \sum_i e \dot{r}_i \qquad (3.1.3.2b)$$

and $\hat{\varepsilon}_E$ is the unit electric polarisation vector parallel to the **E** field of the electro-magnetic radiation.

For magnetic dipole interactions, the appropriate operator is

$$\hat{\mu}_m \cdot \hat{\varepsilon}_B \qquad (3.1.3.3a)$$

where

$$\hat{\mu}_m = \sum_i \frac{-\hbar}{2mc} (\mathbf{l}_i + g_e \mathbf{s}_i) \qquad (3.1.3.3b)$$

where **l** and **s** are the orbital and spin angular momentum operators, and where $g_e = 2.00233$ is the g value of the electron and $\hat{\varepsilon}_B$ is the unit vector along the direction of the **B** field of the electro-magnetic radiation.

Selection rules are determined from group theory considerations. The components of the electric and magnetic field vectors transform according to definite representations of the point group of the local rare-earth environment. A particular transition is either allowed or forbidden according to whether the irreducible representation of the final state is or is not contained in the product of the initial state representation and the representation of the appropriate component of **E** or **B** [109].

A set of selection rules can then be written for both electric and magnetic dipole transitions [94].

For electric dipole transitions, the following rules apply for 4*f* electrons.

$$\begin{aligned} \Delta l &= \pm 1 \text{ (Laporte's rule)} \\ \Delta S &= 0 \\ |\Delta L| &\leq 2l, \text{ i.e. } |\Delta L| \leq 6 \\ |\Delta J| &\leq 2l, \text{ i.e. } |\Delta J| \leq 6 \end{aligned} \qquad (3.1.3.4a)$$

According to Laporte's selection rule, which states that the only allowed transitions are those accompanied by a change in parity ($\Delta l = \pm 1$), $f \leftrightarrow f$ transitions should be forbidden since $l = 3$ for both the initial and the final states. We should therefore not be able to observe any radiative transition in rare-earth doped solids. This is not the case since there is a relaxation of the Laporte rule due to admixing of the odd-parity f-states with even-parity states, usually $5d$- or $5g$-configuration states or charge transfer states.

Also, since S and L are no longer good quantum numbers, only the selection rule on J will remain valid. An additional rule is also set in this case

$$\text{when } J_a \text{ or } J_b = 0 \text{ then } |\Delta J| = 2,4,6 \qquad (3.1.3.4b)$$

This rule remains valid as long as the crystal-field is not strong enough to substantially admix J-states.

In the case of transitions induced by magnetic dipole interactions, the selection rules are as follows

$$\begin{aligned} \Delta l &= 0 \\ \Delta S &= 0 \\ \Delta L &= 0 \\ \Delta J &= 0, \pm 1 \end{aligned} \qquad (3.1.3.5a)$$

$\Delta M_J = 0$ (σ–polarisation)

$\Delta M_J = \pm 1$ (σ and π–polarisation)

For optical transitions of the Eu^{3+} ion (those below ~ 25000 cm^{-1} which are the basis of this study), we may summarise the above mentioned selection rules by the Table 3.1.3.1.

One last comment has to be made about the selection rules with regard to the symmetry of the local environment of the rare earth ion. For point-groups of very low symmetry, such as C_2, C_s or C_1, all $f \leftrightarrow f$ transitions are allowed. The only consideration will then be the relative magnitude of the contribution from each dipole process.

3.1.4 Intensity calculations

Following Condon and Shortley [110], the line strength, S_{ab}, of a radiative transition between individual components a and b of J states A and B is given by the square of the matrix element shown in equation (3.1.3.1)

$$S_{ab} = |\langle b | \mu \cdot \varepsilon | a \rangle|^2 \qquad (3.1.4.1)$$

Electric-dipole intensity calculations are done by using the "full" Judd-Ofelt theory[2] of induced electric dipole transitions [111,112]

[2] There is also an "approximate" Judd-Ofelt theory which neglects any J mixing arising from the presence of mixed states with different J values. The intensity parameters associated with this treatment are presented for manifold to manifold rather than line-to-line transitions [113].

TABLE 3.1.3.1

ALLOWEDNESS OF OPTICAL TRANSITIONS IN Eu^{3+}

Optical Transition	Allowedness
(a) EMISSION	
$^5D_0 \rightarrow {}^7F_0$	forbidden (very weak if observed)
$^5D_0 \rightarrow {}^7F_1$	magnetic dipole allowed
$^5D_0 \rightarrow {}^7F_2$	electric dipole allowed
$^5D_0 \rightarrow {}^7F_{3,5}$	forbidden (very weak if observed)
$^5D_0 \rightarrow {}^7F_{4,6}$	electric dipole allowed
(b) ABSORPTION	
$^5D_0 \leftarrow {}^7F_1$	magnetic dipole allowed
$^5D_0 \leftarrow {}^7F_0$	forbidden (very weak if observed)
$^5D_1 \leftarrow {}^7F_1$	forbidden (very weak if observed)
$^5D_1 \leftarrow {}^7F_0$	magnetic dipole allowed
$^5D_2 \leftarrow {}^7F_1$	magnetic dipole allowed
$^5D_2 \leftarrow {}^7F_0$	electric dipole allowed
$^5D_3 \leftarrow {}^7F_1$	electric dipole allowed
$^5D_3 \leftarrow {}^7F_0$	forbidden (very weak if observed)
$^5L_6 \leftarrow {}^7F_1$	forbidden (very weak if observed)
$^5L_6 \leftarrow {}^7F_0$	electric dipole allowed

The treatment of this theory involves the calculation of the squared matrix elements of the electric dipole operator between crystal field split eigenstates including J-mixing. The effective electric dipole moment operator is given by [114]

$$\mu = -2\sqrt{\frac{7}{3}} \sum_{k,t} (2t+1)\, N_k(t) \left(A^{(k)} U^{(t)}\right)^{(1)}_{q} \qquad (3.1.4.2)$$

where the sum is over the values k=1,3,5,7 and t=2,4,6. The quantity $\left(A^{(k)}U^{(t)}\right)^{(1)}_{q}$ represents the coupling of the irreducible tensors $A^{(k)}$ and $U^{(t)}$ by a Clebsch-Gordan coefficient. $A^{(k)}$ is a tensor whose components are the crystal-field components, A_{km}, presented in equation (3.1.2.3). The $U^{(t)}$ are unit irreducible tensor operators [115]. The $N_k(t)$ parameters contain integrals involving the radial parts of the $4f^n$ wave functions and the excited opposite-parity electronic-state wave functions, and the energies separting these states. Computation of the parameters found in equation (3.1.4.2) and the subsequent calculation of the induced electric-dipole line strength, S^{ED}_{ab}, can be accomplished through methods proposed by Krupke [113] and by Leavitt and Morrison [114].

As we have seen in the previous section, magnetic dipole transitions are parity allowed within the electronic configuration $4f^n$. Because of this, calculation of the line-strength is more straightforward than for the electric dipole case. Equation (3.1.4.1) is again used with the proper dipole moment operator

$$S_{ab}^{MD} = \left| \frac{-\hbar}{2mc} \langle b | \mathbf{L} + g_e \mathbf{S} | a \rangle \right|^2 \qquad (3.1.4.3)$$

where **L** and **S** are the total orbital and spin angular momentum operators

The matrix elements can be evaluated, for the three cases permitted by the $\Delta J=0,\pm1$ selection rule by relationships developed by Broer, Gorter and Hoogschagen [116]. These relationships have been derived for the case where no J-mixing is present. In the present case, J-mixing of eigenstates is included in the calculation of the magnetic-dipole line strengths and a modification of the above-mentioned relationships has been introduced.

In order to calculate the intensity of line-to-line transitions in the simulated emission and absorption spectra, we will use [117] (i) the oscillator strength between the individual components a and b, f_{ab}, for the absorption process

$$f_{ab} = \frac{8\pi^2 mc\sigma_{ab}}{3h} \left| \left(\frac{(n^2+2)^2}{9n} \right) S_{ab}^{ED} + n S_{ab}^{MD} \right| \qquad (3.1.4.4)$$

and, (ii) the transition probability between the individual components a and b, A_{ab}^{ems} for the emission process

$$A_{ab}^{ems} = \frac{32\pi^3 e^2 \sigma^3}{3\hbar 4\pi\varepsilon_0} \left| \left(\frac{n\left(n^2+2\right)^2}{9} \right) S_{ab}^{ED} + n^3 S_{ab}^{MD} \right| \qquad (3.1.4.5)$$

where n is the refractive index at the wavelength of the emitted or absorbed light, σ is the energy difference between initial and final states, $\hbar$ is Planck's constant divided by 2π, e is the electronic charge, ε_0 is the permittivity of vacuum, S_{ab}^{ED} is the electric-dipole strength and S_{ab}^{MD} is the magnetic-dipole strength.

One basis of comparison between the experimentally obtained absorption spectrum and the simulated spectrum will be oscillator strengths. From the absorption spectrum of the experimental glass, we can define the oscillator strength of a manifold to manifold transition between J-states A and B [110,118]

$$f_{AB}^{exp} = \frac{9n}{\left(n^2+2\right)^2} \frac{4mc\,\varepsilon_0}{Ne^2} \int_{\nu} u(\nu)d\nu \qquad (3.1.4.6)$$

where m is the mass of the electron, N is the dopant concentration expressed in #ions/cm^3, and $\int_{\nu} u(\nu)d\nu$ is the integrated absorption coefficient of the transition between the J-states A and B. In order to

compare the experimental values calculated with equation (3.1.4.6) to simulated values calculated with equation (3.1.4.4), we will need to sum individual line-to-line simulated oscillator strengths (eq. 3.1.4.4) over all a and b components of J-states A and B.

Besides electric dipole and magnetic dipole, $f \leftrightarrow f$ transitions can also arise from other mechanisms, such as phonon coupling and higher even electric multipole process (quadrupole, hexadecapole and 64-pole). A review of the various mechanisms contributing to lanthanide-ion transition intensities, has been presented by Peacock [119].

CHAPTER 4

4. EXPERIMENTAL

4.1 PREPARATION OF THE LABORATORY GLASSES

Two europium doped sodium disilicate glass ($Na_2O{\bullet}2SiO_2{:}Eu^{3+}$) samples were prepared and used in different spectroscopic experiments. The first, less concentrated one, was prepared for us by Dr. Peter Taylor at the Whiteshell Laboratories of AECL Research, Pinawa, Manitoba. This sample, denoted "A", has a Eu^{3+} concentration of 0.94%wt ($8.79x10^{19}$ ions/cm^3). The second, more concentrated sample, was prepared by Prof. Marco Bettinelli, of the Dipartimento di Chimica Inorganica, Metallorganica ed Analitica, Universita di Padova, Padova, Italy. This second sample, denoted "B", has a Eu^{3+} concentration of 5.00%wt ($4.52x10^{20}$ ions/cm^3). Sample "A" was prepared by (i) grinding analytical reagent grade oxides and carbonates (SiO_2, Na_2CO_3, Eu_2O_3) (ii) melting the powders at 1200°C for one hour in a platinum rhodium crucible in an electrically heated furnace, (iii) fritting in de ionized water then drying, crushing and remelting at 1200°C for one hour, (iv) annealing for a period of 1 hour at 500°C and then slowly air cooling. Sample "B" was prepared by (i) grinding then melting the powders at 1400°C for 24 hours (ii) air-quenching, (iii) annealing for several hours at 600°C.

The samples were prepared for spectroscopic investigations by polishing them with various grades of sandpaper. The surfaces were finished with a diamond lapping compound having a particle size distribution of 2-3 μm. Before use, the sample was dehydrated in a drying oven at a temperature of 120°C for a few hours and kept in a dessicator.

TABLE 4.1.1

EUROPIUM-DOPED SODIUM DISILICATE GLASS

$Na_2O{\cdot}2SiO_2{:}Eu^{3+}$

	Sample "A"		Sample "B"	
	Mass (g)	**% molar**	**Mass (g)**	**% molar**
SiO_2	5.25093	65.99	5.0000	66.05
Na_2CO_3	4.75084	33.85‡	4.4100	33.02‡
Eu_2O_3	0.0776	0.17	0.3989	0.93

‡ The molar percentage reported is for the oxide, Na_2O, which results from the high temperature decomposition of the carbonate, Na_2CO_3.

4.2 PREPARATION OF THE SIMULATED GLASSES

The FORTRAN programme used to carry out the Molecular Dynamics calculations was obtained from Dr. Thomas F. Soules of the General Electric Company, Cleveland, Ohio. This programme was then extensively modified by us for the specific problem of generating and analysing the doped glasses. These modifications are : (i) the inclusion of

a different potential (Mitra's rather than the modified Born Mayer Huggins), (ii) the addition of a routine which generates and saves configurations at discrete time intervals, (iii) the removal of unnecessary output parameters which apply to transport and thermodynamic properties and (iv) the addition of output parameters which pertain to the analysis of the local environment of the doped glasses.

The simulations were performed on four different computers : (i) an IRIS 4D/25G workstation manufactured by Silicon Graphics Inc. found in the Chemistry Department of Concordia University (ii) a time shared DECsystem 5500 workstation from Digital which is found in the Computing Center of Concordia University , (iii) a time shared VAX 6510 mainframe computer from Digital which is also found in the Computing Center of Concordia University , and (iv) a Sparkstation 1+ workstation from Sun which is found at the Institut de Physico Chimie des Matériaux Luminescents, Université Claude-Bernard Lyon I, Lyon, France. Ensembles of 600 atoms containing the four atom types studied in this thesis can be handled at a rate of approximately 4000 time steps/hour on the IRIS, 6500 time steps/hour (in real time) on the DECsystem and 1500 time steps/hour on the Sparkstation. Real time rates cannot be reported for the VAX mainframe since they vary considerably depending on the number of interactive users and the number of background processes.

All of the simulations were performed using Mitra's potential [65,66,69]. Certain parameters, as defined in equation 2.1.1, were common to all of the simulations. Charges, radii and n were determined

empirically such that they reproduce the observed short-range structure of the corresponding laboratory glasses [15,18]. For the potential used in this study, the energy scale is found to be proportional to the square of the charges. As such, a scaling factor of 1.76 was initially introduced by Mitra *et al.*, to arrive at a simulated glass transition temperature lying within the experimental range of 1200-1800K. Since no reported values were found in the literature concerning Eu-O and Eu-Si bond lengths in silicate glasses, the parameters for the Eu^{3+} ion were determined by considering the crystalline values of europium disilicate $Eu_2Si_2O_7$ [120]. These parameters can be found in Table 4.2.1 .

TABLE 4.2.1

POTENTIAL PARAMETERS COMMON TO ALL SIMULATIONS

hardness parameter n		10
ionic radius σ	oxygen	1.2000 Å
	silicon	0.2374 Å
	sodium	0.8230 Å
	europium	1.1500 Å
ionic charge q	oxygen	-1.136
	silicon	2.272
	sodium	0.5680
	europium	1.7040
time-step Δt		1.00×10^{-15} s

A cubic cell was used throughout these calculations. Periodic boundary conditions were imposed to eliminate any possibility of surface effects. The size of the cell was adjusted to give the correct density at room temperature for the given glass. No variation in the cell volume with temperature was attempted in these calculations. Room temperature densities, ρ, of the sodium silicate glasses were calculated using the equations developed by Jen and Kalinowski [121] :

$$\rho = (23.1 + 15.4R)/(7.9 + 7.0R) \qquad (4.2.1.1)$$

where R, the bridging to non-bridging oxygen ratio, is given by :

$$R = (2-3x)/2x \qquad (4.2.1.2)$$

where x is the molar percentage of Na_2O as found in the general formula $xNa_2O \cdot (1-x)SiO_2$. The density of silica was taken to be 2.203 g/cm^3 [122].

The initial atomic configuration for all of the simulated glasses was taken from an ensemble of atoms that underwent the following treatment. A file containing the atomic positions of 216 molecules of SiO_2 with the β-cristobalite crystalline structure was used to simulate the melting of a single crystal up to a temperature of 15000K. The temperature of this ensemble of atoms was scaled, during a total of 100000 time steps (100ps), from 0K to 15000K. This ensured a homogeneous and random distribution of atoms throughout the melt while still retaining localised electroneutrality. The different atomic

compositions of the various simulated glasses were obtained by transforming the proper number of arbitrarily chosen silicon ions into sodium and/or europium ions and then by removing any extraneous oxygen and silicon ions.

The compositions of the two simulated glasses are found in Table 4.2.2 . This Table contains, for each of the glasses, (i) the molar fraction of Na_2O (ii) the number of atoms of each atomic type that was used in the simulation, (iii) the simulated density of each glass in g/cm^3, (iv) the oxygen molar volume in cm^3/mole O and (v) the length of the box side in Angstroms.

Once these parameters were determined, the doped glasses were simulated from the initial atomic configuration using the following quench procedure. The compositionally modified configurations were thermalised at 15000K for 30000 time steps (30ps). The temperature of the melts was lowered to 7500K and then to 5000K, each in 30000 time steps. The melt was then allowed to thermalize at 5000K for a duration of 18750 (75x250) time steps. After each 250th time step, a configuration was stored for further process. This ensures us a total of 75 configurations for a total of 150 europium ions. Each of these 75 configurations then undergoes a quench from their initial temperature of 5000K to room temperature in four steps : (i) 2500K, (ii) 1250K, (iii) 600K and (iv) 300K. Each of these four temperature steps represents 10000 time steps. Finally, each configuration is thermalised at 300K for an additional 10000 time steps. The number of time steps taken to simulate each of the 75 configurations of a doped glass is between 140250 and

158750, for a total of approximately 140 to 159ps. The quench rate is calculated to be approximately $9x10^{13}$ to $1x10^{14}$ $Ksec^{-1}$. The simulation of one of these doped glasses takes approximately 24 days of calculation with the four computers above-mentioned.

TABLE 4.2.2

SIMULATION PARAMETERS FOR GLASSES OF THE

$xNa_2O•(1-x)SiO_2 : 0.05Eu_2O_3$ SERIES

	RUN101	RUN102
Molar fract. of Na_2O (x)	0.000	0.33
Number of O ions	403	337
Number of Si ions	200	134
Number of Na ions	--------	132
Number of Eu ions	2	2
Density (g/cm^3)	2.203	2.507
Oxygen molar volume	13.637	14.499
Length of box side (Å)	20.907	20.085

4.3 SPECTROSCOPY OF THE LABORATORY GLASSES

A room temperature absorption spectrum of sample "B" was taken between 250 and 900nm with the use of a Perkin-Elmer Lambda 15 spectrophotometer. The resolution used was of 1nm.

Broadband emission spectra were taken by exciting sample "A" with the 514.5nm line of a Coherent CR-18, 25W argon ion laser. A Spectra Physics 375 dye laser operating with Rhodamine 6G[3] (Exciton) pumped by a Coherent CR-18 argon ion laser was used for excitation of the Fluorescence Line Narrowing (FLN) spectra. The dye laser has a typical linewidth of $2cm^{-1}$ full width at half height (FWHH) over the tuning range of 573 to 581 nm used in this thesis.

Emission spectra were recorded by using a Jarrell-Ash 1-m Czerny-Turner double monochromator. The gratings (2400 grooves/inch) are mounted on a cosecant bar driven by a stepper motor with a step size of $0.01cm^{-1}$/step.

The emission signal was monitored by an RCA-C31034-02 photomultiplier, which has a flat spectral response from 200 to 850nm. The photomultiplier was thermoelectrically cooled so that background dark rate was below 2 counts/s. The photomultiplier signal is processed by a preamplifier model SR 440 Stanford Research Systems. The preamp contains four wide bandwidth, dc coupled amplifiers designed to be used independently or cascaded to provide gains of 5, 25, 125, and 625 thus amplifying the output from the photomultiplier tube to the photon counter. The Two Channel Gated Photon Counter Model SR 400 (Stanford Research Systems) is a data acquisition system that interfaces

[3] The concentration of the dye was $10^{-3} mol/dm^3$ in ethylene glycol (Aldrich, spectrophotometric, 99+%).

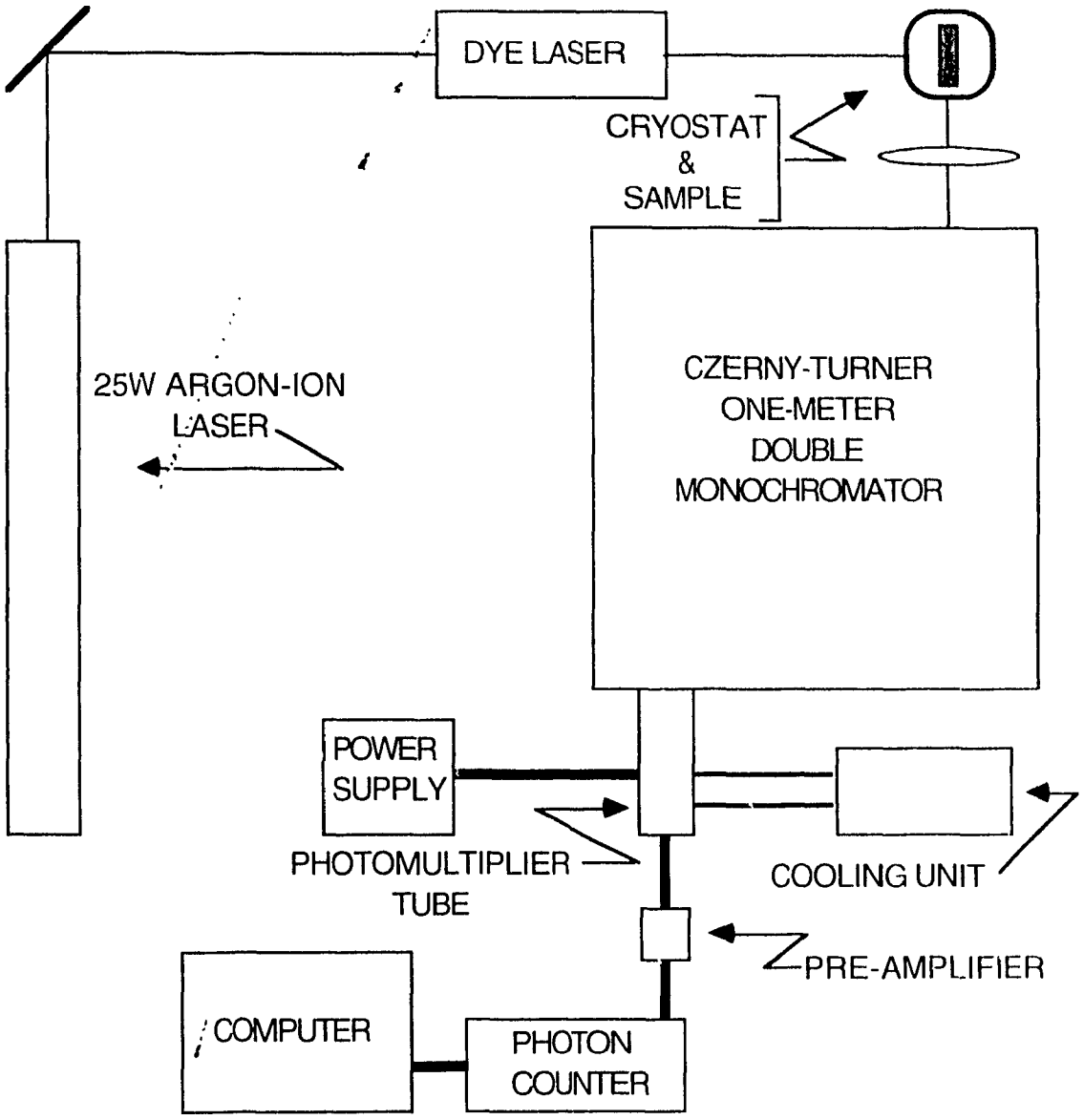

Figure 4.3.1 Schematic arrangement of apparatus for the measurement of emission spectra and for the fluorescence line narrowing experiment.

between the computer and the spectroscopic hardware shown in Figure 4.3.1. The signal is recorded under computer control using the Stanford Research Systems' SR465 software data acquisition/analysis system. The low temperature spectra were acquired at 77K using a Janis Research ST-VP 4 continuous flow cryostat.

4.4 SPECTRAL SIMULATION

The calculation of the crystal-field parameters of the simulated glasses and the subsequent generation of simulated absorption and emission spectra was performed by using a series of FORTRAN programmes, some developed by us and others developed by Drs. Nick Karayianis, Richard P. Leavitt, Donald E. Wortman and Clyde A. Morrison of the Harry Diamond Laboratories, Adelphi MD [123], and modified by us to suit our needs.

The following procedure was used to generate electronic spectra of the Eu^{3+} ions doped in the simulated silicate glasses. The bulk of the procedure is the same for the generation of both emission and absorption spectra. Differences will arise when discussing line intensities.

A principal axis transformation of each of the 150 Eu^{3+} configurations was performed to correlate the energy levels with the structure and charge distribution at each rare-earth site. Starting with a Eu^{3+} ion at the centre of a Cartesian coordinate system representing the glass configuration, we can define the components of the quadrupole

moment tensor at the rare-earth site as a (3x3) matrix such that it's quadratic form is

$$M_{ij} = \sum_{L} \left| \frac{q_L}{R_L^5} \cdot r_i r_j \right| \qquad (4.4.1)$$

where a summation over the entire ensemble of L ligands is carried out. The parameters of the quadratic form are: q_L, the electronic charge of ligand L, R_L, the distance separating ligand L from the Eu^{3+} ion, and r_i,r_j, the x,y or z components of the position of ligand L. The matrix components can be represented as

$$M_{ij} = \begin{vmatrix} m_{xx} & m_{xy} & m_{xz} \\ m_{yx} & m_{yy} & m_{yz} \\ m_{zx} & m_{zy} & m_{zz} \end{vmatrix} \qquad (4.4.2)$$

This symmetric matrix M_{ij} is then diagonalised by the Jacobi method [124] which yields eigenvalues $\lambda_1,\lambda_2,\lambda_3$ and eigenvectors $\mathbf{A}_1$, $\mathbf{A}_2$, $\mathbf{A}_3$. The eigenvectors represent the principal axes of an ellipsoid. The magnitude of the major and minor axes are given by the eigenvalues. Sorting the eigenvalues such that $\lambda_1 > \lambda_2 > \lambda_3$ and rearranging the eigenvectors correspondingly permits us to carry out an alignment of each quadrupole moment ellipsoid. Using a similarity transformation [125], we can apply the rotation obtained through the alignment of the ellipsoids to each of the individual glass configurations.

Once each of the glass configurations is aligned, the calculation of the crystal-field parameters is accomplished by a programme which takes as input (i) the positions of all atoms with respect to the central Eu^{3+} ion and (ii) the charges given to each atom type. It then proceeds to determine the spherical tensors, C_{nm}, using a recursive method which calculates the associated Legendre polynomials. The C_{nm} parameters are used to calculate the crystal-field components, A_{nm}, using equation (3.1.2.3). A subroutine called ROTATE [123] takes the set of crystal field parameters, A_{nm}, and gives a new set of A'_{nm} rotated by the standard rotation angles [126] α,β,γ. The even-n A_{nm} are transformed into crystal field parameters, B_{nm}, using the ρ_n parameters found in Table 3.1.2.1. Two files are output from this programme. The first contains sets of even-n B_{nm} crystal-field parameters which are used to calculate the energy level splittings. The other output file contains sets of odd-n A_{nm} crystal-field components which are used for the intensity calculations.

A modification of the programme REHOME [123,127] called NGLASS was used to calculate the energy levels of all the Stark levels in each J-manifold for each of the 150 Eu^{3+} ions. Transition probabilities (electric dipole and magnetic dipole) from the $^5D_0$ excited state, lifetimes and branching ratios for all excited states are calculated.

Finally, to generate a graphic representation of the simulated emission and absorption spectra, the calculated energies are collated and sorted. A Gaussian band shape is then assigned to each of the energies. The spectral envelope, $\Xi(E)$, is given by

$$\Xi(E) = \frac{1}{\sqrt{2\pi}\cdot w\cdot N_0}\sum_{k=1}^{N_0}\sum_{a,b} I_{k,ab}^{type}\exp\left(-\frac{(E-E_{k,ab})^2}{2w^2}\right) \qquad (4.4.3)$$

where the first sum is over the N_0 =150 Eu^{3+} configurations and the second sum is over either the 49 possible line-to-line $^5D_0 \rightarrow {}^7F_J$ (J=0 to 6) transitions for the emission spectrum or the (4x29) possible line-to-line $^5L_6$, $^5D_3$, $^5D_2$, $^5D_1$, $^5D_0 \leftarrow {}^7F_{0,1}$ transitions for the absorption spectrum. The $E_{k,ab}$ are the line-to-line transition energies for each of the Eu^{3+} ions, such that $E_{k,ab} = |E_a - E_b|_k$. The width, w, of each individual Gaussian has been chosen to be ≈ 75 cm^{-1} for the emission spectrum and ~100 cm^{-1} for the absorption spectrum. These widths were chosen such that the 150 Eu^{3+} ions of the simulated glass effectively represent the macroscopic ensemble of doped ions found in the experimental glass. The difference in these widths stems from the fact that two different types of experimental spectra (absorption and emission) were taken at different resolutions. The intensity parameters $I_{k,ab}^{type}$ are defined as the following

$$I_{k,ab}^{ems} = F_{ab}^{ems}\left[(\beta_{k,ab})\cdot\left(A_{k,ab}^{ems}\right)\right] \qquad (4.4.4a)$$

with $A_{k,ab}^{ems}$ given in equation (3.1.4.5)

and

$$I_{k,ab}^{abs} = F_{ab}^{abs}\cdot f_{k,ab} \qquad (4.4.4b)$$

where the $f_{k,ab}$ are given by equation (3.1.4.4). The F_{ab}^{type} are scaling factors. The β_{ab} are radiative branching ratios for line-to-line

fluorescence transitions. These branching ratios are defined as the ratio of a specific radiative transition from the a emitting state to a specific b state to the sum of all the radiative transitions initiated from the a state of the k*th* Eu^{3+} configuration

$$\beta_{k,\,ab} = \frac{A^{ems}_{k,\,ab}}{\sum_{a,b} A^{ems}_{k,\,ab}} \qquad (4.4.5)$$

where a represents a given emitting state and b represents lower energy states. The $A^{ems}_{k,\,ab}$ are the line-to-line radiative transition probabilities for the k*th* configuration as defined in equation (3.1.4.5), and the sum is over all the possible lower states. The sum of all β_{ab} is necessarily equal to 1.

CHAPTER 5

5. RESULTS AND DISCUSSION

5.1 MD SIMULATION OF THE GLASS STRUCTURE

The first concern which arose when this thesis was initiated, was to be able to replicate reported structural features for the silicate framework of the modeled glasses. Feuston and Garofalini have shown [75] that most two-body potentials fail to accurately reproduce the high degree of short-range order in laboratory glasses. The main differences between two-body and three-body type simulations are the presence of a large number of bond defects (≈ 10% odd-coordinated Si and O atoms) and discrepancies in the O-Si-O and Si-O-Si angle distributions for a two-body type simulation. However, the two-body potential used in this thesis has been shown to simulate the base glasses effectively. This potential, described by Mitra [66,69], possesses a much steeper repulsive part and a deeper well than that of the commonly used modified Born-Mayer-Huggins [6,63], resulting in an important reduction of the aforementioned discrepancies. Figure 5.1.1 shows the pair distribution function (PDF) of the Si-O bond for the simulated $SiO_2:Eu^{3+}$ and $Na_2O \cdot 2SiO_2:Eu^{3+}$ glasses. We observe the characteristically sharp peak found at 1.61Å associated with the first oxygen coordination shell of the silicate tetrahedra. The average coordination number for the Si-O pair is found to be 4.00 as shown in the inset of Figure 5.1.1. A calculation of odd-coordinated silicon atoms (3- or 5- coordinated) and odd-coordinated oxygen atoms (3- coordinated) showed that there was less than 1% of

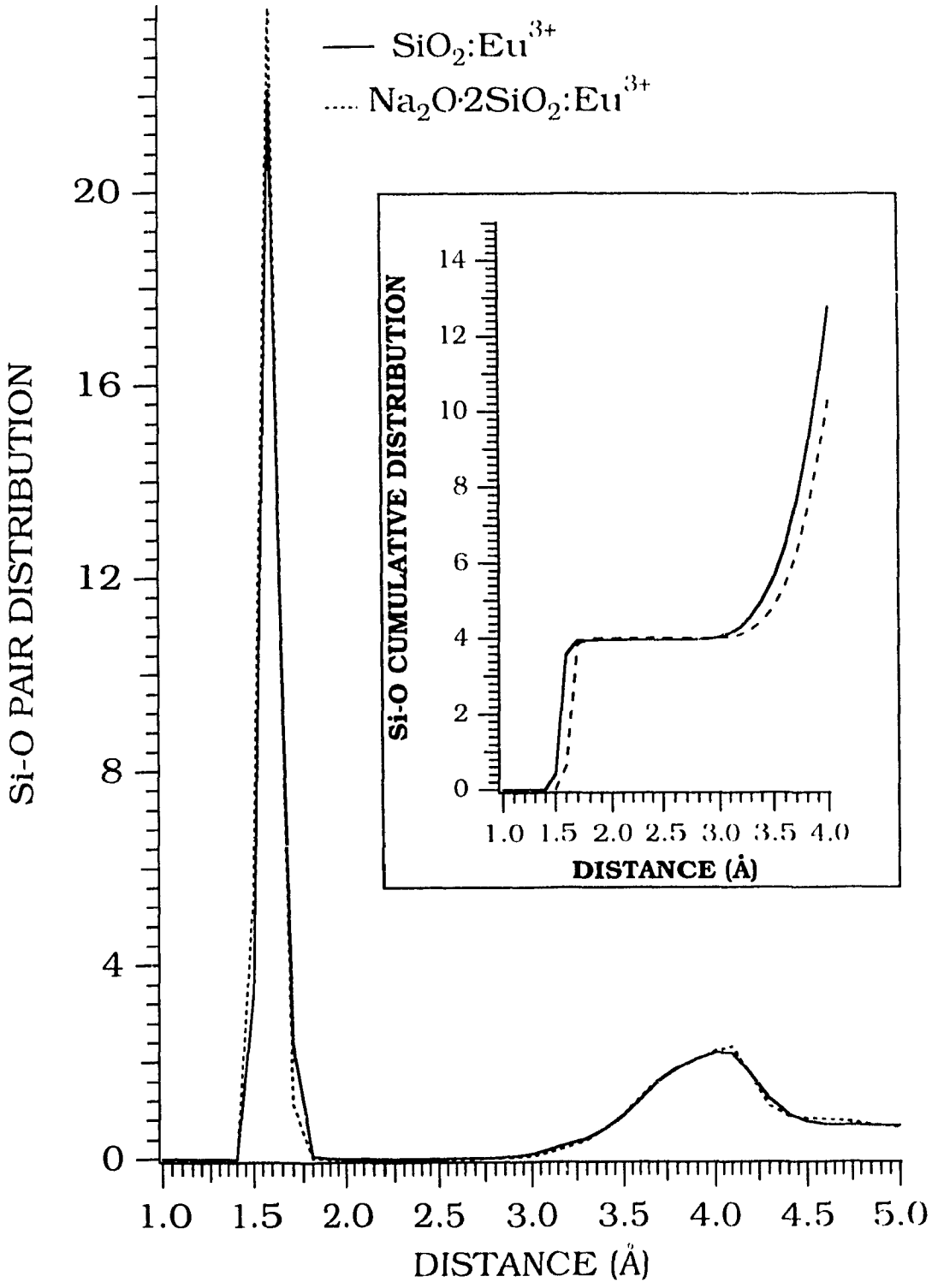

Figure 5.1.1 Si-O Pair Distribution Function (PDF) and Si-O Cumulative Distribution Function (CDF) (shown in inset) for the $SiO_2:Eu^{3+}$ and $Na_2O{\cdot}2SiO_2:Eu^{3+}$ glasses.

these defects. Figure 5.1.2 shows the O-Si-O and Si-O-Si bond angle distributions for these same glasses. The maximum of the bond angle distribution for the O-Si-O tetrahedral angle is found at values of 107° and 106° with a full width at half maximum (FWHM) of 10° and 13.8° for the SiO_2 and $Na_2O{\bullet}2SiO_2$ glasses, respectively. These sharp bond angle distributions, associated with an average oxygen coordination number of 4.00, indicate the presence of well-defined silicate tetrahedra. These tetrahedra are a reflection of the presence of short-range order. The Si-O-Si bond angle, which is the inter-tetrahedral bridging angle, is found to possess maxima at 151° and 153° with a FWHM of 34° and 35° for the SiO_2 and $Na_2O{\bullet}2SiO_2$ glasses, respectively. The Si-O-Si bond angle distribution is much broader and reflect the introduction of randomness in the connectivity of individual silicate tetrahedra.

Table 5.1.1 presents a comparison of structural features derived from radial and cumulative distribution functions for (i) the glasses simulated in this thesis and (ii) previously reported simulated glasses. This Table is organised in the following way.

For a given bond or angle type, one will find that,

(i) the first line presents results from our study,

(ii) the second line presents results from a study which used a typical two-body, modified Born-Mayer-Huggins potential,

(iii) the third line presents results from studies which used a three-body modified Born-Mayer-Huggins potential,

(iv) the fourth line presents results from experimental studies performed on real glasses.

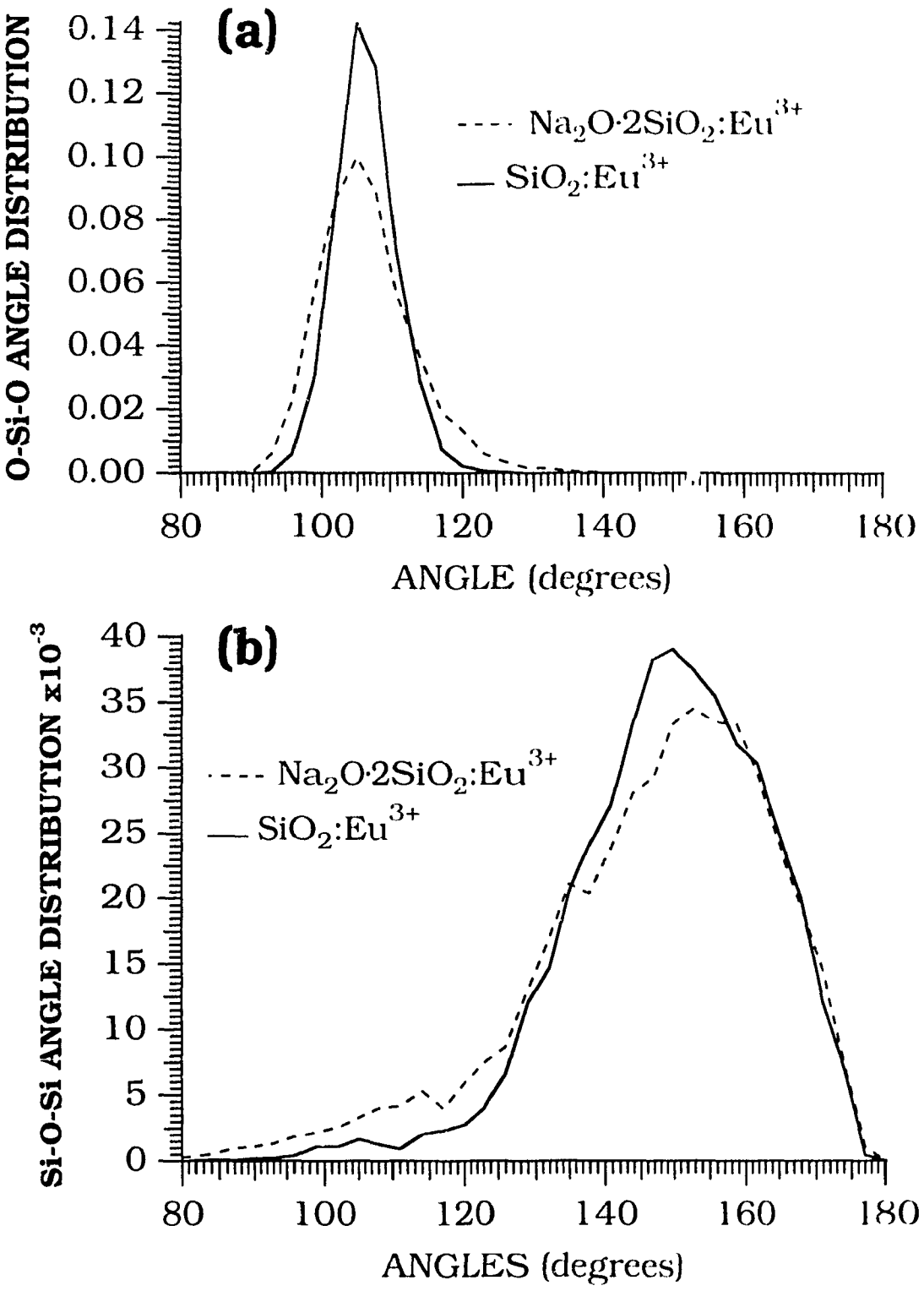

Figure 5.1.2 Bond angle distributions (a) O-Si-O and (b) Si-O-Si for the $SiO_2:Eu^{3+}$ and $Na_2O{\cdot}2SiO_2:Eu^{3+}$ glasses.

TABLE 5.1.1.

STRUCTURAL PARAMETERS DERIVED FROM PAIR, CUMULATIVE AND BOND ANGLE DISTRIBUTION FUNCTIONS FOR SiO_2 AND $Na_2O{\cdot}2SiO_2$ GLASSES FROM VARIOUS SIMULATIONS

Bond type	Source	Bond length (Å) 1st coordination shell		Bond length (Å) 2nd coordination shell		Average coordination†	
		SiO_2	NaS‡	SiO_2	NaS	SiO_2	NaS
O O	(a)	2.60	2.59	4.98	4.98	7.27(3.20)	6.39(3.20)
	(b)	2.55	2.56	4.97	5.0	6.15	5.9
	(c) or (e)	2.64	2.59				4.8
	(d)	2.62-2.65	2.62-2.65	5.1		6	6
O Si	(a)	1.61	1.61	4.00	4.07	4.00(2.10)	4.00(2.10)
	(b)	1.61	1.63	3.93	3.9	4.02	4.4
	(c) or (e)	1.62	1.60			4.00	4.0
	(d)	1.60-1.62	1.60-1.62	4.15		4	4
O Na	(a)	-----	2.24	-----	4.15	-----	4.59(3.10)
	(b)	- ---	2.32	- ---	4.4	-----	4.5 (3.10)
	(c)	-----	2.42	-----		-----	5.0
	(f)	-----	2.30	-----		-----	5
Si - Si	(a)	3.11	3.12	5.10	5.08	4.91(3.60)	3.99(3.60)
	(b)	3.18	3.19	5.25	5.2	4.27	4.0
	(c) or (e)	3.14	3.14				3.7
	(d)	3.11-3.13	3.11-3.13	5.1		4	4
Si Na	(a)	-----	3.28	-----	5.29	-----	4.46(4.00)
	(b)	-----	3.30	-----		-----	5.1
	(c)	-----	3.28-3.35	-----		-----	6.6
	(d)	-----		-----		-----	
Na - Na	(a)	-----	3.15	-----	5.88	-----	3.6 (4.80)
	(b)	-----	3.10	-----		--- .	3.8
	(c)	-----	3.03-3.13	-----		-----	3.6
	(d)	-----		-----		-----	

TABLE 5.1.1. continued...

Angle type	Source	Peak Maxima ( )		Full Width at Half Maxima ( )	
		SiO_2	NaS	SiO_2	NaS
O-Si- O	(a)	107°	106°	10°	13.8°
	(b)	107°		22°	
	(c) or (e)	109.5°	109.5°	7°	12°
	(d)	109.5°		7°	
Si-O-Si	(a)	151°	153°	34°	35°
	(b)	162°		25°	
	(c) or (e)	154°	149°	36°	41°
	(d) or (f)	144°-146°	160°	36°	

The source material is as follows :

(a) This study
(b) Reference 63
(c) Reference 75
(d) Reference 18
(e) Reference 76
(f) Reference 15

† Numbers in parentheses refer to distance (in Ångströms) at which the coordination number has been calculated.

‡ NaS:Eu refers to a sodium disilicate glass, $Na_2O{\cdot}2SiO_2$.

The results obtained in this thesis for the base glasses (SiO_2 and $Na_2O{\cdot}2SiO_2$) are in excellent agreement with those reported by Feuston and Garofalini [75,76] using a Stillinger-Weber three-body modification [81] of a Born-Mayer-Huggins potential.

We present in Figures 5.1.3 and 5.1.4, pictorial representations of the base glasses, showing the typical continuous random network thought to be the medium-range structure of silicate glasses. In these figures, we clearly show the presence of silicate tetrahedra interconnected at the corners. The rules dictated by Zachariasen are respected.

Having established that the modeling of the base glasses was accurate enough for our purposes, we proceeded in doping these base glasses with europium oxide, Eu_2O_3. Figure 5.1.5 shows the pair distribution functions for the Eu-O bond in both $SiO_2{:}Eu^{3+}$ and $Na_2O{\cdot}2SiO_2{:}Eu^{3+}$. We observe that the Eu-O bond length increases from 2.49Å ($SiO_2{:}Eu^{3+}$) to 2.60Å ($Na_2O{\cdot}2SiO_2{:}Eu^{3+}$) for the first coordination shell and from 4.49Å ($SiO_2{:}Eu^{3+}$) to 4.82Å ($Na_2O{\cdot}2SiO_2{:}Eu^{3+}$) for the second coordination shell. The widths of the first peaks were calculated to be $\Delta \approx 0.24$Å FWHM for $SiO_2{:}Eu^{3+}$ and $\Delta \approx 0.30$Å FWHM for $Na_2O{\cdot}2SiO_2{:}Eu^{3+}$. Figure 5.1.6 shows the cumulative distribution function (CDF) for the Eu-O bond. The average coordination numbers were calculated at a cutoff radius (r_{NN}) of 3.2Å which corresponds to the first minimum found between the first and second maxima. The values were found to be 4.20 for $SiO_2{:}Eu^{3+}$ and 5.92 for $Na_2O{\cdot}2SiO_2{:}Eu^{3+}$.

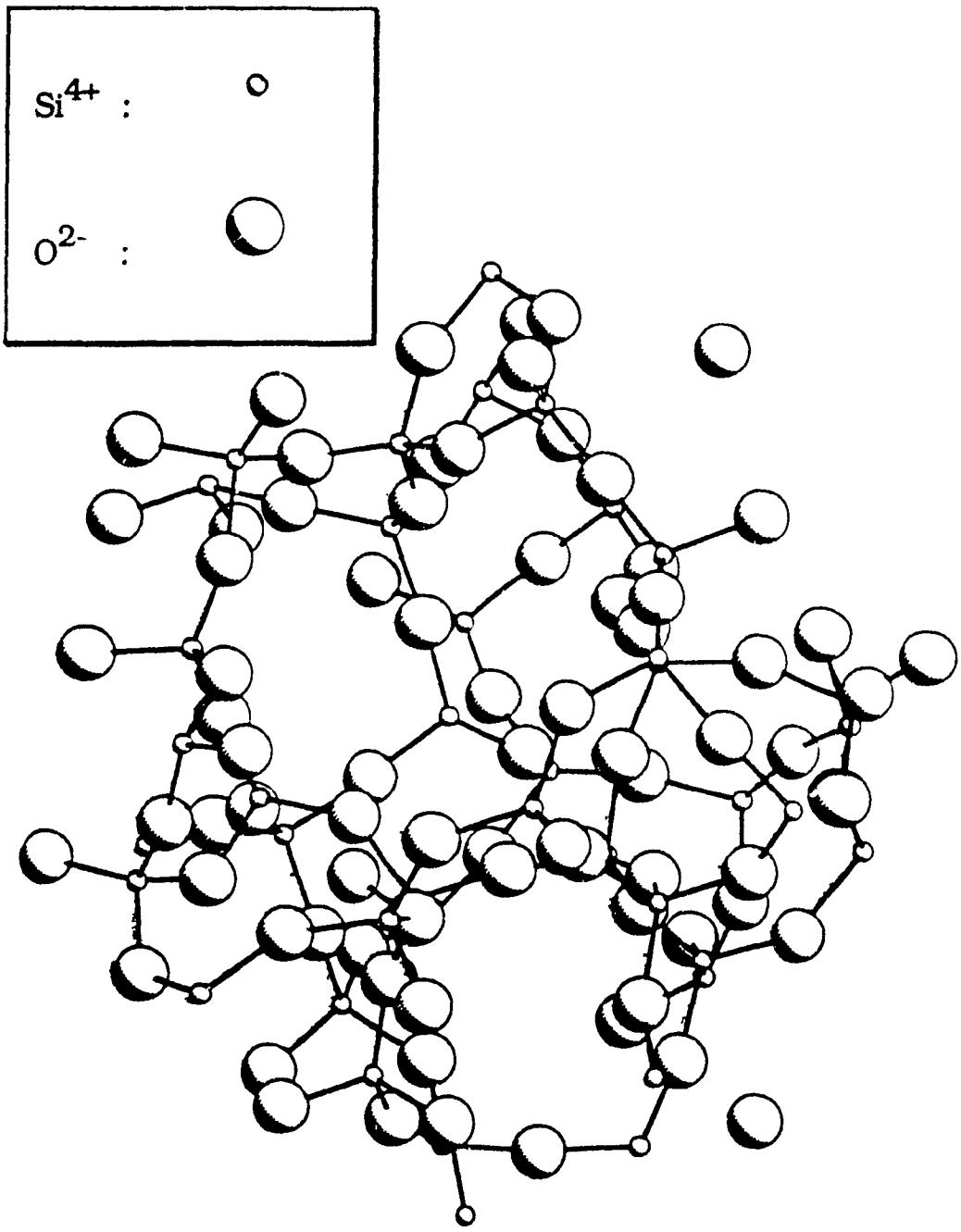

Figure 5.1.3 Pictorial representation of the SiO_2 base glass. The structure represents a sphere of 7.6Å in radius.

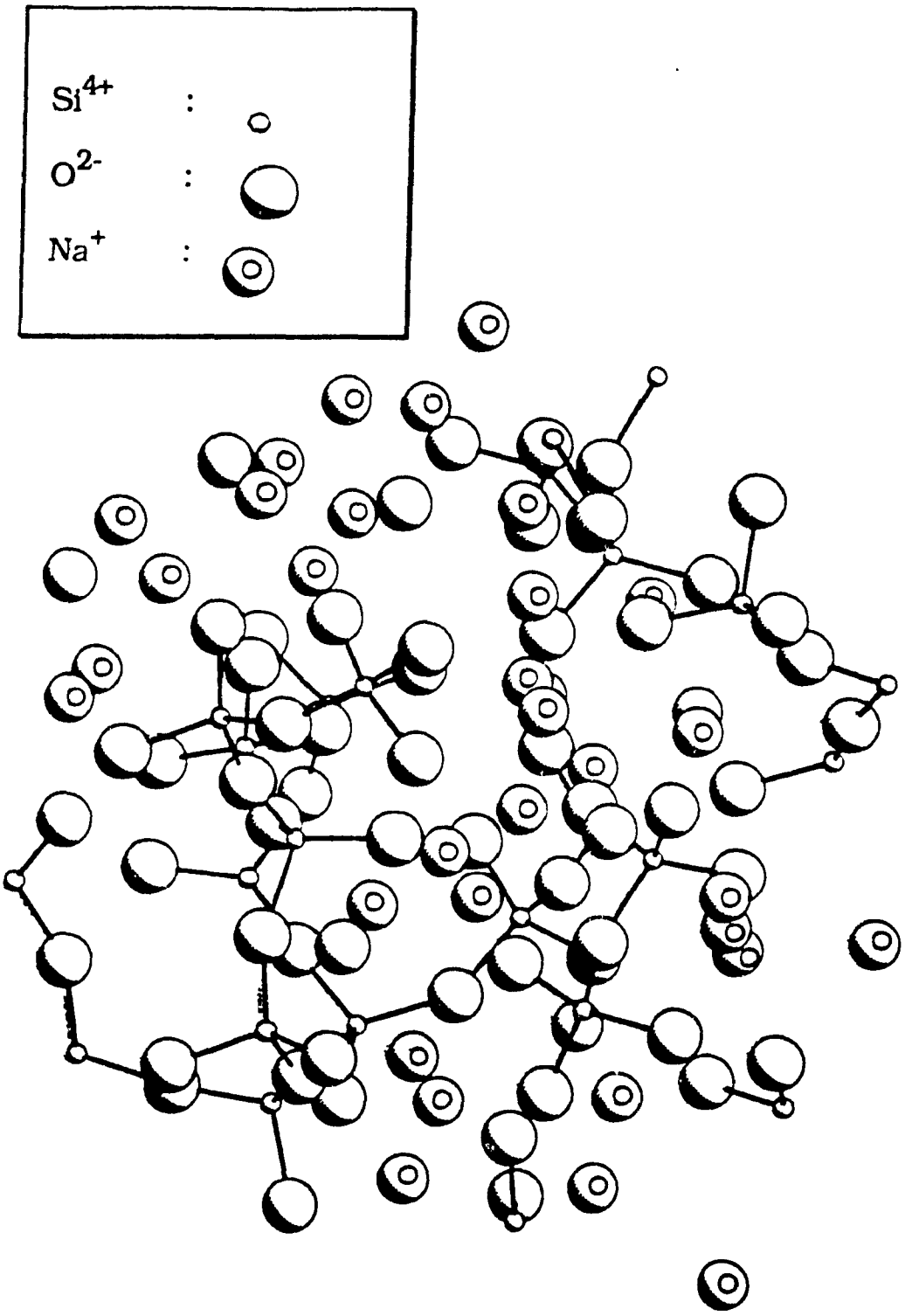

Figure 5.1.4 Pictorial representation of the $Na_2O{\cdot}2SiO_2$ base glass. The structure represents a sphere of 7.4 Å in radius.

Europium-cation pair distribution functions are shown in Figure 5.1.7 for both doped glasses. We observe that the maximum of the first peak for the silicon-europium distribution is situated at approximately 3.9Å, for $SiO_2:Eu^{3+}$. The cation pair distributions for silicon europium and sodium-europium show maxima at approximately 4.0Å and 3.7Å respectively, for $Na_2O \cdot 2SiO_2:Eu^{3+}$. The calculated average coordinations for these three distributions were found to be (i) 7.30 for the Si Eu coordination in $SiO_2:Eu^{3+}$, (ii) 5.99 for the Si-Eu coordination in $Na_2O \cdot 2SiO_2:Eu^{3+}$ and (iii) 11.88 for the Na Eu coordination in $Na_2O \cdot 2SiO_2:Eu^{3+}$. These coordination numbers have been calculated at the first minimum after the first coordination shell peak for the given europium-cation distribution. We have used r_{NN} values of 4.50Å for the Si-Eu distributions and 5.8Å for the Na-Eu distribution. We observe that the first-coordination peak for the Na-Eu distribution is much broader and less well defined than for the two Si-Eu distributions. This would indicate that in the $Na_2O \cdot 2SiO_2:Eu^{3+}$ glass, the europium ions prefer to be located in a sodium-rich environment as shown by (i) the lengthening of the Si-Eu bond length in $Na_2O \cdot 2SiO_2:Eu^{3+}$ and (ii) the Na Eu bond length in $Na_2O \cdot 2SiO_2:Eu^{3+}$ which is smaller than the Si-Eu bond length in $SiO_2:Eu^{3+}$.

To further quantify the local environment of the europium ions, the two bond angle distributions O-Eu-O and Si-O-Eu were calculated. In Figure 5.1.8 (a), we observe three reasonably distinct peaks in the distribution of the O-Eu-O angle for the $SiO_2:Eu^{3+}$ and $Na_2O \cdot 2SiO_2:Eu^{3+}$ glasses. The first peak appears at approximately 50°

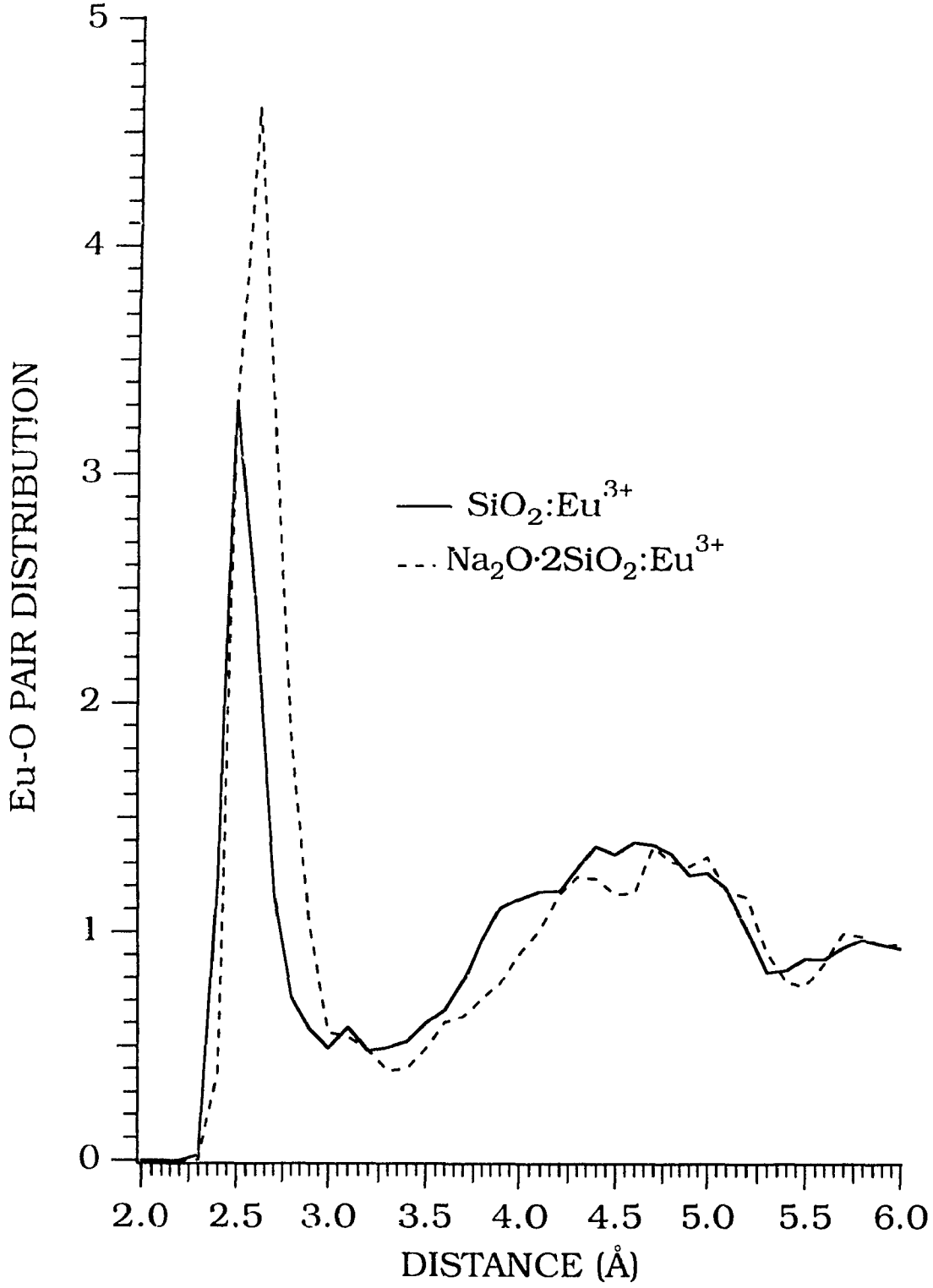

Figure 5.1.5 Eu-O Pair Distribution Function (PDF) for the $SiO_2:Eu^{3+}$ and $Na_2O{\cdot}2SiO_2:Eu^{3+}$ glasses.

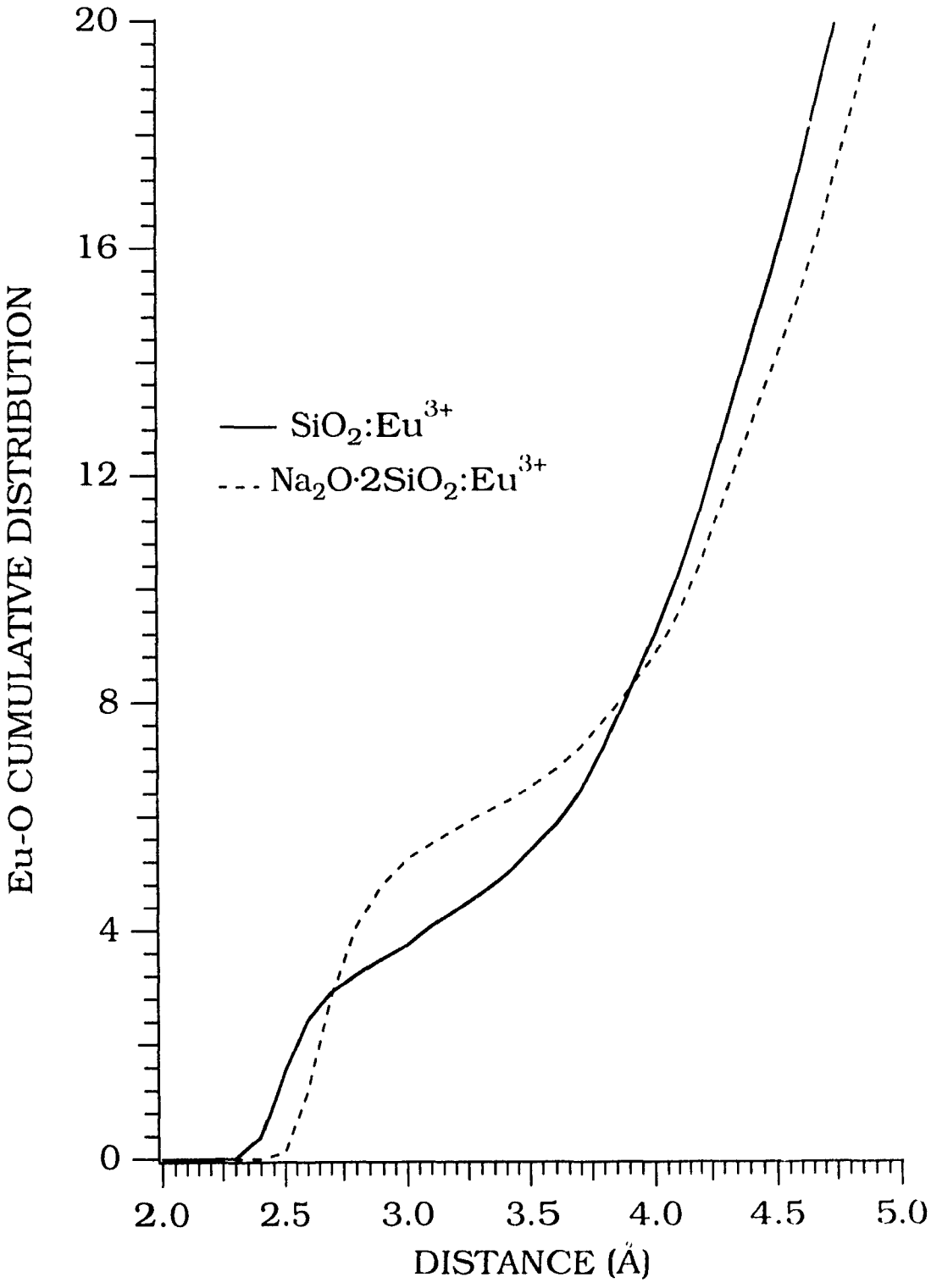

Figure 5.1.6 Eu-O Cumulative Distribution Function (CDF) for the $SiO_2:Eu^{3+}$ and $Na_2O{\cdot}2SiO_2:Eu^{3+}$ glasses.

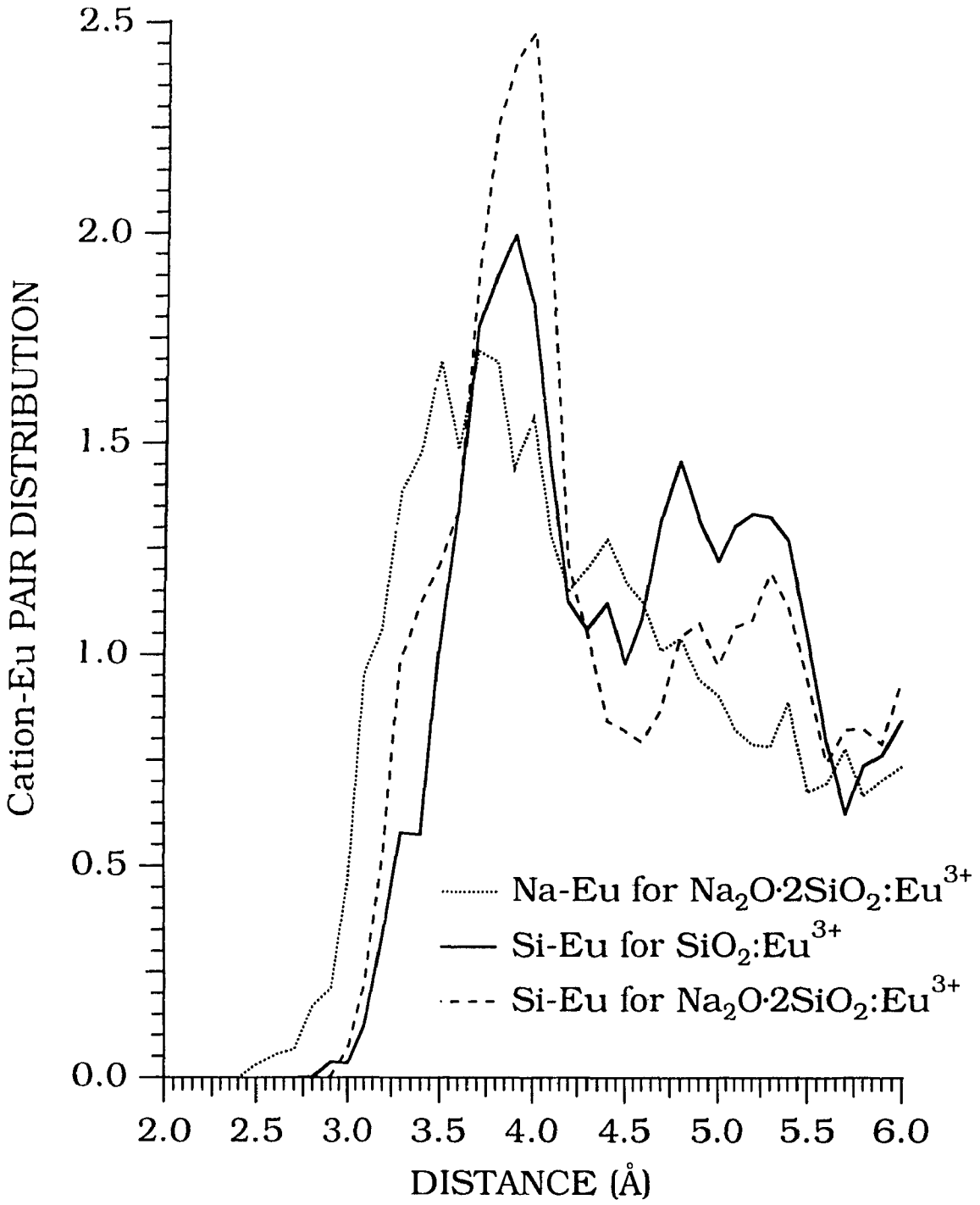

Figure 5.1.7 Eu-cation Pair Distribution Function for the $SiO_2:Eu^{3+}$ and $Na_2O{\cdot}2SiO_2:Eu^{3+}$ glasses. Shown are (i) Eu-Si for the $SiO_2:Eu^{3+}$ glass (ii) Eu-Si for the $Na_2O{\cdot}2SiO_2:Eu^{3+}$ glass and (iii) Eu-Na for the $Na_2O{\cdot}2SiO_2:Eu^{3+}$ glass.

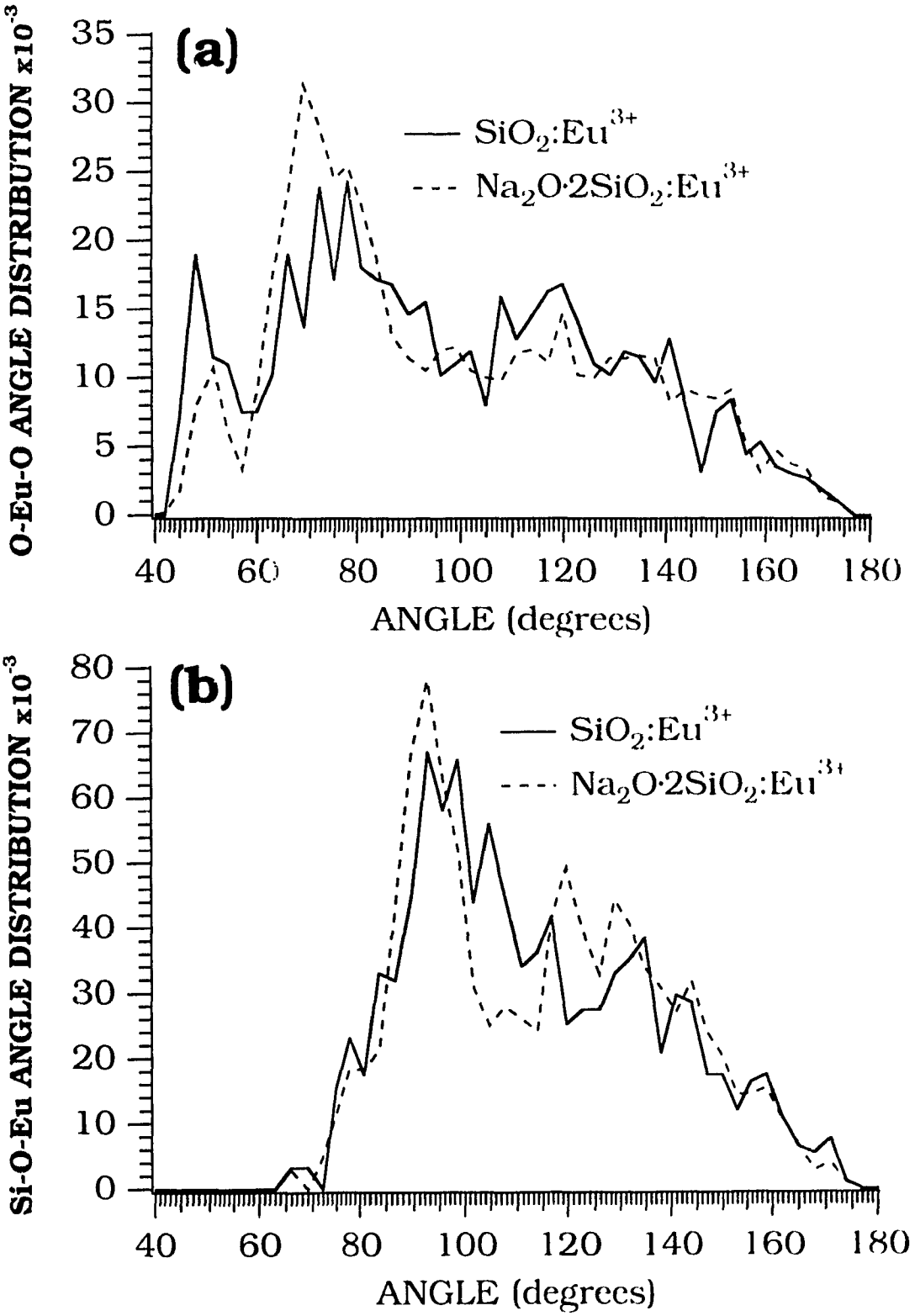

Figure 5.1.8 Bond angle distributions (a) O-Eu-O and (b) Si-O-Eu for the $SiO_2:Eu^{3+}$ and $Na_2O{\cdot}2SiO_2:Eu^{3+}$ glasses.

and has a FWHM of ≈10° for both glasses. The second peak is broader, having maxima at approximately 74° for both glasses, and FWHM of 30° and 23° for SiO_2:Eu^{3+} and Na_2O•$2SiO_2$:Eu^{3+} glasses, respectively. The third peak is very broad, with angles found between 100-180° and maxima at approximately 120° for both glasses. Figure 5.1.8(b) shows the Si-O-Eu bond angle distribution. Two broad peaks can be discerned in these distributions. The first is found at 98° with a FWHM of ≈ 26° for the SiO_2:Eu^{3+} glass and at 93° with a FWHM of ≈15° for the Na_2O•$2SiO_2$:Eu^{3+} glass. The second peak of the Si-O-Eu distribution is found at approximately 124° with a FWHM of approximately 35° in both the SiO_2:Eu^{3+} and Na_2O•$2SiO_2$:Eu^{3+} glasses. As expected for a cationic species which is not a network-former, the O-Eu-O and Si-O-Eu bond angle distributions are very broad, reflecting the disordered nature of the europium sites. The europium angle distributions are slightly better defined for the Na_2O•$2SiO_2$:Eu^{3+} glass. This would indicate that in this glass, the europium environment is less perturbed. Since the bond angle distributions presented in Figure 5.1.8(a) are unresolved, we decided to calculate these distributions using a large number of time steps in order to average out any effects which would be due to a presence of noise. The averaging was carried out over 20000 time steps, with one sample taken at every 10 time steps. The results of this averaging are shown in Figure 5.1.9, for both the SiO_2:Eu^{3+} and Na_2O•$2SiO_2$:Eu^{3+} glasses. A noticeable narrowing of the O-Eu-O distribution is found for the SiO_2:Eu^{3+} glass. It can be postulated that this narrowing is present only in this glass since the Eu-O polyhedra are surrounded by a silicate framework which is considerably more rigid because of the absence of network-modifier cations. This is not the case for the Na_2O•$2SiO_2$:Eu^{3+} glass.

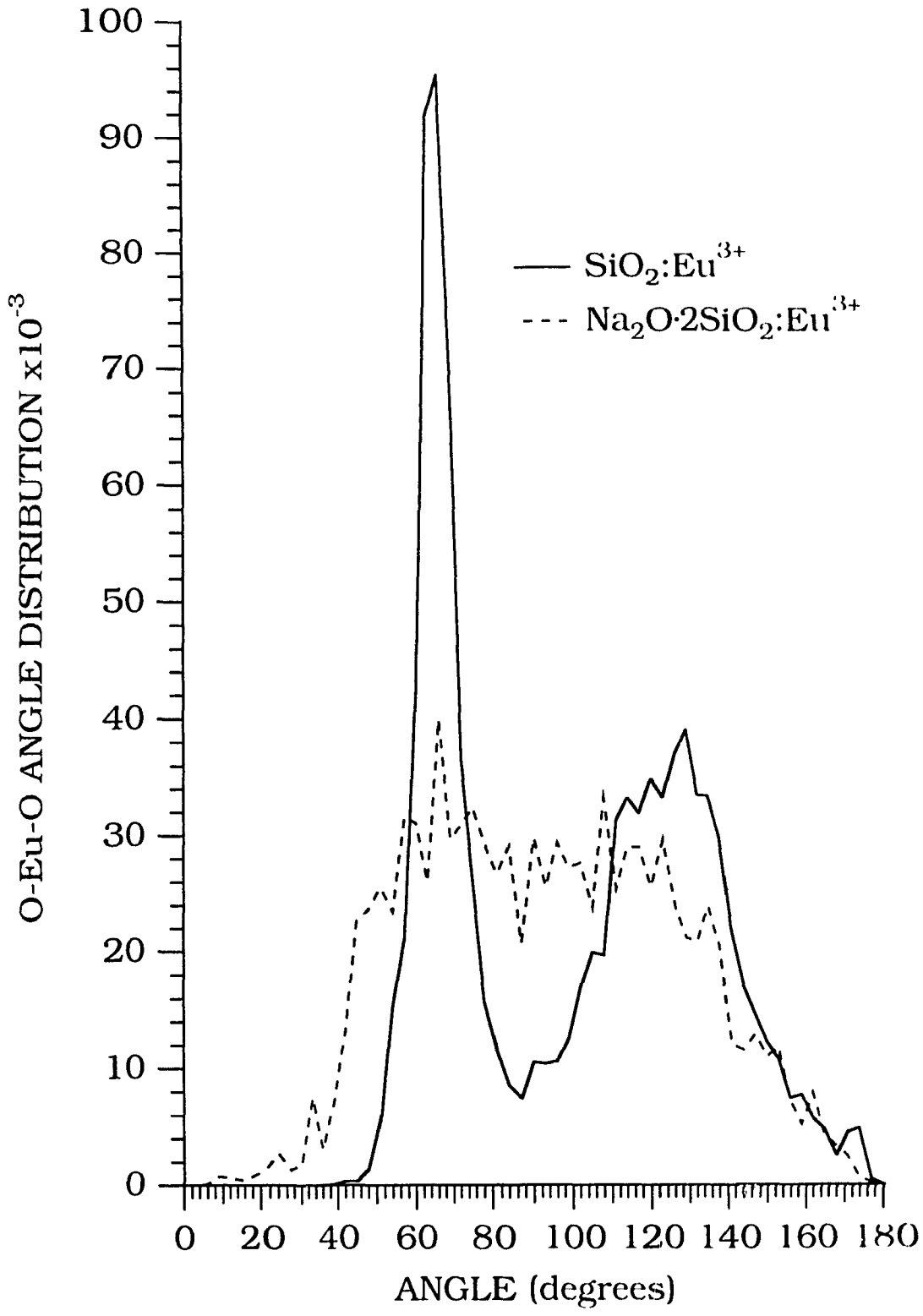

Figure 5.1.9 Time-averaged bond angle distributions of O-Eu-O for the SiO_2:Eu^{3+} and $Na_2O{\cdot}2SiO_2$:Eu^{3+} glasses.

The pair distribution functions, shown in Figure 5.1.5, are quite broad and do not return to a null value after the first peak, indicating that the distribution of local environments for the Eu^{3+} must vary considerably from site-to-site. Therefore, we have chosen to further quantify this observation by calculating the probability that a Eu^{3+} ion has exactly x oxygen neighbours within a certain distance. The probability distribution of oxygen neighbours surrounding the europium ions, for each glass, is shown in Figure 5.1.10. The radius of the coordination sphere was taken to be 3.2Å, corresponding to the first minimum of the Eu-O PDF. We observe that, although the range of coordination varies from 2 to 8 in the silica glass and from 4 to 9 for the modified silicate glass, the most likely coordination for the Eu^{3+} ion in the SiO_2 glass is 4 and in the $Na_2O{\cdot}2SiO_2$ glass is 6. In Figure 5.1.8(a), we observe the presence of O-Eu-O bond angles having very low values, typically smaller than 90°, and as small as 50°. This is explained by the distribution in the Eu-O coordination number, leading to the presence of coordinating polyhedra with a greater number of ligands (6 to 10) than the reported averages of 4 and 6 (for the SiO_2:Eu^{3+} and $Na_2O{\cdot}2SiO_2$:Eu^{3+} glasses, respectively). These distorted polyhedra would necessarily have O-Eu-O bond angles with values smaller than 90° (which corresponds to the O-M-O bond angle found in a regular octahedron) and conceivably as small as 50°.

A summary of the results pertaining to the europium local environments for both simulated glasses is presented in Table 5.1.2.

Figures 5.1.11 and 5.1.12 show "snapshots" of the typical local environment of the Eu^{3+} ions, in SiO_2:Eu^{3+} and $Na_2O \cdot 2SiO_2$:Eu^{3+} respectively, at 300K. The "snapshots" are taken such that a europium ion is located at the center of a sphere of 6.0Å in radius. All ions found within this sphere are displayed. Bonds between the europium and oxygen ions which are less or equal to 3.20Å in length are shown as dotted-lines. The silicate back-bone is also displayed with bonds which are less or equal to 2.10Å. We observe that the Eu^{3+} ion is surrounded by four nearest-neighbour oxygens, forming a distorted tetrahedron (Figure 5.1.11) in the SiO_2 glass with an average Eu-O bond length of 2.58Å. In the $Na_2O \cdot 2SiO_2$ glass, the Eu^{3+} ion is surrounded by 6 nearest neighbour oxygens (Figure 5.1.12) with an average Eu-O bond length of 2.76Å. In both Figures, the oxygens which are bonded to the europium ions are clearly seen to be non-bridging.

In order to quantify the spatial arrangement of the oxygen ligands about the Eu^{3+} ion, we calculated the quadrupole moment for each of the configurations. This procedure is identical in format to that presented in section 4.4., and in particular to the application of equation (4.4.1). As stated before, the eigenvectors represent the principal axes of an ellipsoid. These eigenvectors are directly related to the charge distribution about the europium ion. The eigenvalues must then represent the shape of the ellipsoid and consequently the shape of the charge distribution. Depending on the values of λ_1,λ_2 and λ_3 the shape of the ellipsoid can range from roughly spherical ($\lambda_1 \approx \lambda_2 \approx \lambda_3$), to a flatter distribution ($\lambda_1 \approx \lambda_2 >> \lambda_3$) and finally to a needle-shaped distribution ($\lambda_1 >> \lambda_2 \approx \lambda_3$).

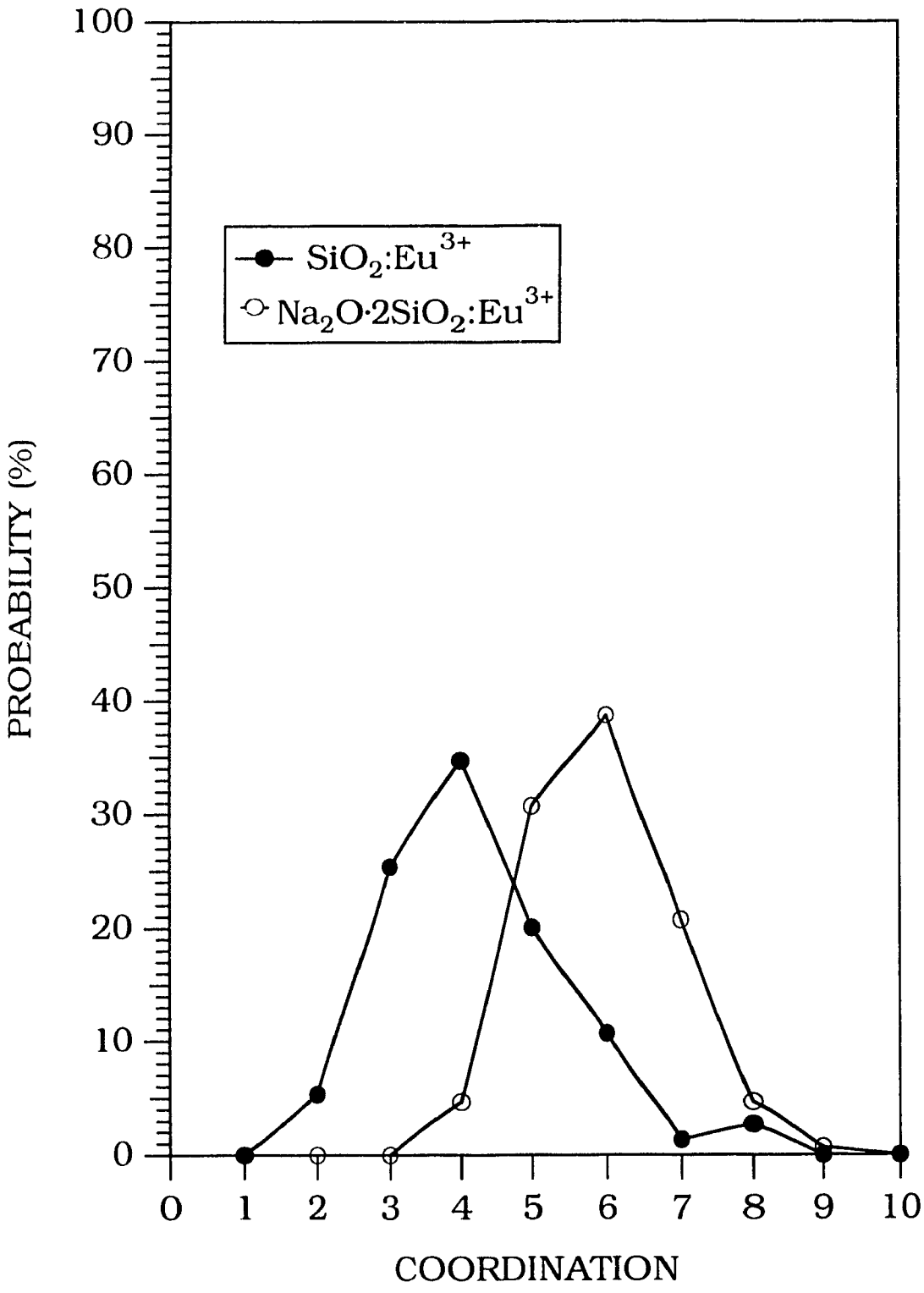

Figure 5.1.10 Probability distribution of oxygen neighbours about a Eu^{3+} ion within a coordination sphere of 3.2Å.

TABLE 5.1.2.

STRUCTURAL PARAMETERS DERIVED FROM EUROPIUM PAIR, CUMULATIVE AND BOND ANGLE DISTRIBUTION FUNCTIONS FOR $SiO_2:Eu^{3+}$ AND $Na_2O{\cdot}2SiO_2:Eu^{3+}$ GLASSES

Bond type	Bond length (Å) 1st coord. shell		Bond length (Å) 2nd coord. shell		Average coordination*	
	$SiO_2:Eu^{3+}$	NaS:Eu^{3+}	$SiO_2:Eu^{3+}$	NaS:Eu^{3+}	$SiO_2:Eu^{3+}$	NaS:Eu^{3+}
O - Eu	2.49Å	2.60Å	4.49Å	4.82Å	4.20 (3.20)	5.92 (3.20)
Si - Eu	≈ 3.9Å	≈ 4.0Å	≈ 5.0Å	≈ 5.2Å	7.30 (4.50)	5.99 (4.50)
Na -Eu	-----	≈ 3.7Å	-----	≈ 7.0Å	-	11.88 (5.8)
Angle	Peak Maxima (°)		FWHM (°)			
	$SiO_2:Eu^{3+}$	NaS:Eu^{3+}	$SiO_2:Eu^{3+}$	NaS:Eu^{3+}		
O-Eu-O	50°, 74°,120°	50°, 74°,120°	10°,30°,40°	10°,23°,40°		
Si-O-Eu	98°,124°	93°,124°	26°,35°	15°,35°		

* Numbers in parentheses refer to distance (in Å) at which the coordination number has been calculated.

**NaS:Eu^{3+} refers to the doped sodium disilicate glass, $Na_2O{\cdot}2SiO_2:Eu^{3+}$.

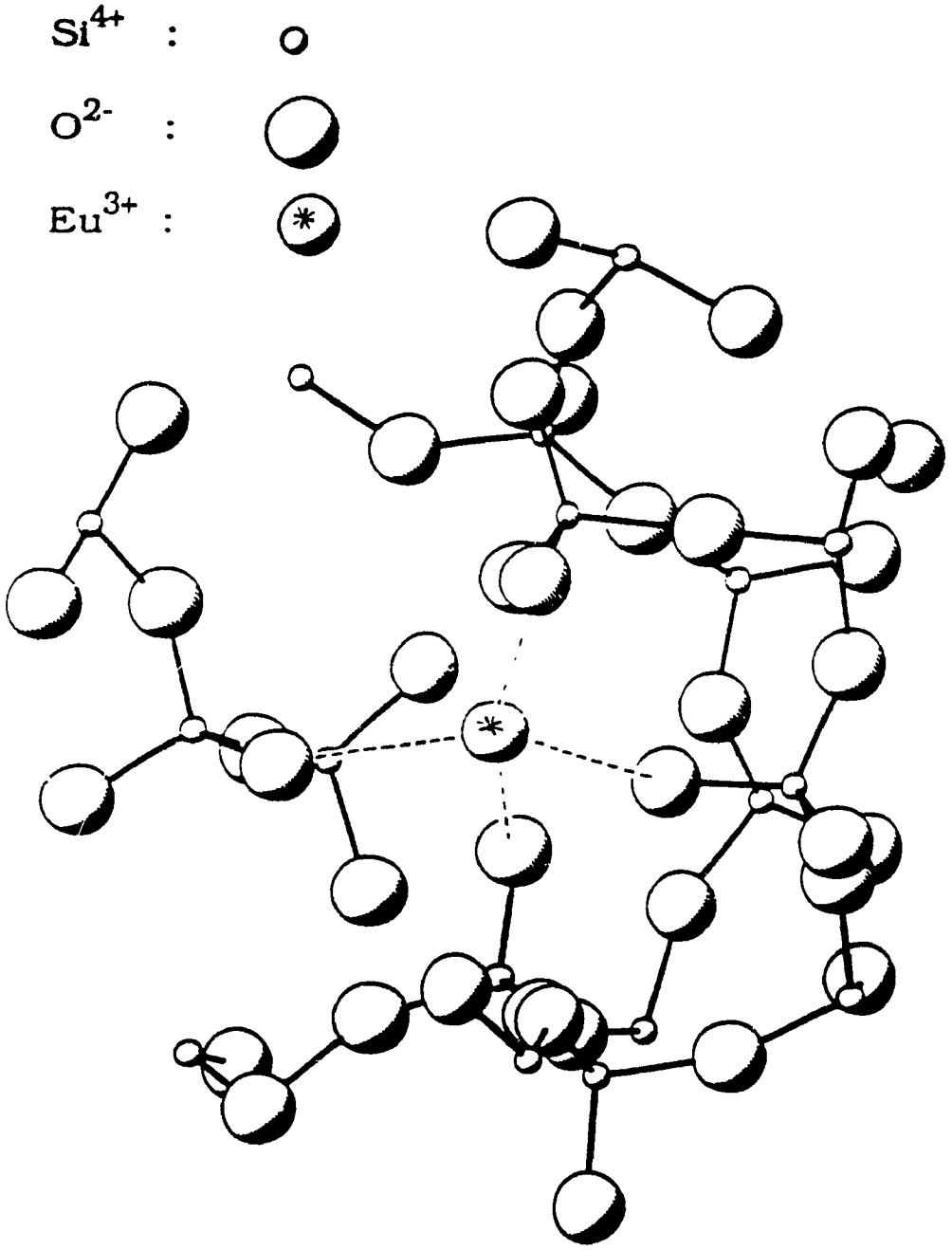

Figure 5.1.11 Schematic representation of the local environment about an average Eu^{3+} in SiO_2:Eu^{3+} glass. The structure represented is a sphere of 6.0 Å in radius.

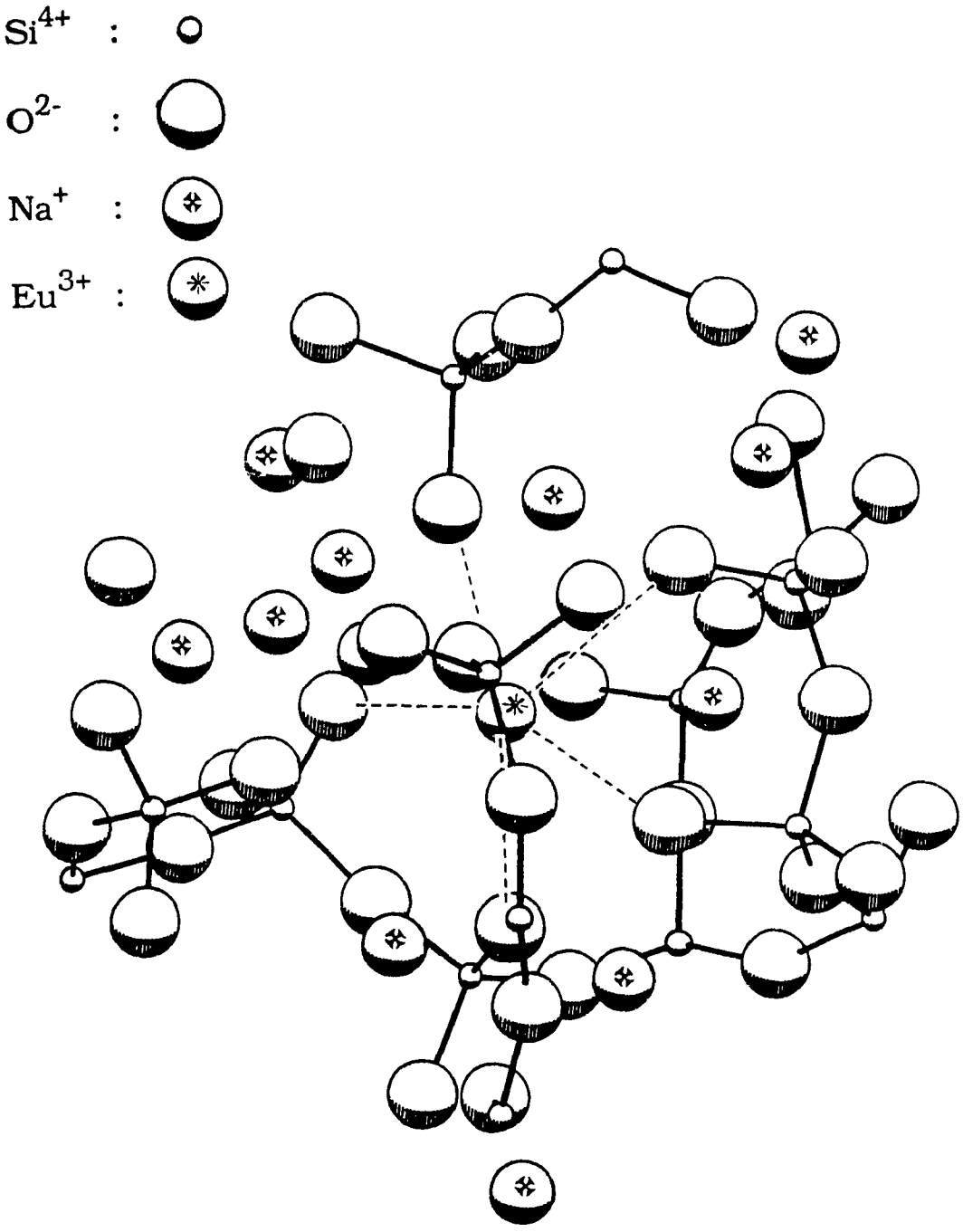

Figure 5.1.12 Schematic representation of the local environment about an average Eu^{3+} in $Na_2O{\cdot}2SiO_2{:}Eu^{3+}$ glass. The structure represented is a sphere of 6.0 Å in radius.

Figure 5.1.13 shows the eigenvalues λ_i of the oxygen ligand distribution surrounding the Eu^{3+} ion calculated for the 150 configurations simulated in the SiO_2 and $Na_2O{\cdot}2SiO_2$ glasses. The configurations are ordered such that the λ_3 are increasing in value. This figure confirms the presence of a large variation in the local environment of the dopant ions and that no two configurations are identical. The range of values for the λ_i in SiO_2:Eu^{3+} is seen to be slightly larger, indicating a more distorted "average" environment in this glass. This observation is consistent with the fact that the peaks shown for the O-Eu-O and Si-O-Eu bond angle distributions (Figure 5.1.8) are less defined for the SiO_2:Eu^{3+} glass. We also observe that the λ_i values are never equal. This fact allows us to conclude that none of the configurations possess a high degree of symmetry. It is nevertheless difficult to relate the numerical values of the calculated eigenvalues to a given shape or to a measure of distortion of the polyhedron without a basis of comparison. To solve this dilemma, we have chosen to compare the eigenvalues calculated from the Eu^{3+} local environments shown in Figures 5.1.11 and 5.1.12 to those calculated from the corresponding regular polyhedron. For the SiO_2:Eu^{3+} glass (Figure 5.1.11), the calculated eigenvalues are $\lambda_1=1.575\times10^{-1}$, $\lambda_2=8.287\times10^{-2}$, $\lambda_3=3.591\times10^{-2}$. The corresponding regular polyhedron would be an undistorted tetrahedron having "bond" lengths of 2.58Å (average Eu-O bond length for the Eu^{3+} environment shown in Figure 5.1.11). The calculated eigenvalues of this perfect tetrahedron are $\lambda_1=7.768\times10^{-2}$, $\lambda_2=7.767\times10^{-2}$, $\lambda_3=7.767\times10^{-2}$. The quadrupole of the simulated structure shows an elongation on one of its ellipsoid axis

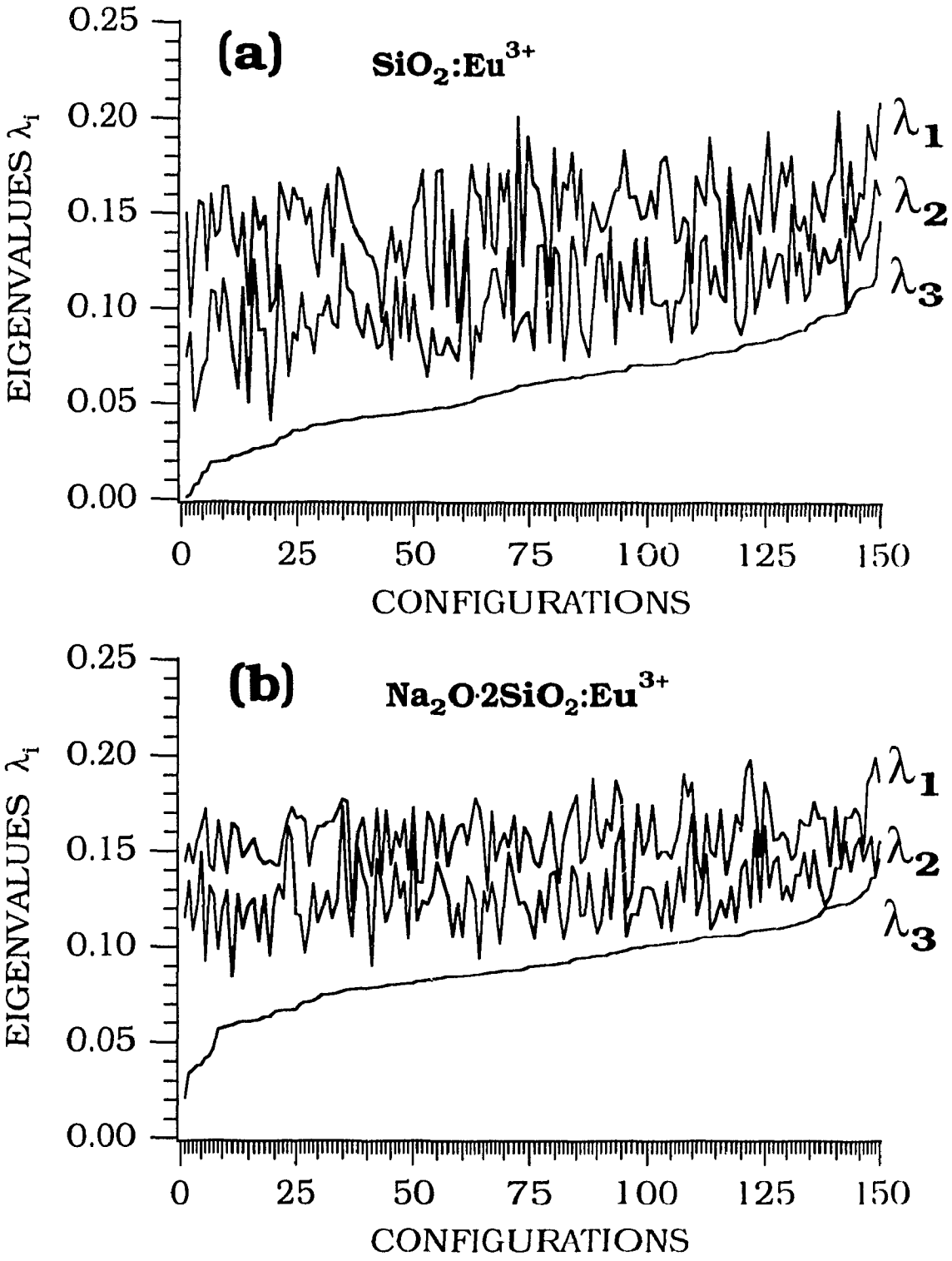

Figure 5.1.13 Eigenvalues λ_i of the oxygen ligand distribution about the Eu^{3+} ion calculated for the 150 sites of **(a)** $SiO_2:Eu^{3+}$ and **(b)** $Na_2O{\cdot}2SiO_2:Eu^{3+}$ glasses.

and a shortening of the other. This would indicate that the local structure displayed in Figure 5.1.11 is highly distorted when compared with the spherical quadrupole of the perfect tetrahedron. In the case of the $Na_2O{\cdot}2SiO_2{:}Eu^{3+}$ glass (Fig. 5.1.12), the eigenvalues are $\lambda_1=1.429x10^{-1}$, $\lambda_2=1.264x10^{-1}$, $\lambda_3=6.599x10^{-2}$. An undistorted octahedron having "bond" lengths of 2.76Å would have values of $\lambda_1= 9.513x10^{-2}$, $\lambda_2= 9.513x10^{-2}$, $\lambda_3= 9.513x10^{-2}$. This would indicate that the structure shown in Figure 5.1.13 has a slightly distended and flatter shape then the perfect octahedron, due to an eigenvalue distribution which resembles $\lambda_1=\lambda_2>\lambda_3$.

In an electronic and vibrational spectroscopic study of transition metal ions dissolved in alkali-silicate melts and glasses, Nelson *et al.* [128,129] investigated the local environments of the doped ions. With the optical data obtained from the studied glasses and from literature data, they proposed that the transition metal ions occupy several different types of *sites* in silicate glasses. They suggested four possibilities of structural type for the dopant ion: (i) the transition metal ion acts as a molecular entity , it (transition metal) is coordinated by oxygens which are not part of the silicate framework, as exemplified by the chromate and dichromate ions in silicate and borate glasses [130], (ii) the transition metal ion acts as a quasi-molecular complex such that it modifies the spatial geometry of the nearby silicate network to suit its own bonding requirements, (iii) the transition metal acts as a network-modifier and occupies an individual *site* which is imposed by the configuration of the structural units present in the glass in the same way as sodium ions, (iv) the transition metal ion acts as a network-

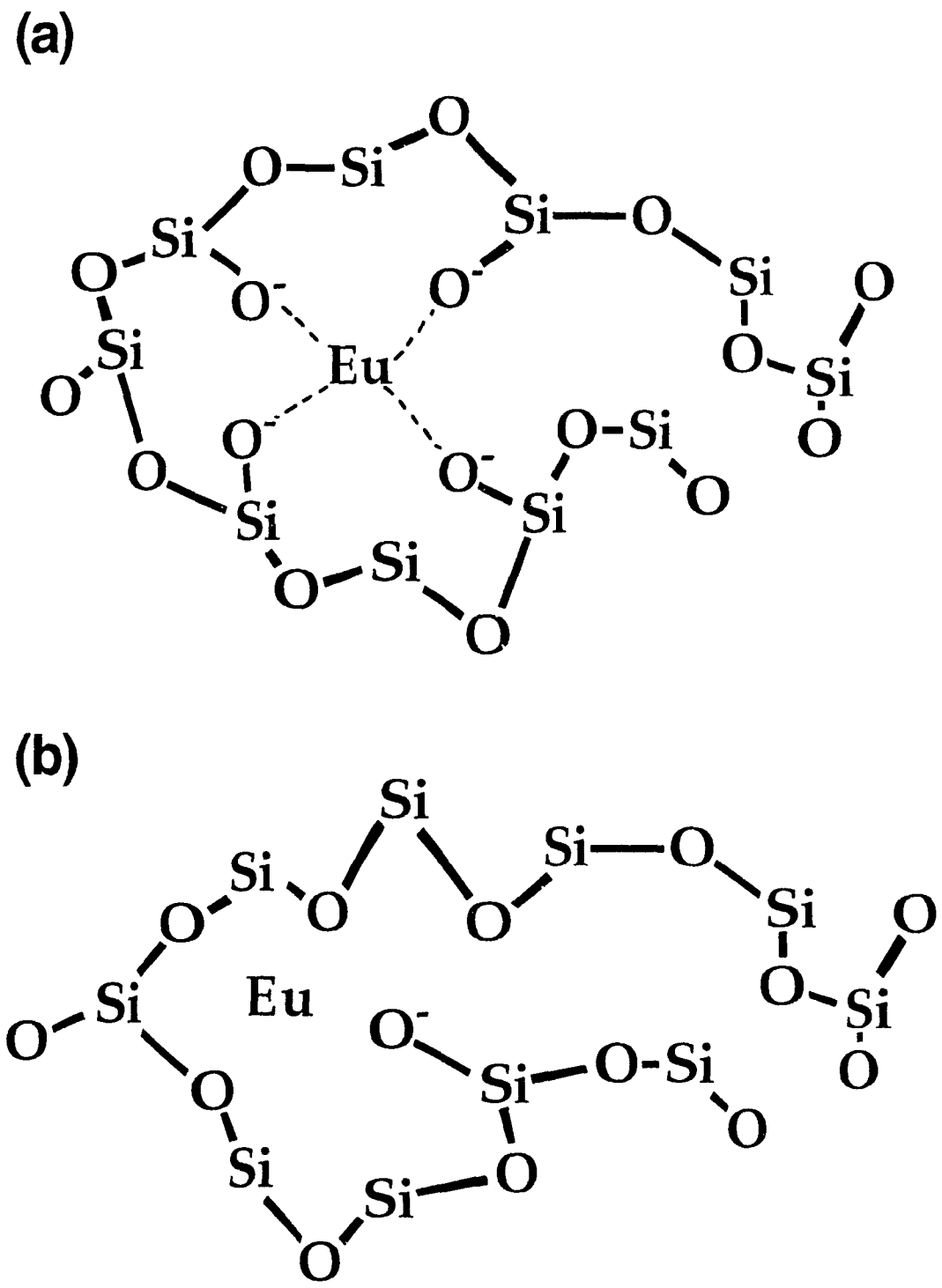

Figure 5.1.14 Schematic diagrams of the Eu^{3+} ion represented as **(a)** a quasi-molecular complex and **(b)** a network modifier.

former either by substitution into Si^{4+} sites or by the polymerisation of transition metal polyhedra.

Molecular entities are expected to be formed by small, highly charged ions such as the Cr^{6+} ion. Evidently this is not the case of the Eu^{3+} ion. Because of its size and charge compared to those of the Si^{4+} ion, the Eu^{3+} ion is not expected to be a network-former. In Figure 5.1.14, we show schematic diagrams of the Eu^{3+} ion represented as the two types of interstitial species most likely to be found in silicate glasses. The two cases represented in this Figure are the limits of a continuous range of possibilities which will depend upon the balance between the network bonding strength and the bonding and energetic requirements of the doped ion.

Evidence that the Eu^{3+} ions predominantly form quasi-molecular complexes in the SiO_2:Eu^{3+} and the $Na_2O{\cdot}2SiO_2$:Eu^{3+} glasses can be obtained by distinguishing the type of oxygen ions bonded to the europiums. This was done by identifying the oxygens within 3.2Å to a given Eu^{3+} and calculating the number of nearest-neighbour silicon ions (within 2.1Å) to each of these oxygens. These results are presented in Table 5.1.3.

In the sodium disilicate glass, we find that a very high percentage (roughly 93%) of the oxygens bonded to the europiums are non-bridging ($-O^-$). The ratio of bridging oxygens ($-O-$) to non-bridging oxygens for the $Na_2O{\cdot}2SiO_2$ base glass was calculated to be 1.52 [40], which would give 60.32% bridging oxygens and 39.68% of non-bridging

oxygens. In the vicinity of the Eu^{3+} ions, the percentage of bridging oxygens was calculated to be 7.11% (Table 5.1.3). Assuming that the effect of the sodium ions, which act as network-modifiers, is felt equally

TABLE 5.1.3
PERCENTAGE OF FIRST-COORDINATION SHELL OXYGEN IONS HAVING *x* NUMBER OF BONDED SILICON IONS

x	SiO_2:Eu^{3+}	Na_2O·2SiO_2:Eu^{3+}
3 and higher	0.00%	0.00%
2	32.01%	7.11%
1	67.99%	87.58%
0	0.00%	5.31%

throughout the glass, it is reasonable to assume that this drastic decrease in bridging oxygens is entirely due to the Eu^{3+} ions. An analogous result is observed for SiO_2:Eu^{3+} where we find the presence of only 32% bridging oxygens in the vicinity of the Eu^{3+}. Thus we conclude that the europium ions are promoting the formation of a high number of non-bridging oxygens. This fact coupled with the observation that there is a large variation in site-to-site environments, and that the Eu-O bond length distribution is small ($\Delta \approx 0.24$Å FWHM and $\Delta \approx 0.30$Å FWHM for SiO_2:Eu^{3+} and Na_2O·2SiO_2:Eu^{3+} respectively), leads us to propose that

each europium ion modifies the network locally to provide an environment which not only satisfies it's bonding requirements but also it's local field (or crystal-field) energy requirements.

Marcus and Polman [131] presented a brief study of the local structure of Er^{3+} ions doped (or implanted) in silica and sodium silicate glasses by the EXAFS and photoluminescence techniques. Their interpretation of the EXAFS results, following from a qualitative study of model compounds[4], tentatively indicates that in the sodium silicate sample the Er^{3+} ions are surrounded by 6.3 oxygen atoms showing neither detectable disorder nor a Er-Si shell. They attribute this to the presence of an ErO_6 moiety with sodium atoms decoupling the moiety from the silicate backbone. This interpretation resembles our own findings for the simulated $Na_2O{\cdot}2SiO_2{:}Eu^{3+}$ glass, given that we accept (i) the "quality" of the model compounds and any interpretation which derives from them and (ii) the replacement of the Eu^{3+} ions by Er^{3+} ions. Using the same model compounds, the findings they report for the "doped" silica samples show that the Er^{3+} ions are also 6-coordinated (5.5-6.0), but are in a more disordered environment. Also, an Er-Si shell was observed, which they ascribe to Er^{3+} ions bonded to non-bridging oxygens. Because of the methods[5] used to prepare the two $Er^{3+}{:}SiO_2$

[4] The model compounds are : (i) Er_2O_3 and $Er[(C_3F_7C(O)CH_2(O)C(CH_3)_3]_3$ as models for the Er-O bond distance and coordination, and, (ii) an annealed film of atomic Er deposited on a Si(100) substrate, showing the presence of $ErSi_2$, as a model for the Er-Si bond distance and coordination.

[5] The two methods are the following : (i) MeV ion implantation on a silica film, (ii) creation of a porous silica film on a bulk silica substrate, followed by doping in a H_2O/propanol solution of $ErCl_3H_6$ with subsequent sintering and air-quenching.

samples, it is doubtful that these samples represent "bulk" samples as those prepared by classical methods. As such, any structural information derived from these samples is deemed to give unlikely bases of comparison.

It is interesting that we observe the presence of *free* oxygens (O^{2-}) in the $Na_2O{\cdot}2SiO_2{:}Eu^{3+}$ glass (Table 5.1.3). These oxygens are independent of the silicate framework and exist due to the presence of the surrounding sodium and/or europium cations. Brawer and Weber [87], observed the presence of free fluorines (F^-) in a calcium-modified fluoroberyllate europium-doped glass. These authors ascribed the formation of free fluorines to the presence of neighbouring cations with large field strengths. The field strength of a cation is given by

$$F \propto \frac{q}{r^2} \qquad (5.1.1)$$

where q is the charge of the cation and r is it's ionic radius. Sodium ions have a field strength of approximately 0.96, whereas the europium ions have a field strength of approximately 3.32. In the sodium disilicate base glass, we found that 0.25% of oxygens are free. However, in the $Na_2O{\cdot}2SiO_2{:}Eu^{3+}$ glass we find the percentage of free oxygens to be 5.31% in the local environment of the Eu^{3+}. Thus, the process for the formation of free oxygen can be conceived in the following way: (i) sodium ions locally disrupt the silicate network and create non-bridging oxygens, (ii) a europium ion attracts a non-bridging oxygen into its potential field and frees it from the silicate network, and (iii) local sodium cations are rearranged to meet the requirements of

electroneutrality (local). This mechanism will only occur if both cations are present. Further support for the mechanism proposed is derived from the absence of free oxygens in both the undoped and Eu^{3+}- doped SiO_2 glasses, suggesting that the presence of sodium ions is necessary for this process to occur.

In summary, a reasonably complete picture of the local environment of Eu^{3+} ions doped in SiO_2 and $Na_2O{\cdot}2SiO_2$ glasses has evolved from the Molecular Dynamics study. The following points should be stressed :

The average coordination number of the Eu^{3+} ion was found to be 4 and 6 in SiO_2 and $Na_2O{\bullet}2SiO_2$ glasses, respectively.

The oxygens bonded to the Eu^{3+} ions were shown to belong to distinct silicate tetrahedra.

The local structure of the europium ions is influenced to a greater degree by its bonding and energetic requirements than by the topology of the silicate framework. As such, we suggest that the europium ions form quasi-molecular complexes and that they do not behave as network-modifiers.

5.2 SPECTROSCOPY OF THE SIMULATED AND EXPERIMENTAL $Na_2O{\bullet}2SiO_2:Eu^{3+}$ DOPED GLASSES

The structural model of the $Na_2O{\cdot}2SiO_2:Eu^{3+}$ glass, presented in the previous section, is the starting point of a calculation which is related to the *lattice-summation* technique [132,133]. Crystal-field parameters are derived from the interaction between the impurity ion and the electrostatic potential of the surrounding lattice. Knowing the position and charge of each atom, the electrostatic potential at the rare-earth site can be calculated by summing each individual atomic contribution. The calculated crystal-field parameters will then be used (i) in the calculation of the splitting of each J-manifold and (ii) in the calculation of the transition probabilities between all individual components of each J-manifold. In effect, this will give us a simulated emission or absorption spectrum with correct energies and relative intensities.

In order to validate both the structural model derived from the Molecular Dynamics simulation and the crystal-field model, we will make a comparison to the experimental data obtained from absorption and fluorescence spectroscopy of the corresponding laboratory glass. Finally, we will investigate spectra-structure correlations of doped inorganic glasses.

5.2.1 Computational choices

Several choices had to be made prior to calculating the optical spectra of Eu^{3+} ions doped in the simulated glass. These choices pertain to the type of calculation and to certain assumptions made in order to predict the electronic wavefunctions of each Eu^{3+} configuration in the simulated glasses. Specifically, the following points had to be considered.

5.2.1.1 Choice of *ab initio* model

Several *ab initio* models for predicting the energy level schemes of rare-earth ions doped in solid matrices have been successfully proposed, the electrostatic model [134], the method of operator equivalents [41], the superposition model [135], the angular overlap model [136], and molecular orbitals calculations [137]. The choice of the point-charge Crystal-Field model based on the Three-Parameter Theory developed by Leavitt *et al.* [104] is justified with regards to the type of molecular modeling we have performed. In effect, the MD technique, using a two-body potential, considers only electrostatic (ionic) interactions; no bond directionality is introduced with this type of potential to simulate covalent interactions or orbital overlaps. Therefore, the use of ligand-field theory or molecular orbital theory would not be justifiable in this context.

5.2.1.2 Choice of point-group symmetry

As we have seen in Section 5.1 (Figure 5.1.13), none of the 150 glass configurations presents a high degree of symmetry. This is normally expected due to the disordered nature of the glass matrix which dictates that the lowest symmetry possible must prevail. As such, the point symmetry of the "sites" occupied by the rare-earth ions should be regarded as C_1. This lack of symmetry removes all selection rules and the simple point-charge CF calculations are nearly impossible to perform. Brecher and Riseberg [50,51] used a C_{2v} symmetry in their treatment of FLN spectra. The reasons they invoked were (i) that this was the highest symmetry in which the full splitting of the $^7F_1$ and $^7F_2$ levels is accounted for (see Table 5.2.1.2.1), (ii) it is a subgroup of almost all of the higher point symmetries and therefore allowed the application of the descending symmetries technique [139,140] and (iii) it was, at that time, the lowest symmetry for which simple CF calculations could be performed. In the case at hand, the choice of a C_2 point symmetry for the rare-earth environment was dictated by similar considerations. As stated in section 3.1.2, 14 B_{nm} parameters need to be considered. In effect, a fifteenth parameter exists, the imaginary part of B_{22}, but by a simple rotation of the ensemble of ligands about the z-axis of the Cartesian system B_{22} can be made real.

5.2.1.3 Choice of free-ion barycentres

By placing a rare-earth ion into a solid-state lattice, the ion will be influenced by the inhomogeneous electric fields arising from the

TABLE 5.2.1.2.1

NUMBER OF CRYSTAL FIELD LEVELS FOR DIFFERENT SYMMETRIES

J-value	Triclinic Monoclinic Rhombic	Trigonal Hexagonal	Tetragonal	Cubic
0	1	1	1	1
1	3	2	2	1
2	5	3	4	2
3	7	5	5	3
4	9	6	7	4
5	11	7	8	4
6	13	9	10	6
7	15	10	11	6
8	17	11	13	7

Triclinic	C_1 C_i
Monoclinic	C_s C_2 C_{2h}
Rhombic	C_{2v} D_2 D_{2h}
Trigonal	C_3 S_6 C_{3v} D_3 D_{3d}
Hexagonal	C_{3h} C_6 C_{6h} D_{3h} C_{6v} D_6 D_{6h}
Tetragonal	S_4 C_4 C_{4h} D_{2d} C_{4v} D_4 D_{4h}
Cubic	T T_h T_d O O_h

presence of the atoms of the lattice (the crystal-field). As discussed in section 3.1.1, this will cause the lifting of the degeneracy of the J-levels of the free-ion. Table 5.2.1.3.1 presents (i) values for the energy-level barycentres of Eu^{3+} computed using the free-ion parameters reported by Carnall, Fields and Rajnak [101], (ii) the experimental barycentres of the J-manifolds found for the absorption and emission spectra of the $Na_2O{\cdot}2SiO_2{:}Eu^{3+}$ laboratory glass, and (iii) values of the barycentres of the J-manifolds used in the present simulation, adjusted in order to obtain a proper fit with experimental results.

TABLE 5.2.1.3.1
ENERGY-LEVEL BARYCENTRES FOR VARIOUS Eu^{3+} IONS

J-manifold	E_{calc} (cm^{-1})[a]	E_{exp} (cm^{-1})[b]	E_{sim} (cm^{-1})[c]
$^7F_0$	0.0	0	0
$^7F_1$	381.0	380	350
$^7F_2$	1049.5	961	925
$^7F_3$	1911.9	1980	1939
$^7F_4$	2897.9	3055	3000
$^7F_5$	3958.7	3842	3886
$^7F_6$	5060.2	4922	4882
$^5D_0$	17316.6	17275	17228
$^5D_1$	19057.3	19008	19000
$^5D_2$	21529.8	21523	21500
$^5D_3$	24420.7	24440	24390
$^5L_6$	25406.3	25450	25375

[a] fitted parameters for Eu^{3+} (aq) found in ref. 101

[b] experimental barycentres of the $Na_2O{\cdot}2SiO_2{:}Eu^{3+}$ experimental glass

[c] best-fit parameters used for the $Na_2O{\cdot}2SiO_2{:}Eu^{3+}$ simulated glass

5.2.1.4 Choice of cut-off radius in the *ab initio* calculation

In their original contribution on the simulation of rare-earth optical spectra (Eu^{3+} doped in BeF_2 and alkali-modified BeF_2 glasses), Brawer and Weber [86] restricted their consideration to the ligands of the first coordination shell, i.e. F^- ligands that were found inside a sphere of 2.75Å of radius with the Eu^{3+} lying at it's center. They limited their calculations to the second-order parameters (B_{2m}) in the crystal-field expansion which simplified the relationship between energy levels and structure. In Figures 5.2.1.4.1 (a) to (c), we show the behaviour of the B_{nm} parameters with respect to the radius of a sphere surrounding an arbitrarily chosen Eu^{3+} configuration. Only the atoms which are included in this sphere will take part in the determination of the electrostatic field at the Eu^{3+} position. The crystal-field parameters converge to a given value only after a distance of ≈12Å. It is obvious that limiting the calculation to the first coordination shell, which in the Eu-O case is 3.2Å, will unavoidably be incorrect. The observed convergence of the B_{nm} parameters prompted us to take into account all the atoms in our simulated ensemble. This represents a sphere of approximately 18Å in radius. In effect, as was stated before, this is closely related to the crystalline lattice summation technique, where the electrostatic crystal-field at an impurity site is determined by summing the contributions of all atoms in a given volume of crystallographic space. Such a calculation is feasible for a crystal because of the inherent translational symmetry of the unit cell. For an experimental glass this is impossible since the unit cell is infinite. However, in the case of a computer glass, where atomic positions are known, such a calculation is possible.

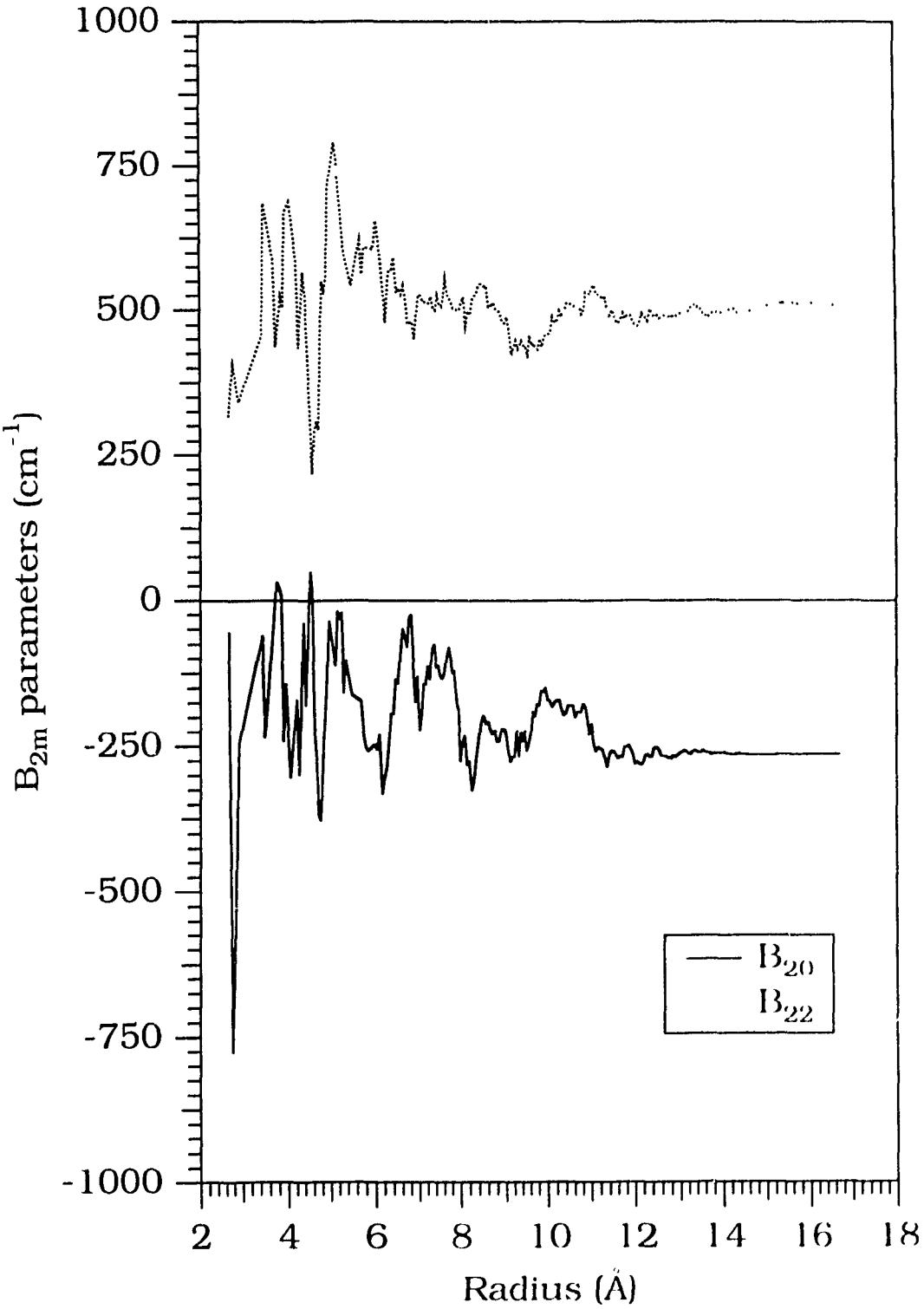

Figure 5.2.1.4.1a Variation of the B_{2m} (real and m even) parameters in function of the radius of a sphere surrounding an arbitrarily chosen Eu^{3+} ion of the simulated $Na_2O{\cdot}2SiO_2{:}Eu^{3+}$ glass.

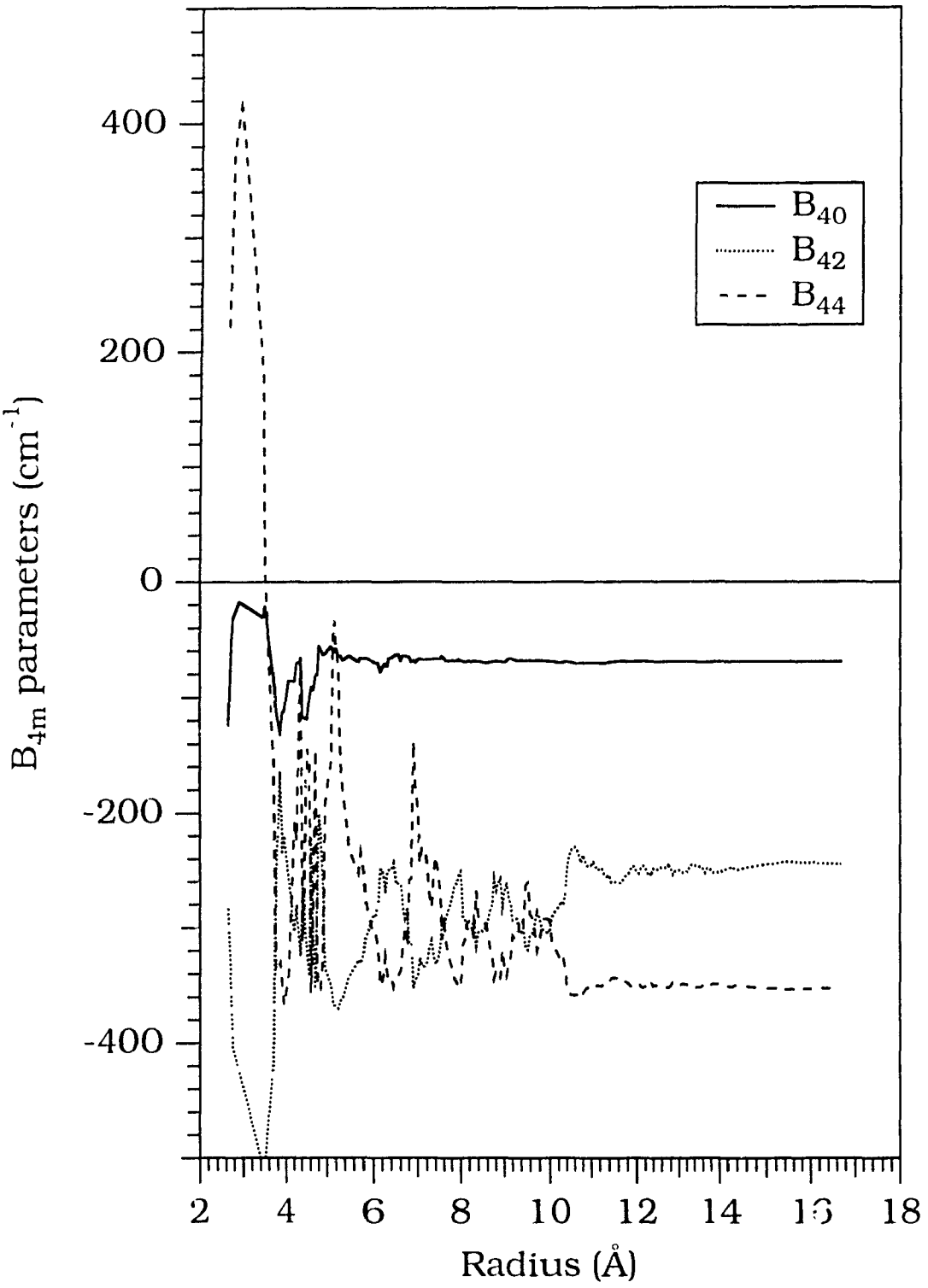

Figure 5.2.1.4.1b Variation of the B_{4m} (real and m-even) parameters in function of the radius of a sphere surrounding an arbitrarily chosen Eu^{3+} ion of the simulated $Na_2O{\cdot}2SiO_2{:}Eu^{3+}$ glass.

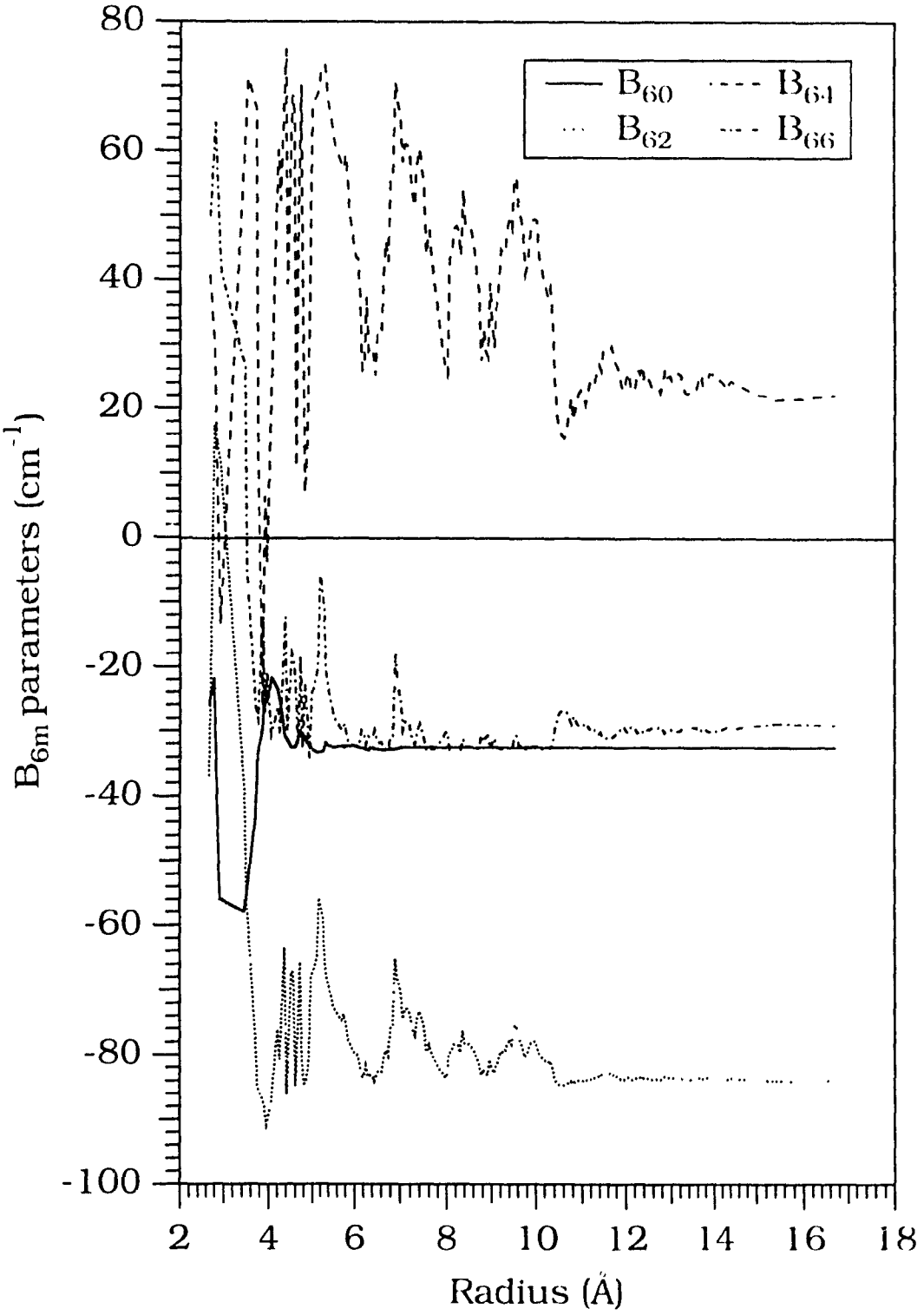

Figure 5.2.1.4.1c Variation of the B_{6m} parameters (real and m-even) as a function of the radius of a sphere surrounding an arbitrarily chosen Eu^{3+} ion of the simulated $Na_2O{\cdot}2SiO_2{:}Eu^{3+}$ glass.

5.2.1.5 Choice of atomic partial charges

The last point of concern was the use of partial charges in the crystal-field calculation. While performing the calculations using Equation (3.1.2.3) for rare-earth ions doped in several crystalline materials, Karayianis and Morrison [132] investigated the effects of varying the charges from their purely ionic values to partial charges. They found that the introduction of partial charges had a significant effect on the fitting of experimentally obtained energy-levels. Effectively, the inclusion of partial charges used in a reanalysis of the optical spectra of a number of rare-earth ions doped in $CaWO_4$, resulted in a different interpretation of experimental data for Tb^{3+}:$CaWO_4$ [140]. The inclusion of partial charges in the crystal-field calculation reduces the magnitude of the electrostatic interaction between atoms which leads to a simulation of the effects of covalency. This does not in any way constitute the introduction of a covalency term in the crystal-field calculation. In Figure 5.2.1.5.1, we show the effect of the variation of the oxygen and silicon charges upon the simulated $^5D_0 \leftarrow {}^7F_0$ transition. Choosing a value between -2.0 and -1.0 for the charge on the oxygen ions and keeping the full charge value on the europium and sodium ions. the charges on the silicon were varied to maintain the electroneutrality of the whole ensemble of atoms. We observed the following trends with decreasing charge on the O^{2-} and the Si^{4+} ions : (i) a red shift of the maxima, (ii) a narrowing of the peaks, (iii) a decrease in the intensity of the peaks, and (iv) the disappearance of the high-energy asymmetry. All of these observations are consistent with what one would observe from an increase in the covalency of the silicate framework. Thus the choice of

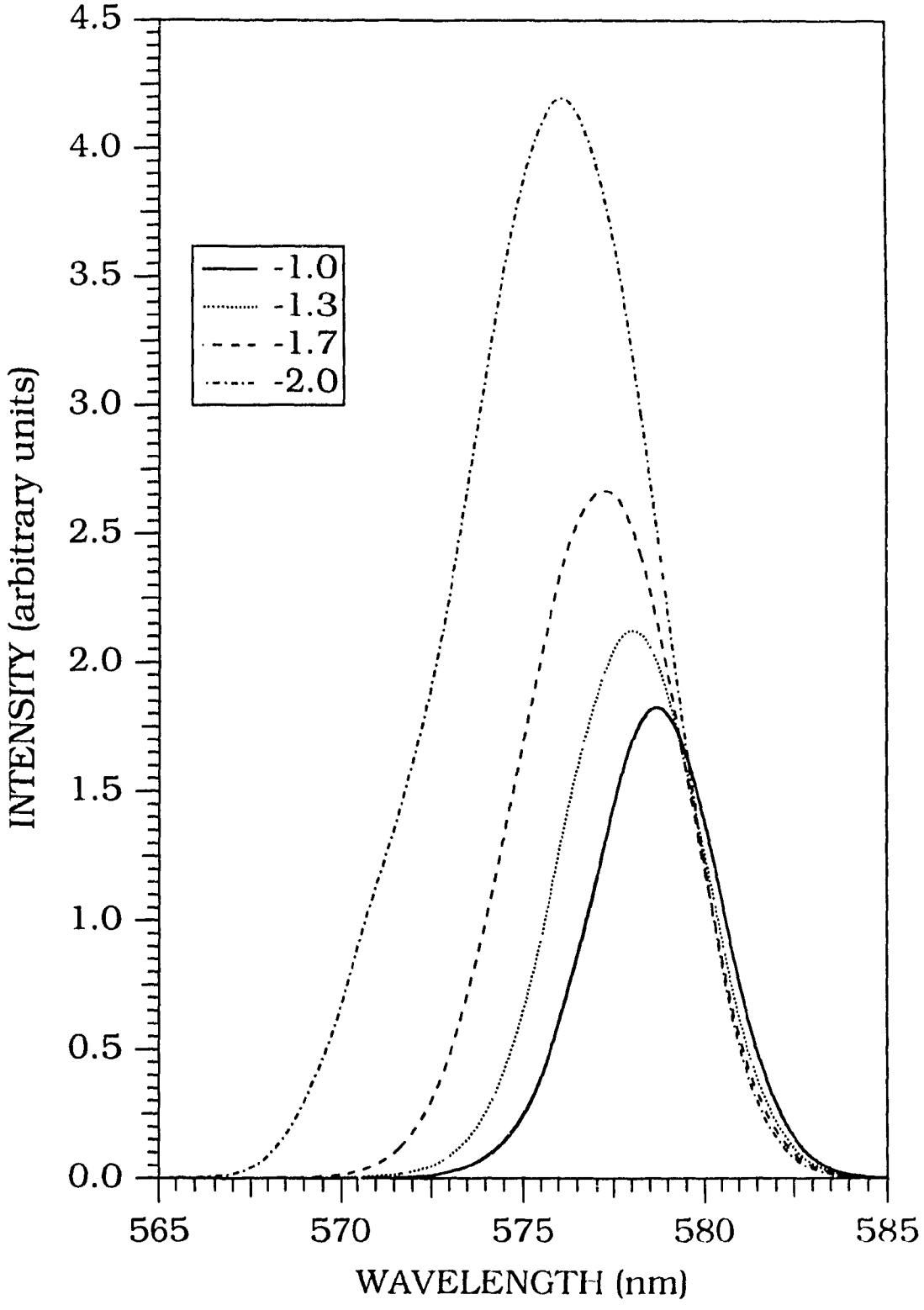

Figure 5.2.1.5.1 Variation of the oxygen and silicon charges upon the $^5D_0 \leftarrow ^7F_0$ transition of the simulated $Na_2O{\cdot}2SiO_2{:}Eu^{3+}$ glass.

ionic charges was dictated by how well we could reproduce various spectral features.

Firstly, we considered the position, width and shape of the $^5D_0 \leftarrow ^7F_0$ transition. The europium-doped sodium disilicate glass shows, for this room-temperature absorption transition, the following features: (i) a maximum situated at 578.9 nm (17274 cm^{-1}), (ii) a pronounced asymmetry on the high-energy side of the band and (iii) a full-width at half-maximum (FWHM) of 88 cm^{-1}, all of which are confirmed by the results of Kurkjian *et al.* [23]. Secondly, we considered the width and shape of the $^5D_0 \rightarrow ^7F_1$ transition with the specific intention of reproducing the noticeable splitting due to the triplet nature of the $^7F_1$ state.

These considerations lead us to simulate the spectra with the following ionic charge values:

oxygen :	-1.000
silicon :	+1.485
sodium :	+1.000
europium :	+3.000

These values are in good agreement with the partial ionic charges for the SiO_4^{4-} tetrahedron reported by Pauling [80]

oxygen :	-1.27
silicon :	+1.06

which were determined by considering (i) the difference in electronegativity of silicon and oxygen and (ii) the partial double bond character of the SiO_4^{4-} tetrahedron.

Since the A_{nm} parameters, of equation (3.1.2.3), are dependent on the charge of each atom contributing to the electrostatic field, the B_{nm} parameters plotted in Figures 5.2.1.4.1.(a)-(c) have been calculated with the above-mentioned partial ionic charges.

5.2.2 Comparison of the spectroscopy of the simulated and laboratory $Na_2O{\cdot}2SiO_2:Eu^{3+}$ glasses

5.2.2.1 Absorption spectra

Figure 5.2.2.1.1a shows the uncorrected room-temperature absorption spectrum of the experimental $Na_2O{\cdot}2SiO_2:Eu^{3+}$ glass (sample "B"). A correction for a rapidly rising background has been made and the corrected spectrum is shown in Figure 5.2.2.1.1b. A spectral scan was performed between 350 nm and 600 nm for this sample. In this region we observe several inhomogeneously broadened transitions originating from the $^7F_0$ ground state and the thermally populated $^7F_1$ state to the upper excited states of the $4f^6$ electronic configuration. Since the barycentre of the $^7F_1$ state lies at $387cm^{-1}$ above the $^7F_0$ ground state, the fractional thermal population of these two ^7F_J-states are approximately 0.54 for the J=0 state and 0.46 for the J=1 state. The background severely limits

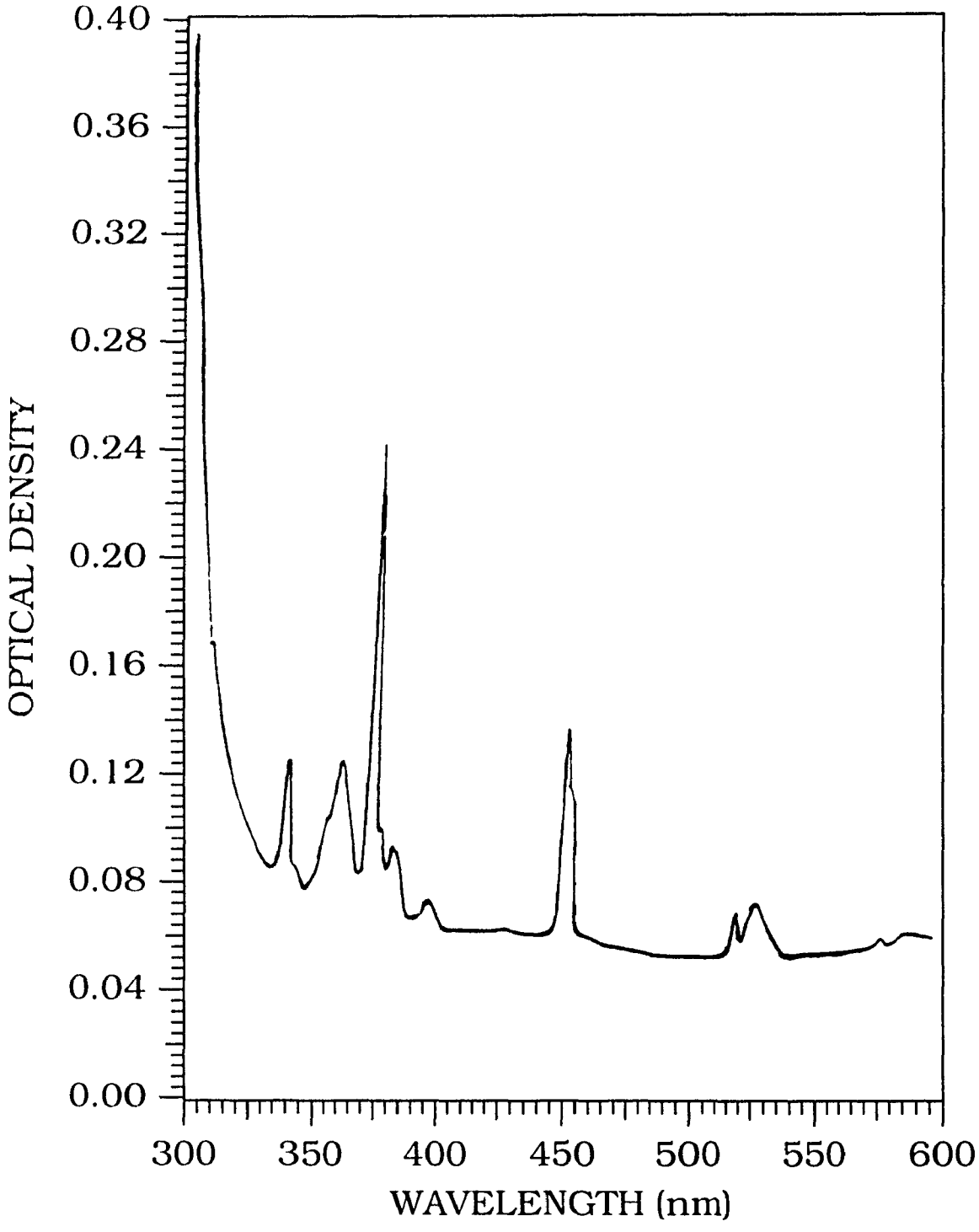

Figure 5.2.2.1.1a Uncorrected room-temperature absorption spectrum of the experimental $Na_2O{\cdot}2SiO_2{:}Eu^{3+}$ glass.

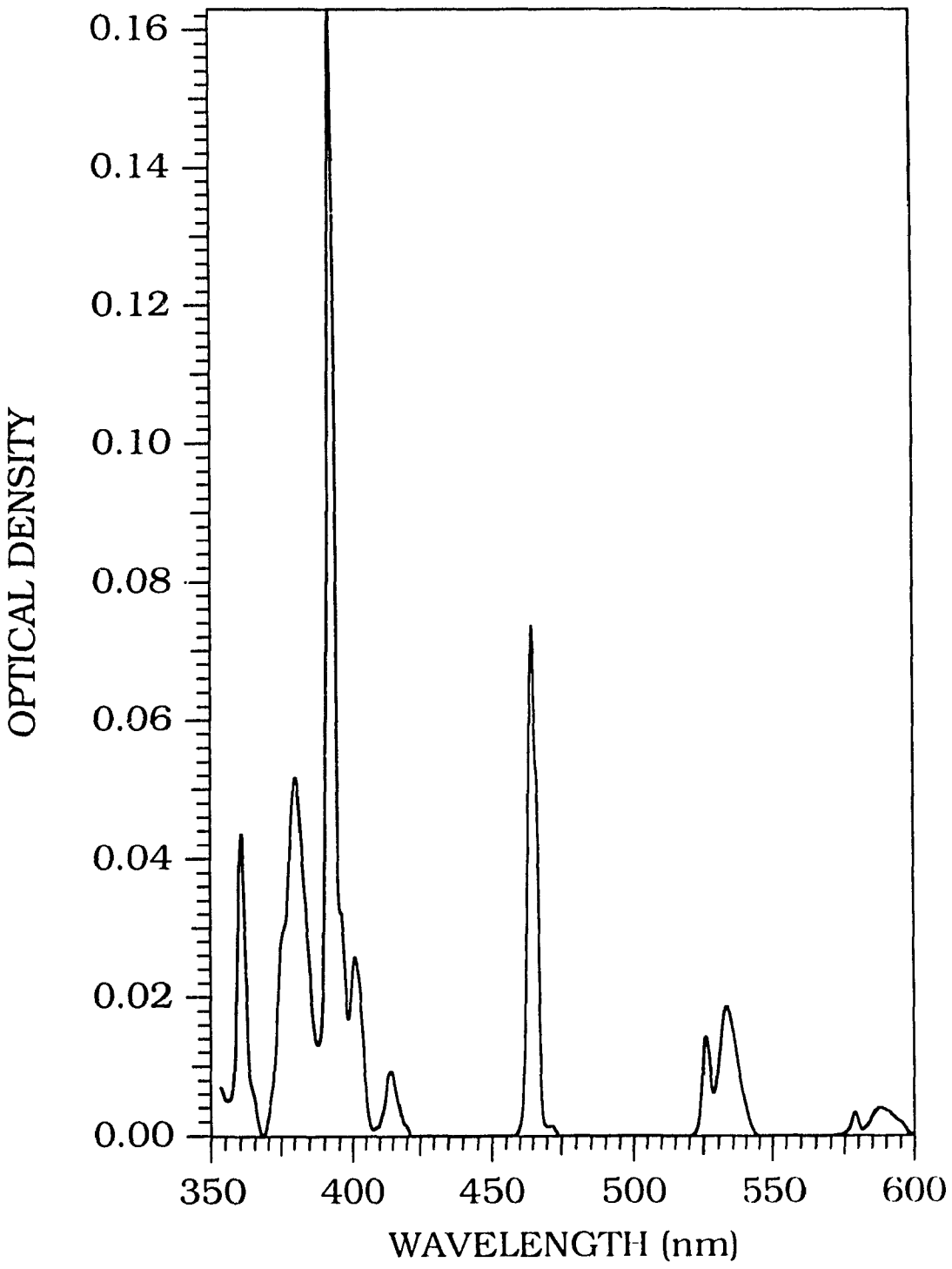

Figure 5.2.2.1.1b Corrected room-temperature absorption spectrum of the experimental $Na_2O{\cdot}2SiO_2{:}Eu^{3+}$ glass.

the observation of absorption bands with transitional energies higher than 28000 cm $^{-1}$ (≈ 350 nm).

The position of the observed transition barycentres, together with band assignments are presented in Table 5.2.2.1.1. The transition energies found for this glass are similar to those reported for the Eu^{3+} ion doped in various oxide glasses [23,42,44,48]. The assignment of bands in the 25000 cm^{-1} (and higher) region, is difficult because of the presence of many electronic manifolds which are thoroughly mixed. A low-temperature study, which would eliminate transitions arising from the thermally populated $^7F_1$ state, and limit homogeneous broadening (due to thermal phonons) should render the identification of these bands possible. This has not been done due to experimental limitations.

The experimental oscillator strengths have been calculated using equation 3.1.4.6. In order to do this calculation, the integrated absorption coefficients had to be determined from the absorption spectrum. This is done by converting the absorption spectrum such that the abscissa has units of frequency (s^{-1}) and the ordinate has units of absorption coefficient (cm^{-1}) followed by the determination of the area under each absorption curve. The results of this calculation are presented in Table 5.2.2.1.2. These results are comparable to those reported for various Eu^{3+}-doped silicate glasses [141,142].

Figure 5.2.2.1.2 shows a comparison between the absorption spectrum of the laboratory glass and that for the simulated $Na_2O{\cdot}2SiO_2{:}Eu^{3+}$ glass, in the region between 350 and 600nm. The

TABLE 5.2.2.1.1

ROOM-TEMPERATURE ABSORPTION BARYCENTRES AND LINEWIDTHS OF THE EXPERIMENTAL $Na_2O{\cdot}2SiO_2{:}Eu^{3+}$ GLASS

Assignment	Barycentre (cm^{-1})	FWHM (cm^{-1})
$^5D_0 \leftarrow ^7F_1$	16978†	321†
$^5D_0 \leftarrow ^7F_0$	17275	88
$^5D_1 \leftarrow ^7F_1$	18758	260
$^5D_1 \leftarrow ^7F_0$	19008	94
$^5D_2 \leftarrow ^7F_1$	21189	a
$^5D_2 \leftarrow ^7F_0$	21523	230
$^5D_3 \leftarrow ^7F_1$	24143	280
$^5L_6 \leftarrow ^7F_1$	24925 25242	a
$^5L_6 \leftarrow ^7F_0$	25450	191
$^5L_7 \leftarrow ^7F_1$	26021	a
$^5L_7 \leftarrow ^7F_0$	26281	614
$^5G_{4,5,6} \leftarrow ^7F_0$	26653	a
$^5D_4 \leftarrow ^7F_1$	27405	a
$^5D_4 \leftarrow ^7F_0$	27730	238

† Since the absorption spectrum was not continued past 600nm, this band is incomplete. Therefore the values presented are not exact.

(a) indicates a shoulder.

TABLE 5.2.2.1.2

EXPERIMENTAL OSCILLATOR STRENGTHS DERIVED FROM THE ROOM-TEMPERATURE ABSORPTION SPECTRUM OF THE EXPERIMENTAL $Na_2O{\cdot}2SiO_2{:}Eu^{3+}$ GLASS

Assignment	Area ($cm^{-1}s^{-1}$)	f ($\times 10^{-7}$)
$^5D_0 \leftarrow ^7F_1$	1.70×10^{11}	0.11
$^5D_0 \leftarrow ^7F_0$	4.83×10^{10}	0.03
$^5D_1 \leftarrow ^7F_1$	7.41×10^{11}	0.46
$^5D_1 \leftarrow ^7F_0$	2.39×10^{11}	0.15
$^5D_2 \leftarrow ^7F_1$	4.80×10^{10}	0.03
$^5D_2 \leftarrow ^7F_0$	1.95×10^{12}	1.21
$^5D_3 \leftarrow ^7F_1$	4.60×10^{11}	0.29
$^5L_6 \leftarrow ^7F_1$	a	a
$^5L_6 \leftarrow ^7F_0$	5.64×10^{12}	3.46
$^5L_7 \leftarrow ^7F_1$	1.64×10^{12}	1.01
$^5L_7 \leftarrow ^7F_0$	3.28×10^{12}	2.01
$^5G_{4,5,6} \leftarrow ^7F_0$	a	a
$^5D_4 \leftarrow ^7F_1$	a	a
$^5D_4 \leftarrow ^7F_0$	1.67×10^{12}	1.02

(a) cannot be calculated since this is a shoulder.

simulated absorption spectrum shows only the $^5L_6$, $^5D_3$, $^5D_2$, $^5D_1$, $^5D_0 \leftarrow {}^7F_{0,1}$ transitions. These levels possess energies below 25000 cm $^{-1}$, this being the limit where energy-levels are still uncomplicated by extraneous mixing. Because of complications arising from the calculation of crystal-field split J-levels, we have limited our simulation to only these levels.

The relative population of the $^7F_0$ and $^7F_1$ manifolds was taken into account in the simulated absorption spectrum by calculating the Boltzmann distribution at a temperature of 300K and by scaling the intensity parameter (equations 4.4.3 and 4.4.4b) of each calculated line to-line transition accordingly. The simulated absorption lineshape is seen to reproduce well the features of the experimental spectrum. The relative intensities of both the simulated and experimental spectra are also shown to be in complete agreement with the predicted allowedness, derived from the electric- and magnetic-dipole selection rules, as presented in Table 3.1.3.1.

A comparison between (i) the position of the barycentres, (ii) widths and (iii) oscillator strengths of the simulated and experimental absorption spectra is presented in Table 5.2.2.1.3. The scaling factors of equation (4.4.4b) are also found in Table 5.2.2.1.3. These factors were chosen such that (i) the relative intensities of the simulated manifolds approximate those of the experimental manifolds, and (ii) the simulated oscillator strength (equation 3.1.4.6) of the $^5D_2 \leftarrow {}^7F_0$ transition is equal to that of the experimental transition. The $^5D_2 \leftarrow {}^7F_0$ transition was specifically chosen because of its relatively high optical density and

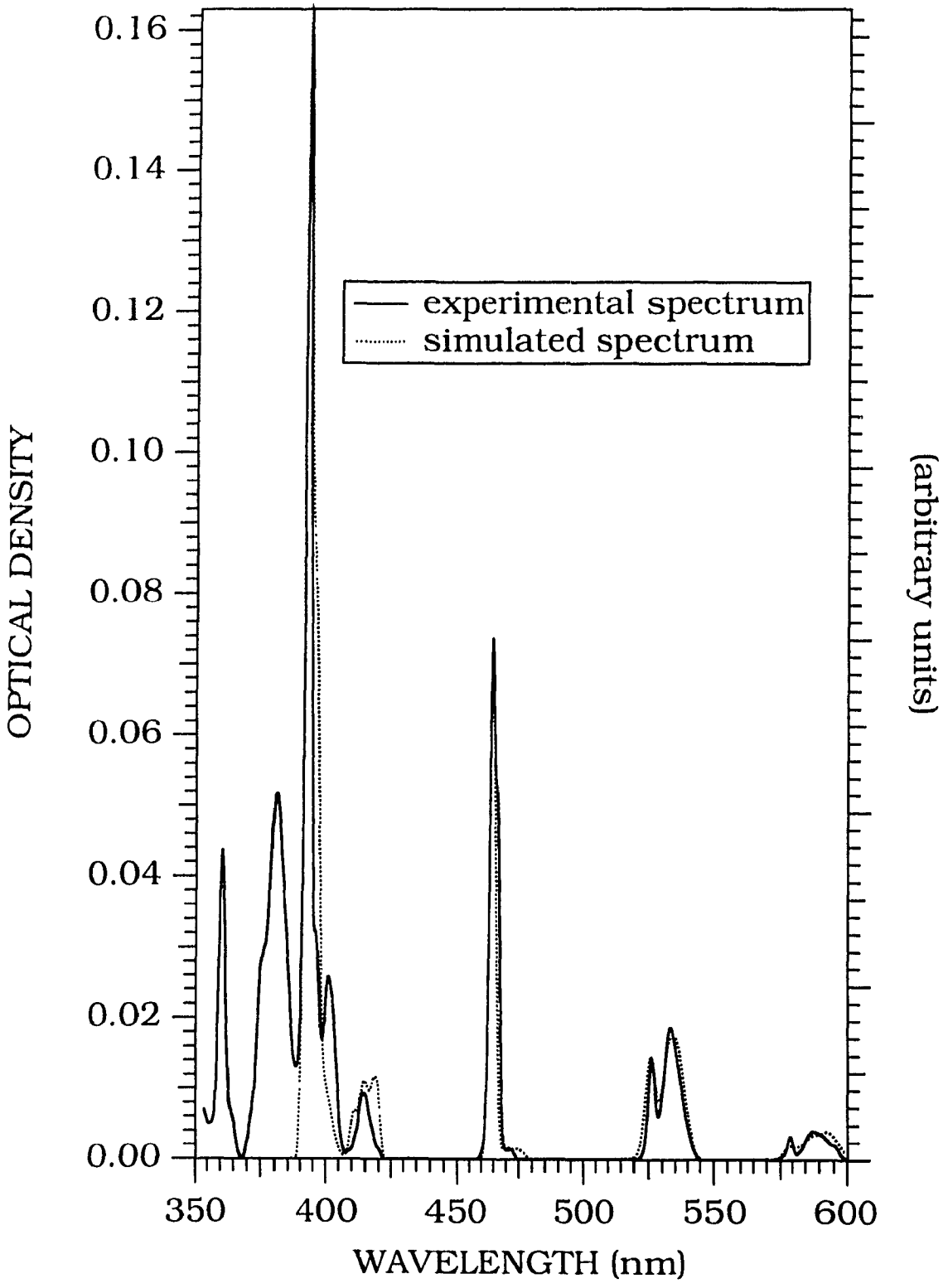

Figure 5.2.2.1.2 Comparison between the room-temperature absorption spectrum of the experimental and simulated $Na_2O{\cdot}2SiO_2{:}Eu^{3+}$ glasses.

TABLE 5.2.2.1.3

ABSORPTION BARYCENTRES, LINEWIDTHS AND OSCILLATOR STRENGTHS OF THE EXPERIMENTAL AND SIMULATED $Na_2O{\cdot}2SiO_2:Eu^{3+}$ GLASSES[a]

	$Na_2O{\cdot}2SiO_2:Eu^{3+}$ Experimental glass			$Na_2O{\cdot}2SiO_2:Eu^{3+}$ Simulated glass			
	Bary-centre (cm^{-1})	FWHM (cm^{-1})	f ($\times 10^{-7}$)	Bary-centre (cm^{-1})	FWHM (cm^{-1})	f ($\times 10^{-7}$)	Scaling factors (b)
$^5D_0 \leftarrow {}^7F_1$	16978	321	0.105	16901	328	0.064	1.32
$^5D_0 \leftarrow {}^7F_0$	17275	88	0.030	17282	102	0.028	1.32
$^5D_1 \leftarrow {}^7F_1$	18758	260	0.459	18704	236	0.253	1.32
$^5D_1 \leftarrow {}^7F_0$	19008	94	0.148	19008	150	0.209	1.32
$^5D_2 \leftarrow {}^7F_1$	21189	(c)	0.030	21144	(c)	0.029	1.32
$^5D_2 \leftarrow {}^7F_0$	21523	230	1.207	21528	120	1.212	1.32
$^5D_3 \leftarrow {}^7F_1$	24143	280	0.285	24128	372	0.227	4.42
$^5D_3 \leftarrow {}^7F_0$	-------	-------	-------	24436	(c)	0.067	4.42
$^5L_6 \leftarrow {}^7F_1$	(d)	(d)	(d)	25076	(c)	0.233	4.62
$^5L_6 \leftarrow {}^7F_0$	25450	191	3.494	25444	212	5.624	4.62

(a) Only the electronic transitions which have been simulated are reported.

(b) Factors defined in equation (4.4.4b).

(c) indicates a shoulder.

(d) the presence of other transitions interferes with the identification of this band.

because it is situated in a region free from interfering transitions. The scaling factors for transitions to the three lowest excited-states are close to unity, whereas factors for the two highest excited-states (the $^5D_3$ and $^5L_6$) are approximately 4.5. The higher scaling factors in the latter case might be due to the presence of several transitions, in the region between 24000 and 27000 cm^{-1}, which were not taken into account in the calculation. Because of broadening and overlap these unaccounted transitions will lend some intensity to the experimental transitions, forcing the overcompensation of the intensities of these transitions calculated for the sake of comparison.

5.2.2.2 Broadband emission spectrum

The room temperature emission spectrum of the experimental $Na_2O{\cdot}2SiO_2{:}Eu^{3+}$ glass (sample "A") is presented in Figures 5.2.2.2.1 and 5.2.2.2.2. The spectrum was excited at 514.5 nm, which corresponds to an energy greater than that necessary to directly excite the $^5D_1 \leftarrow {}^7F_0$ absorption band. At this wavelength, it is expected that the full ensemble of Eu^{3+} ions will be excited. Figure 5.2.2.2.1 presents the entire $^5D_0 \rightarrow {}^7F_J$ (J=0-6). The inset shows in greater detail the $^5D_0 \rightarrow {}^7F_{4,5,6}$ region. Figure 5.2.2.2.2 presents the $^5D_0 \rightarrow {}^7F_{0,1,2}$ region. The full Stark splitting of the $^5D_0 \rightarrow {}^7F_{1,2}$ emissions is observed, confirming the low site symmetry of the Eu^{3+} in this glass.

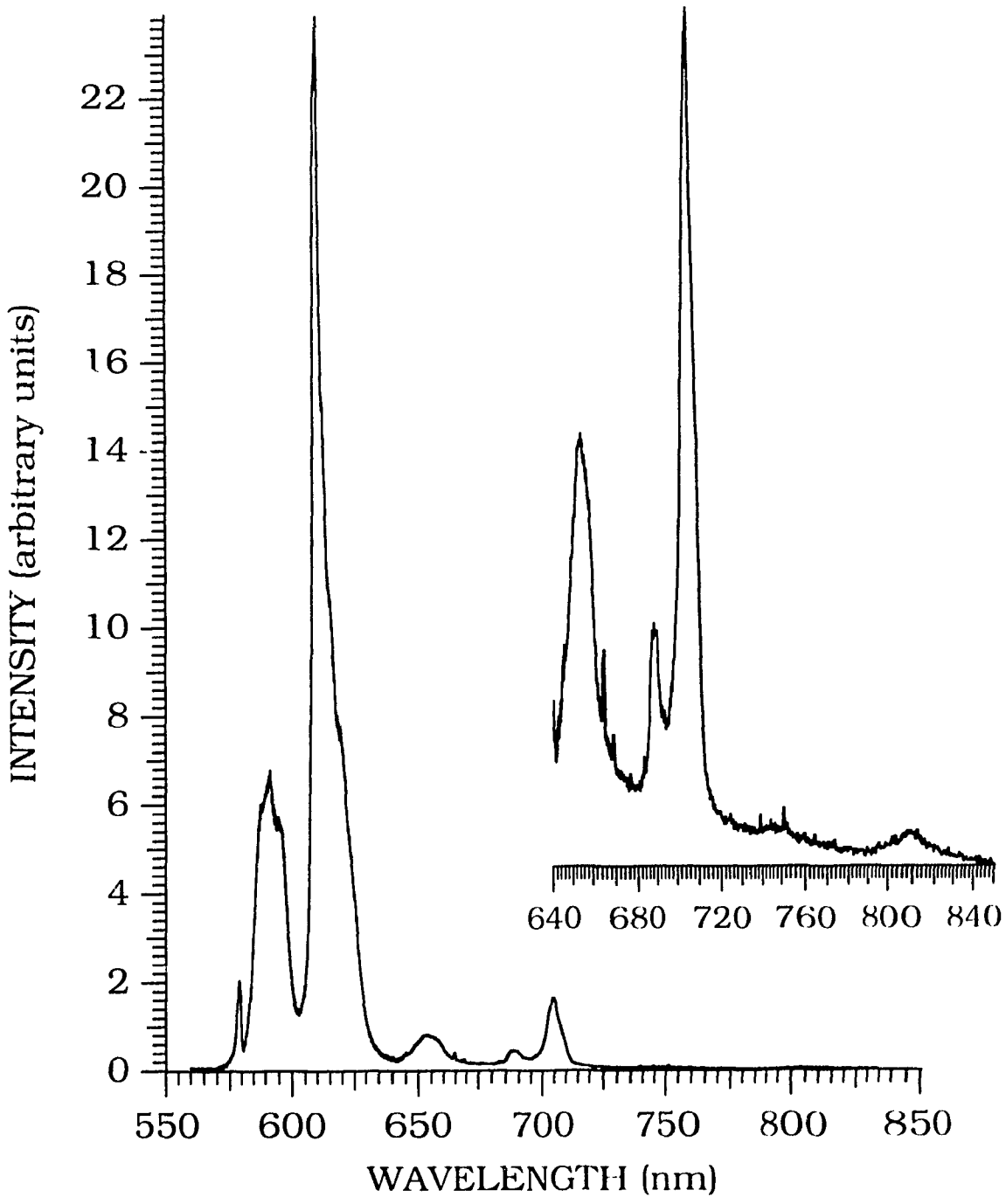

Figure 5.2.2.2.1 Broadband room-temperature emission spectrum of the $^5D_0 \rightarrow {}^7F_J$ (J=0-6) region of the experimental $Na_2O{\cdot}2SiO_2{:}Eu^{3+}$ glass. The excitation wavelength is λ_{exc} = 514.5 nm. The inset shows details of the $^5D_0 \rightarrow {}^7F_{3,4,5,6}$ region.

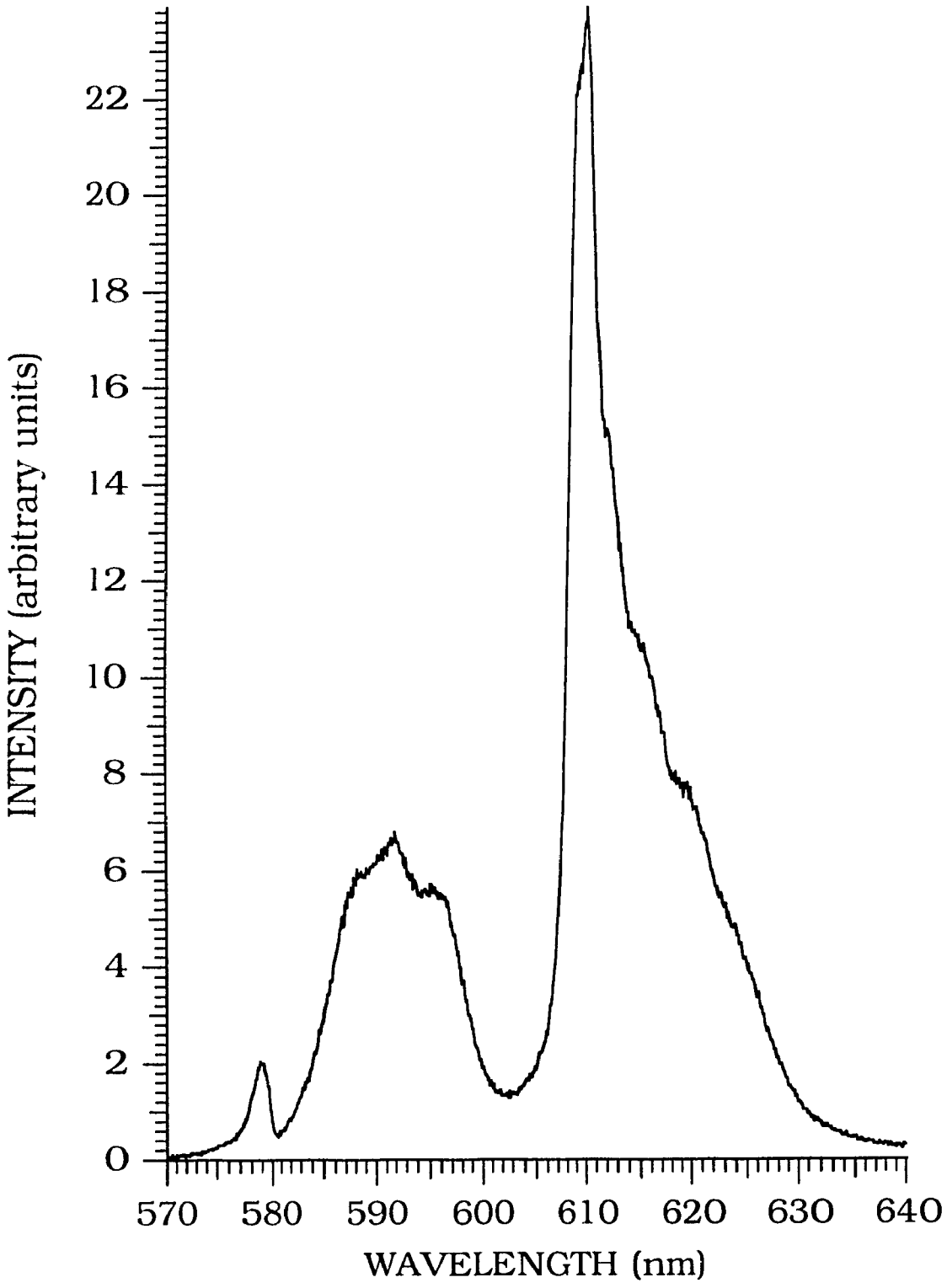

Figure 5.2.2.2.2 Broadband room-temperature emission spectrum of the $^5D_0 \rightarrow {}^7F_{0,1,2}$ region of the experimental $Na_2O{\cdot}2SiO_2{:}Eu^{3+}$ glass. The excitation wavelength is λ_{exc} = 514.5 nm.

We find in Table 5.2.2.2.1, band positions, widths and relative intensities for the room-temperature broadband emission spectrum of the experimental $Na_2O{\cdot}2SiO_2{:}Eu^{3+}$ glass. The spectrum and the related parameters are typical of Eu^{3+} doped in oxide glasses [23,46-50, 143]. One point of interest is the observation of the $^5D_0 \rightarrow {}^7F_6$ transition which is usually not seen because of its low branching ratio.

TABLE 5.2.2.2.1
ASSIGNMENTS, POSITIONS,WIDTHS AND RELATIVE INTENSITIES OF BANDS FOR THE ROOM TEMPERATURE EMISSION SPECTRUM OF $Na_2O{\cdot}2SiO_2{:}Eu^{3+}$ GLASS

Assignment	Barycentre (cm^{-1})	FWHM (cm^{-1})	Relative intensities[†]
$^5D_0 \rightarrow {}^7F_0$	17288	75	12.45
$^5D_0 \rightarrow {}^7F_1$	16901	375	48.36
$^5D_0 \rightarrow {}^7F_2$	16314	355	100.00
$^5D_0 \rightarrow {}^7F_3$	15306	285	5.90
$^5D_0 \rightarrow {}^7F_4$	14215 14524	155 100	11.78
$^5D_0 \rightarrow {}^7F_5$	(a)	(a)	(a)
$^5D_0 \rightarrow {}^7F_6$	12344	215	0.45

[†]values taken at barycentres.

(a) barely observable transition

Figure 5.2.2.2.3 shows a comparison of the experimental and simulated emission spectrum of the $^5D_0 \rightarrow {}^7F_J$ (J= 0 to 4) transitions for the same glasses. Although they have been calculated, the $^5D_0 \rightarrow {}^7F_{5,6}$ transitions are not shown in this Figure for reasons of clarity.

We find in Table 5.2.2.2.2, a comparison of band positions, widths and relative intensities for the simulated and experimental room temperature emission spectra for the $Na_2O{\cdot}2SiO_2{:}Eu^{3+}$ glasses. The scaling factors of equation (4.4.4 a) are also found in Table 5.2.2.2.2. Overall, a good qualitative agreement has been obtained for the positions and energy splittings of the simulated emission transitions. It is evident that discrepancies arise between the laboratory and simulated emission spectra. The most probable reason is due to the fact that we are simulating a "*static*" spectrum. We have considered the amorphous environment as merely supplying a static average electrostatic field. Any dynamic process [144] which occurs in the laboratory sample, such as ion-lattice coupling (vibronic coupling) or ion-ion coupling (energy transfer), which affect specific aspects of the laboratory spectrum will necessarily be missing from the simulated spectrum. For example, Tables 5.2.2.1.3 and 5.2.2.2.2 show the presence of a Stokes shift between the experimental $^5D_0 \leftarrow {}^7F_0$ absorption and $^5D_0 \rightarrow {}^7F_0$ emission transitions. Since we have not included a vibronic coupling term in the perturbation Hamiltonian, we are evidently not able to simulate such effects as Stokes shifts or vibronic sidebands.

The model we present here fails in reproducing accurately the $^5D_0 \rightarrow {}^7F_2$ transition. As seen in Figure 5.2.2.2.3, the overall intensity of

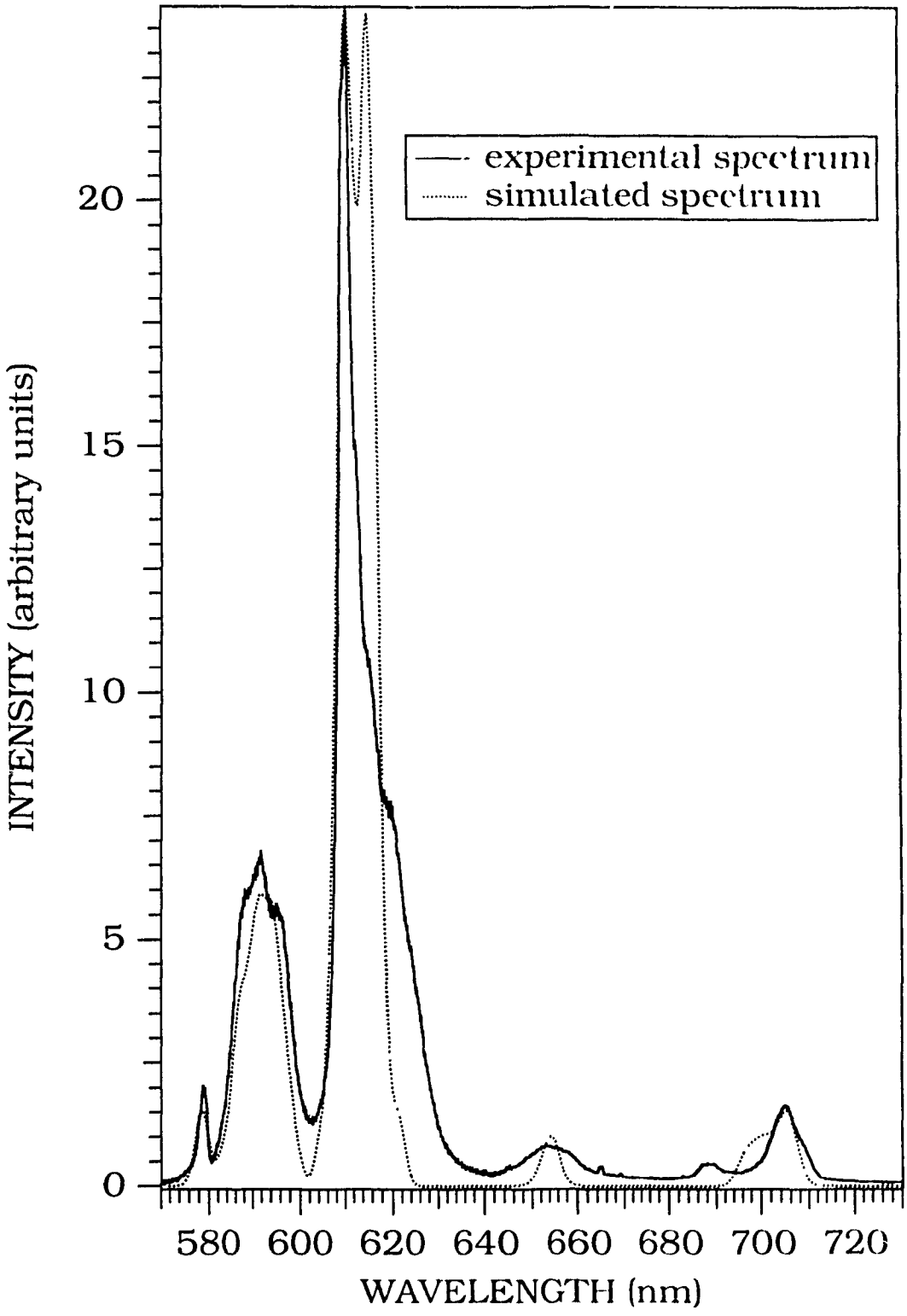

Figure 5.2.2.2.3 Comparison between the room-temperature emission spectrum of the experimental and simulated $Na_2O{\cdot}2SiO_2{:}Eu^{3+}$ glasses.

TABLE 5.2.2.2.2

EMISSION BARYCENTRES† AND LINEWIDTHS OF THE EXPERIMENTAL AND SIMULATED $Na_2O{\cdot}2SiO_2:Eu^{3+}$ GLASSES

	$Na_2O{\cdot}2SiO_2:Eu^{3+}$ Experimental glass		$Na_2O{\cdot}2SiO_2:Eu^{3+}$ Simulated glass		
	Bary-centre (cm^{-1})	FWHM (cm^{-1})	Bary-centre (cm^{-1})	FWHM (cm^{-1})	Scaling factors[a]
$^5D_0 \rightarrow {}^7F_0$	17288	75	17282	102	5.5
$^5D_0 \rightarrow {}^7F_1$	16901	375	16901	328	2.0
$^5D_0 \rightarrow {}^7F_2$	16314	355	16328	272	1.0
$^5D_0 \rightarrow {}^7F_3$	15306	285	15289	114	1.1
$^5D_0 \rightarrow {}^7F_4$	{ 14215 / 14524 }	{ 155 / 100 }	14233	254	1.0
$^5D_0 \rightarrow {}^7F_5$	(a)	(b)	13352	224	5.0
$^5D_0 \rightarrow {}^7F_6$	12344	215	12349	148	0.07

(a) Factors defined in equation (4.4.4 a)

(b) barely observable transition

† The barycentres were determined by calculating the surface of the bands then by finding the energies where the values of the surfaces were halved.

the simulated $^5D_0 \rightarrow {}^7F_2$ transition is adequate, but we were not able to reproduce the observed intensity distribution of the five Stark components of this transition. The five components of the experimental $^5D_0 \rightarrow {}^7F_2$ transition are situated at 15982, 16107, 16255, 16385 and 16410 cm^{-1}. To obtain the barycentre positions of each component, the spectra were deconvoluted using a Gaussian band least-squares minimization routine which employs a Marquardt algorithm [124,145]. It is clear that these five components have very different transition probabilities and thus, contribute to the appreciable asymmetry of the $^5D_0 \rightarrow {}^7F_2$ transition. The simulated $^5D_0 \rightarrow {}^7F_2$ transition only shows three distinct components with unexpected relative intensities. The first, found at 16088 cm^{-1}, corresponds to the 16107 cm^{-1} component of the experimental transition. The second, found at 16256 cm^{-1}, corresponds to the 16255 cm^{-1} component of the experimental transition. The third component, found at 16388 cm^{-1}, corresponds to the 16385 and 16410cm^{-1} components of the experimental transition.

One possible explanation for the apparent absence of certain energy components is the likelihood of other radiative transitions appearing in the same energy range of the experimental spectrum. The presence of $^5D_1 \rightarrow {}^7F_4$ transition components within the same energy range as the $^5D_0 \rightarrow {}^7F_2$ manifold has been observed in various solid state hosts [146]. Nevertheless, it is very unlikely that radiative $^5D_1 \rightarrow {}^7F_4$ transitions appear in the experimental emission spectrum because of the presence of very efficient multiphonon processes in silicate glasses [147], which will induce non-radiative $^5D_1 \rightarrow {}^5D_0$ transitions.

TABLE 5.2.2.2.2

EMISSION BARYCENTRES[†] AND LINEWIDTHS OF THE EXPERIMENTAL AND SIMULATED $Na_2O{\cdot}2SiO_2:Eu^{3+}$ GLASSES

	$Na_2O{\cdot}2SiO_2:Eu^{3+}$ Experimental glass		$Na_2O{\cdot}2SiO_2:Eu^{3+}$ Simulated glass		
	Bary-centre (cm^{-1})	FWHM (cm^{-1})	Bary-centre (cm^{-1})	FWHM (cm^{-1})	Scaling factors[a]
$^5D_0 \rightarrow {}^7F_0$	17288	75	17282	102	5.5
$^5D_0 \rightarrow {}^7F_1$	16901	375	16901	328	2.0
$^5D_0 \rightarrow {}^7F_2$	16314	355	16328	272	1.0
$^5D_0 \rightarrow {}^7F_3$	15306	285	15289	114	1.1
$^5D_0 \rightarrow {}^7F_4$	14215 14524	155 100	14233	254	1.0
$^5D_0 \rightarrow {}^7F_5$	(a)	(b)	13352	224	5.0
$^5D_0 \rightarrow {}^7F_6$	12344	215	12349	148	0.07

(a) Factors defined in equation (4.4.4 a)

(b) barely observable transition

[†] The barycentres were determined by calculating the surface of the bands then by finding the energies where the values of the surfaces were halved.

the simulated $^5D_0 \rightarrow {}^7F_2$ transition is adequate, but we were not able to reproduce the observed intensity distribution of the five Stark components of this transition. The five components of the experimental $^5D_0 \rightarrow {}^7F_2$ transition are situated at 15982, 16107, 16255, 16385 and 16410 cm^{-1}. To obtain the barycentre positions of each component, the spectra were deconvoluted using a Gaussian band least-squares minimization routine which employs a Marquardt algorithm [124, 145]. It is clear that these five components have very different transition probabilities and thus, contribute to the appreciable asymmetry of the $^5D_0 \rightarrow {}^7F_2$ transition. The simulated $^5D_0 \rightarrow {}^7F_2$ transition only shows three distinct components with unexpected relative intensities. The first, found at 16088 cm^{-1}, corresponds to the 16107 cm^{-1} component of the experimental transition. The second, found at 16256 cm^{-1}, corresponds to the 16255 cm^{-1} component of the experimental transition. The third component, found at 16388 cm^{-1}, corresponds to the 16385 and 16410cm^{-1} components of the experimental transition.

One possible explanation for the apparent absence of certain energy components is the likelihood of other radiative transitions appearing in the same energy range of the experimental spectrum. The presence of $^5D_1 \rightarrow {}^7F_4$ transition components within the same energy range as the $^5D_0 \rightarrow {}^7F_2$ manifold has been observed in various solid-state hosts [146]. Nevertheless, it is very unlikely that radiative $^5D_1 \rightarrow {}^7F_4$ transitions appear in the experimental emission spectrum because of the presence of very efficient multiphonon processes in silicate glasses [147], which will induce non-radiative $^5D_1 \rightarrow {}^5D_0$ transitions.

Disregarding the disparity in transition energies, the main problem still lies in the relative intensities of the various components of this simulated transition. In their theoretical treatment of the Eu^{3+} emission spectrum in $Na_3[Eu(oxydiacetate)_3]\cdot 2NaClO_4\cdot 6H_2O$, Morley *et al.* [148] observed that their calculations failed to account for the intensity distribution observed for the $^5D_0 \rightarrow {}^7F_2$ transition. They stated that the most likely explanation was found in an analysis of the dynamic coupling model[6] reported by Kuroda *et al.* [149,150]. Electrostatic interactions between the trivalent lanthanide ion and its surrounding environment can be divided into two categories. The first, static-coupling, represents electrostatic interactions between the metal ion multipoles and the net charges of the ligand atoms. Only the ligand charges and atomic coordinates are used in this scheme. The second, dynamic-coupling, represents electrostatic interactions between the metal ion multipoles and the multipoles of the ligand charge distribution. Isotropic ligand polarizabilities and atomic coordinates are normally used in this second scheme. Kuroda *et al.* concluded that the presence of dynamic coupling and in particular the inclusion of ligand polarizability anisotropy was essential for the proper calculation of the electric dipole intensity distribution of transitions which exhibit quadrupole (Eu^{3+}) - dipole (ligand) coupling mechanisms, such as the $^5D_0 \rightarrow {}^7F_2$ transition. According to the ligand polarization mechanism, *f-f* transitions attain an electric-dipole moment through a Coulombic correlation of the dipoles induced in each ligand atom by the potential of

[6] It has been shown by Judd [151], that the dynamic coupling model is formally identical to a mechanism based on an inhomogeneous dielectric medium surrounding the rare earth ion.

the electric-multipole moment of the metal-ion transition. The induced dipoles are proportional to the components of the electric dipole polarizability tensor of each of the ligands. If anisotropy of the ligand polarizability is taken into account, non-vanishing matrix elements for the electric-dipole strength can appear, modifying the spectral features of the transition.

In the present study, only the static coupling scheme has been implemented in the calculation of the electric dipole strengths. It is evident that the inclusion of the dynamic coupling scheme, including ligand polarizability anisotropy, should resolve any discrepancies for transitions with an important electric quadrupole character.

Overall, a good qualitative agreement has been obtained for the positions and energy splittings of the simulated absorption and emission transitions. Also, there is very good quantitative agreement between the experimental and calculated oscillator strengths.

5.2.2.3 Fluorescence Line Narrowing

To date, laser-induced Fluorescence Line Narrowing (FLN) has been extensively used in an attempt to extract relevant spectra-structure correlations of doped inorganic glasses. In this section, we shall present FLN emission, excited via the $^5D_0 \leftarrow {}^7F_0$ transition, of the laboratory $Na_2O{\cdot}2SiO_2{:}Eu^{3+}$ glass. A phenomenological crystal-field analysis will be conducted and the results will be analysed using Brecher and Riseberg's model [50,51] which was introduced in section 1.2.2. We shall then turn

our attention to the structural and spectroscopic models discussed in the previous sections of Chapter 5 and attempt to recreate the FLN spectra.

FLN measurements have been performed, at liquid nitrogen temperatures (T=77K), on the experimental $Na_2O{\cdot}2SiO_2{:}Eu^{3+}$ glass (sample "A"). Twelve different emission spectra, of the $^5D_0 \rightarrow {}^7F_{1,2}$ region, have been measured using different excitation wavelengths within the inhomogeneously broadened $^5D_0 \leftarrow {}^7F_0$ absorption band. Each of these spectra corresponds to the fluorescence of a given subset of energetically equivalent "sites" whose homogeneous absorption exactly coincides with the wavelength of the exciting radiation. The spectra are shown in Figures 5.2.2.3.1 (a) through (d). These spectra are comparable with those reported in various other oxide systems [47-50,152], yet show distinct features usually not present in other systems.

Qualitatively, the FLN spectra show resolvable Stark components for both the $^5D_0 \rightarrow {}^7F_1$ (3 components) and $^5D_0 \rightarrow {}^7F_2$ (5 components) transitions. The barycentre positions of each component were obtained by deconvoluting the spectra using a Gaussian band least-squares minimization routine which employs a Marquardt algorithm [124,145]. The energies of the Stark components of the $^7F_1$ and $^7F_2$ multiplets are presented in Table 5.2.2.3.1 The calculated Stark levels presented in Table 5.2.2.3.1 were determined from a simple point-charge crystal-field calculation [153] based on the operator-equivalent method developed by Stevens [41]. A C_{2v} point symmetry was used for reasons detailed in Section 5.2.1.2. The calculation is done in two distinct steps. Firstly,

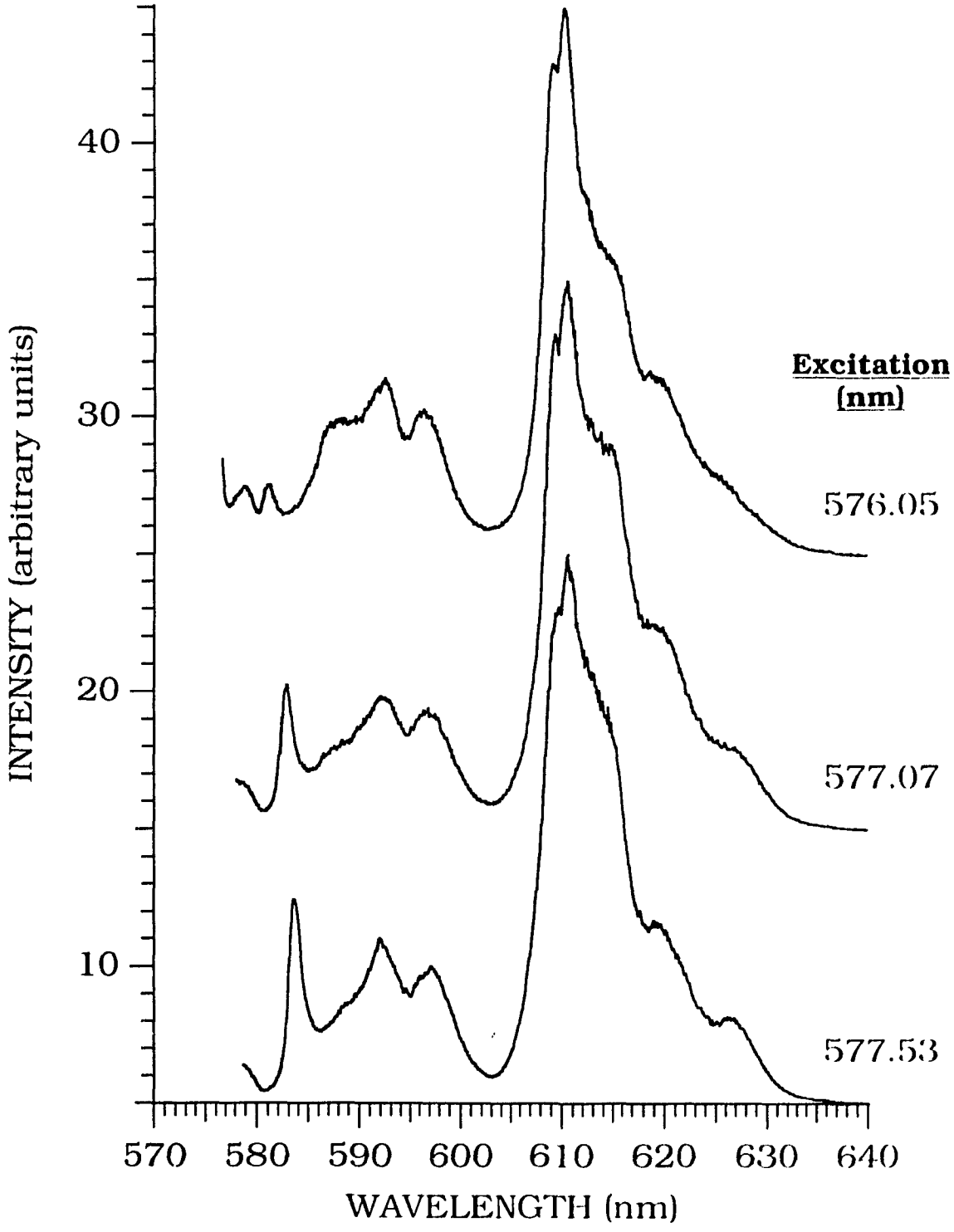

Figure 5.2.2.3.1a Emission spectra of the $Na_2O{\cdot}2SiO_2{:}Eu^{3+}$ glass at 77K excited at various wavelengths within the $^5D_0 \leftarrow {}^7F_0$ absorption band. Excitation wavelengths : 576.05, 577.07, 577.53 nm.

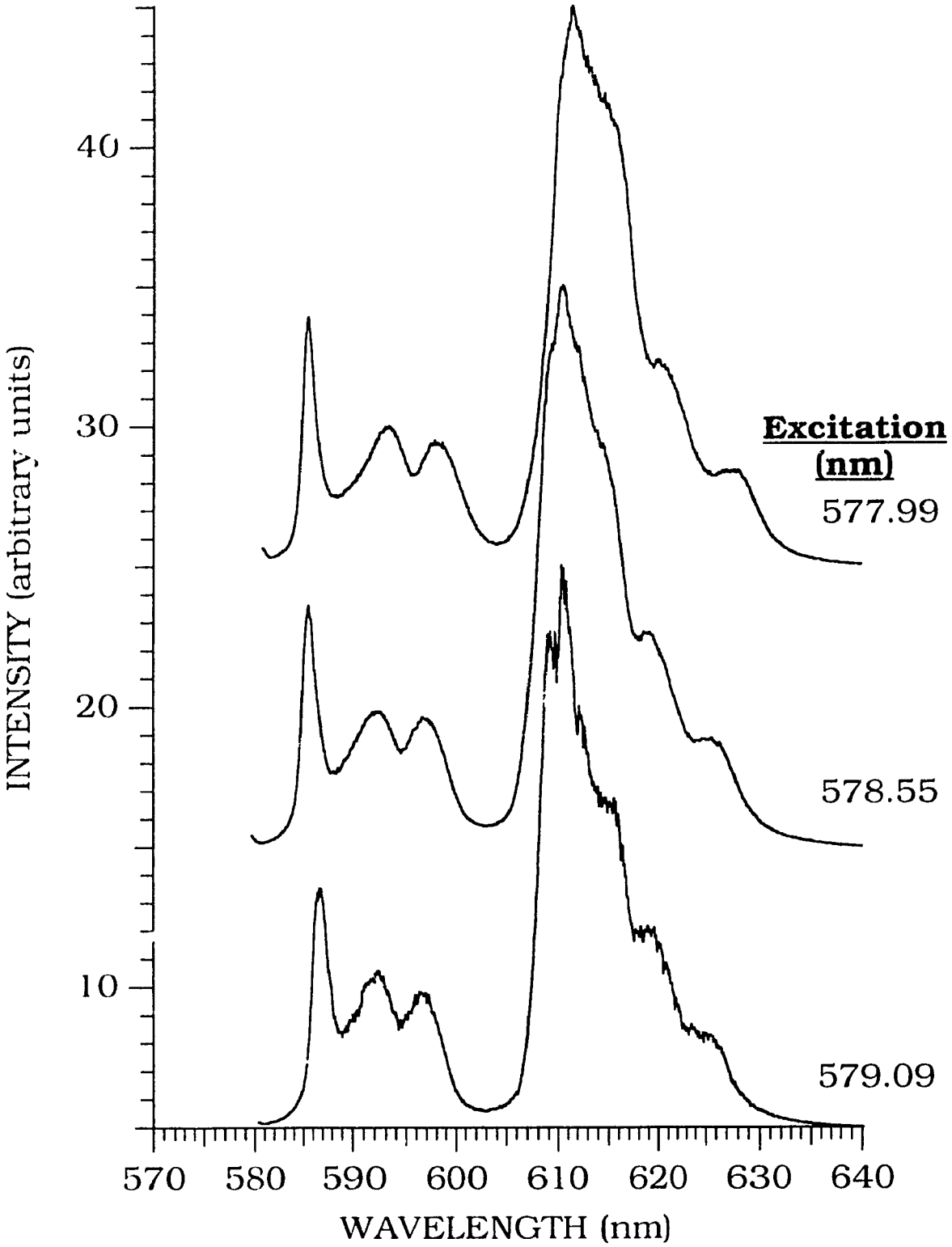

Figure 5.2.2.3.1b Emission spectra of the $Na_2O{\cdot}2SiO_2{:}Eu^{3+}$ glass at 77K excited at various wavelengths within the $^5D_0 \leftarrow {}^7F_0$ absorption band. Excitation wavelengths : 577.99, 578.55, 579.09 nm.

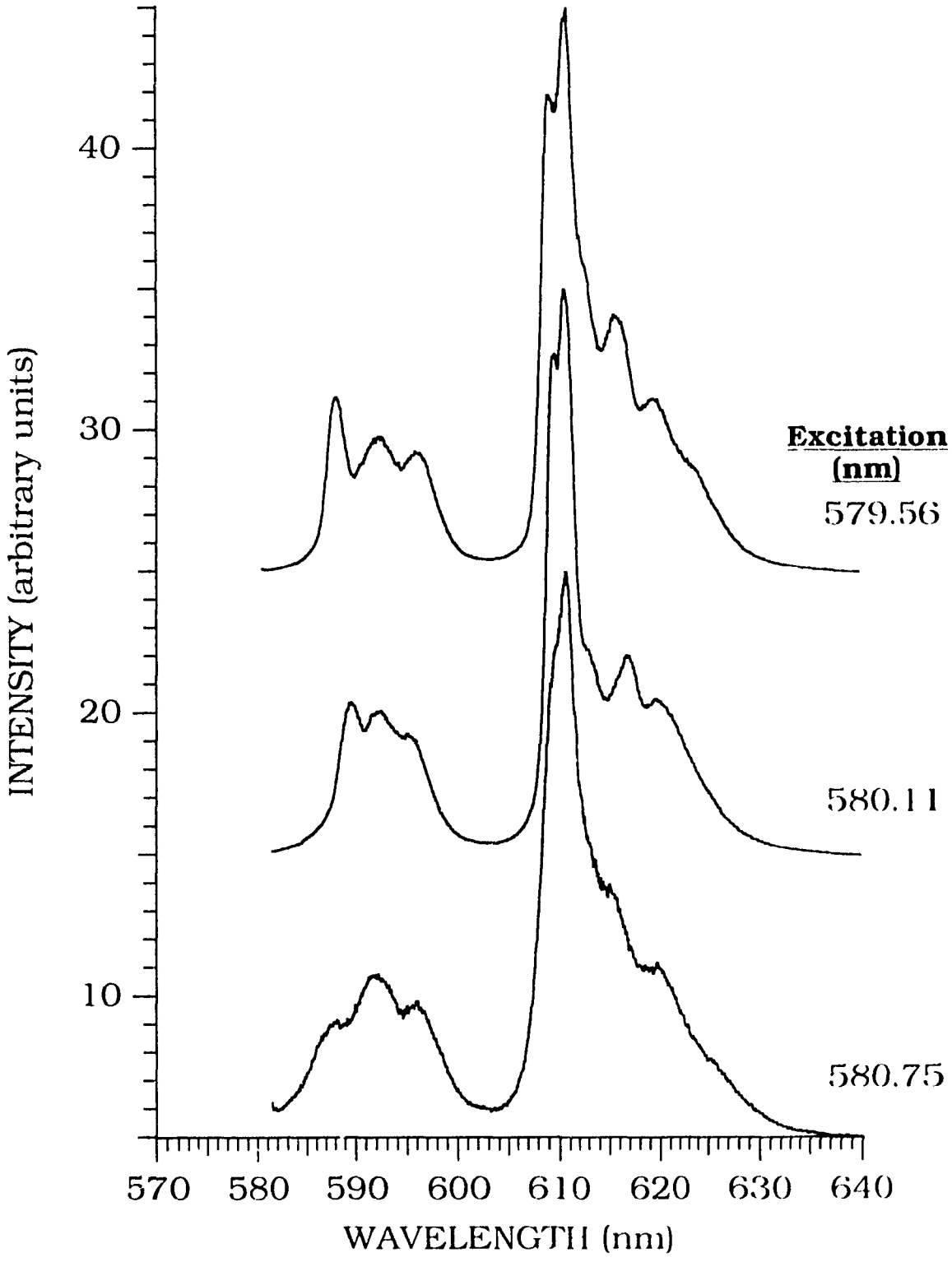

Figure 5.2.2.3.1c Emission spectra of the $Na_2O{\cdot}2SiO_2{:}Eu^{3+}$ glass at 77K excited at various wavelengths within the $^5D_0 \leftarrow {}^7F_0$ absorption band. Excitation wavelengths : 579.56, 580.11, 580.75 nm.

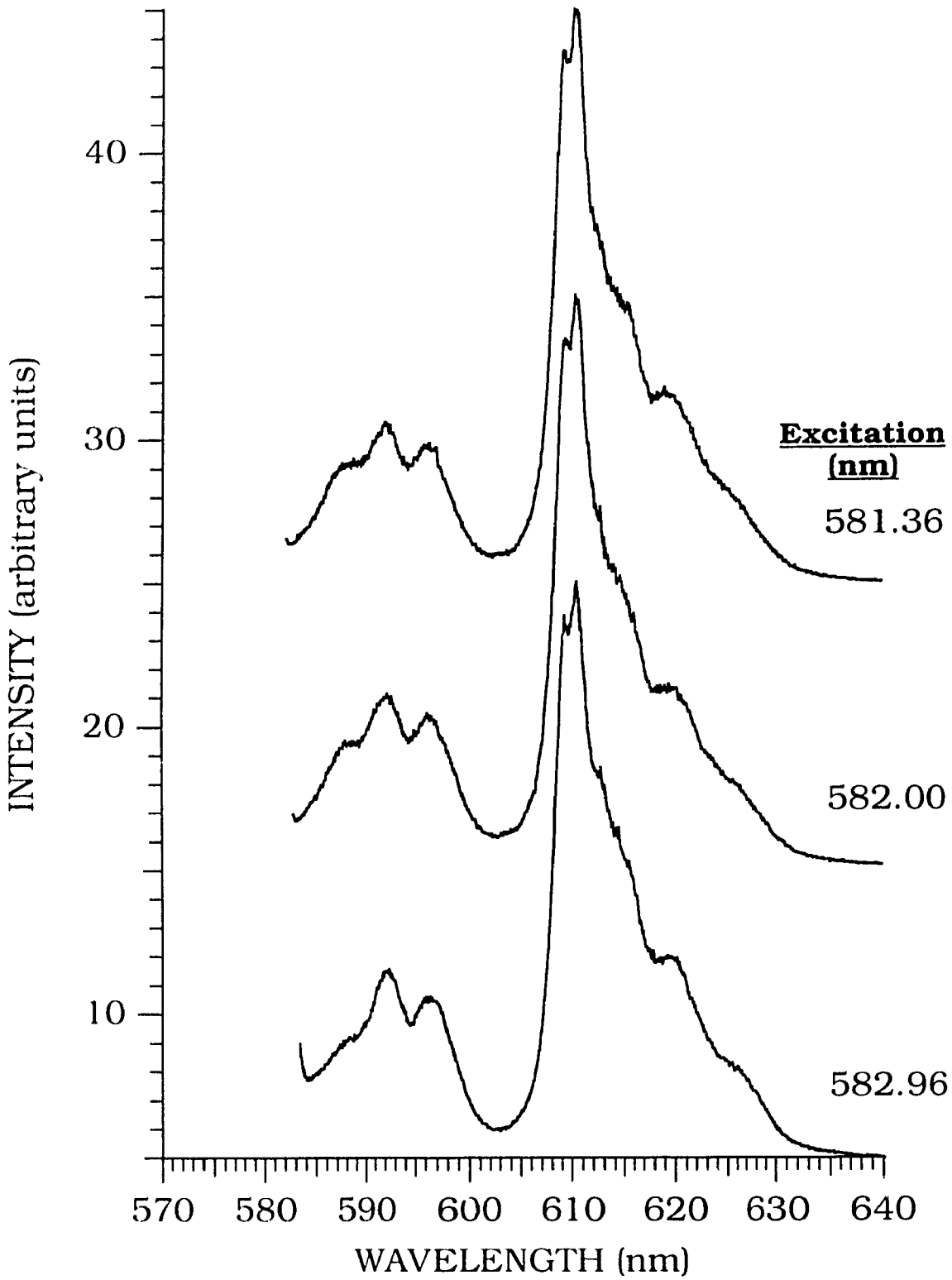

Figure 5.2.2.3.1d Emission spectra of the $Na_2O{\cdot}2SiO_2{:}Eu^{3+}$ glass at 77K excited at various wavelengths within the $^5D_0 \leftarrow {}^7F_0$ absorption band. Excitation wavelengths : 581.36, 582.00, 582.96 nm.

TABLE 5.2.2.3.1
ENERGY OF THE STARK COMPONENTS OF THE $^7F_1$ AND $^7F_2$
MANIFOLDS AS A FUNCTION OF EXCITATION

Excitation (nm)		**$^7F_1$** (cm^{-1})			**$^7F_2$** (cm^{-1})				
576.05	**obs.**	151	478	600	943	987	1116	1232	1348
	calc.	156	480	594	944	982	1111	1235	1353
577.07	**obs.**	169	442	584	909	973	1082	1204	1369
	calc.	166	439	590	907	978	1087	1201	1364
577.53	**obs.**	181	428	582	898	956	1059	1176	1365
	calc.	175	423	592	895	964	1067	1172	1357
577.99	**obs.**	192	410	578	892	945	1050	1165	1352
	calc.	186	404	580	887	956	1060	1160	1342
578.55	**obs.**	209	394	549	866	939	1028	1134	1310
	calc.	206	389	557	862	946	1034	1132	1303
579.09	**obs.**	225	370	524	844	917	1026	1139	1295
	calc.	223	362	534	837	926	1034	1137	1286
579.56	**obs.**	245	360	486	841	900	1016	1112	1189
	calc.	245	360	486	841	901	1017	1112	1189
580.11	**obs.**	269	349	448	826	891	1023	1098	1175
	calc.	269	347	449	824	892	1024	1098	1174
580.75	**obs.**	191	322	450	800	859	981	1083	1177
	calc.	190	319	454	797	863	984	1082	1173
581.36	**obs.**	196	313	433	784	830	956	1063	1188
	calc.	194	298	449	773	844	969	1061	1174
582.00	**obs.**	168	294	426	767	802	923	1052	1173
	calc.	166	278	444	753	819	938	1051	1157
582.96	**obs.**	176	271	393	737	762	903	1016	1185
	calc.	177	243	420	714	789	925	1017	1159

crystal-field parameters (B_{20}, B_{22}, B_{40}, B_{42}, B_{44}) are calculated by solving equations for the matrix elements of the perturbation Hamiltonian (while neglecting J-mixing). Secondly, using a fitting procedure which minimizes the sum of the squared residuals between observed and calculated values, calculated energies are determined using the equations developed by Lempicki, Samelson and Brecher [153]. The crystal-field parameters which are derived from the Stark energies of the $^7F_1$ and $^7F_2$ manifolds are tabulated in Table 5.2.2.3.2 as a function of the excitation wavelength.

The energies of the Stark components of the $^7F_1$ and $^7F_2$ multiplets are also shown in Figures 5.2.2.3.2 and 5.2.2.3.3 as a function of the $^5D_0$ excitation energy. Essentially, both Figures present the same information, but Figure 5.2.2.3.2 clearly presents the evolution in the position of the Stark components as a function of excitation, whereas Figure 5.2.2.3.3 qualitatively relates the position of the Stark components with the position of the excitation energy with respect to the $^5D_0 \leftarrow ^7F_0$ absorption band envelope. Figure 5.2.2.3.2 clearly shows a "break", at approximately 580 nm, in the smooth evolution of the position of the Stark components. In Figure 5.2.2.3.3, we see that this "break" corresponds to an excitation near the $^5D_0 \leftarrow ^7F_1$ absorption band, which indicates that we are exciting two very different subsets of energy "sites", the first being excited through the $^5D_0 \leftarrow ^7F_0$ absorption band, the second through the $^5D_0 \leftarrow ^7F_1$. This would suggest that the low energy components of the $^7F_1$ manifold are thermally populated, even at the low temperatures of this experiment.

TABLE 5.2.2.3.2
CRYSTAL-FIELD PARAMETERS DERIVED FROM THE STARK ENERGIES OF THE $^7F_1$ AND $^7F_2$ MANIFOLDS AS A FUNCTION OF EXCITATION

Excitation (nm)	$\mathbf{B_{20}}$ (cm^{-1})	$\mathbf{B_{22}}$ (cm^{-1})	$\mathbf{B_{40}}$ (cm^{-1})	$\mathbf{B_{42}}$ (cm^{-1})	$\mathbf{B_{44}}$ (cm^{-1})
576.05	-635.523	284.927	-60.585	892.397	-243.592
577.07	-581.558	378.099	-97.341	1018.016	315.916
577.53	-553.539	420.718	-102.217	1027.466	-378.885
577.99	-509.978	441.953	-106.163	1046.589	-326.980
578.55	-445.720	419.218	-119.084	1023.664	-254.247
579.09	-375.417	429.872	-135.660	1130.445	-26.679
579.56	-295.937	316.374	-102.497	953.517	196.073
580.11	-215.740	255.149	-109.522	997.424	285.022
580.75	-327.295	339.047	-108.008	1016.330	158.069
581.36	-299.122	376.592	-122.035	1078.953	149.135
582.00	-325.791	416.779	-125.216	1070.200	180.456
582.96	-257.086	443.129	-145.849	1196.699	186.361

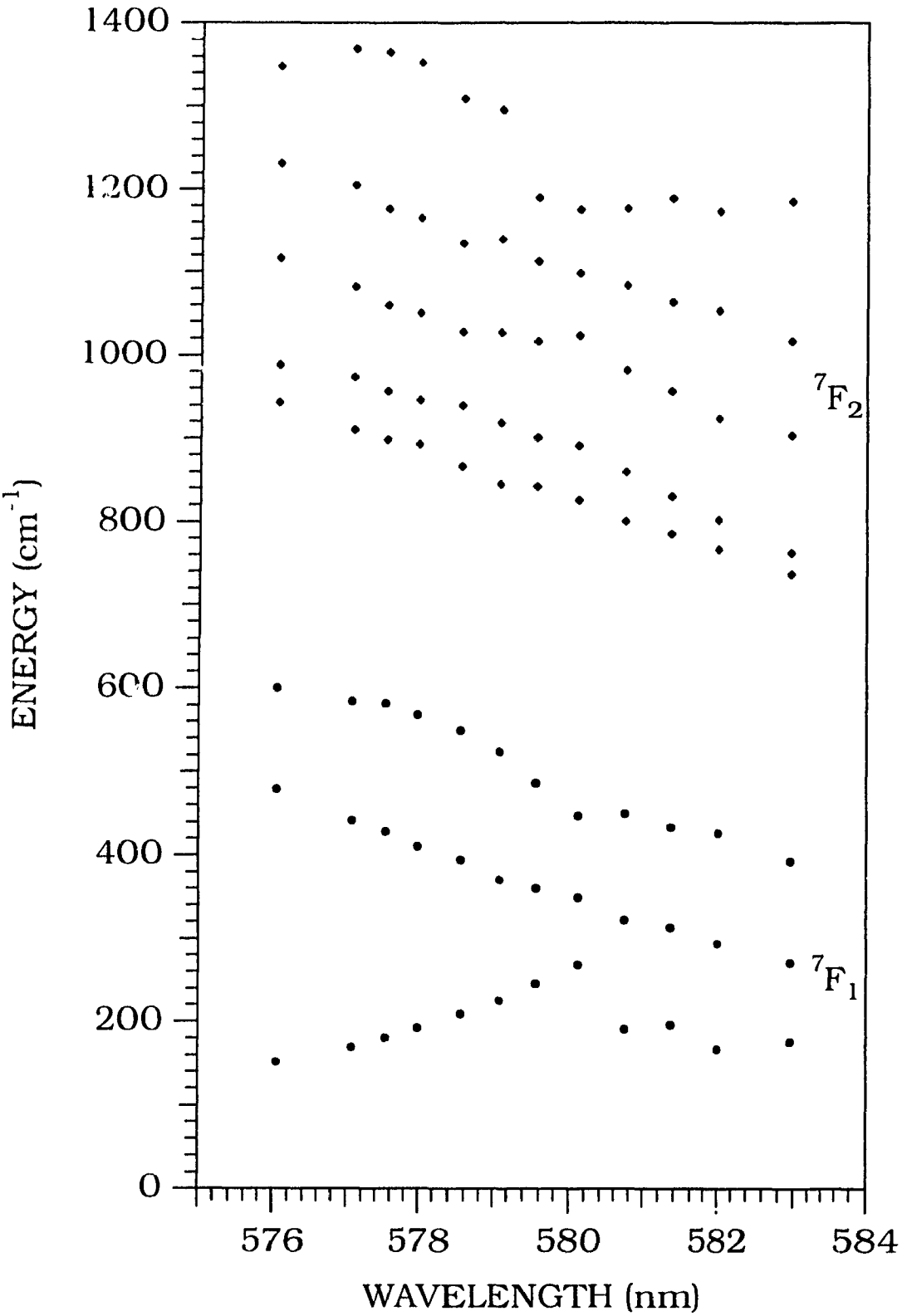

Figure 5.2.2.3.2 Energy of the Stark components of the $^5D_0 \rightarrow {}^7F_{1,2}$ transitions as a function of the excitation wavelength.

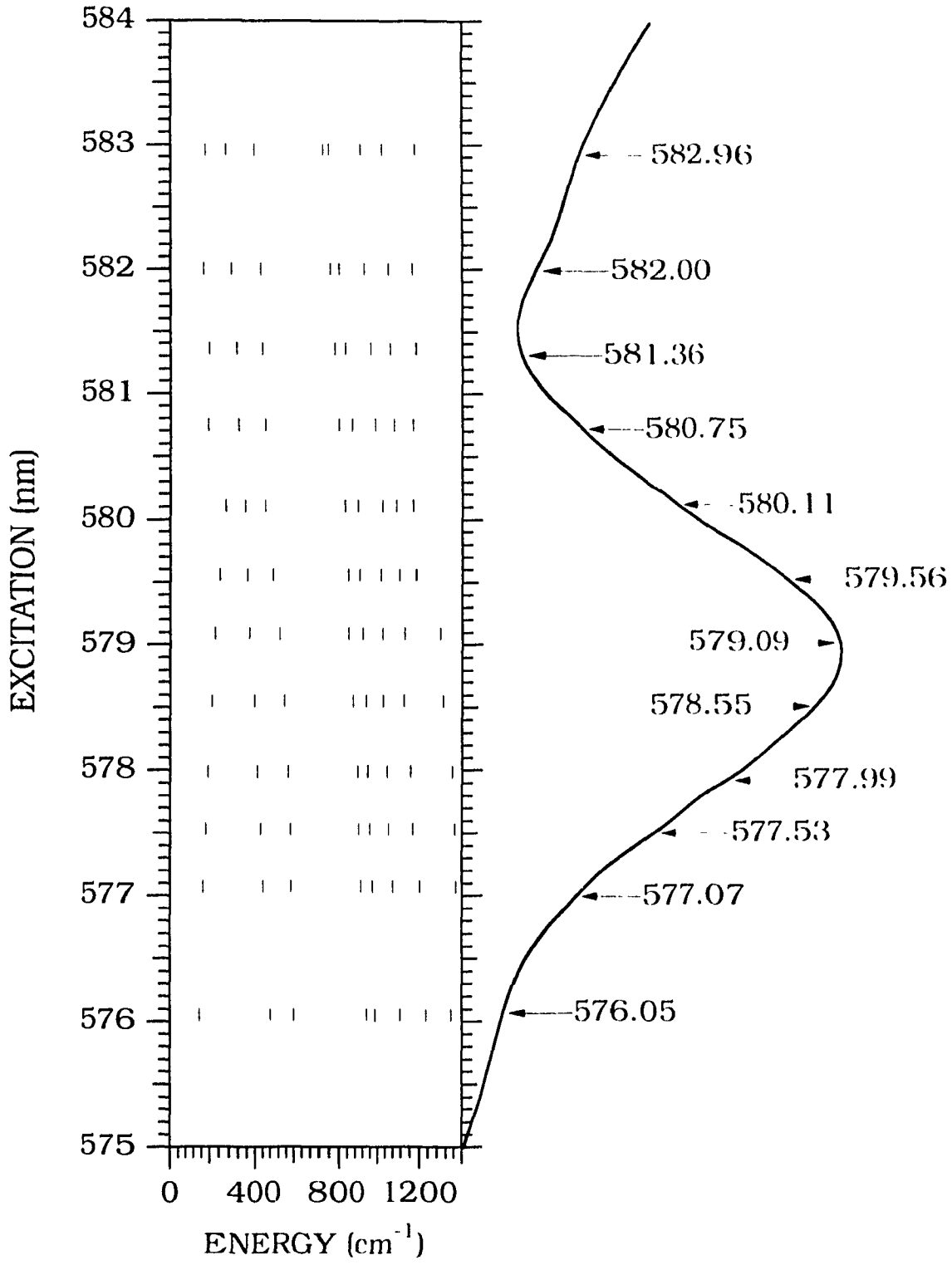

Figure 5.2.2.3.3 (a) $^5D_0 \leftarrow ^7F_0$ absorption band. Shown are the FLN excitations. **(b)** Energy of the components of the $^5D_0 \rightarrow ^7F_{1,2}$ transitions.

The dependence of the measured crystal-field parameters on the excitation wavelength is presented in Figure 5.2.2.3.4, where we see gradual and systematic changes in the parameters. Because of the difficulties presented by the analysis of the spectra excited with wavelengths longer than 580.5nm, only the crystal-field parameters corresponding to the excitation into the $^5D_0 \leftarrow {}^7F_0$ absorption band are presented.

In their analysis of the FLN spectra of a highly modified Eu^{3+}-doped NaBaZn silicate glass, Brecher and Riseberg proposed a geometric model for the behaviour of the first coordination shell of the Eu^{3+} ion in an amorphous matrix. They achieved good agreement between their geometric model and experimentally derived crystal-field parameters. All of the model-derived crystal-field parameters were seen to increase and decrease in the appropriate manner and all had the appropriate signs throughout. The crystal-field parameters presented in Figure 5.2.2.3.4, follow the same trends as those reported by Brecher and Riseberg. The fact that both these glasses follow the same overall trends is not surprising. Both of these Eu^{3+}-doped glasses, i.e. the sodium disilicate (of this thesis) and the sodium-barium-zinc silicate (of Brecher and Riseberg), are silicate glasses. It would then be normal to expect that they follow the same behaviour. The fluoroberyllate glass, also studied by Brecher and Riseberg [51] with the same premises, shows an altogether different behaviour. However, the apparent "normal" behaviour of both Eu^{3+}-doped silicate glasses hides a significant difference.

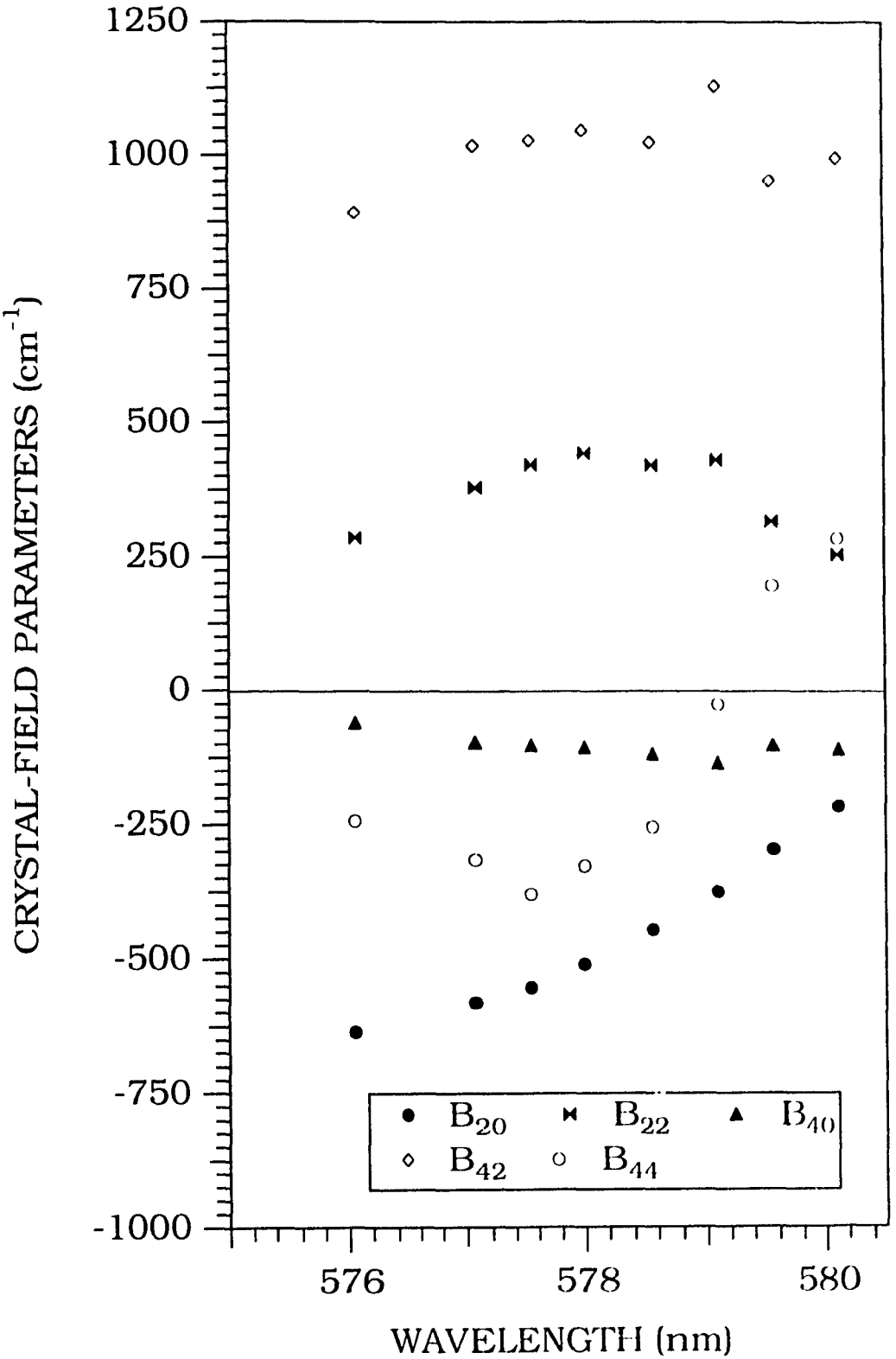

Figure 5.2.2.3.4 Experimentally determined crystal-field parameters (B_{nm}) for the laboratory $Na_2O{\cdot}2SiO_2{:}Eu^{3+}$ glass.

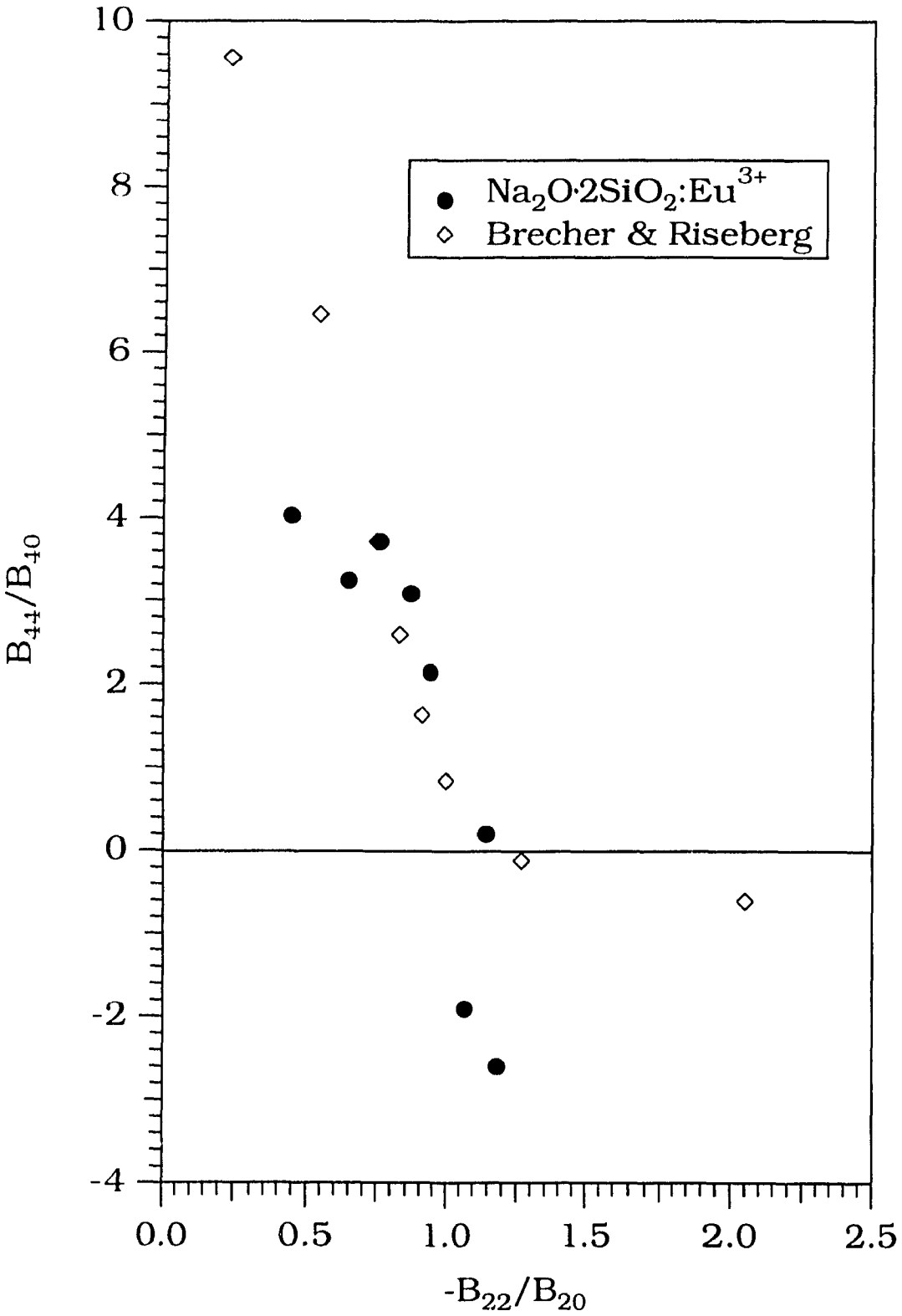

Figure 5.2.2.3.5 Behaviour of the major crystal-field ratios $-B_{22}/B_{20}$ and B_{44}/B_{40}. Shown are values calculated from Brecher and Riseberg's model [50] and for the laboratory $Na_2O{\cdot}2SiO_2:Eu^{3+}$ glass.

Brecher and Riseberg postulated that purely orientational information can be extracted, from the FLN spectra, by considering ratios of crystal-field parameters of the same order, i.e. B_{22}/B_{20} and B_{44}/B_{40}. The behaviour of these are shown, for the laboratory $Na_2O{\cdot}2SiO_2{:}Eu^{3+}$ glass, in Figure 5.2.2.3.5, together with the values calculated from Brecher and Riseberg's geometric model. This Figure plainly shows that the Eu^{3+}-doped sodium disilicate glass does not follow Brecher and Riseberg's model, but rather follows closely the behaviour shown by a Eu^{3+}-doped cordierite[7] glass [47].

Capobianco *et al.* have applied Brecher and Riseberg's model to various distinct types of oxide glasses: (i) a sodium-calcium-aluminum titanosilicate glass [154], (ii) a sodium-aluminosilicate glass [47] and (iii v) barium, zinc and lead metaphosphate glasses [48]. All of these have shown fair to poor correlation with Brecher and Riseberg's model. One main point common to all the silicate glasses, is that the experimental values calculated for the $-B_{22}/B_{20}$ vs. B_{44}/B_{40} plot do not fall on the theoretical line, but rather show clustering in particular regions of the graph. Capobianco *et al.* suggested that, within the confines of Brecher and Riseberg's geometric model, this behaviour indicates that the local geometrical environment of the Eu^{3+} ion is more constant than suggested by the model. They concluded by stating that this is consistent with the Eu^{3+} acting as a quasi-molecular complex. Although the same conclusion is reached here, as discussed in Section 5.1, an important nuance has to be mentioned. The geometric model, and any structural

[7] Cordierite is a magnesium aluminosilicate of chemical formula $Mg_2Al_4Si_5O_{18}$

information which may be derived, is limited by the fact that it does not take into account the overall energy of the rare-earth *"site"*.

In retrospect, we propose that Brecher and Riseberg's model was specifically *"designed"* or *"fitted"* to obtain a good correlation with the behaviour of experimentally derived crystal-field parameters for the sodium-barium-zinc silicate glass. It therefore fails one of the basic requirements for a "good" model which asks that a model be generalized. The fault, if one exists, must lie in the fact that they considered only the first coordinating shell of oxygen ligands thereby ignoring the rest of the immediate environment (network-modifiers and the silicate backbone) and the effect it has on the crystal-field felt by the Eu^{3+} ion. In effect, their model is too simple to effectively represent the average local environment of a rare-earth dopant ion in an oxide glass.

Although some very useful information has been obtained in the present FLN study, a thorough reexamination of the FLN spectroscopy of the $Na_2O{\cdot}2SiO_2{:}Eu^{3+}$ glass is warranted to explain (i) the presence of the so-called energy-transfer bands [155] in the $^7F_1$ region which appear when exciting in the high-energy side of the $^5D_0 \leftarrow {}^7F_0$ absorption band, and (ii) the behaviour of the Stark levels when exciting close to or in the $^5D_0 \leftarrow {}^7F_1$ absorption band. This sample shows unusually intense emission and remarkably clear Stark splittings of the $^7F_2$ manifold, making the $Na_2O{\cdot}2SiO_2{:}Eu^{3+}$ glass a perfect candidate for such a study. This study has not been done since it is outside the scope of this thesis.

An attempt to recreate the FLN spectra from the simulated glass structure was unsuccessful due to the extremely small number of Eu^{3+} configurations which we have examined in this simulation. The purpose of the FLN experiment is to take spectral "samples" throughout the $^5D_0 \leftarrow ^7F_0$ absorption band. We had initially thought that it would be straightforward to do the same with the simulated Eu^{3+} environments, i.e. (i) sorting the Eu^{3+} environments by $^5D_0 \leftarrow ^7F_0$ energy, (ii) delmiting ≈10-15 energy "ranges" throughout the simulated $^5D_0 \leftarrow ^7F_0$ absorption band, then (iii) convoluting the emission spectra of the Eu^{3+} environments found in each of the individual energy ranges, thus in effect, "sampling" the Eu^{3+} environments. This did not work because most of the energy "ranges" did not contain enough Eu^{3+} environments which we could effectively convolute without creating a discontinuous spectrum. By itself, this procedure is not wrong and would work, but only if the number of Eu^{3+} environments was multiplied by several orders of magnitude.

In the laboratory glass, the 0.94%wt Eu_2O_3 concentration is equivalent to 8.79×10^{19} ions/cm^3. Since in the FLN experiment we are using a narrowband excitation of approximately 2 cm^{-1}, and the inhomogeneously broadened $^5D_0 \leftarrow ^7F_0$ absorption has a bandwidth of 90 cm^{-1}, we are in effect averaging out the spectral contributions of 1.5×10^{18} emitters at the maximum of the band and of roughly 5×10^{16} emitters at its tail (positioned at 10% of the maximal intensity of the Gaussian). In the case of the simulated glass, the sample size which corresponds to the 2 cm^{-1} bandwidth of the exciting laser is typically 1 or 2 Eu^{3+} configurations. Although there is a definite selectivity in FLN spectra of

experimental glasses, the experiment still corresponds to the investigation of a "macroscopic" behaviour of a doped glass. Due to this, any attempts to infer structural information from these experiments is bound to be complicated by the fact that one is looking at an overwhelming amount of accidental degeneracies [46]. Seeking for "uniqueness" in a structural model for doped inorganic glasses might well be futile.

Although we have not been able to simulate FLN spectra for the $Na_2O{\cdot}2SiO_2{:}Eu^{3+}$ glass, we are still able to derive various features normally associated with FLN spectroscopy. Shown in Figure 5.2.2.3.6 are the positions of the three $^7F_1$ and five $^7F_2$ Stark levels for each of the 150 Eu^{3+} configurations as function of the excitation ($^5D_0 \leftarrow {}^7F_0$) energy. In Figure 5.2.2.3.7, we show the same plot with data points which were averaged out from Stark levels of configurations having approximately the same excitation ($^5D_0 \leftarrow {}^7F_0$) energy. These results present Stark splittings for the $^7F_1$ and $^7F_2$ manifolds which are equivalent in magnitude and position to those presented in Figure 5.2.2.3.2, (necessarily those for a $^5D_0 \leftarrow {}^7F_0$ excitation).

The comparison between Figures 5.2.2.3.2 and 5.2.2.3.7 reveals that the simulated model is remarkably accurate, especially in reproducing the Stark components of the $^7F_1$ manifold. Only the lowest energy Stark component of the $^7F_2$ manifold seems to be absent, but this is related to what was discussed in Section 5.2.2.2 and shown in Figure 5.2.2.2.3.

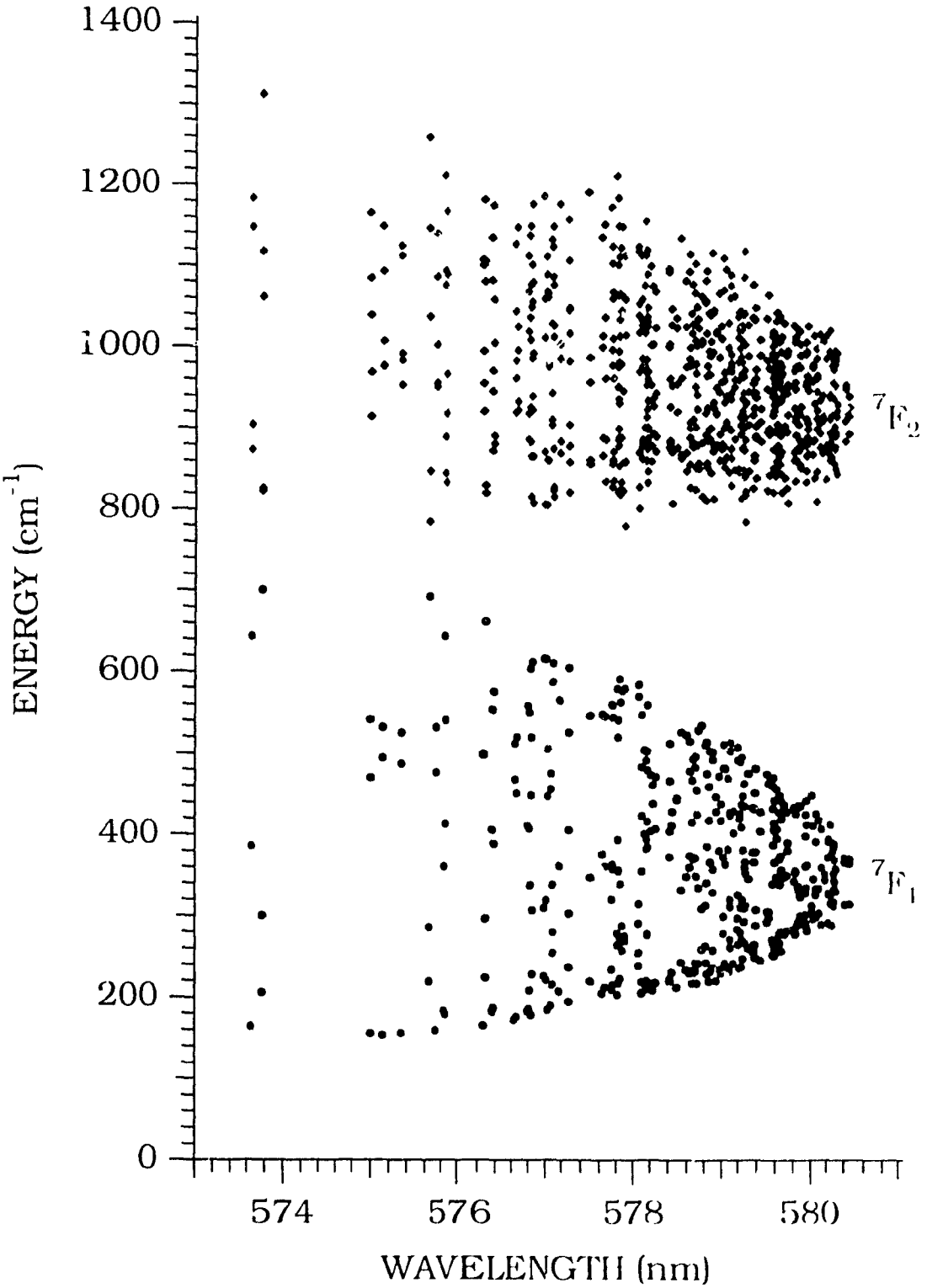

Figure 5.2.2.3.6 Energy of the Stark components of the $^7F_{1,2}$ manifolds as a function of the simulated excitation ($^5D_0$<-$^7F_0$) wavelength. Representation of the 150 Eu^{3+} configurations.

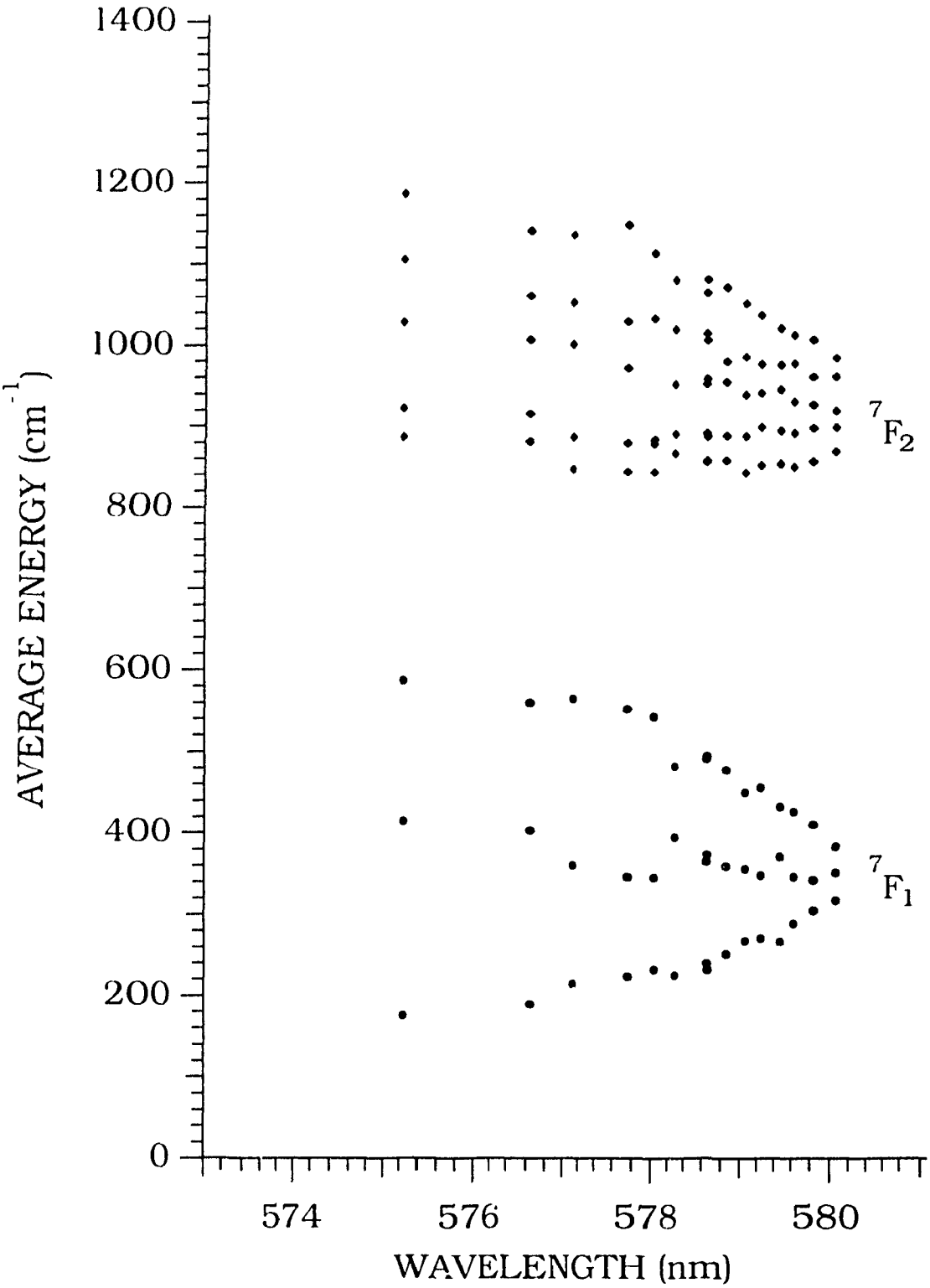

Figure 5.2.2.3.7 Energy of the Stark components of the $^7F_{1,2}$ manifolds as a function of the simulated excitation ($^5D_0 \leftarrow {}^7F_0$) wavelength. Averaged energies of the Eu^{3+} configurations.

5.2.3 Structure/Spectra correlations

The ability to infer structural features from spectra has been, over the past few decades, one of the main goals of optical spectroscopy. Some success has come from the study of doped crystals. Nevertheless, any attempt to do so with glasses was seen to fail. Since, in this thesis, we are not restricted by the direct study of an experimental spectrum, it was possible for us to establish an indirect link between a structural model of europium doped sodium disilicate glass and the experimental spectra of the corresponding laboratory glass. This was presented in the previous Sections, where we have validated the structural model through a comparison between the simulated and experimental spectra.

In this Section, further spectra-structure correlations will be investigated. Each stems from the knowledge of the exact local atomic configurations surrounding each of the doped ions and by the possibility to identify and isolate individual structural contributions to the simulated spectra. This is exemplified in the following two Figures. Figure 5.2.3.1 presents a graphic representation of a typical Eu^{3+} local environment. The ions displayed are those found in a sphere of 4.0Å radius centered at the position of the Eu^{3+} ion. The four atomic types of the simulated glass are represented in this Figure, i.e., the central ion is the europium which is bonded to 7 oxygens which are themselves attached to silicon atoms (the 4 smallest spheres), while the 3 sodium atoms are represented with no bonds. In this configuration, the average Eu-O bond length is 2.7Å, calculated with a cut-off of 3.2Å. Figure

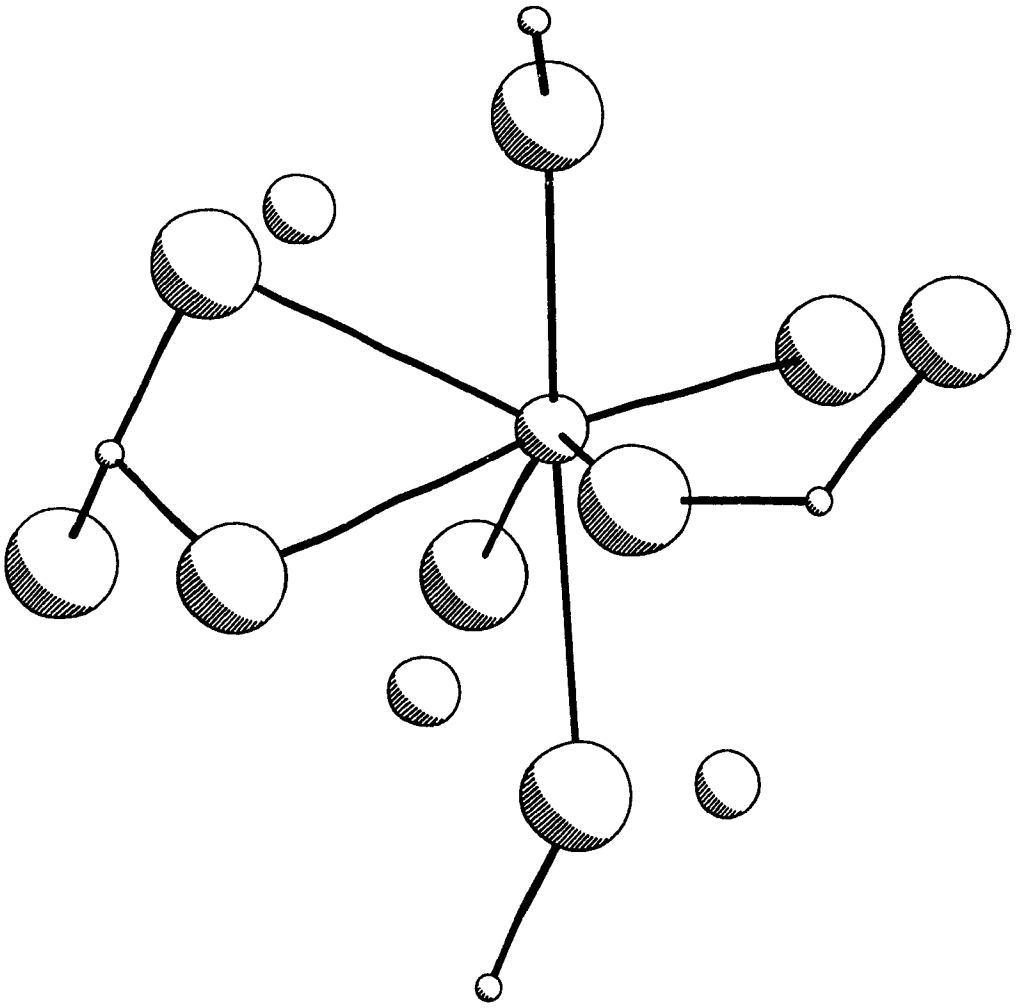

Figure 5.2.3.1 Schematic representation of the local environment of one of the 150 simulated Eu^{3+} ions. All atoms found at a distance of at most 4.0Å from the Eu^{3+} ion are displayed.

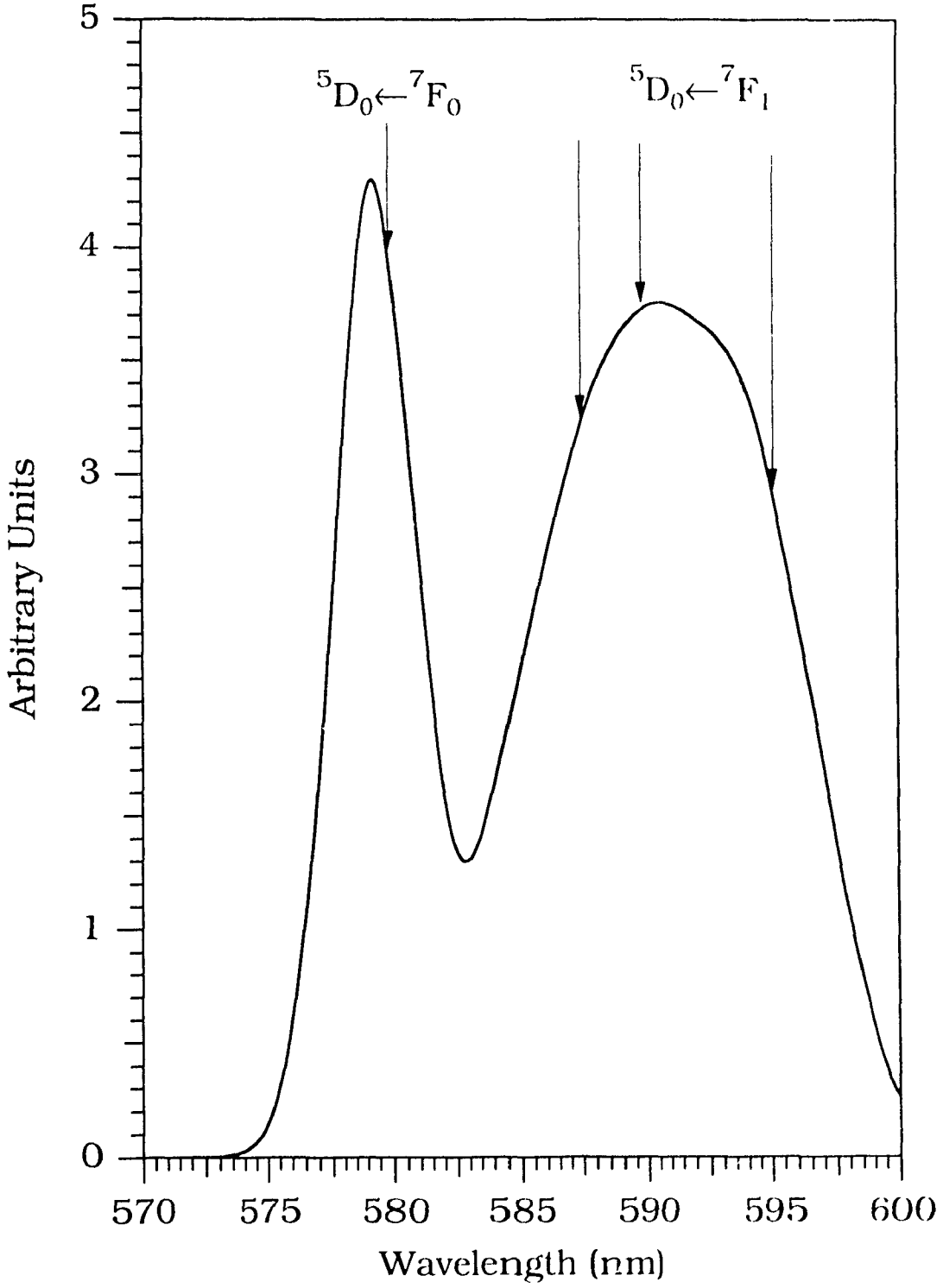

Figure 5.2.3.2 $^5D_0 \leftarrow {}^7F_{0,1}$ region of the absorption spectrum of the simulated Eu^{3+}-doped $Na_2O{\cdot}2SiO_2$ glass. Arrows indicate the location of the transition energies for the Eu^{3+} configuration represented in Figure 5.2.3.1.

5.2.3.2 shows the $^5D_0 \leftarrow {}^7F_{0,1}$ region of the simulated spectrum, with the exact energies of the Eu^{3+} configuration represented in Figure 5.2.3.1 indicated by the 4 arrows.

In optical spectroscopy of glasses, it is common practice to examine the evolution of various spectroscopic features as a function of the excitation energy of an absorption band. As an example, features such as crystal-field parameters and their ratios, energy barycentres, radiative decay times and Judd-Ofelt parameters have been examined through Fluorescence Line Narrowing [45-51,152,154]. This was interpreted as indirectly examining structural/spectral relationships in order to infer details of the local environment of the doped luminescent probe ions. With these experimental investigations, various structural properties and models were postulated. These were described in the Introduction and further discussed in Section 5.2.2.3. We shall take the same approach and try to recreate some of these experimentally derived relationships.

The first relationship to be investigated is the possible influence of the crystal-field on the barycentre energy of the Eu^{3+} J- manifolds. To a first approximation (point-charge crystal-field model, no J-mixing, no covalency terms or other correction terms to the perturbation Hamiltonian), the only effect the crystal-field will have is to lift the degeneracy of the J-manifold. Under this approximation, the barycentres of the J-manifolds will be identical to the corresponding free-ion barycentres. Therefore, the only difference between two Eu^{3+} configurations will be in the amount of splitting of the respective J-

manifolds. The width observed, for transitions of rare-earth ions doped in a glass, could be interpreted as follows. Configurations having high-field strengths will show a large splitting and they will be sitting on either side of the inhomogeneously broadened band. Conversely, configurations having low-field strengths will have a small splitting and will be sitting in the middle of the inhomogeneously broadened band. Keeping with this approximation, a $J=0 \leftrightarrow J'=0$ transition, since the manifolds involved cannot be split, should show a width that corresponds to homogeneous broadening and should not show any inhomogeneous broadening. This is not the case for the $^5D_0 \leftrightarrow {}^7F_0$ transitions of the trivalent europium ion doped in sodium disilicate (Figures 5.2.2.1.1 and 5.2.2.2.1), nor is it true for any other Eu^{3+}-doped inorganic glass. This first approximation is thus inadequate to explain the width of such transitions and it is reasonable to assume that it is also inadequate for transitions where J and/or J' are different from 0. The question then remains: How does the crystal-field affect the position of the individual manifold barycentres which make up the inhomogeneously broadened bands of doped glasses ?

In order to investigate this point, the crystal-field strength, S_{CF}, (Equation 3.1.2.7) has been plotted versus the excitation wavelength (the position of the $^5D_0$ manifold representing the $^5D_0 \leftarrow {}^7F_0$ transition) for each of the 150 Eu^{3+} configurations. This plot is shown in Figure 5.2.3.3. In this Figure, we observe a linear decrease, between 574.5 and 579 nm, of the crystal-field strength followed by a sharp fall. The general trend for this transition, could then be interpreted as a blue shift of the transitional energy with crystal-field strength. This blue shift could be construed as an indication of the overall covalency effect which was

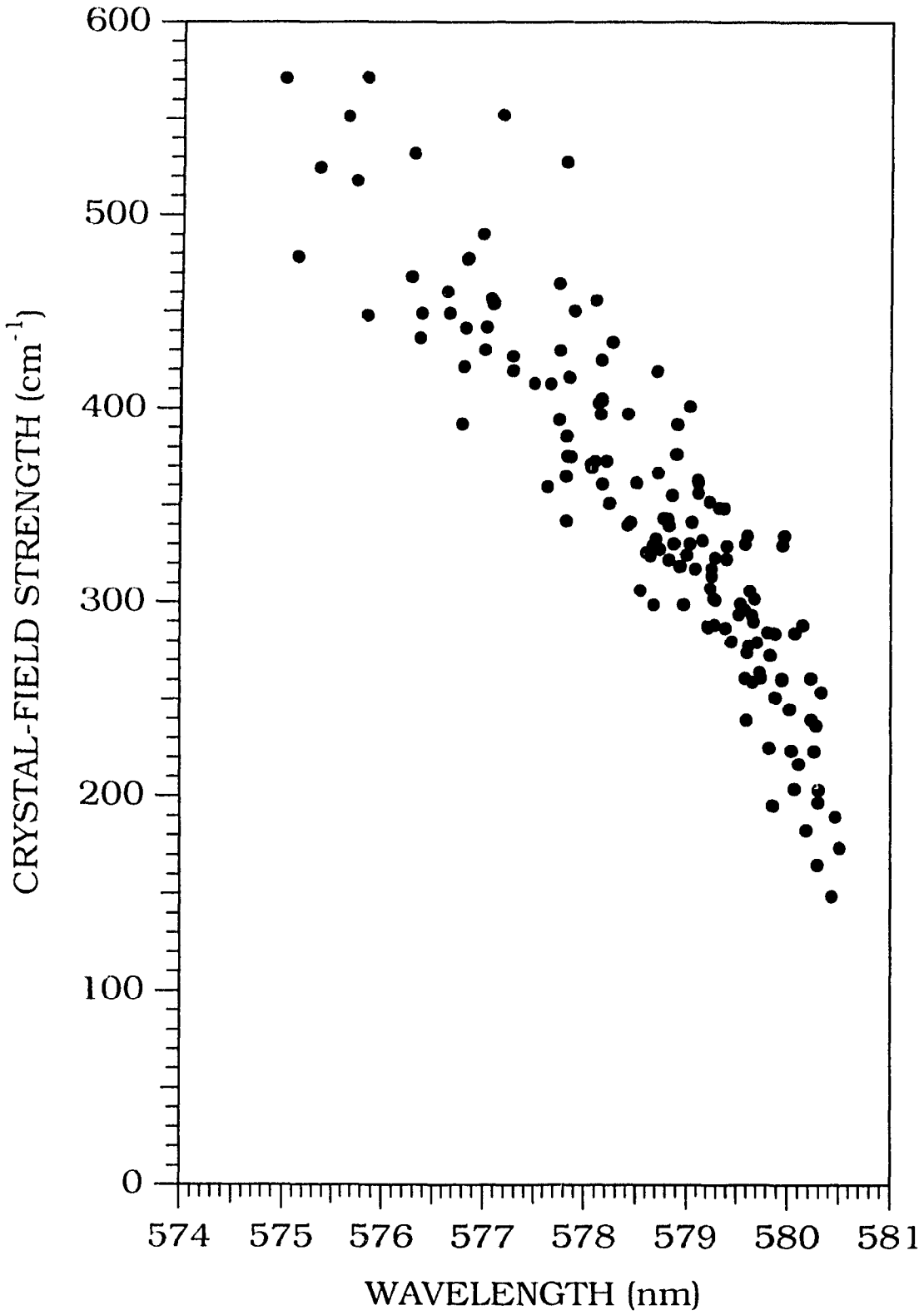

Figure 5.2.3.3 Plot of the crystal-field strength, S_{CF}, as a function of the simulated $^5D_0 \leftarrow ^7F_0$ transition wavelength.

introduced in the crystal-field model by the inclusion of partial charges. This could be likened to the observation of a red-shift of the transitional barycentre with a decrease in the oxygen partial charge, as observed in Figure 5.2.1.5.1. Since the crystal-field strength is a representation of the electrostatic interaction between the rare-earth ion and its local environment, it could be expected that a decrease of the crystal field strength is a representation of an increase in covalent interactions. However, since we have not formally introduced a covalent interaction term in the crystal-field Hamiltonian, it could be deemed improper to make such a statement.

In order to investigate further this indication of covalency, we have plotted the energy barycentres of the simulated $^5D_0 \rightarrow {}^7F_J$ (J= 0 to 6) transitions as a function of the crystal-field strength. These plots are shown in Figures 5.2.3.4 (a) through (c). Two horizontal lines are seen to cross each of the graphs. The dotted lines represent the energy of the free-ion barycentres (2nd column of Table 5.2.1.3.1). The full lines represent the energy of the simulated transitional barycentres (Table 5.2.2.2.2). Several general observations[8] can be made from these Figures. Firstly, the transitions do not present the same behaviour towards crystal-field strength. The $^5D_0 \rightarrow {}^7F_{0,1,2,3,4}$ transitions present a blue shift of the barycentre energy with increasing crystal-field strength, whereas the $^5D_0 \rightarrow {}^7F_{5,6}$ transitions present a red-shift of the barycentre energy with increasing crystal-field strength. Secondly, except for the

[8] We will not take into account the graph for the $^5D_0 \rightarrow {}^7F_2$ transition. As we have seen in Section 5.2.2.2, this transition is poorly simulated due to its electric quadrupole (hypersensitive) nature. Because of this, we feel that any observations made from this transition will not be pertinent to the present discussion.

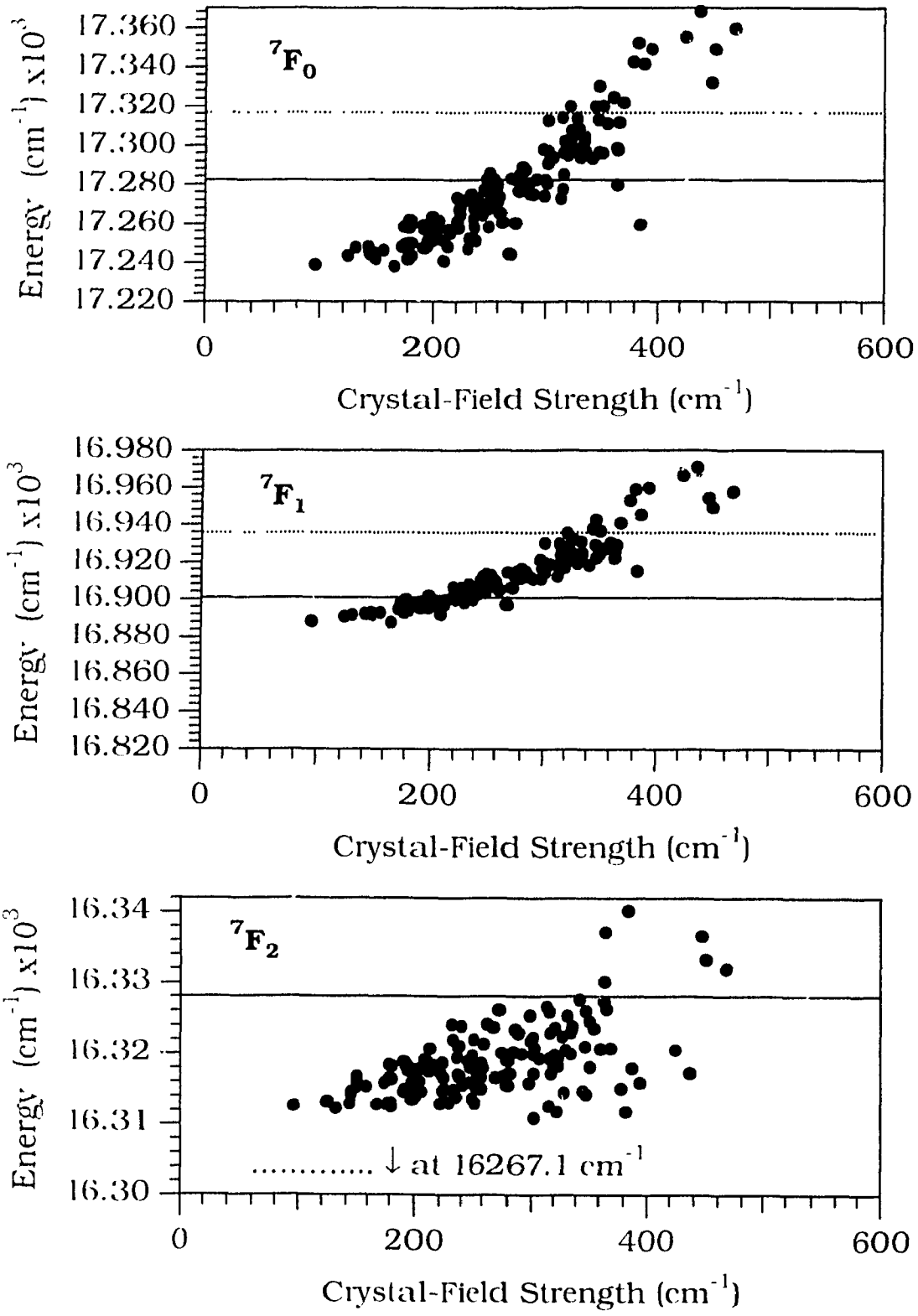

Figure 5.2.3.4a Energy barycentres for the $^5D_0 \rightarrow {}^7F_{0,1,2}$ transitions versus crystal-field strength.

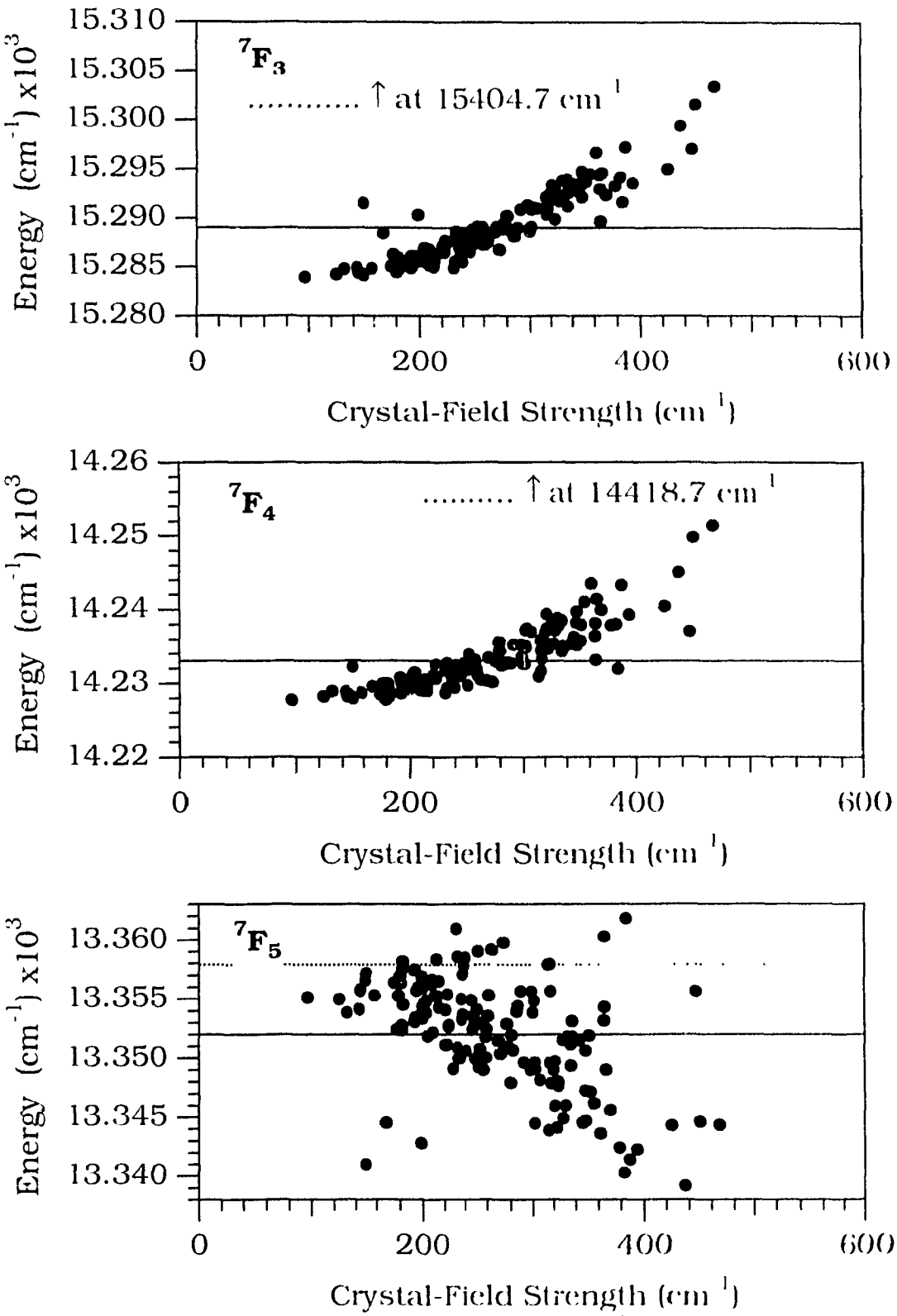

Figure 5.2.3.4b Energy barycentres for the $^5D_0 \rightarrow {}^7F_{3,4,5}$ transitions versus crystal-field strength.

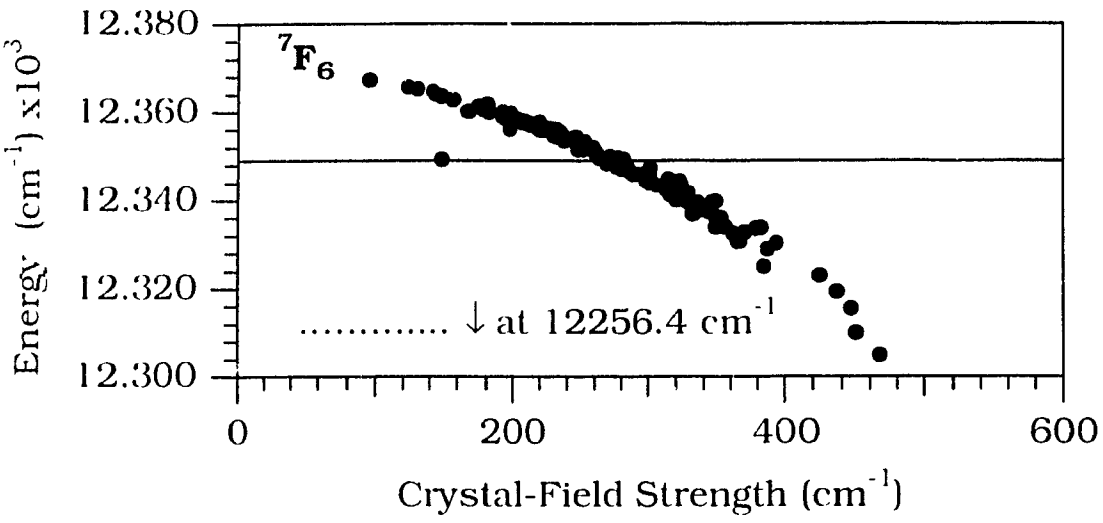

Figure 5.2.3.4c Energy barycentres for the $^5D_0 \rightarrow {}^7F_6$ transitions versus crystal-field strength.

$^5D_0 \rightarrow {}^7F_6$ transition, all the transitions present a decrease in the energy of the overall simulated barycentre when compared with the free ion barycentre. This is likened to the experimental observation of the nephelauxetic effect seen in rare-earth doped crystals [142]. We must note that, since no covalency term has been included in the perturbation Hamiltonian, the nephelauxetic effect cannot be calculated by the present crystal-field model. However, this effect is observed because of the use of partial charges which red-shift the position of the overall barycentres of each transitions (Figure 5.2.1.5.1). Thirdly, the magnitude of the energy shifts of the overall transitional barycentres are different from one level to another. The magnitude of the effect of the overall covalency should be different for each level [156,157]. Finally, it is observed that the magnitude and the shape of the crystal field strength dependent energy shift is different from one level to another.

The only factor included in the crystal-field model, which could explain all of the above-mentioned observations, is J mixing. J mixing is defined as the interaction (or mixing) of states belonging to different free ion levels (which ordinarily have different J-values). The influence of J mixing is usually considered small when the free-ion levels are relatively isolated. In the present case, although the $^5D_0$ and ^7F_J states are well separated from one another, the individual J manifolds of the ^7F_J states are only separated by approximately 1000 cm^{-1}, from one to the next. As for the $^5D_0$ state, it is close to the $^5D_{1,2,3}$ and $^5L_6$ levels. Since the crystal-field strength is directly responsible for any variation of the splitting of a J-manifold, individual Stark levels will be at different energies from one Eu^{3+} configuration to another. Because of this, J

mixing will also be different from one Eu^{3+} configuration to another, causing the observed shift in the energies of transitional barycentres. Also, since each J-manifold presents a different amount of J mixing, each of the $^5D_0 \rightarrow {}^7F_J$ transitions will present a variation in the magnitude of the energy shift and a variation in overall behaviour. In all probability, this is the reason for the observed blue shift of the $^5D_0 \rightarrow {}^7F_{0,1,2,3,4}$ transitions and the red-shift of the $^5D_0 \rightarrow {}^7F_{5,6}$ transitions. Since the $^7F_{5,6}$ states are much closer to the $^5D_0$ state, this reversal could be explained by J-mixing with the lower ^7F_J states and the higher $^5D_0$ state.

To our knowledge, this is the first observation of the influence of the crystal-field strength on J-mixing. To verify this experimentally, one would need to separate the individual contributions of electrostatic interaction, covalency, J-mixing and a multitude of other effects [158]. This is complicated enough for rare-earth ions doped in crystals, it is deemed impossible for rare-earth ions doped in glasses. To investigate the effect of J-mixing theoretically, is also an insurmountable task. Specifically, to be able to predict the behaviour of the energy of the barycentres of individual J-states, due to a variation of J-mixing with crystal-field strength, would require an enormous amount of computational time. When J-mixing is taken into consideration in a crystal-field calculation, the matrix elements of all the possible $\alpha JM,\alpha'J'M'$ combinations must be calculated. In the present crystal field calculation, where we have dealt only with the lowest 12 [SL] J states (which represent a total of 78 individual Stark levels) of the Eu^{3+} ion, the matrix of the perturbation Hamiltonian will have 78 x 78 elements,

with 78 diagonal matrix elements and 6006 off-diagonal matrix elements. These off-diagonal matrix elements are responsible for the effect of J-mixing.

As we have seen in the previous Sections, absorption and emission spectra of ions doped in glasses consist of bands which are broadened due to the superposition of contributions from individual ions distributed among the entire ensemble of local environments. This is the classical textbook definition of inhomogeneous broadening. Yet, very little is known about the microscopic origins of inhomogeneous broadening [159]. To this definition, we might add that one of the main contributions to inhomogeneous broadening is due to the variation of J-mixing amongst the entire ensemble of local environments.

As we can see in Figures 5.2.3.5 and 5.2.3.6, there are no distinguishable correlations between the excitation energy and the numbers and average distances of the oxygen ligands surrounding the subsets of Eu^{3+} ions excited at a given energy. This leads us to believe that the presence of a limited number of distorted "sites" as discussed by various authors [23,27,29,31,32,34-39,42-44,50,51] is fallacious and that the rare-earth environments are rather composed of a continuous distribution of local-fields which satisfy energetic bonding requirements of the Eu^{3+} ions while disregarding structural bonding requirements normally attributed to complexes or crystalline compounds. In this context, it is perfectly understandable that a Eu^{3+} ion surrounded by four oxygen ligands could experience the same crystal-field as an eight

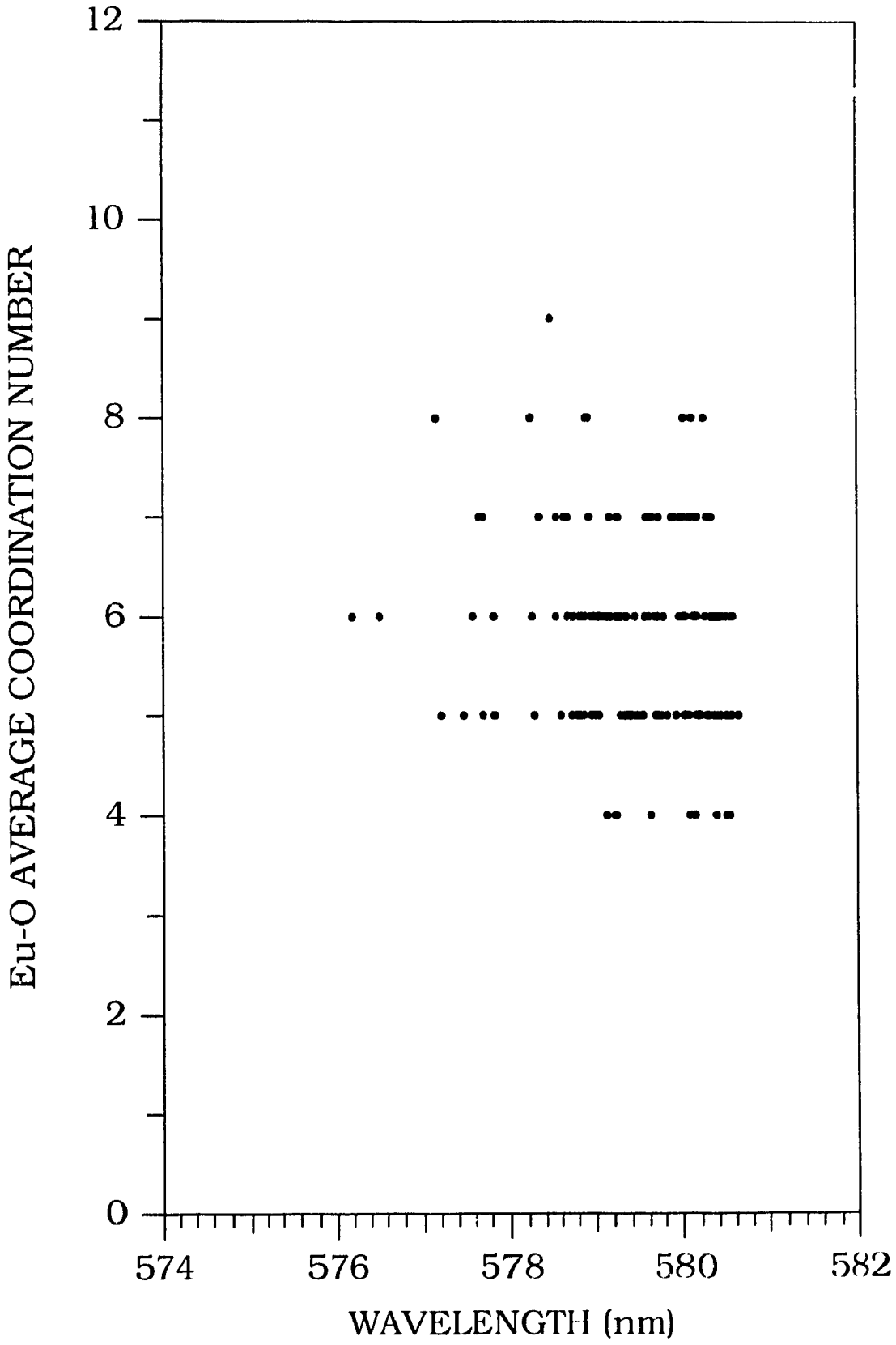

Figure 5.2.3.5 Europium coordination number (oxygen ligands) as a function of the simulated $^5D_0 \leftarrow ^7F_0$ transition wavelength.

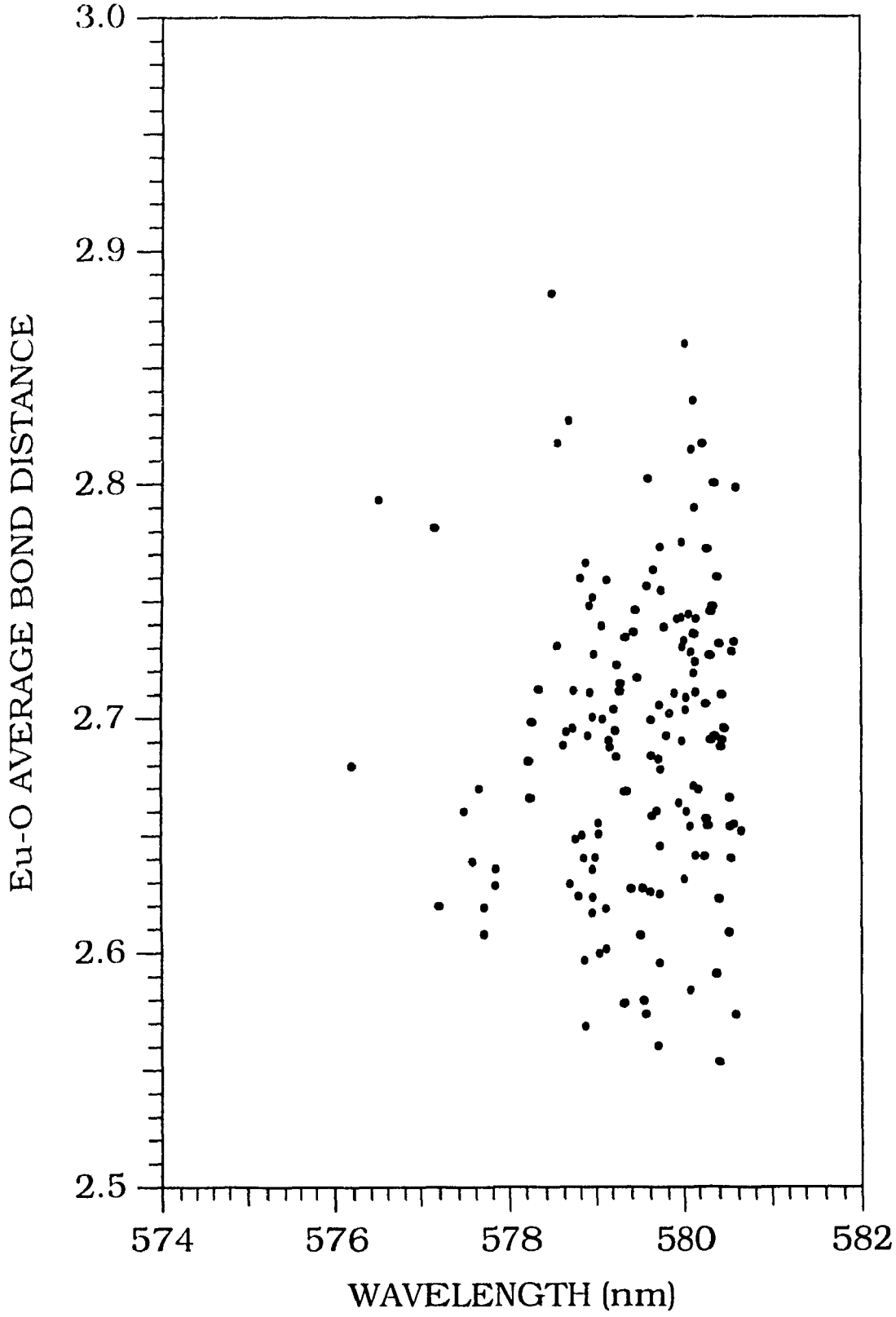

Figure 5.2.3.6 Average europium-oxygen ligand distance as a function of the simulated $^5D_0 \leftarrow ^7F_0$ transition wavelength.

coordinated one; this has been previously referred to as "accidental degeneracies" [46] and must be more widespread than was thought of before.

Another indication of the wide presence of these degeneracies is found in Figure 5.2.3.3, where a vertical spread in CF strength values can be found for any given wavelength of excitation. That is to say that two or several Eu^{3+} configurations can have the same energy for the $^5D_0 \leftarrow {}^7F_0$ transition but still show drastic differences in their CF strength.

In addition to coordination number and the spatial distribution of ligands, other factors will definitely influence the local-field of a Eu^{3+} ion. Amongst them, we can cite the following.

Firstly, each oxygen ligand which is in the first coordination shell of the Eu^{3+} ion, will bring about various numbers of "*free*" negative charges. This is due to the fact that in a oxide glass, three possible types of oxygens can exist, namely, bridging, non-bridging or free. Secondly, the presence of network-modifying cations in close vicinity with the Eu^{3+} ion will affect the density of charge of the surrounding oxygens. Thirdly, the Eu^{3+} ion should be influenced by the magnitude of covalent interactions of the surrounding atoms (oxygen ligands, network modifiers and the silicate framework). Figures 5.2.3.3 and 5.2.3.4 have shown that the crystal-field varies with the excitation wavelength and we postulated that this was due to a variation of J-mixing and indirectly to covalency. Individual structural factors such as local point-group

symmetry, coordination number and average bond distances are known to have an important effect on the electronic spectra of rare-earth ions doped in crystals. As seen in Figures 5.2.3.5 and 5.2.3.6, the Eu^{3+} coordination number and the Eu-O average bond distance have slight individual influence on the energy of the individual $^5D_0 \leftarrow ^7F_0$ transitions. Since there is no symmetry involved in the make-up of the individual sites, this would tend to prove *a contrario* that no one individual structural factor greatly influences the electronic spectra of doped ions in inorganic glasses. Rather, we present evidence that it is the overall electrostatic and covalent energy of the individual sites together with the site-to-site variation of this energy which hold the greatest influence. To pursue this matter further, an extension of the structural and crystal-field models, i.e. the inclusion of a three-body potential in the MD simulation and the use of ligand-field theory or molecular-orbital calculations, would be dictated.

5.2.4 Simulated spectroscopy of the $SiO_2:Eu^{3+}$ glass

In Section 5.1, we presented a structural model for two rare-earth doped inorganic glasses, $SiO_2:Eu^{3+}$ and $Na_2O{\cdot}2SiO_2:Eu^{3+}$. The validity of the structural model of the Eu^{3+}-doped sodium disilicate glass was assessed by comparing the absorption and emission spectra of the simulated and experimental samples. Since we were able to reproduce the experimental spectra within the framework of the point-charge crystal-field theory, we felt that the simulated structure was an accurate representation of the experimental glass structure.

In order to validate the simulated structural model for the Eu^{3+} doped silica glass, the same approach has to be taken. One problem arose in the course of this work. To our knowledge, no experimental sample of the SiO_2:Eu^{3+} glass exists. Several unrelated factors combine to make the fabrication of this glass a near impossibility. Firstly, it has been reported that the solubility of rare-earth ions is extremely low in amorphous silica [9]. Typically, in silica prepared by melting, crystallization occurs at rare-earth concentrations of 0.1 mol% and higher. At higher concentration, clustering occurs and a rare-earth silicate phase appears. Secondly, because of the very high melting point of silica (> 2000°C), the conventional techniques employed to produce modified silicate glasses are ineffective. One of the only methods capable of obtaining the necessary temperature is the use of a plasma or an oxy hydrogen torch. The use of such torches creates conditions which are highly reducing and absorption measurements show that the doped europium ions are present as the divalent species rather than the trivalent species [160]. A heat treatment with oxidizing conditions has been attempted in order to limit the amount of Eu^{2+} ions. The following conditions have been attempted [160],

$$Eu^{2+} \underset{H_2}{\overset{O_2}{\underset{(1100°C)}{\rightleftharpoons}}} Eu^{3+}$$

but the changes were not sufficient to allow the observation of the trivalent Eu^{3+} species by optical spectroscopy. The divalent europium

ions presents a broad, featureless and very intense emission band centered at approximately 480 nm and extending between 400 and 750 nm. This band can be attributed to a very strong $4f^6 5d^1 \rightarrow 4f^7$ transition showing strong vibronic coupling features. Transitions within the $4f^7$ configuration of the Eu^{2+} and the $4f^6$ configuration of the Eu^{3+}, although necessarily present, will be masked. Because of this, heat treatment of the sample is insufficient to ensure observation of the Eu^{3+} ion.

Nevertheless, within the confines of the point-charge crystal-field model, it is possible to calculate the simulated absorption and emission spectra of the SiO_2:Eu^{3+} glass. These are shown in the following Figures (5.2.4.1 and 5.2.4.2).

As mentioned above, the validation of the simulated spectra has to proceed through a comparison with experimental data. Without such a comparison, we can only speculate on the validity of the simulation. Thus an experimental sample containing unclustered Eu^{3+} ions is required to validate the present simulated structure/spectra model of SiO_2:Eu^{3+} glass.

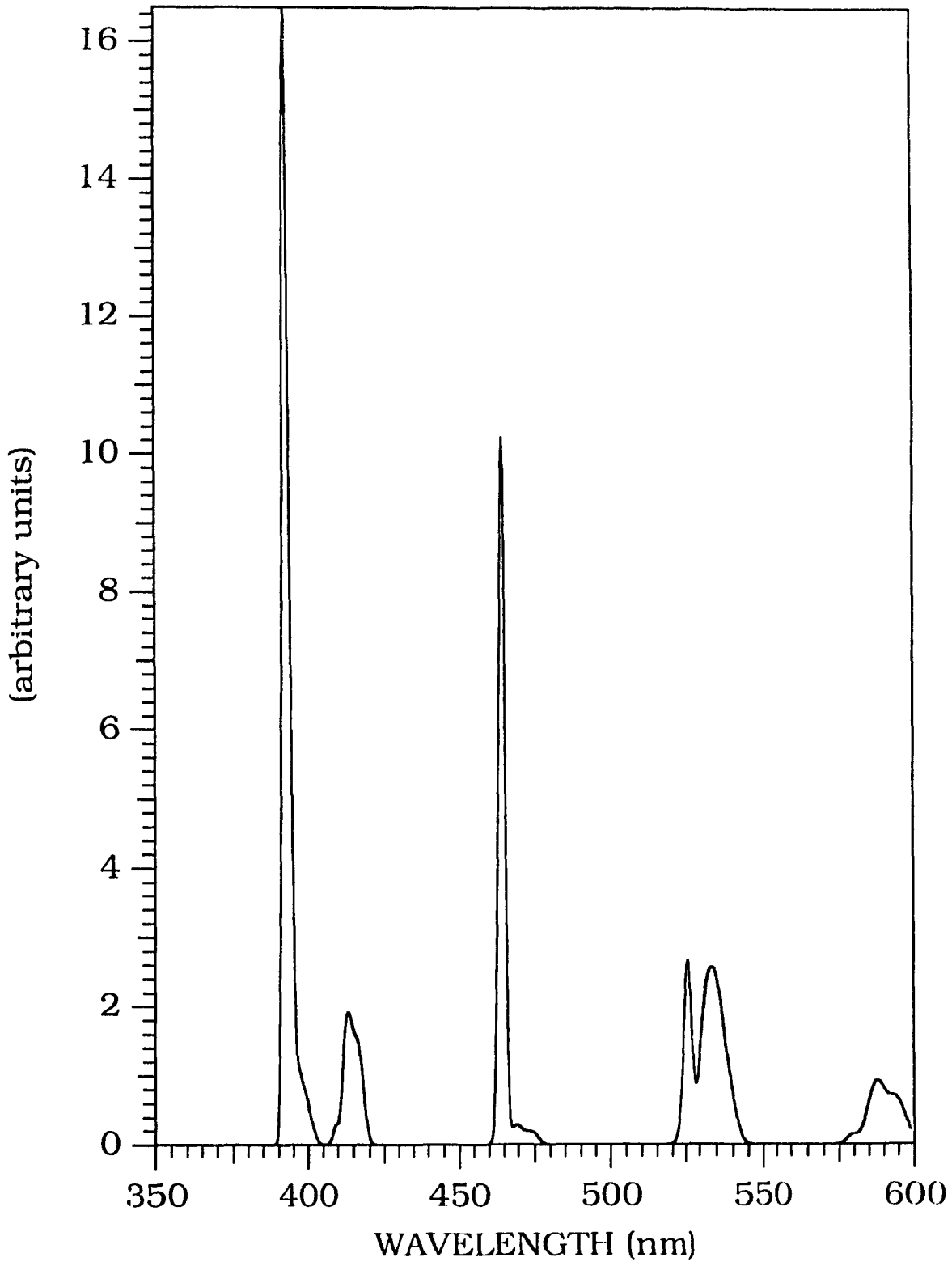

Figure 5.2.4.1. Absorption spectrum for the simulated SiO_2:Eu^{3+} glass.

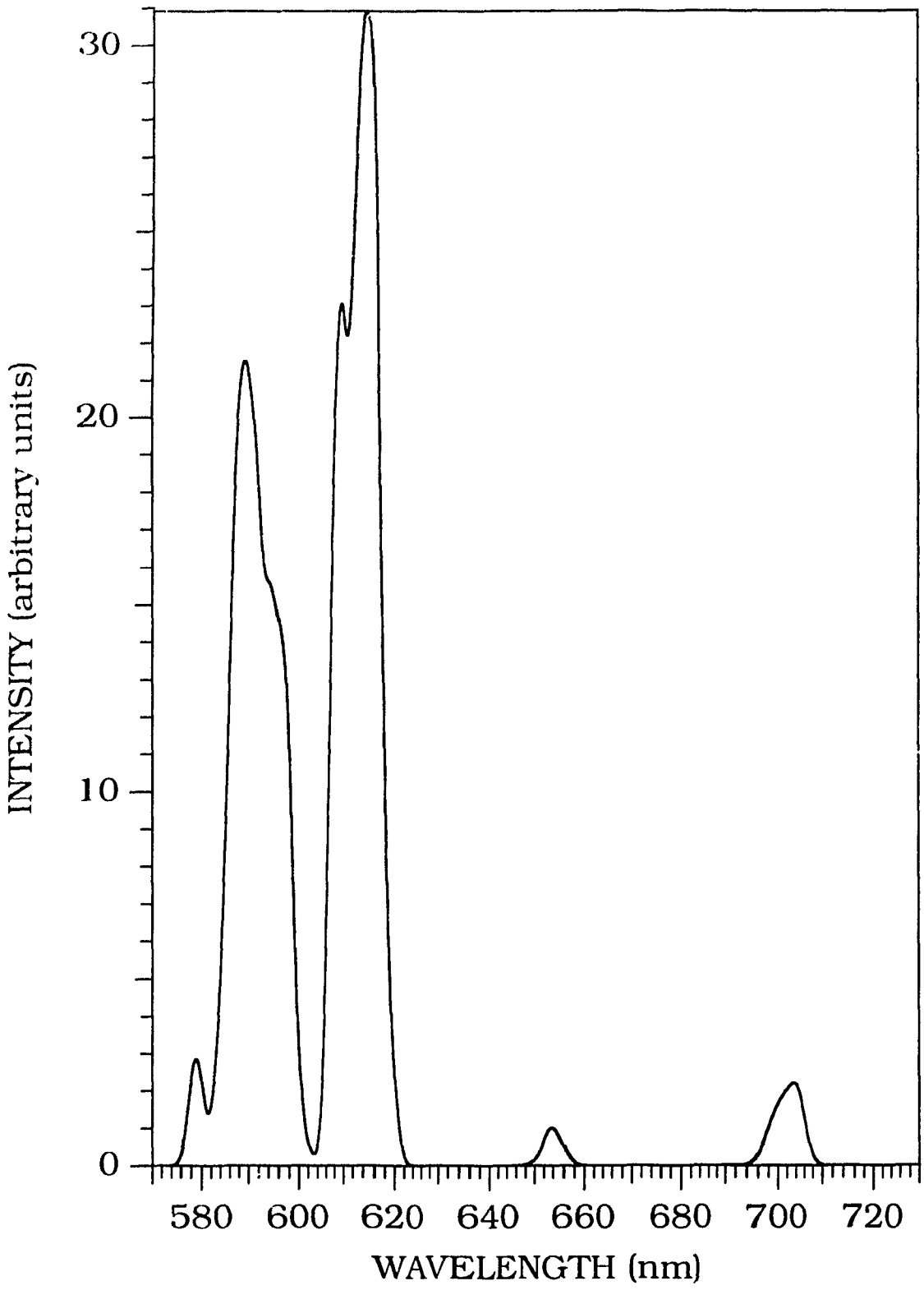

Figure 5.2.4.2. Emission spectrum for the simulated $SiO_2:Eu^{3+}$ glass.

5.3 DILUTION NARROWED LASER SPECTROSCOPY

Narrowing techniques, such as Fluorescence Line Narrowing, enable the spectroscopist to greatly clarify a fluorescence spectrum of trivalent rare-earth ions doped in inorganic vitreous matrices. Nevertheless, as we have seen in Section 5.2.2.3, these techniques remain macroscopic in nature. We might wonder what information could be obtained if the investigating technique was able to attain the ultimate limit of optical detection of a single impurity ion. Information such as the distribution of possible local environments could be envisioned, but also the relationship which exists between the impurity ion and its surroundings. This could lead to the direct investigation of local perturbations and to the localized descriptions of impurity relaxation and excitation transfer.

In 1979, Süsse *et al.* [161] proposed the experimental conditions to observe a single atomic impurity in a crystalline lattice. However, the observation of a few impurity ions (e.g. 1 to 10) was only realised 9 years later by Lange et al. [162]. These authors measured the variation of fluorescence intensity of Sm^{2+} ions doped in crystalline CaF_2 as a function of observation volume. They attributed this variation to the statistical distribution of the Sm^{2+} ions in the crystal. In the past few years, some work has dealt with the observation of single organic molecules imbedded in spectroscopically inert matrices. For example, Moerner and Kador used two different double modulation techniques to

detect single molecules of pentacene in p-terphenyl crystals [163]. The main advantage of working with organic molecules stems from the fact that the oscillator strengths for such molecules are approximately 10^7 greater than those of tr'valent rare-earth ions. It is therefore not surprising that the observation of single rare-earth ions in solid matrices has yet to be satisfactorily achieved.

The "macroscopic" behaviour discussed above for FLN spectroscopy is to be distinguished from the "microscopic" behaviour resulting from the extremely small sample size which is found for the doped simulated glasses presented in this thesis. The latter behaviour can result in spectra very much akin to those obtained from the Dilution Narrowed Laser Spectroscopy (DNLS) technique developed by Yen and co-workers [164] who have tentatively shown single-ion excitation spectra in a sample of Nd^{3+}-activated quartz fiber. Since it is possible to generate DNLS spectra by reducing considerably the associated linewidths of the simulated transitions (the w factor of equation 4.4.3), the simulation technique presented in this thesis is seen as an important analytical tool capable of interpreting DNLS spectra.

The Dilution Narrowed Laser Spectroscopy technique is based upon the sampling, of a very small number of rare-earth ions present in a extremely dilute sample, by an excitation source focused down as much as possible so that it interacts with a small volume of the material.

The excitation spectra, presented by Yen, were taken from a Nd^{3+}-doped silica fiber (6µm Ø). A single-mode tunable ring-dye laser was

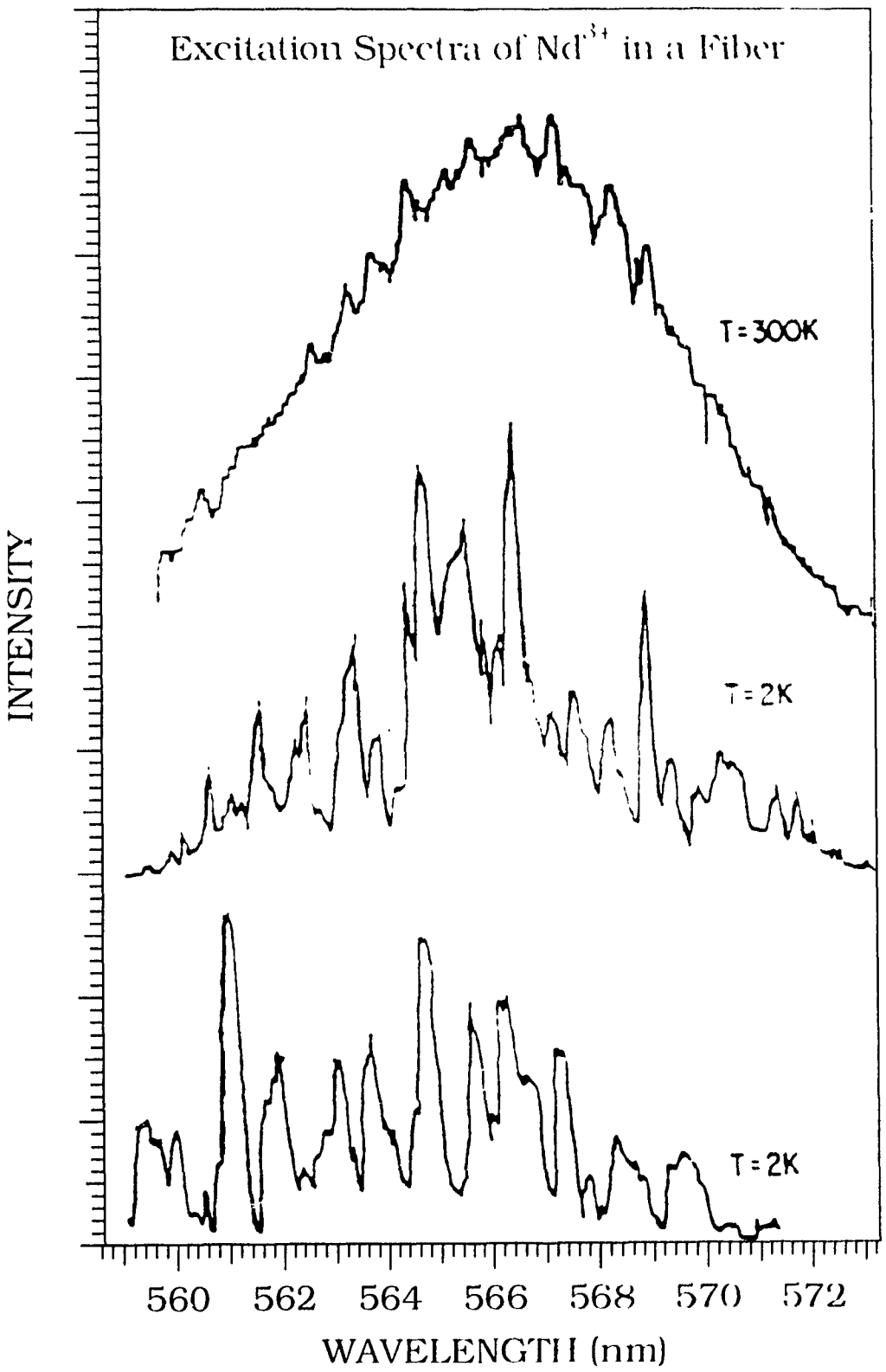

Figure 5.3.1 DNLS excitation spectra observed in a dilute Nd^{3+} doped glass fiber at room and at low temperature. Taken from Ref. 164.

tuned through the $^2G_{7/2},^4G_{5/2} \leftarrow {}^4I_{9/2}$ absorption bands while the $^4F_{3/2} \rightarrow {}^4I_{9/2}$ fluorescence was monitored. No emission monochromator was employed, the photomultiplier tube being directly illuminated by the fiber, resulting in an increase of sensitivity at the detriment of selectivity. The reported excitation spectra are presented in Figure 5.3.1. The spectrum at the top of Figure 5.3.1, represents a room temperature excitation spectrum, whose shape and width is reminiscent of the broadband spectrum of the $^2G_{7/2},^4G_{5/2} \leftarrow {}^4I_{9/2}$ absorption bands. The band spans the region between 559 and 573nm and has a FWHM of $\approx 225 cm^{-1}$. In this case, phonon broadening enlarges the individual contributions of the sampled ions, resulting in the broad convoluted bandshape. When the temperature is lowered to 2K, as shown in the middle spectrum of Figure 5.3.1, the individual transitions are no longer broadened and the spectrum reveals a toothed structure. This structure arises from the sampling of the individual Nd^{3+} ions within the excited volume which fluoresce at the monitored wavelength. At the bottom of Figure 5.3.1, the spectrum shown was recorded using exactly the same conditions as that of the middle spectrum, except that a different volume of the fiber was sampled. Since the distribution of Nd^{3+} ions is spatially random, one would expect a completely different DNLS spectrum. An analysis was performed in order to determine the number of ions which comprises one of the features seen in the wings of the low-temperature DNLS spectrum. By examining the lifetimes and the number of photons of the emitting levels, the author estimated that the number of individual ions was thirty to fifty. Single-ion spectroscopy could then be considered with resonant frequency selective excitation inside one of the

features shown in the DNLS spectrum. Such a study has been underway for the past several years [165].

The structural model that we have simulated, gives us the opportunity to investigate the samples at the microscopic level. In the previous Sections, we have presented spectroscopic results which were compared to broadband emission and absorption spectra of a laboratory glass. In order to make this comparison, we had to convolute individual spectral contributions by associating each transitional energy with a Gaussian bandshape having an broad width. This was done through the width (w) factor of equation (4.4.3). In Figure 5.3.2, we present the effect of the variation of the width factor on the $^5D_0 \leftarrow {}^7F_0$ transition of the simulated $Na_2O{\cdot}2SiO_2{:}Eu^{3+}$ glass. From top to bottom, the lineshapes were calculated with four different width factors (detailed in Table 5.3.1).

TABLE 5.3.1
WIDTH FACTORS AND CONVERSIONS
TO SPECTRALLY RELEVANT UNITS
FOR THE SPECTRA SHOWN IN FIGURE 5.3.2

width factor	energy (cm^{-1})	frequency	Type of spectra
45	≈ 100	≈ 3 THz	Broadband
5	≈ 10	≈ 300 GHz	
0.5	≈ 1	≈ 30 GHz	dye laser with a three-plate birefringent filter
$1.5e^{-3}$	≈ 0.003	≈ 100 MHz	ring dye laser with a low finesse etalon

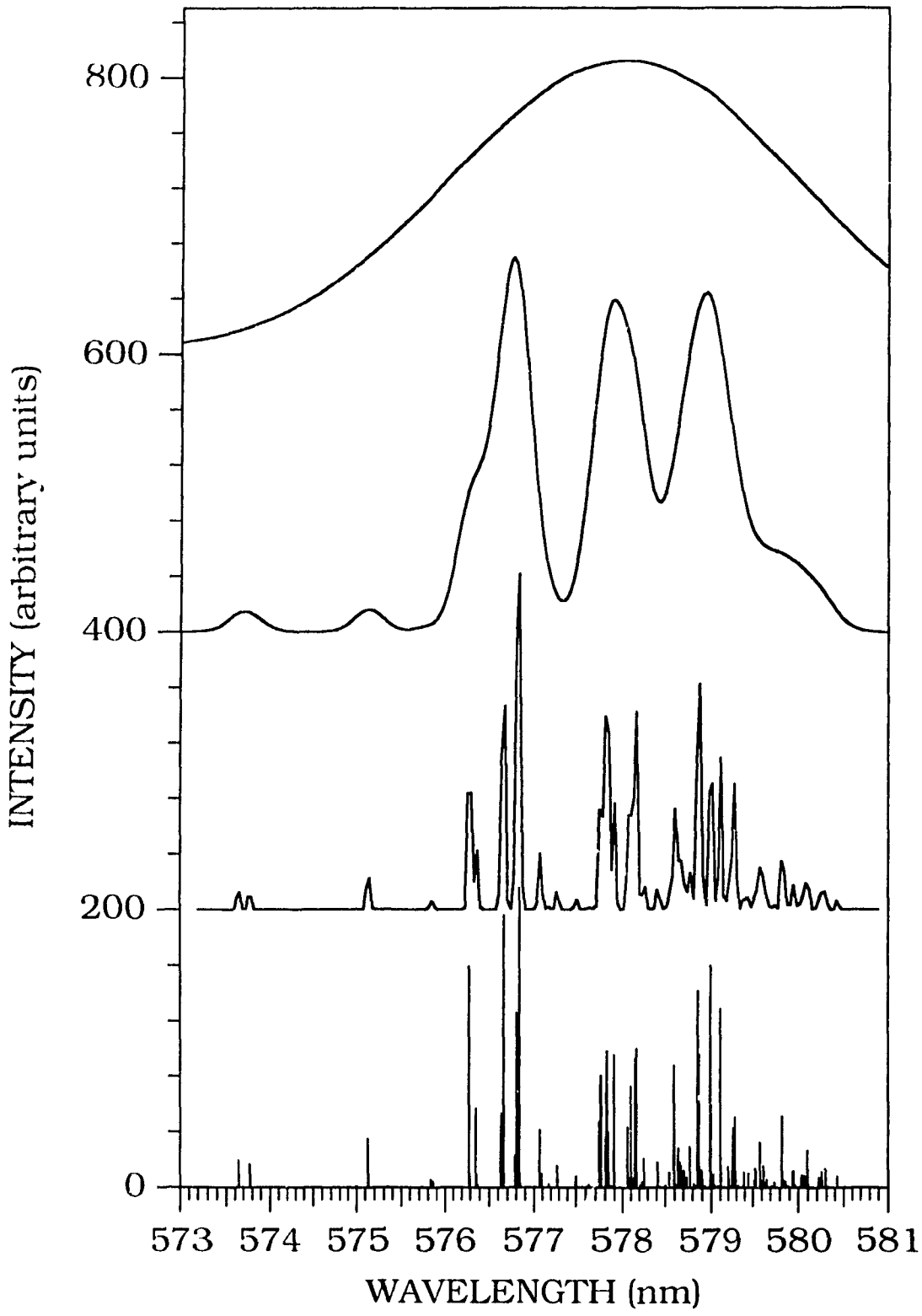

Figure 5.3.2 Variation of the width parameter of equation (4.4.3). Effect on the $^5D_0 \leftarrow ^7F_0$ transition of the simulated $Na_2O{\cdot}2SiO_2{:}Eu^{3+}$ glass.

Figure 5.3.2 clearly shows the effect of dilution narrowing, i.e. the evolution between probing the sample at a macroscopic and microscopic level. The top spectrum is a detail of the simulated $^5D_0 \leftarrow {}^7F_0$ transition taken from Figure 5.2.2.1.2. The width parameter used in this spectrum is large enough so that the bandshape is continuous and does not show any features, mimicking the experimental spectrum. By reducing the value of the width parameter, there is a continuous emergence of details; different average energetic environments appear in the second spectrum which then resolve into individual components in the subsequent spectra. The transition between dilution narrowed spectroscopy and single-ion spectroscopy is clearly seen in the bottom two spectra, where a complete deconvolution of the individual transitions occur. Although the bottom spectrum appears as composed of extremely narrowed transitions, the width employed (≈ 100 MHz) is still several orders of magnitude greater than the expected width of actual single-ion transitions. The ultimate limit will be the description of each individual transition by a Lorentzian bandshape with a linewidth corresponding to the homogeneous linewidth of each individual rare-earth ion. Homogeneous linewidths of rare-earth ions have been determined to be approximately 1 kHz to 1 MHz [159]. Individual homogeneous linewidths should be slightly different from each other, since each of the ions is coupled to a different local environment and should decay by slightly different dephasing mechanisms.

The simulated "*single-ion*" spectrum taken from Figure 5.3.2 is shown in greater detail in Figure 5.3.3. Several striking features are seen in this Figure. The first is the wide disparity between the intensities

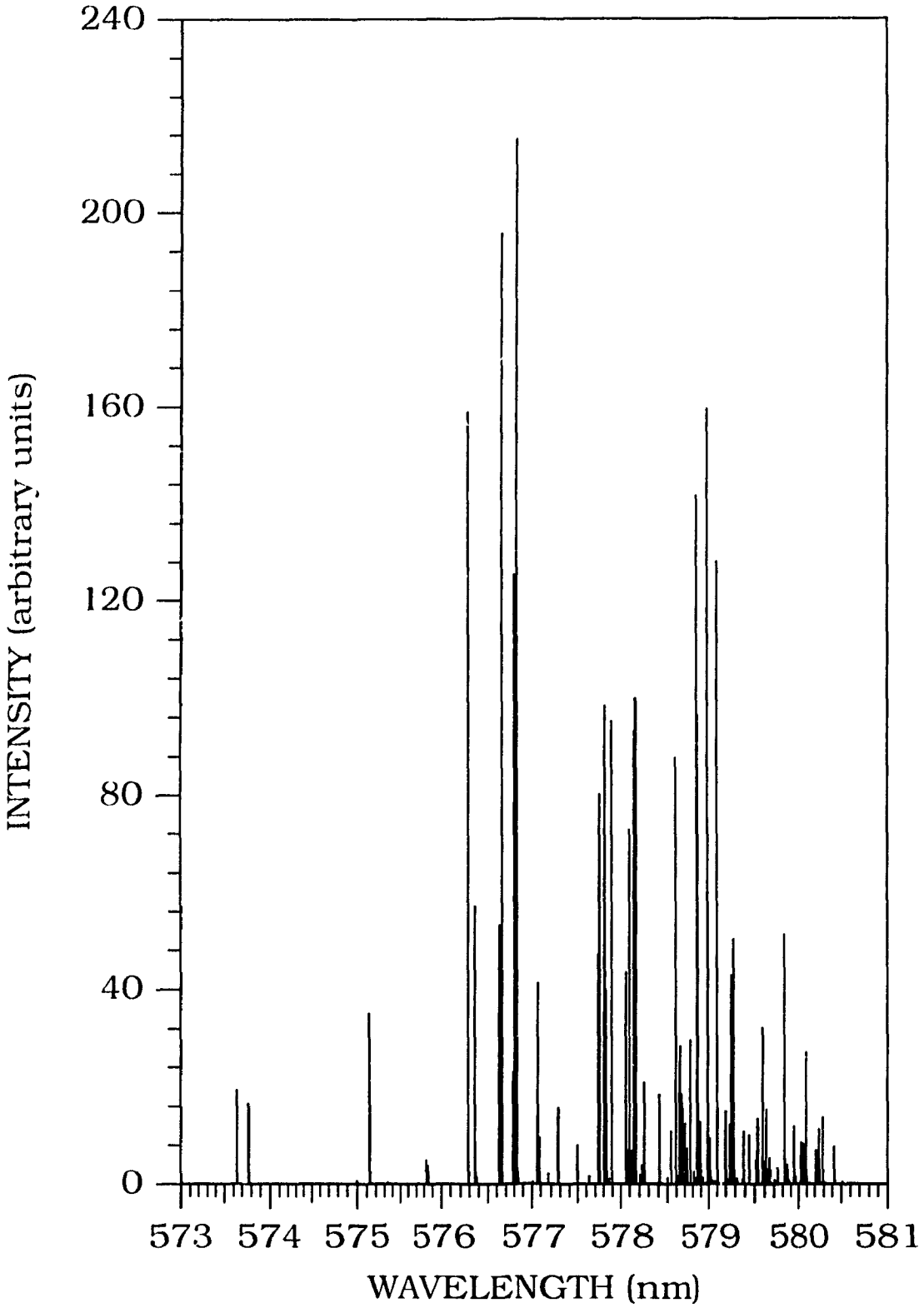

Figure 5.3.3 Simulated "*single-ion*" spectrum of the $^5D_0 \leftarrow ^7F_0$ transition for the simulated $Na_2O{\cdot}2SiO_2{:}Eu^{3+}$ glass.

of individual peaks. A careful examination of the transitional energies confirmed that none of the lines was made up of contributions from two or more Eu^{3+} ions. The difference in intensity will then necessarily stem from a difference in oscillator strength. The individual oscillator strengths of the $^5D_0 \leftarrow {}^7F_0$ transition for the 150 Eu^{3+} configurations span five orders of magnitude, from $f \approx 10^{-12}$ to 10^{-7}. The average value for this simulated transition was determined to be $f = 2.8 \times 10^{-9}$ (Table 5.2.2.1.3). Although selection rules dictate that this band should be formally forbidden, the wide range of oscillator strengths is not surprising since the local environment is one of the main factors for the lifting of the forbiddeness of this transition. The wide range of local environments sampled by the Eu^{3+} ions will necessarily be translated in a wide range of oscillator strengths for any given transition.

Secondly, the continuous distribution of rare-earth environments which is expected for a macroscopic sample is not observed in this Figure. Rather, the spectrum can be interpreted as showing a random sample (150 simulated Eu^{3+} ions) taken from the continuous random distribution of possible energetic sites ($\approx 10^{20}$ Eu^{3+} ions in a doped experimental glass). Experimentally, the sampling of a different excitation volume will lead to an entirely different spectrum (Figure 5.3.1). This behaviour can also be seen for the distribution of rare-earth environments in the simulated doped glasses. Glasses simulated from different initial atomic configurational files or with different temperature/time-step conditions will, invariably, lead to different equilibrated structures. The simulated ions will be in different spatial positions but their spatial organization will be equivalent, (e.g. silicate

tetrahedra will be present, network-modifiers will not be surrounded by an immoderate number of oxygen ions). This will lead to identical average structural and spectroscopic properties, (e.g. RDFs and CDFs, average coordination numbers, average crystal-field strengths, transitional baryecntres, average oscillator strengths, etc.), albeit for minor variations. To repeat, this is exactly the same as with DNLS. Different excitation volumes will lead to different spectra, albeit the average spectroscopic properties (transitional energy range, average transition probabilities, average homogeneous linewidths), of these spectra will necessarily be the same.

We must note that Figure 5.3.3 departs from reality since an actual single-ion spectrum would not span such a large energy domain. To resolve such an experimental spectrum, one would require an inordinately huge amount of data points. It is possible to resolve individual transitions having linewidths in the order of 1 kHz to 1 MHz, but, in order to remain tractable, such a spectrum would span an energy domain of not more than a few GHz (1 GHz $\approx$ 0.033 cm^{-1}).

In conclusion, the preliminary results presented by Yen [164,165] reveal the feasibility of single-ion spectroscopy of rare-earth ions doped in glass fibers. In order to extract relevant structural information from this experimental technique, one would need to turn to a structural/spectral model, such as that developed in this thesis. By simulating the exact stoichiometric composition as the studied fiber sample, then calculating the broadband, dilution narrowed and single-ion spectra of the rare-earth ions, it will be possible to identify plausible

structures which give rise to the experimentally observed single-ion features. Because of accidental degeneracies, each of the associated structure/spectroscopic features will not be unique solutions. Nevertheless, it is possible to present an exact solution to the local environment of every rare-earth ion probed within the excitation volume.

CONCLUSIONS

Optical spectroscopic methods are routinely employed to characterize the local atomic structure about rare-earth ions doped in crystalline matrices. However, similar studies performed on rare-earth doped glasses only reflect the average structural characteristics of the glass. At the time this thesis was initiated, we felt that none of the proposed structural models, based on spectroscopic investigations, sketched a realistic picture of the local environment of rare-earth ions doped in inorganic glasses.

With this thesis, we set out to investigate the local environment of rare-earth ions doped in inorganic glasses. We hoped to achieve this by the creation of a mathematically derived structural model, based on basic physical principles, which was to be validated by the comparison of experimentally obtained and simulated physical properties. By doing so, we ultimately ended up, not only with answers to the problem at hand, but also with the creation and refinement of a computational tool which allows such studies.

By the technique of Molecular Dynamics and using a two-body electrostatic potential having a Pauling repulsive term, we have simulated structural models of two rare-earth doped inorganic glasses. The following glasses were studied : $Na_2O{\cdot}2SiO_2{:}Eu^{3+}$ and $SiO_2{:}Eu^{3}$. The structure of the base glasses and the local environment of the doped trivalent europium ions were investigated with the help of radial distribution functions, cumulative distribution functions and bond angle

distributions of the various atomic species found in both glasses. The following can be concluded from these studies.

(i) The average coordination number of the Eu^{3+} ion was found to be 4 and 6 in SiO_2 and $Na_2O{\cdot}2SiO_2$ glasses, respectively.

(ii) The point symmetry of the local environment of the Eu^{3+} ions was found to be, without any exceptions, C_1.

(iii) The oxygens bonded to the Eu^{3+} ions were shown to belong to distinct silicate tetrahedra.

(iv) The local structure of the europium ions was found to be influenced to a greater degree by it's bonding and energetic requirements than by the topology of the silicate framework. We suggest that the Eu^{3+} ions form quasi-molecular complexes.

(v) The role of the Eu^{3+} ion in the formation of "*free*" oxygens has been elucidated and a mechanism has been proposed.

A successful validation of the simulated structural model of the $Na_2O{\cdot}2SiO_2{:}Eu^{3+}$ glass was performed through a comparison between (i) room-temperature absorption and broadband emission spectra of the experimental glass and (ii) calculated $^5L_6$, $^5D_3$, $^5D_2$, $^5D_1$, $^5D_0 \leftarrow {}^7F_{0,1}$ absorption and $^5D_0 \rightarrow {}^7F_J$ (J= 0 to 6) emission spectra of the simulated glass. The simulated spectra were obtained using a point-charge crystal field model, which allows the calculation of the energies and transition probabilities of the electronic manifolds belonging to the simulated Eu^{3+} ions.

This validation culminated in the creation of an indirect link between the simulated structural model and the experimental spectra of the corresponding laboratory glass. This link permitted the investigation of various spectral properties of rare-earth doped glasses, amongst them, Fluorescence Line Narrowing measurements, spectral correlations of individual structural factors and the effects of J-mixing and overall covalency on transitional energies and inhomogeneous broadening.

This study lead us to conclude that the presence of a limited number of distorted "*sites*" for rare-earth ions doped in oxide glasses is fallacious and tends to disprove the various structural models previously proposed for local rare-earth environments. The rare-earth environments are rather composed of a continuous distribution of local-fields which satisfy energetic bonding requirements of the Eu^{3+} ions while disregarding structural bonding requirements normally attributed to complexes or crystalline compounds. It was found that none of the individual structural factors greatly influences the electronic spectra of doped ions in inorganic glasses. Rather, we present evidence that it is the overall electrostatic and covalent energy, with an emphasis on the preponderance of J-mixing, of the individual sites which hold the greatest influence.

Due to the lack of an experimental SiO_2:Eu^{3+} glass sample, we were not able to validate the structure of this glass nor its spectroscopy. Nevertheless, we have proposed simulated absorption and emission spectra for the simulated SiO_2:Eu^{3+} glass.

Finally, we have theoretically investigated an experimental technique named Dilution Narrowed Laser Spectroscopy (DNLS) which could eventually lead to the observation of the optical spectrum of isolated rare-earth ions doped in glass fibers. We propose that the structural/spectral model created through Molecular Dynamics and point-charge crystal-field calculations is presently the most reliable means to interpret DNLS and single-ion spectra.

FUTURE WORK

The study initiated in this thesis has opened up many avenues of investigation. As mentioned in the Introduction, one of the ultimate goals for glass and laser scientists, would be to create an expert system which would be able to investigate all the compositional possibilities in order to find a doped glass with a defined set of optical properties. As such, the work presented in this thesis is amongst the first which could eventually lead us to the creation of such an expert system. The road to this expert system should (and must) also lead us to a more profound understanding of the nature of amorphous materials. It could then finally be said that Zachariasen's statement no longer holds.

In this thesis, we have merged two entirely different computational methods in order to create a new *tool* which allows the investigation of rare-earth doped oxide glasses. Any future work will have to proceed with the improvement of the two methods used; the first to simulate a structural model of the doped amorphous matrix and the second to calculate the electronic spectrum of the dopant in this matrix. Finally, investigations must also be extended towards the understanding of the varying properties of the simulated materials.

Specifically, the following points should be considered in detail.

The structural model

Molecular Dynamics is the ideal choice for the simulation of insulator glasses. Nevertheless certain improvements can be brought to the actual simulation method

(i) Implementation of a three-body potential in order to simulate bond directionality in the framework created by the network-former.

(ii) Implementation of a greater dopant sample size, which would improve the statistical reliability of spectral properties of the dopant ions. This could also allow the study of spectral effects such as energy migration and structural effects such as rare-earth ion clustering.

(iii) Implementation of a smaller quenching rate, in order to simulate a glass with fewer number of high energy defects.

(iv) Calculation of the frequency spectrum of the glass, which would serve in the calculation of the normal vibrational modes for the doped rare-earth ion and the calculation of the phonon density of states.

Presently, only one factor limits the proper implementation of these four items: availability of computational power. The availability of

clustered Unix workstations, which bring together the computational power of supercomputers with the manageability of personal computers and a relatively low purchase price, is the most immediate solution to this problem.

The spectral model

The spectra which we have simulated in this thesis are basically "*static*" in nature; they do not include any dynamic processes which modify the spectral response of the dopant ion with time. Such processes can be divided in two distinct groups, (i) non-radiative processes where energy is transferred between the dopant ion and the surrounding matrix and (ii) energy transfer processes, where energy is transferred between adjacent dopant ions. The inclusion of such effects, in the present simulation, could be taken care of by considering the following

(i) Inclusion of a ion-lattice coupling term in the perturbation Hamiltonian. This term would couple the electronic centre with the phonon density of state of the glass matrix. Thus, non-radiative transitions due to single- and multi-phonon processes could be calculated.

(ii) Inclusion of a ion-ion coupling term in the perturbation Hamiltonian, which together with kinetic and population factors could result in the calculation of energy transfer processes. These calculations could possibly lead to the prediction of up-conversion processes. Energy-transfer

from dissimilar ions, resulting from co-doping, could also be investigated.

The point-charge crystal-field model, used in this study, would also greatly benefit by the inclusion of various distinct contributions. Several major contributions could be investigated

(i) Lattice-induced multipole contributions, where mutual interaction of the polarizable point charges which represent the ions of the glass matrix, yields a set of permanent multipole moments.

(ii) Ion-induced multipole contributions, where the interaction between the electrons of the unfilled $4f$ shell of the dopant rare-earth ion and the surrounding polarizable ligands, is calculated.

Materials

The investigation, on an atomic basis, of the structural and optical properties of rare-earth doped inorganic glasses could proceed with the use of the present computational tool. Specifically, the following need to be considered

(i) Technologically important rare-earth ions, such as Nd^{3+} and Er^{3+}, could be investigated especially in regards with non-radiative and energy transfer processes which

influence directly the efficiency of up-conversion and laser mechanisms.

(ii) Technologically important glass compositions, such as phosphate glasses which possess many attractive features for lasers and fiber amplifiers.

(iii) Influence of network-modifier ions upon the local environment of the rare-earth dopant, has to be investigated systematically, with a focus on the charge and the size of such ions. The subsequent influence on the optical spectra should be kept in perspective in order to accumulate data for any future investigations on compositional predictability.

(iv) The structural model of the $SiO_2:Eu^{3+}$ glass should be validated with the obtention of an experimental sample.

Laser Spectroscopy

We have presented in Section 5.2.2.3, Fluorescence Line Narrowing results of the laboratory $Na_2O{\cdot}2SiO_2:Eu^{3+}$ glass. This investigation was not complete and several points still need to be addressed. Specifically,

(i) understanding the presence of *"energy transfer"* bands observed in the spectra excited on the high-energy side of

the $^5D_0 \leftarrow ^7F_0$ absorption band.

(ii) understanding the behaviour of the Stark levels when exciting close to or in the $^5D_0 \leftarrow ^7F_1$ absorption band.

Finally, Section 5.3 presents a theoretical investigation on Dilution Narrowed Laser Spectroscopy and single-ion spectroscopy. With the eventual realisation of experimental spectra, studies will need to be perfomed on the proper structural/spectral model in order to extract relevant structural information.

BIBLIOGRAPHY

1. W.H. Zachariasen, "The atomic arrangement in glass", J. Am. Chem. Soc. **54** 3841-3851 (1932).

2. E.A. Porai-Koshits, "Overview", in *Glass: Science and technology, vol. 4A, Structure, Microstructure and Properties* , D.R. Uhlmann and N.J. Kreidl, Academic Press, (1990) 1-31

3. J. Zarzycki, *Glasses and the vitreous state*, Cambridge University Press, 1991, Chap. 4 .

4. *ibid*, Chap.5

5. G.N. Greaves, "EXAFS and the structure of glass", J. Non-Cryst. Solids, **71** 203-217 (1985).

6. L.V. Woodcock, C.A. Angell and P. Cheeseman, "Molecular dynamics studies of the vitreous state : Simple ionic systems and silica", J. Chem. Phys. **65** 1565-1577 (1976) .

7. L.V. Woodcock and K. Singer, "Thermodynamic and structural properties of liquid ionic salts obtained by Monte Carlo computation", Trans. Faraday Soc. **67** 12-30 (1971) .

8. N. Jacquet-Francillon, " Verres pour l'immobilisation de déchets nucléaires", Verre (Paris) **5(1)** 9-21 (1991) .

9. M.J. Weber, "Science and technology of laser glass" , J. Non-Cryst. Solids, **123(1-3)** 208-222 (1990) .

10. W.J. Miniscalco, "Erbium-doped glasses for fiber amplifiers at 1500nm", J. Lightwave Technol. **9(2)** 234-250 (1991) .

11. R.J. Araujo and N.F. Borrelli, in *Optical Properties of Glasses*, D.R. Uhlmann and N.J. Kreidl, eds. American Ceramic Society, (1990).

12. K.Bange, T. Gambke, "Electrochromic materials for optical switching devices", Adv. Mater. **2(1)** 10-16 (1990).

13. W.E. Moerner, W. Lenth and G.C. Bjorklund , "Frequency domain optical storage and other applications of persistent spectral hole burning", in *Persistent Spectral Hole-Burning: Science and Applications*, W.E. Moerner, ed., Springer-Verlag (1988) 251 307 .

14. S.E. Stowkowski, "Laser glass : An engineered material", in *Lasers, Spectroscopy and new ideas. A tribute to Arthur L. Schawlow* , W.M. Yen and M.D. Levenson, eds., Springer-Verlag (1987) 47-88.

15. G.N. Greaves, A. Fontaine, P. Lagarde, D. Raoux and S.J. Gurman, "Local structure of silicate glasses", Nature, **293** 611-616 (1981).

16. B.E. Warren, H. Krutter and O. Morningstar, "Fourier analysis of X-ray patterns of vitreous SiO_2 and B_2O_3", J. Am. Ceram. Soc., **19** 202-206 (1936).

17. H.J.L. Trap and J.M. Stevels, "Physical properties of invert glasses", Glastech. Ber. **32 K** VI/31-52 (1959).

18. R.L. Mozzi and B.E. Warren, "The structure of vitreous silica", J. Appl. Cryst. **2** 164-172 (1969).

19. H. Bethe, "Termaufspaltung in Kristallen", Ann. Phys. (Leipzig) **3** 133-208 (1929).

20. P. Pringsheim and S. Schlivitch "Über die Fluoreszenz von Praseodym- und Neodymglas", Z. Phys. **61** 297-306 (1930).

21. R. Rosenhauer and F. Weidert "Spectral absorption of Neodymium glasses" , Glastech. Ber. **16** 51-57 (1938).

22. R. Tomaschek, "On the application of phosphorescence spectra to the investigation of the structure of solids and solutions", Trans. Faraday Soc. **35** 148-154 (1939).

23. C.R. Kurkjian, P.K. Gallagher, W.R. Sinclair and E.A. Sigety, "The absorption and fluorescence spectra of trivalent europium in silicate glasses", Phys. Chem. Glasses **4** 239-246 (1963).

24. T. Bates, and R.W. Douglas, "Absorption bands of Cr^{3+} in solutions, crystals and glasses", J. Soc. Glass Tech. **43** 289-307 (1959).

25. C.R. Bamford, " Application of the ligand field theory to colored glasses" , Phys. Chem. Glasses **3(6)** 189-202 (1962).

26. R. Tomaschek, "Regularities in the line spectra of solids", Z. Phys. **33** 878-884 (1932).

27. S. Mockovciak, J. Pantoflicek and K. Patek, "Crystal field calculations of transition probabilities in Nd^{3+} in glass", Phys. Stat. Sol. **11** 401-405 (1965).

28. C.K. Jörgensen, R. Pappalardo and H.H. Schmidtke, " Do the 'ligand field' parameters in lanthanides represent weak covalent bonding ?", J. Chem. Phys. **39(6)** 1422-1430 (1963).

29. S.K. Barber, "The ytterbium ion as a microprobe in oxide glasses", in *Interaction of radiation with solids*, A. Bishay ed., Plenum, New York (1967) 593-606.

30. R. Pappalardo and D.L. Wood, "Spectrum of Yb^{3+} in yttrium gallium garnet", J. Chem. Phys. **33(6)** 1734-1742 (1960).

31. D.K. Rice and L.G. DeShazer, "Spectral broadening of europium ions in glass", Phys. Rev. **186(2)** 387-392 (1969).

32. M.M. Mann and L.G. DeShazer, "Energy levels and spectral broadening of neodymium ions in laser glass", J. Appl. Phys. **41(7)** 2951-2957 (1970).

33. D.K. Rice and L.G. DeShazer, "Spectra of europium in monoclinic gadolinium sesquioxide", J. Chem. Phys. **52(1)** 172-178 (1970).

34. C.C. Robinson and J.T. Fournier, "Coordination of Yb^{3+} in some inorganic glasses from optical absorption and emission studies", Chem. Phys. Lett. **3(7)** 517-519 (1969).

35. C.C. Robinson and J.T. Fournier, "Co-ordination of Yb^{3+} in phosphate, silicate and germanate glasses", J. Phys. Chem. Solids, **31** 895-904 (1970).

36. J.T. Fournier, and R.H. Bartram, "Inhomogeneous broadening of the optical spectra of Yb^{3+} in phosphate glass", J. Chem. Phys. Solids **31** 2615-2624 (1970).

37. C.C. Robinson, "Evidence of sixfold coordination of Nd^{3+} in barium rubidium silicate glass", J. Chem. Phys. **54(8)** 3572-3578 (1971).

38. C.C. Robinson, "Multiple sites for Er^{3+} in alkali silicate glasses (I). The principal sixfold coordinated site of Er^{3+} in silicate glass", J. Non-Cryst. Solids **15** 1-10 (1974).

39. C.C. Robinson, "Multiple sites for Er^{3+} in alkali silicate glasses (II). Evidence of four sites for Er^{3+}", J. Non-Cryst. Solids **15** 11-29 (1974).

40. K.R. Lea, M.J.M. Leask and W.P. Wolf, "The raising of angular momentum degeneracy of *f*-electrons by cubic crystal fields", J. Phys. Chem. Solids, **23** 1381-1405 (1962).

41. K.W.H. Stevens, "Matrix elements and operator equivalents connected with the magnetic properties of rare earth ions", Proc. Phys. Soc. Lond. **A65** 209-215 (1952).

42. R. Reisfeld, R. Velapoldi, L. Boehm and M. Ish-Shalom, "Transition probabilities of europium in phosphate glasses", J. Phys. Chem. **75(26)** 3980-3983 (1971).

43. R. Reisfeld and Y. Eckstein, "Absorption and emission spectra of thulium and erbium in borate and phosphate glasses", J. Solid State Chem. **5** 174-185 (1972).

44. R. Reisfeld and N. Lieblich, "Optical spectra and relaxation of Eu^{3+} in germanate glasses", J. Phys. Chem. Solids, **34** 1467-1476 (1973).

45. L.A. Riseberg, "Laser-induced fluorescence line narrowing spectroscopy of glass:Nd", Phys. Rev. A **7(2)** 671-678 (1973).

46. M.J. Weber, "Laser excited fluorescence spectroscopy in glass", in *Laser Spectroscopy of Solids*, W.M. Yen and P.M. Selzer, eds., Springer-Verlag 2nd edition 189-239 (1986).

47. J.A. Capobianco, P.P. Proulx and N. Raspa, "Laser-excited fluorescence spectroscopy and crystal-field analysis of europium(III)-doped cordierite glass",Chem. Phys. Lett. **160(5,6)** 591-596 (1989) .

48. J.A. Capobianco, P.P. Proulx, M. Bettinelli and F. Negrisolo, "Absorption and emission spectroscopy of Eu^{3+} in metaphosphate glasses", Phys. Rev. B **42(10)** 5936-5944 (1990) .

49. J.A. Capobianco, P.P. Proulx, B. Andriananosolo and B. Champagnon, "Nucleation kinetic studies of a europium-doped aluminosilicate glass : Low-frequency inelastic scattering and fluorescence line narrowing", Phys. Rev. B **43(13-A)** 10031-10035 (1991).

50. C. Brecher and L.A. Riseberg, "Laser-induced fluorescence line narrowing in Eu glass : A spectroscopic analysis of coordination structure", Phys. Rev. B **13(1)** 81-93 (1976).

51. C. Brecher and L.A. Riseberg, "Laser-induced line-narrowing of Eu^{3+} fluorescence in fluoroberyllate glass : Site-dependent spectroscopic properties and their structural implications" , Phys. Rev. B. **21(6)** 2607-2618 (1980).

52. W.W. Wood and F.R. Parker, "Monte-Carlo equation of state of molecules interacting with the Lennard-Jones potential", J. Chem. Phys. **27** 720-724 (1957).

53. B.J. Alder and T.E. Wainwright, "Phase transition for a hard sphere system", J. Chem. Phys. **27** 1208-1209 (1957).

54. A. Rahman, "Correlations in the motion of atoms in liquid argon", Phys. Rev. **136(2A)** 405-411 (1964).

55. C.A. Angell, J.H.R. Clarke and L.V. Woodcock, "Interaction potentials and glass formation : A survey of computer experiments", Adv. Phys. Chem. **48** 397-453 (1981).

56. M. Dove, "Molecular dynamics simulations in the solid state sciences", NATO ASI Ser. C, **225** 501-590 (1988).

57. T.F. Soules, "Stochastic and molecular dynamic models of glass structure", in *Glass: Science and technology, vol. 4A, Structure, Microstructure and Properties*, D.R. Uhlmann and N.J. Kreidl, Academic Press, (1990) 267-337.

58. G. Ciccotti and W.G. Hoover, *Molecular-Dynamics simulation of statistical-mechanical systems*, *Proceedings of the International School of Physics « Enrico Fermi»*, North-Holland (1986).

59. J.M. Haile, *Molecular Dynamics Simulation, Elementary Methods*, John Wiley & Sons, (1992).

60. A. Rahman, R.H. Fowler and A.H. Narten, "Structure and motion in liquid BeF_2, $LiBeF_3$ and LiF from molecular dynamics calculations", J. Chem. Phys. **57(7)** 3010-3011 (1972).

61. R.J. Bell and P. Dean , "The structure of vitreous silica : Validity of the Random Network Theory", Phil. Mag. **25** 1381-1398 (1972).

62. L.V. Woodcock, C.A. Angell and P. Cheeseman, "Molecular dynamics studies of the vitreous state : Simple ionic systems and silica", J. Chem. Phys. **65(4)** 1565-1577 (1976).

63. T.F. Soules, "A molecular dynamics calculation of the structure of sodium silicate glasses", J. Chem. Phys. **71(11)** 4570-4578 (1979).

64. T.F. Soules and R.F. Busbey, "Sodium diffusion in alkali silicate glass by molecular dynamics", J. Chem. Phys. **75(2)** 969-975 (1981).

65. S.K. Mitra, M. Amini, D. Fincham and R.W. Hockney, "Molecular dynamics simulation of silicon dioxide glass", Phil. Mag. B **43(2)** 365-372 (1981).

66. S.K. Mitra, "Molecular dynamics simulation of silicon dioxide glass", Phil. Mag. B **45(5)** 529-548 (1982).

67. S.H. Garofalini, "Molecular dynamics simulation of the frequency spectrum of amorphous silica", J. Chem. Phys. **76** 3189-3192 (1982).

68. S.H. Garofalini, "Pressure variation in molecular dynamics simulated vitreous silica", J. Non-Cryst. Solids **55** 451-454 (1983).

69. S.K. Mitra and R.W. Hockney, "Molecular dynamics simulation of the structure of soda silica", Phil. Mag. B **48(2)** 151-167 (1983).

70. S.H. Garofalini, "Defect species in vitreous silica -- a molecular dynamics simulation", J. Non-Cryst. Solids **63** 337-345. (1984).

71. K. Hirao and N. Soga, "Molecular dynamics study of $2R_2O{\cdot}SiO_2$ glasses", J. Non-Cryst. Solids **84** 61-67 (1986).

72. A.A. Tesar and A.K. Varshneya, "Molecular dynamics simulation of alkali-silicate glass structures", J. Chem. Phys. **87(5)** 2986-2989 (1987).

73. H. Inoue and I. Yasui , "A molecular dynamics simulation of the structure of silicate glasses", Phys. Chem. Glass, **28(2)** 63-69 (1987).

74. J.D. Kubicki and A.C. Lasaga, "Molecular dynamics simulations of SiO_2 melt and glass: Ionic and covalent models", Am. Mineral. **73** 941-955 (1988).

75. B.P. Feuston and S.H. Garofalini, "Empirical three-body potential for vitreous silica", J. Chem. Phys. **89(9)** 5818-5824 (1988).

76. R.G. Newell, B.P. Feuston and S.H. Garofalini, "The structure of sodium trisilicate glass via molecular dynamics employing three-body potentials", J. Mater. Res. **4(2)** 434-439 (1989).

77. C. Huang and A.N. Cormack, "The structure of sodium silicate glass", J. Chem. Phys. **93(11)** 8180-8186 (1990).

78. H. Melman and S.H. Garofalini, "Microstructural evaluation of simulated sodium silicate glasses", J. Non-Cryst. Solids **134** 107-115 (1991).

79. W.H. Busing, "Interpretation of the crystal structure of Li_2BeF_4 in terms of the Born-Mayer-Huggins model", J. Chem. Phys. **57(7)** 3008-3009 (1972).

80. L. Pauling, *The nature of the chemical bond*, 3rd ed., Cornell University Press, Ithaca NY, (1960) 321.

81. F.H. Stillinger and T.A. Weber, "Computer simulation of local order in condensed phases of silicon", Phys. Rev. B **31(8)** 5262-5271 (1985).

82. Y. Matsui and K. Kawamura, "Computer simulation of structures of silicate melts and glasses", in *Materials science of the Earth's interior*, I. Sunagawa ed., Terra Scientific, (1984), 3-23.

84. H. Ogawa and Y. Waseda, "A review of Molecular Dynamics studies on silica and silicate melts", Sci. Rep. Res. Inst., Tohoku Univ., Ser A.**36(1)** 20-35 (1991).

85. S.A. Brawer, and M.J. Weber," Monte-Carlo simulation of Eu^{3+}-doped BeF_2 glass", Phys. Rev. Lett. **45(6)** 460-463 (1980).

86. S.A. Brawer, and M.J. Weber, "Theoretical study of the structure and optical properties of rare-earth-doped BeF_2 glass", J. Non-Cryst. Solids **38 & 39** 9-14 (1980).

87. S.A. Brawer, and M.J. Weber, "Molecular dynamics simulation of the structure of rare-earth-doped beryllium fluoride glasses", J. Chem. Phys. **75(7)** 3522-3541 (1981) .

88. S.A. Brawer, and M.J. Weber, " Neodymium fluorescence in glass : Comparison with computer simulations of glass structure", J. Lumin. **24/25** 115-118 (1981).

89. M.J. Weber, and S.A. Brawer, "Comparison of optical spectra and computer-simulated structure of rare-earth doped fluoroberyllate glasses", J. Non-Cryst. Solids **52** 321-336 (1982).

90. M.J. Weber and S.A. Brawer "Investigations of glass structure using fluorescence line narrowing and molecular dynamics simulations", J. Phys. (Paris) **Coll. C9 suppl. au n°12, tome 43** 291-301 (1982).

91. M.J. Weber, "Ab Initio calculations of the optical properties of ions in glass", J. Non-Cryst. Solids **73** 351-357 (1985).

92. Hirao, K. and Soga, N. "Molecular dynamic simulation of Eu^{3+} doped sodium borate glasses and their fluorescence spectra", J. Am. Ceram. Soc. **68 (10)** 515-521 (1985) .

93. L. Verlet, "Computer experiments on classical fluids. I. Thermo dynamical properties of Lennard-Jones Molecules", Phys. Rev. **159(1)** 98-103 (1967).

94. B.G. Wybourne, *Spectroscopic properties of rare earths* , Interscience (1965).

95. S. Hüfner, *Optical spectra of transparent rare earth compounds*, Academic, (1978).

96. J.C. Slater, "The theory of complex spectra", Phys. Rev. **34** 1293 1322 (1929).

97. L.H. Thomas, " The motion of the spinning electron", Nature **107** 514 (1926).

98. J. Frenkel, "Die Elektrodynamik des rotierenden Elektrons", Z. Phys. **37** 243-262 (1926).

99. E.U. Condon and G.H. Shortley, *The theory of atomic spectra*, Cambridge University Press, (1957).

100. G.H. Dieke , *Spectra and energy levels of rare earth ions in crystals*, Interscience, (1968).

101. W.T. Carnall, P.R. Fields and K. Rajnak, "Electronic energy levels of the trivalent lanthanide aquo ions. IV. Eu^{3+}", J. Chem. Phys. **49(10)** 4450-4455 (1968).

102. C.A. Morrison and R.P. Leavitt, in *Handbook on the Physics and Chemistry of Rare-Earths*, K.A. Gschneider and L. Eyring eds., North-Holland, (1982), chap.46.

103. C.A. Morrison, *Crystal-fields for transition-metal ions in laser host materials*, Springer-Verlag (1992).

104. R.P. Leavitt, C.A. Morrison and D.E. Wortman, *Rare earth ion-host crystal field interactions 3. Three-parameter theory of crystal fields*, Harry Diamond Laboratories Report TR-1673 (1975).

105. S. Fraga, K.M.S. Saxena and J. Karwowski, *Physical Science Data 5, Handbook of atomic data*, Elsevier, New York (1976).

106. R.M. Sternheimer, M. Blume and R.F. Peierls, "Sheilding of crystal fields at rare-earth ions", Phys. Rev. **173** 376- (1968).

107. C.A. Morrison and R.P. Leavitt, "Crystal-field analysis of triply ionized rare earth ions in lanthanum trifluoride", J. Chem. Phys. **71(6)** 2366-2374 (1979).

108. R.P. Leavitt, "On the role of certain rotational invariants in crystal field theory", J. Chem. Phys. **77(4)** 1661-1663(1982).

109. M. Tinkham, *Group theory and quantum mechanics*, McGraw-Hill, New York, (1964).

110. E.U. Condon and G.H. Shortley, *The theory of atomic spectra*, Cambridge University Press, (1957) Chap.9.

111. B.R. Judd, "Optical absorption intensities of rare-earth ions", Phys. Rev. **127(3)** 750-761 (1962).

112. G.S. Ofelt, "Intensities of crystal spectra of rare-earth ions", J. Chem. Phys. **37(3)** 511-520 (1962).

113. W.F. Krupke, "Optical absorption and fluorescence intensities in several rare-earth-doped Y_2O_3 and LaF_3 single crystals", Phys. Rev. **145(1)** 325-337 (1966).

114. C.A. Morrison, R.P. Leavitt, J.B. Gruber and N.C. Chang, "Optical spectra, energy levels, and crystal-field analysis of tripositive rare earth ions in yttrium (III) oxide. III. Intensities and g values for C_2 sites", J. Chem. Phys. **79(10)** 4758-4763 (1983).

115. C.W. Nielson and G.F. Koster, *Spectroscopic coefficients for the p^n,d^n, and f^n configurations*, MIT (1963).

116. L.J.F. Broer, C.J. Gorter and J. Hoogschagen, "On the intensities and the multipole character in the spectra of the rare earth ions", Physica **11(4)** 231-249 (1945).

117. W.T. Carnall, in *Handbook on the Physics and Chemistry of Rare Earths*, K.A. Gschneider and L. Eyring eds., North-Holland, (1979), chap.24.

118. M.J. Weber, T.E. Varitimos and B.H. Matsinger, "Optical intensities of rare-earth ions in yttrium orthoaluminate", Phys. Rev. B **8(1)** 47-53 (1973).

119. R.D. Peacock, in *Structure and Bonding*, vol. 22 J.D. Dunitz *et al.*, eds. Springer-Verlag (1975) 83.

120. J. Felsche, in *Structure and Bonding*, vol. 13 J.D. Dunitz *et al.*, eds. Springer-Verlag (1973) 99.

121. J.S. Jen and M.R. Kalinowski, " An ESCA study of the bridging to non-bridging oxygen ratio in sodium silicate glass and the correlations to glass density and refractive index", J. Non-Cryst. Solids **38-39(1)** 21-26 (1980).

122. G.W. Morey, *The Properties of Glass* , Reinhold Publishing Corp. (1938) p. 229 .

123. C.A. Morrison and R.P. Leavitt, "Programs at HDL for calculating optical properties of rare earth ions in single crystal hosts", Harry Diamond Laboratories, Internal Report (1991).

124. W.H. Press, B.P. Flannery, S.A. Teukolsky and W.T. Vetterling, ***Numerical Recipes***, *The art of scientific computing*, Cambridge University Press, (1989), pp.346-349.

125. see for example, R.E. Christoffersen, *Basic Principles and Techniques of Molecular Quantum Mechanics*, Springer-Verlag, (1989), Chap. 3.

126. M.E. Rose, *Elementary theory of angular momentum*, Wiley, 1967.

127. C.A. Morrison, R.P. Leavitt and D.E. Wortman, "Crystal-field analysis of triply ionized lanthanides in $Cs_2NaLnCl_6$", J. Chem. Phys. **73(6)** 2580-2598 (1980).

128. C. Nelson, *Transition elements in alkali-aluminosilicate melts: Spectroscopy and thermodynamics of glass analogues*, Ph.D. Thesis, Pennsylvania State University, (1981).

129. C. Nelson, T. Furukawa, and W.B. White, "Transition metal ions in glasses : Network modifiers or quasi-molecular complexes", Mat. Res. Bull. **18** 959-966 (1983).

130. S.A. Brawer and W.B. White, "Optical properties of trivalent chromium in silicate glasses : A study of energy levels in the crossing region", J. Chem. Phys. **67(5)** 2043-2055 (1977).

131. M.A. Marcus and A. Polman, "Local structure around Er in silica and sodium silicate glasses", J. Non-Cryst. Sol. **136** 260-265 (1991).

132. N. Karayianis and C.A. Morrison , *Rare Earth Ion-Host Crystal Interactions 1. Point charge lattice sum in Scheelites*, Harry Diamond Laboratories, HDL-TR-1648 (October 1973).

133. N. Karayianis and C.A. Morrison , *Rare Earth Ion-Host Crystal Interactions 2. Local distortion and other effects in reconciling lattice sums and phenomenological* B_{km}, Harry Diamond Laboratories, HDL-TR-1682 (January 1975).

134. M.T. Hutchings and D.K. Ray, "Origin of crystalline electric field effects on rare earth ions. I. Neighbouring induced moments", Proc. Phys. Soc. **81** 663-676 (1963).

135. M.M. Curtis, D.J. Newman and G.E. Stedman, "Crystal fields in rare earth trichlorides. IV. Parameter variations", J. Chem. Phys. **50(3)** 1077-1085 (1969) .

136. C.K. Jörgensen, *Modern aspects of ligand field theory*, North-Holland, (1971).

137. M.M. Curtis and D.J. Newman, "Crystal fields in rare earth trichlorides. V. Estimation of ligand-ligand overlap effects", J. Chem. Phys. **52(3)** 1340-1344 (1969) .

138. G. Turrell, *Infrared and Raman spectra of crystals*, Academic Press, New York, (1972), p.338, Appendix D.

139. W.G. Fateley, F.R. Dollish, N.T. MacDevitt and F.F. Bentley, *Infrared and Raman selection rules for molecular and lattice vibrations : The correlation method*, Wiley-Interscience, New York (1972).

140. R.P. Leavitt, C.A. Morrison and D.E. Wortman, "Description of the crystal field for terbium(3+) ion in calcium tungstate (VI)", J. Chem. Phys. **61(3)** 1250-1251 (1974) .

141. R. Reisfeld, in *Structure and Bonding*, vol. 13 J.D. Dunitz *et al.*, eds. Springer-Verlag (1973) 58.

142. F. Fermi, L. Tellini, G. Ingletto, A. Vinattieri and M. Bettinelli, "Absorption and luminescence spectroscopy of Eu^{3+} in lead silicate glasses", Inorg. Chim. Acta, **150** 141-146 (1988).

143. E.W.J.L. Oomen and A.M.A. van Dongen, "Europium(III) in oxide glasses. Dependence of the emission spectrum upon glass composition", J. Non-Cryst. Sol. **111** 205-213 (1989).

144. W.M. Yen and P.M. Selzer, eds., *Laser Spectroscopy of Solids*, Springer-Verlag 2nd edition (1986) Chaps. 1 and 2.

145. D.W. Marquardt, "An algorithm for least-squares estimation of nonlinear parameters", J. Soc. Indust. Appl. Math. **11** 431-441 (1963).

146. see for example, **(i)** C. Brecher, H. Samelson, R. Riley and A. Lempicki, "Polarized spectra and crystal-field parameters of Eu^{3+} in YPO_4", J. Chem. Phys. **49(7)** 3303-3311 (1968). **(ii)** J.P. Morley, J.D. Saxe and F.S. Richardson, "The chiroptical luminescence spectra of Eu^{3+} in trigonal $Na_3[Eu(oxydiacetate)_3]\bullet 2NaClO_4\bullet 6H_2O$", Molec. Phys. **47(2)** 379-406 (1982).

147. C.B. Layne, W.H. Lowdermilk and M.J. Weber, "Multiphonon relaxation of rare-earth ions in oxide glasses", Phys. Rev. B **16(1)** 10-20 (1977).

148. J.P. Morley, J.D. Saxe and F.S. Richardson, "The chiroptical luminescence spectra of Eu^{3+} in trigonal $Na_3[Eu(oxydiacetate)_3]\cdot 2NaClO_4\cdot 6H_2O$", Molec. Phys. **47(2)** 379 406 (1982).

149. R. Kuroda, S.F. Mason and C. Rosini, "Anisotropic contributions in the ligand polarization model for the *f-f* transition probabilities of Eu(III) complexes", Chem. Phys. Lett., **70(1)** 11-16 (1980).

150. R. Kuroda, S.F. Mason and C. Rosini, "Crystal structure and single-crystal spectra of $Gd(Eu)Al_3(BO_3)_4$: Anisotropic ligand polarization contributions to the *f-f* transition probabilities in Eu(III)", J. Chem. Soc., Faraday Trans. 2, 2125-2140 **77** (1981).

151. B.R. Judd, "Ionic transitions hypersensitive to environment", J. Chem. Phys. **70(11)** 4830-4833 (1979).

152. J. Hegarty, W.M. Yen and M.J. Weber, "Spectroscopic properties of excited states of ions in glass measured using laser-induced fluorescence line narrowing", Phys. Rev. B **18(10)** 5816-5819 (1978).

153. A. Lempicki, H. Samelson and C. Brecher, "The europium ion in octacoordiante crystal fields : Symmetry, potential and level splittings", J. Mol. Spectrosc. **27** 375-401 (1968).

154. J.A. Capobianco, T.F. Belliveau, G. Lord, D.J. Simkin, J. Tait and P.J. Hayward, "Laser-excited site-selective spectroscopy of Eu^{3+} in sphene ($CaTiSiO_5$) and glasses and glass ceramics of the sodium calcium-aluminum titanosilicate system", Phys. Rev. B **34(6)** 4204-4212 (1986).

155. N. Motegi and S. Shionoya, "Excitation migration among inhomogenously broadened levels of Eu^{3+} ions", J. Lumin. **8** 1-17 (1973).

156. P. Caro, O. Beaury and E. Antic, "L'effet néphélauxétique pour les configurations $4f^N$ en phase solide", J. Phys. (Paris), **37** 671-676 (1976).

157. C.K. Jörgensen, Structure and Bonding , vol. 25 (1976) 2.

158. C.A. Morrison , *Angular momentum theory applied to interactions in solids*, Harry Diamond Laboratories, HDL-SR-87-1(February1987).

159. R.M. Macfarlane, "Optical spectral linewidths in solids", in *Lasers, Spectroscopy and new ideas. A tribute to Arthur L. Schawlow* , W.M. Yen and M.D. Levenson, eds., Springer-Verlag (1987) 205-223.

160. Z. Gu, "Spectroscopic properties of doped silica glasses", J. Non-Crystal. Sol. **52** 337-345 (1982).

161. K.E. Süsse, W. Vogel, D.G. Welsch and B. Wilhelmi, "Photon antibunching in resonance fluorescence from impurity atoms in solids", Opt. Commun. **28(3)** 389-391 (1979).

162. R. Lange, W. Grill and W. Martienssen, "Observation of single impurity ions in a crystal", Europhys. Lett. **6(6)** 499-503 (1988).

163. W.E. Moerner and L. Kador, "Optical detection and spectroscopy of single molecules in a solid", Phys. Rev. Lett. **62(21)** 2535-2538 (1989).

164. W.M. Yen, "Optical spectroscopy of materials with restricted dimensions", Third Int. Conf. on Trends in Quant. Electron., SPIE Vol.**1033** 183-190(1988).

165. W.M. Yen (Private communication), January 1993.